UNIVERSITÉ DE STRASBOURG

École Doctorale de Physique et Chimie

Physique - ED 182

Institut Pluridisciplinaire Hubert Curien

THÈSE présentée par :

Abhilasha Singh

pour obtenir le grade de : **Docteur de l'Université de Strasbourg**

Discipline/Spécialité : **Physique subatomique**

Metrological study of the shape of beta spectra and experimental validation of theoretical models

Thèse dirigée par :	
M. Abdel-Mjid Nourreddine	Professeur Université de Strasbourg
Rapporteurs :	
M. Elias Khan	Professeur Université Paris-Sud
Mme. Muriel Fallot	Maitre de Conférences, Université de Nantes
Autres membres du jury :	
M. Philippe Dessagne	Directeur de Recherches, CNRS/IPHC, Strasbourg
M. Karsten Kossert	Chercheur, Physikalisch-Technische Bundesanstalt, Allemagne
M. Xavier Mougeot	Chercheur, CEA/LNHB, Saclay (Encadrant)

"Science makes people reach selflessly for truth and objectivity; it teaches people to accept reality, with wonder and admiration, not to mention the deep awe and joy that the natural order of things brings to the true scientist."

- Lise Meitner

Acknowledgments

"No one who achieves success does so without the help of others. The wise and confident acknowledge this help with gratitude"

I want to express my warmest and most profound thanks to all people associated with me for their support, friendship and guidance in fulfilling the goals of the PhD.

First of all, many thanks to my thesis director, Prof. Abdel-Mjid Nourreddine, for always encouraging me despite his busy schedule, he has always tried to follow up on the work.

I want to express my sincere thanks to the reviewers, Prof. Elias Khan, Ms Muriel Fallot, for accepting to review this thesis and providing a report. I also want to thanks the other jury members Mr Philippe Dessagne and Mr Karsten Kossert, for agreeing to examine my thesis work.

My deepest gratitude goes to my thesis adviser Mr Xavier Mougeot, who guided me throughout the PhD. I am thankful to him for teaching me many things and having scientific discussions. I appreciate his time devotions, reading and re-reading of my thesis. Working with him was a great opportunity. The way he has taken beta decay studies so far is remarkable and I am glad to be a part of it.

I would like to thank the former heads of LMA and LNHB, Thierry Branger and Loïc De Carlan respectively and also to the present ones, Mark Kellett and Isabelle Aubineau for hosting me in the lab.

My special thanks to Mark, who has always welcomed and supported me. I am going to miss our discussions. I will remember the conferences time with you having scientific and funny talks.

Many thanks to Martin Loidl, who is not only a kind person but also a great experimentalist. It is delightful working with him, and I got to learn neat experimental skills. I am thankful to him for his help in the design of the cooling system of our device. I will always cherish the fun at the conference. I feel good to say that we made a productive team with Xavier for beta spectrometry.

I have no words for the encouragement by Philippe Cassette, his door was always open for me. Whenever I was disappointed by something wrong in an experiment, I would go and discuss, and he always ended up in saying "It is not easy, but you can do it". I am grateful to

him for providing such a pleasant surrounding.

My appreciation also goes to Benoit sabot, the man I disturbed quite often, thanks to him for helping with me all the “DIY” especially fine soldiering of electronics. I am also thankful to him for helping me with the first prototype of our system. He is not only a good colleague but also a friend. I will miss working with him.

I believe that Christophe Dulieu’s help in everyone’s work is very meaningful. I want to thank him for solving my computer-related problems, French learning and also reading my thesis. I cannot express my gartidue for dealing with the organisation of my defense.

Cheick Thiam solved all the problems of my virtual machine; his efforts are so evident. Many thanks go to him for helping me with the simulations on the cluster. I was happy to share the office with you; it was fun learning French with you.

I want to express my deepest gratitude to Carole Frechou, who has always been moral support and stood by the side. I do not have enough words to thank her for a thorough reading of my thesis.

I also want to thank the gamma spectrometry group: Marie Christine, Benoit, Sylvie, Yves and Laurine. I am so much thankful to Sylvie for our discussions over tea breaks, and I am going to miss this.

I would like also to thank all the other members of the LMA: Matias, Vanessa, Christophe and Mikaël including the radioactive source group: Valerie, Didier, Margot, Sophie for helping me with the sources preparation. Special thanks to Didier for devoting his time to teach me the source preparation techniques.

I thank my friends who have always been there for fun consevrations, trips and parties: Pooja, Kamnashish, Shivani, Tripty, Mayank, Ankit, Jonathan, Mikaël, Livia, Oscar and Riham. I cannot express in words the gratitude for Ankush, who helped and supported me for pursuing a PhD in a foreign country. All my friends have been an essential part of this journey.

I am very thankful to the man who taught me the meaning of physics, Dr Amit Tanwar.

In the end, I would like to thank my family: my mother and father, Abhishek (brother), Archana (sister-in-law) and Kihu (niece). I cannot express in words their endless love and motivation even when I am so far away. This is dedicated to them.

Contents

Introduction

This study was conducted in the Laboratoire National Henri Becquerel (LNE-LNHB) which is designated to assume the role of National Metrology Laboratory in the field of ionising radiation. It is one of the laboratories of the Laboratoire d'Intégration des Systèmes et des Technologies (LIST) institute, situated on the site of Paris-Saclay of the Commissariat à l'Énergie Atomique (CEA). The French metrology in general is federated and coordinated by the Laboratoire National de métrologie et d'Essais (LNE).

The mission of LNE-LNHB since 1970 is to implement, maintain and transfer the derived units of the International System of Units (SI) for radioactivity and dosimetry: the becquerel (Bq), the sievert (Sv) and the gray (Gy). It essentially consists in realising calibration standards and ensuring their consistency at both the international and the national levels. This is based on a strong and continuous chain of traceability from the highest precision primary standards to the final users.

In radionuclide metrology, a certain prior knowledge of nuclear decay data is necessary to choose the most suitable instrumentation and method for a given radionuclide standardisation. The LNHB is highly involved in both the measurement and the evaluation of decay data and coordinates the international Decay Data Evaluation Project (DDEP), whose datasets are officially recommended by the BIPM (Bureau International des Poids et Mesures) for the ionising radiation metrology community.

One of the main radioactivity primary measurement technique, namely the liquid scintillation counting technique, requires the precise knowledge of the energy spectrum of the particles emitted in beta decay in order to model the emission of light. The low-energy part of the spectrum is of particular importance as the detection efficiency drastically decreases in this region. The uncertainty budget on the activity of the standard must include a component that reflects the degree of knowledge on this parameter [1].

A few years ago, a theoretical code named "BetaShape" was developed at LNHB for the calculations of beta decays. Among other quantities, this code calculates the energy spectra of the emitted β particles for allowed and forbidden unique transitions and includes a database of 130 experimental shape factors available in the literature. These types of transition can be calculated with good approximation without any nuclear wave functions. The calculations exhibit complexity in the case of forbidden non-unique transitions because of their high sensitivity

to nuclear structure. As each forbidden non-unique transition would require a detailed study and an input from a precise nuclear model, BetaShape treats the transition as an allowed or a forbidden unique one of the same variation of total angular momentum, the so-called ξ approximation [2]. These theoretical predictions must be validated, or constrained, by experimental results especially in the case of forbidden non-unique transitions.

However, measurements of beta spectra are quite rare in the literature nowadays. Numerous experiments had been carried out until the 1970s and the topic suffered from a limited interest since then. The experiments were mainly performed with magnetic spectrometers, proportional counters or liquid scintillation spectrometers and were focused on allowed and first forbidden transitions. Accurate measurement of β decay exhibits many difficulties as the spectra can be easily distorted because of self-absorption within the radioactive source or back-scattering on the detector, for example. In order to eliminate such distortions, the spectra must be corrected, which would require a deconvolution process and the accurate knowledge of the response function of the experimental setup. This type of study has rarely been observed in the literature.

At LNHB, a high-precision technique called "Metallic Magnetic Calorimetry (MMC)" has been developed and adapted for the last ten years to the measurement of β decays from 100 eV to 500 keV end-point energies. The measurements performed with this technique have already contributed to the validation of some theoretical calculations, highlighting the influence of the atomic effects on the shape of β spectra [3]. Despite their performance, Metallic Magnetic Calorimeters are limited to low energy spectra and are too difficult to implement to produce quality measurements in quantity. Therefore, another measurement technique complementary to MMC but with greater flexibility is essential. In this regard, an experimental approach with silicon detectors had been initiated at LNHB. In this case, some measurements were performed with one silicon detector (less than 2π solid angle). The results highlighted the strong distortion of the spectra due to backscattering, and thus partial energy deposit of the electron in the detector [4]. Although those distortions could be corrected, the more the corrections, the more the uncertainty. Improvement of this technique is necessary to reach better performances, to minimise the corrections and thus to obtain better precision.

The main objective of this thesis work is to build a precise β spectrometer based on silicon detectors. The experimental set-up must account for all origins of distortions and limit them as much as possible. The response of the detection system must be known accurately in order to correct for the remaining distortions and then obtain the initially measured spectrum. The experimental shape factors must be extracted and compared to the existing results in the literature and to theoretical calculations.

In this thesis, work will be presented in the following manner:

- In the first chapter, the motivation of the work is discussed together with the basic knowledge of radiation physics required to follow the analysis.

- The second chapter is dedicated to the step-by-step explanation of the developments on the experimental device. Starting from the former experimental set-up at LNHB, we will see the requirements for a revised apparatus. This will lead to the new detection configuration, in a quasi-4π geometry. Further, it will include one of the most critical parts of experiments, the radioactive sources. Their preparation techniques and the procedures will be detailed. The experimental set-up optimisation using Monte Carlo simulations will be explained.

- In the third chapter, an overview is first provided about the methods used. Then, the measurements and their analysis are presented in three stages, following the developments that led to improved performances: preliminary measurements providing confidence in the approach but showing a need for improvements; experiments at room temperature; and final measurements at low temperature (100 K).

- Finally, the development of the deconvolution process for the removal of remaining distortions is explained in chapter 4. Then, by retrieving the actual spectra after corrections, the experimental shape factor extraction is discussed.

"The noblest pleasure is the joy of understanding."

- Leonardo da Vinci

Chapter 1

General aspects

This chapter introduces the context of the study of the shape of β spectra. We briefly start with an overview of nuclear data and their importance. Some significant applications of β spectra are then discussed. Next, a summary and a brief reminder of the basic notions of radiation physics that are needed for the experimental study is given. This also refers to the essential physics associated with the modelling of Monte Carlo simulations used in the analysis of measured β spectra, which is presented in the next chapters. Finally, the historical approaches of measuring β spectra are presented, and the use of Si detectors for this work is discussed.

1.1 Nuclear decay data

Nuclear data are quantitative results of scientific investigations of the nuclear properties of matter. These data describe the physical properties of an atomic nucleus and the fundamental physical relationships governing their interactions. Usually, only a part of the nuclear properties is needed for a specific scientific application. For example, the nuclear reactor community looks at nuclear data mainly as information related to fission yields (the fraction of a fission product produced per fission), while the nuclear structure community thinks of nuclear data in terms of nuclear levels and the associated properties. The nuclear medicine community is more often concerned with radioactive decay data such as α, β and γ radiation energies and emission intensities. Consequently, the databases are elaborated as per the requirements.

Atomic and nuclear decay data cover the following parameters:

- half-life;
- Q-values;
- branching ratios;
- α particle energies and emission probabilities;

– β particle energies, emission probabilities and transition types;

– electron-capture probabilities, ratios of transition probabilities when competing with a β^+ transition and transition type;

– γ transitions: energies and emission probabilities, internal conversion coefficients, conversion electron energies and emission probabilities;

– atomic relaxation: X-ray energies and emission probabilities, fluorescence yields, Auger electron energies and emission probabilities;

– spontaneous fission properties;

– and delayed-particle energies and emission probabilities.

Nevertheless, there is a need for a wide range of research to analyse the Chart of Nuclides, which gathers all known nuclei (see Figure 1.1). Current nuclear datasets lack accurate knowledge for many nuclei and some of their properties. For example, β decays, whose precise knowledge is highly essential for different users, suffer from limited experimental understanding. In the absence of experimental data, theoretical calculations may be used. However, they depend on nuclear models, which are not sufficiently accurate to predict some specific transitions such as forbidden non-unique [2]. This is why experimental studies are crucial.

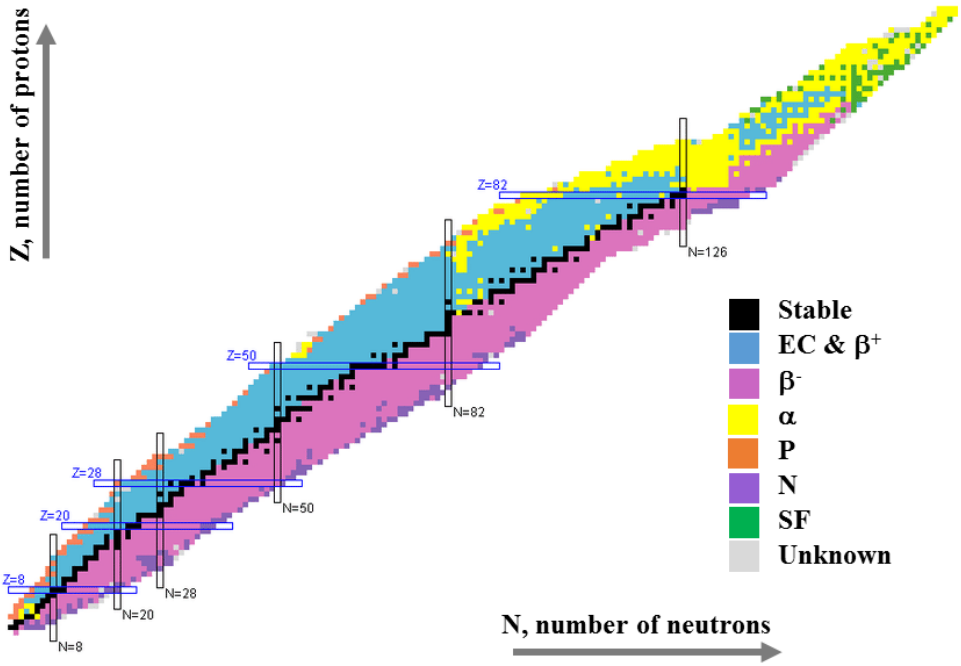

Figure 1.1 – The Chart of Nuclides.

Different scientific results are available in the literature for a particular nucleus, obtained from diverse experimental techniques. However, these results may or may not be compatible with each other. Besides, results are also coupled with their respective uncertainties, whose analysis is critical. Therefore, they need to be scrutinised to find the "best estimate" of the value. In this perspective, nuclear physicists work together on the improvement of nuclear data in order to evaluate and deliver them in a comprehensive manner.

Several nuclear data libraries are available. In the following, the two most fundamental nuclear structure and decay data libraries are presented. They are based on evaluations of the available experimental data.

1.1.1 Decay Data Evaluation Project (DDEP)

The Decay Data Evaluation Project is an international collaboration established in 1995, in an agreement between the Laboratoire National Henri Becquerel (LNHB), France and the Physikalisch-Technische Bundesanstalt (PTB), Germany in the framework of radionuclide metrology. Afterwards, the collaboration was formally established with scientists from the USA and later from China, Romania, Russia, Spain and the UK [5, 6]. The associated library contains comprehensive atomic and nuclear decay data evaluated for about 220 selected radionuclides at present. They are of interest to the ionising radiation metrology community and in nuclear medicine, including pharmaceuticals for both diagnosis and therapy. The DDEP evaluated data are recommended by the Bureau International des Poids et Mesures (BIPM) for all the national metrology institutes around the world and are edited by the LNHB after a peer review process as a volume of the BIPM-5 monograph [7–11]. They are also available on the website of LNHB[1] and published in a pocket format as the Mini-Table of Radionuclides by EDP sciences.

1.1.2 Evaluated Nuclear Structure Data File (ENSDF)

The Evaluated Nuclear Structure Data File is the most complete library of nuclear structure and decay data given in a specific 80-column format, which was designed in 1977 and is still used today with some changes. The International Atomic Energy Agency (IAEA) network of Nuclear Structure and Decay Data Evaluations (NSDD) assembles evaluators who contribute to the database, which is maintained by the National Nuclear Data Center (NNDC) at Brookhaven National Laboratory (BNL, USA). The evaluations are undertaken for a complete mass chain and are updated with the new data available every 10-15 years (depending on the mass chain). These evaluations are published in the *Nuclear Data Sheets* journal and are available on the website of NNDC[2]. At present, the ENSDF database contains almost 19 100 datasets for around 3 346 nuclides.

[1] `http://www.lnhb.fr/nuclear-data/`
[2] `https://www.nndc.bnl.gov/ensdf/`

1.2 Scientific users of beta decay

As discussed in the nuclear data section, the decay properties of radionuclides are essential in many scientific domains. The most important applications requiring good knowledge of β decays are now presented.

1.2.1 Ionising radiation metrology

The objective of radionuclide metrology is to develop and maintain activity standards of radionuclides with the best achievable uncertainties. Some of the activity measurement techniques (e.g. ionisation chambers, gas proportional counters, or liquid scintillation) require accurate knowledge of the emission probabilities at different energies for the radionuclide of interest. For instance, in the Triple to Double Coincidence Ratio (TDCR) method used in the Liquid Scintillation Counting (LSC) technique, the β spectrum is necessary to model the emission of light in order to establish the relationship between the detection efficiency and the experimental TDCR value. The final uncertainty assessment associated with the activity measurement must include the contribution of the β spectrum uncertainty.

Many studies have shown the importance of the β spectrum in the activity measurements of radionuclides [1, 12, 13]. The typical LSC uncertainty is 0.5%. In the study performed to examine the effect of the β spectrum on the activity concentration for ^{63}Ni, Kossert [1] found a significant bias of 1.3% on the final activity if it is determined using a simple theoretical β spectrum or a theoretical spectrum including the atomic exchange effect. A similar study was performed in the case of ^{60}Co, and a bias of 0.5% was again observed depending on the β spectrum used [13].

However, the theoretical calculations are only reliable for allowed and forbidden unique transitions (some exceptions exist). In the case of forbidden non-unique transitions, calculations are more complicated due to their high sensitivity to nuclear structure. This implies that β spectra measurements with the lowest possible uncertainties are essential to constrain and validate theoretical models.

1.2.2 Medical care sector

Development of new pharmaceuticals, in particular for cancer treatment, is an active research field. The use of radionuclides is increasing for cancer therapy. For example, radionuclides such as ^{32}P, ^{89}Sr and ^{131}I have been used for imaging and radiotherapy [14] since the 1930s. Besides, some new radionuclides such as ^{90}Y and ^{177}Lu are also used [15]. The emitted β particles have a short-range in water and are therefore suitable for radiotherapy.

The process of radiotherapy includes the selection of appropriate radionuclides (physical properties: energies, half-lives, etc.), their behaviour within the biological environment and

the carrier molecule with which the radionuclide will be targeted to cancer tumours. This carrier molecule has to be chosen carefully based on its ability (biological mechanism such as oxygenation, vascular permeability, etc.) to target the infected tissues.

Any treatment with ionising radiation requires the exact knowledge of the dose deposition to ensure the security and efficiency in the treatment process. In order to estimate this dose accurately, there are two major aspects to be addressed: the first one is to know the distribution of the carrier molecule in the tumour zone, and its consequences over time; the second is the calculation of the delivered dose in the volumes of interest according to the radionuclide quantity. The β particles emitted by the radiopharmaceutical drug have high ionising power and are the origin of most of the absorbed dose within the tumour [16]. The cell elements that are sensitive to the absorbed dose are polymers (DNA, RNA, proteins) whose spatial structures are typically less than 130 nm.

The linear energy transfer (LET), which is a quantity defining the energy transferred in the medium, increases strongly at low energy for electrons (see Figure 1.2). A better knowledge of the shape of β spectra, especially at low-energy, is thus essential in order to improve the estimation of the dose absorption in the patient's cells [14].

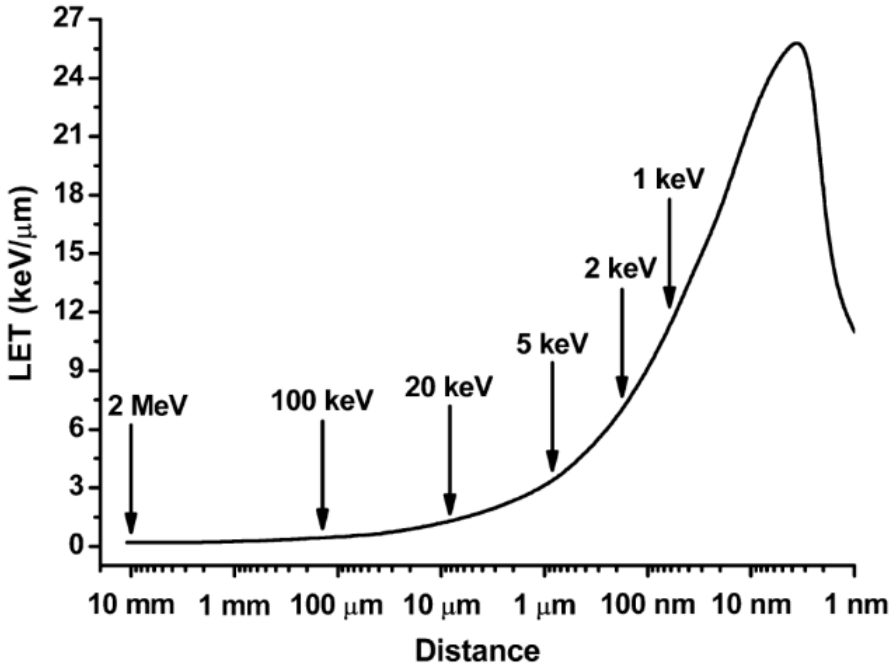

Figure 1.2 – Linear energy transfer (LET) of electrons according to the distance travelled. Figure from [17]

1.2.3 Nuclear power industry

In the nuclear power industry, the source of power generation is a nuclear reactor, and its safety is an important concern. Decay heat, which comes from the decay of produced radionuclides in the core, dominates the thermal power after reactor shutdown. Based on the

identification of the nuclei produced after nuclear fission and their decay chain, this residual power can be estimated using experimental measurements or theoretical calculations. The predictions used to control the reactor are based on general models that must be validated by measurements to ensure their reliability. Good agreement between the residual power measurements and the calculations indicates good control of all the processes involved in the operation of the reactor. However, the estimated residual power has an uncertainty that is determined using the information extracted from the nuclear databases. Therefore, the final uncertainty results from the uncertainties on half-lives, fission yields, nuclear reaction and transition energies, etc. Many studies have shown a significant discrepancy in the decay data for short-lived fission products [18].

Many of these fission products with complex decay schemes are very poorly characterised due to overestimation of the average energy released by the β-particles and an underestimation of the energy carried away by the γ-rays. This poor estimation of the decay heat comes from the so-called "Pandemonium effect" [19]. It is due to measurements of the γ spectra emitted during the decay of fission products with germanium detectors. The decay schemes, including the β branches, are reconstructed from the γ-ray intensities. However, germanium detectors have the disadvantage that their efficiency decreases significantly at high energies. Consequently, the γ-rays from de-excitation of high energy levels are in practice (almost) not observed, and the β branches feeding these levels are poorly determined. Measurements with "Total Absorption Gamma-ray Spectrometry (TAGS)", a technique developed to study the β-decay intensity distribution of fission products, has shown a better understanding of the decay scheme by avoiding the Pandemonium effect [20–22]. In order to improve the decay schemes, many new measurements are being implemented using this technique [23, 24].

Accurate quantification of the residual heat from the decay of fission products after reactor shutdown requires good knowledge of β decays [25]. Indeed, β decays and their energy spectra have a significant impact on the safety operations, on various regulatory constraints and on the economic aspects of nuclear power. It is also a significant impact factor for the fuel management operations after irradiation: fuel unloading, transport, storage and cooling, waste treatment, etc. These quantitative studies require a complete set of nuclear data, reliable estimates and well-established uncertainties [26]. A better knowledge of the shape of the β spectra would improve the understanding and uncertainties of the residual power calculations.

1.2.4 New developments

The direct conversion of energy from radioactive decay to electrical power has attracted great interest. Beta-voltaic batteries are experiencing a renewed interest in recent years [27–32]. Nuclear batteries are ideal for a number of applications requiring long-life energy sources of low power: space probes, pacemakers, microsystems, remote sensors, etc. Thermoelectric devices

use an indirect method to produce electricity. In comparison, beta-voltaic batteries convert the energy of β disintegration directly into electrical current and are therefore much more efficient.

The main idea is to use the current generated in a semi-conductor by electrons emitted from a high activity source. Among the different possible radionuclides, ^{63}Ni is one of the most promising candidates because of its long half-life and the low energy of the emitted particles, which minimises the damage to the semi-conductor and ensures that the radiation does not escape from the battery. In addition, its abundance in nuclear waste produced by nuclear power plants makes it more promising. For instance, Young Rang Uhm has described a beta-voltaic battery using ^{63}Ni in a sandwiched design as shown in Figure 1.3 to enhance the performance of the battery [33]. The source plays a major role in battery performance because a high activity source is necessarily thick, which induces significant electron absorption in the source itself. The usual devices are flat, but ongoing research aims to design three-dimensional geometries using gallium phosphide nanowires to bypass the problem of self-absorption and improve battery efficiency [34].

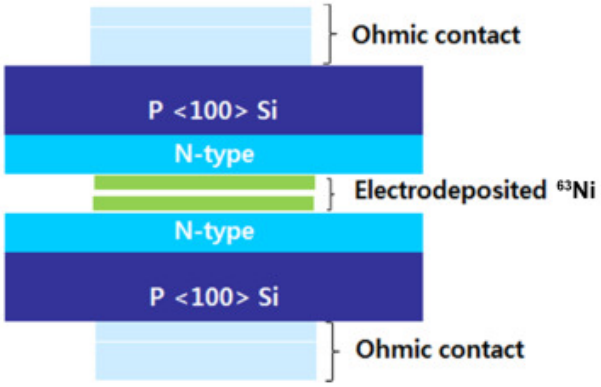

Figure 1.3 – A schematic design for a beta-voltaic battery with electrodeposited ^{63}Ni [33].

1.2.5 Fundamental research

The precise measurements performed in ionising radiation metrology can have a strong impact on fundamental physics. The studies of β spectra have been carried out mostly in the late 1960s and had significantly contributed to establishing the characteristics of the weak interaction, such as parity violation and neutrino helicity.

In nuclear structure studies, the log-ft[3] values of β decays have been used to assign spin and parity to nuclear levels. However, a log-ft value is calculated according to the degree of forbiddenness of the transition, which is defined as per the spins and parities of the nuclear levels. A long-term study of super-allowed transitions performed by Hardy and Towner allowed some of the Standard Model predictions to be tested, and possibly the existence of new physics [35, 36].

[3] "f" is the integral of the β spectrum and "t" is the partial half-life.

The current most accurate constraint on the unitarity of the Cabibbo-Kobayashi-Maskawa (CKM) matrix comes from the study of the ft-values of these super-allowed transitions. However, the precision of log-ft values has reached its limit with current nuclear instrumentation and improving the uncertainties will be a real experimental challenge. This approach is not sufficient to highlight the effects of new physics.

The energy spectrum of antineutrinos emitted from a nuclear reactor has been the subject of intense study in the past decade. Nuclear reactors produce antineutrinos intensively, about 10^{20} s^{-1}. The antineutrinos are emitted from the decay of the fission products of ^{235}U, ^{238}U, ^{239}Pu and ^{241}Pu which are used as nuclear reactor fuel. The fission products are radioactive neutron-rich nuclei, which undergo β minus decay and therefore emit an electron and an antineutrino.

The total antineutrino spectrum emitted by a nuclear reactor results from the summation of thousands of β spectra, as shown on the left of Figure 1.4. A re-evaluation of the antineutrino spectrum from reactors was performed in 2011 for the Double Chooz neutrino experiment. It showed a deficit in the number of observed antineutrinos at a distance within 100 m of the reactor compared to what was expected in the last 30 years. This is called the antineutrino reactor anomaly [37,38]. A new measurement of antineutrino spectra was performed at Chinese Daya Bay reactor, a few years ago. This study also highlighted a disagreement between the theoretical predictions compared to the measured shape of the antineutrino spectra, the so-called shape anomaly [39], shown in Figure 1.4 on the right. These anomalies could be explained by an additional contribution to the neutrino mass oscillation with the existence of a sterile neutrino.

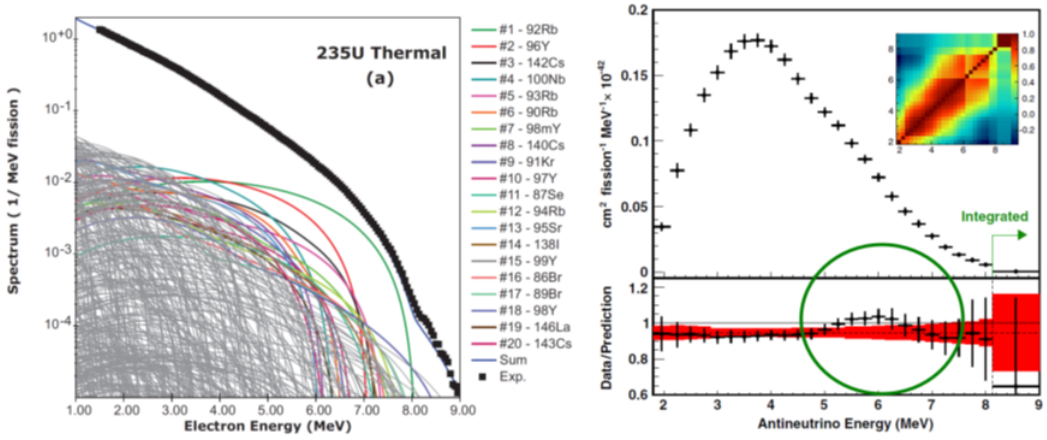

Figure 1.4 – Left: The β spectra emitted from the thermal neutron induced fission of ^{235}U. Taken from [40]. Right: The antineutrino anomaly from measurement at Daya Bay (the famous 6 MeV bump). Taken from [39].

This could be an open door to new physics beyond the Standard Model and has generated many proposals for experiments [41]. However, a study performed by Hayes et al. [42] has high-

lighted the significant influence of the uncertainties associated with β spectrum calculations which questions about the existence of the antineutrino reactor anomaly. Indeed, the calculations carried out using analytical models are not very accurate [43]. Improving theoretical predictions of β spectra can have a major impact on the prediction of the total antineutrino spectrum. However, theoretical calculation improvements would require an improvement in current nuclear models, which have to be constrained and validated by precise experimental studies.

1.3 Radioactive decay

Radioactivity was first discovered by Henri Becquerel in 1896 by observing the spontaneous emission of uranium radiation on a photographic plate [44–48].

Later, Marie Curie coined the term radioactivity, and both were awarded the Nobel Prize in physics in 1903 for the discovery of radioactivity [49]. Further, it led to the discovery of three types of radiations (α, β and γ) based on their ability to penetrate through different thicknesses of material, as shown in Figure 1.5, and on their electric charge (an α-ray is positively charged, β-rays can be positively or negatively charged, and γ-rays are neutral, being an electromagnetic emission). The α particles are the heaviest, and this makes these particles less penetrating than β particles and γ-rays. They typically travel 3 to 5 cm in air and are completely stopped by a sheet of paper. The β particles are the lightest and are free electrons or positrons (not in orbit around an atom). They travel faster than α particles and have greater penetration ability. The γ-rays are mostly high energy radiation which can travel up to 1.5 km in the open air and have a great ability to go through materials.

The three main types of radioactive processes are: α, β (including β^- and β^+ decay) and electron capture (ϵ).

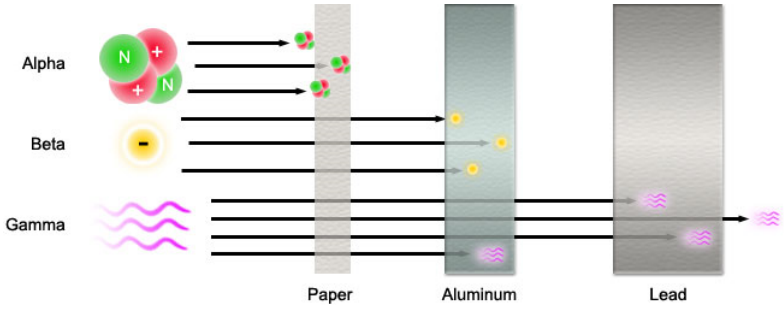

Figure 1.5 – A scheme of the penetration power of α, β and γ radiations through different materials.

1.3.1 α decay

In this type of radioactive disintegration, an unstable nucleus dissipates an excess amount of energy by spontaneously ejecting an α particle. This particle is equivalent to a helium nucleus, having two protons and two neutrons as shown in equation 1.1.

$$ {}^{A}_{Z}X \rightarrow {}^{A-4}_{Z-2}Y + {}^{4}_{2}\alpha \tag{1.1} $$

1.3.2 β decay

Beta decay is a weak interaction disintegration process which occurs between two neighbouring isobars. This is a three-body interaction process due to which the energy and momentum of the transition are shared among the three bodies. This leads to a continuous β spectrum whose shape depends on the nature of the transition. Since the discovery of β radiation, it is known that β particles are about 100 times more penetrating than α particles.

There are three ways of viewing β decay: a general "radiological physics view", a "nuclear physics view" and the microscopic view which is the "particle physics view". They are expressed below.

1.3.2.1 β^- decay

$$ {}^{A}_{Z}X \rightarrow {}^{A}_{Z+1}Y + \beta^- + \overline{\nu}_e \tag{1.2} $$

$$ n \rightarrow p + e^- + \overline{\nu}_e \tag{1.3} $$

$$ d \rightarrow u + e^- + \overline{\nu}_e \tag{1.4} $$

where n stands for the neutron, p for the proton and $\overline{\nu}_e$ for the anti-neutrino having a lepton number of -1. Equation 1.4 represents the transition between the down (d) and up (u) quarks.

1.3.2.2 β^+ decay

$$ {}^{A}_{Z}X \rightarrow {}^{A}_{Z-1}Y + \beta^+ + \nu_e \tag{1.5} $$

$$ p \rightarrow n + e^+ + \nu_e \tag{1.6} $$

$$ u \rightarrow d + e^+ + \nu_e \tag{1.7} $$

where ν_e is the neutrino having a lepton number of +1. Equation 1.7 represents the transition between the up (u) and down (d) quarks. This decay can only occur if the Q value is at least twice the electron rest mass, i.e. 1022 keV.

In this work, we are interested in measuring the energy distribution of electrons from β^- decay. Neutron rich nuclei are more common than the neutron deficient ones due to the Coulomb repulsion of protons. As shown in equation 1.2, this three-body decay shares the momentum

and kinetic energy. However, the kinetic energy of the recoil nucleus is very low due to its high mass and can safely be neglected. We can thus consider that the kinetic energy and the momentum of the decay are shared between the β particle and the antineutrino. The β particle energy varies from null energy to the maximum energy available in the transition (E_{max}), as shown for ^{14}C in Figure 1.6. The shape of the β spectrum depends on the nature of the β transition.

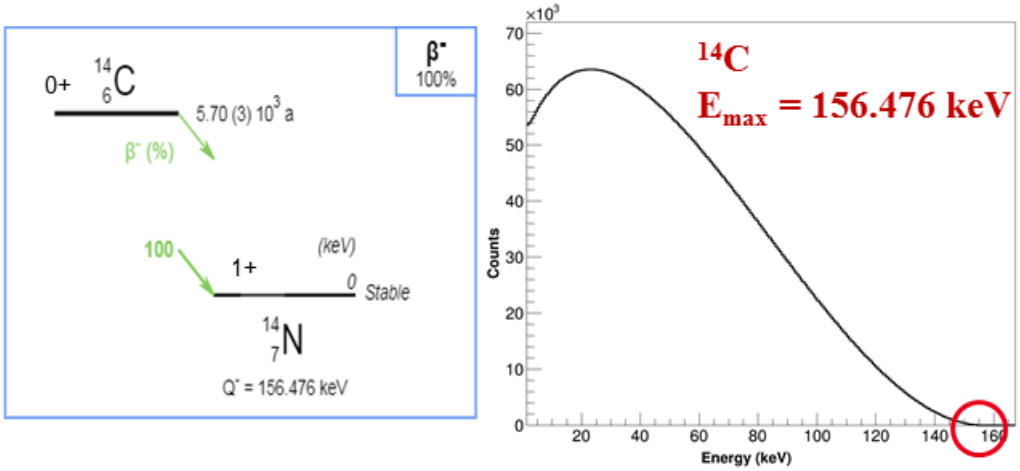

Figure 1.6 – Left: The decay scheme of ^{14}C. Right: The energy distribution of ^{14}C decay calculated theoretically by the BetaShape program [50]. The red circle shows the maximum energy, E_{max}.

1.3.2.3 Classification of beta transitions

The nature of these transitions mainly depends on the following parameters:

- The change in the total angular momentum of the parent (initial state) and the daughter (final state) nuclei. However, the electron-antineutrino pair can carry away orbital angular momentum with quantum number $L_\beta = 0$, 1, 2, etc, and the particles have their intrinsic spin S_β that can be 0, 1 or -1. The total angular quantum number of the initial state being J_i and the final state J_f, one has $J_i = J_f + L_\beta + S_\beta$ and $\Delta J = |J_i - J_f|$.
- The change in the parity between the initial π_i and the final π_f states: $\pi_i \pi_f = (-1)^{L_\beta}$, resulting +1 if the parity does not change and -1 if the parity changes.

According to these parameters, the transitions can be *Allowed*, *Forbidden unique* or *Forbidden non-unique*, as presented in Table 1.1.

1.3.2.4 Calculation of beta spectra

The kinetic energy E of the particles in the continuous spectrum of a β decay is determined by the Q-value and the energies of the initial and final states involved. The total energy of

Nature of the transition	Order of forbiddenness (L_β)	ΔJ	$\pi_i\pi_f$
Allowed	0	$0,1$	$+1$
Forbidden unique	1	2	-1
	2	3	$+1$
	3	4	-1
	4	5	$+1$
	(ΔJ−1)	>1	$(-1)^{\Delta J-1}$
Forbidden non-unique	1	$0,1$	-1
	2	2	$+1$
	3	3	-1
	4	4	$+1$
	ΔJ	>1	$(-1)^{\Delta J}$

Table 1.1 – Classification of β transitions

the particle, i.e. its kinetic energy plus its rest mass, is given by $W = 1 + E/m_e$, with m_e the electron rest mass. The maximum energy E_0 or E_{max} is given by $W_0 = 1+E_0/m_e$ ($m_e = \mathrm{c} = 1$). The momentum of the β particle is given by $p = \sqrt{W^2 - 1}$. The ν particle is assumed to be massless, which means that its total energy is equal to its kinetic energy and its momentum is given by $q = W_0 - W$.

The shape of a β spectrum is proportional to:

(i) pWq^2, which is the phase space factor corresponding to the momentum distribution of leptons;

(ii) the Fermi function $F(Z, W)$ which corrects for the static Coulomb field generated by the nucleus;

(iii) and a shape factor $C(W)$, which accounts for the coupling of the nuclear structure with the lepton dynamics.

The shape can be expressed as:

$$\frac{dN}{dW} \sim pWq^2F(Z,W)C(W)S(Z,W)R(Z,W)dW \tag{1.8}$$

where the screening correction S(Z,W) and the radiative corrections R(Z,W) have been added [2].

Fermi function

The electron rest mass (511 keV) is too small compared with possible maximum energies in β decays (up to 30 MeV) to consider a non-relativistic formalism. Beta particles embedded in the central Coulomb field of the nucleus are thus described by the Dirac equation:

$$[-(\vec{\alpha}.\vec{p}) - \beta - \mathbb{I}\{W - V(r)\}]\psi(\mathbf{r}) = 0 \tag{1.9}$$

where $V(r)$ is the Coulomb potential of the spherically symmetrical nucleus and $\psi(\mathbf{r})$ is the relativistic wave function of the electron. A non-relativistic description would follow the Schrödinger equation:

$$i\hbar\frac{\partial}{\partial t}\psi(\mathbf{r},t) = \left[-\frac{\hbar^2}{2m}\boldsymbol{\nabla}^2 + V(\mathbf{r},t)\right]\psi(\mathbf{r},t) \tag{1.10}$$

However, the Schrödinger equation is unable to explain some effects such as the Zeeman effect, the splitting of spectral line into two or more components in the presence of magnetic field. The study of this effect along with the Stern and Gerlach experiment led to the discovery of the electron spin in 1925 [51, 52]. In 1927, Pauli developed a theory that allowed spin to be introduced into non-relativistic quantum mechanics. The components of electron spin are defined by three matrices also known as Pauli's matrices:

$$\sigma_x = \begin{pmatrix} 0 & 1 \\ 1 & 0 \end{pmatrix} \qquad \sigma_y = \begin{pmatrix} 0 & -i \\ i & 0 \end{pmatrix} \qquad \sigma_z = \begin{pmatrix} 1 & 0 \\ 0 & -1 \end{pmatrix} \tag{1.11}$$

With this formulation, it was possible to obtain theoretical predictions for atomic spectra in excellent agreement with experimental results. Nevertheless, to be comprehensive, it must be expressed in a relativistic form.

In the Dirac equation, the Pauli's matrices are used to define the matrix components of $\vec{\alpha}$ and $\vec{\sigma}$ and the β matrix that are 4×4 matrices defined by:

$$\alpha_k = \begin{pmatrix} 0 & \sigma_k \\ \sigma_k & 0 \end{pmatrix} \qquad \beta = \begin{pmatrix} \mathbb{I} & 0 \\ 0 & -\mathbb{I} \end{pmatrix} \tag{1.12}$$

where $\mathbb{I}$ is the 2×2 unitary matrix, and σ_k are the Pauli's matrices defined in (1.11). It is also convenient to introduce the γ_k matrices defined for all $k = 1, 2, 3$ as $\gamma_k = -i\beta\alpha_k$, $\gamma_4 = -\beta$. The electron wave function is defined in spherical symmetry from the radial wave functions $f_\kappa(r)$ (small component) and $g_\kappa(r)$ (large component) and the spin orbital functions χ^μ_κ by:

$$\psi(\mathbf{r}) = \psi^\mu_\kappa = \begin{pmatrix} S_\kappa f_\kappa(r)\chi^\mu_{-\kappa} \\ g_\kappa(r)\chi^\mu_\kappa \end{pmatrix} \tag{1.13}$$

where $S_\kappa = \kappa/|\kappa|$ is the sign of κ. It is noteworthy that if we define $\mathbf{L} = \mathbf{r} \times \mathbf{p}$ as the orbital angular momentum operator, the L^2 operator does not commute with the Hamiltonian. Instead, the appropriate operator to be considered is $K = \beta\{(\boldsymbol{\sigma} \cdot \mathbf{l}) + 1\}$, with the non-null eigenvalue $\kappa = \pm 1, \pm 2, ...$ The quantity $k = |\kappa|$ is usually introduced.

Starting from equation (1.9), the following coupled differential equations for the radial wave functions can be established:

$$\begin{cases} \dfrac{\mathrm{d}f_\kappa}{\mathrm{d}r} &= \dfrac{(\kappa-1)}{r} f_\kappa - [W-1-V(r)]g_\kappa \\ \\ \dfrac{\mathrm{d}g_\kappa}{\mathrm{d}r} &= [W+1-V(r)]f_\kappa - \dfrac{(\kappa+1)}{r} g_\kappa \end{cases} \tag{1.14}$$

Analytical solutions exist only for free particles ($V(r) \equiv 0$) and for a Coulomb potential generated by a point charge, i.e. in relativistic units ($\hbar = m_e = c = 1$):

$$V(r) = -\frac{\alpha Z}{r} \tag{1.15}$$

where α is the fine structure constant and Z the atomic number. These analytical solutions can be found in [53] and give the usual, analytical Fermi function:

$$F_0 = 4(2pR)2(\gamma_1 - 1)\exp(\pi y)\frac{|\Gamma(\gamma_1 + iy)^2|}{\Gamma(2\gamma_1+1)^2} \tag{1.16}$$

with R the nucleus radius, $\Gamma(\dots)$ the Gamma function and :

$$y = \alpha Z \frac{W}{p} \qquad \gamma_1 = \sqrt{1-(\alpha Z)^2} \tag{1.17}$$

In the Behrens and Bühring formalism [54], the Fermi function $F(Z,W)$ is defined differently as the product of the analytical Fermi function F_0 by the L_0 quantity which corrects for the distortion of the electron wave functions by a non-point like nuclear charge. The Coulomb potential is generated by a uniformly charged sphere of radius R:

$$V(r) = \begin{cases} -\dfrac{\alpha Z}{2R}\left[3 - \left(\dfrac{r}{R}\right)^2\right] & \text{for } 0 \le r \le R \\ \\ -\dfrac{\alpha Z}{r} & \text{for } R \le r \le \infty \end{cases} \tag{1.18}$$

The Fermi function is then defined related to the Coulomb amplitudes α_κ of the relativistic electron wave functions as:

$$F(Z,W) = F_0 L_0 = \frac{\alpha_{-1}^2 + \alpha_{+1}^2}{2p^2} \tag{1.19}$$

With this definition, the effect of a finite size of the nucleus is inherently accounted for in the modelling. However, the equations (1.14) have to be solved numerically even for such a simple potential as in equation (1.18).

Shape factor

In the early 1960s, a formulation of the disintegration theory by Stech *et al.* [55] and by Bühring are proposed in order to separate the kinematics effects, the effects of electromagnetic

interactions between the electron and the nucleus, and the effects related to the nuclear model. Behrens and Bühring gave a complete description of this formulation in [54].

The method is to perform a multipole expansion of both the hadron and lepton currents that are used to define the Hamiltonian. Eventually, the shape factor $C(W)$ can be established as the sum of coefficients linked to the different multipole orders involved in the transition. As a first approximation, but with excellent accuracy, the hadron current contribution can be factored out in the case of allowed and forbidden unique transitions. The β spectrum shape then depends only on lepton parameters and the shape factor is given by:

$$C(W) = (2L-1)! \sum_{k=1}^{L} \lambda_k \frac{p^{2(k-1)}\, q^{2(L-k)}}{(2k-1)![2(L-k)+1]!} \tag{1.20}$$

where the λ_k parameters are defined from the Coulomb amplitudes of the electron wave functions by:

$$\lambda_k = \frac{\alpha_{-k}^2 + \alpha_k^2}{\alpha_{-1}^2 + \alpha_1^2} \tag{1.21}$$

In the case of forbidden non-unique transitions, such an approximation is not possible, and the shape factor depends on transition matrix elements that require the nuclear wave functions of the initial and final states involved in the decay, making the calculation much more difficult. For some first forbidden non-unique transitions, it can be demonstrated that they behave as allowed if the so-called ξ approximation is fulfilled [56]:

$$2\xi = \frac{\alpha Z}{R} \gg E_{\max} \tag{1.22}$$

The shape factor allows us to analyse the results of a β decay experiment, and conversely, they are the only quantities that can be deduced from the experimental data. Experimental shape factors available in the literature have been analysed and recommended in [2].

1.3.3 Electron capture ϵ

Electron capture is in competition with β^+ decay, but it is not a threshold reaction and it can occur at any energy. In this case the transitions are also classified as allowed, forbidden unique and forbidden non-unique. In electron capture decay, an electron from an atomic shell is captured by the nucleus accordingly with the selection rules from ΔJ and $\pi_i \pi_f$. This results in a change of the atomic number with the emission of a neutrino:

$${}^{A}_{Z}X + e^- \rightarrow {}^{A}_{Z-1}Y + \nu_e \tag{1.23}$$

$$e^- + p \rightarrow n + \nu_e \tag{1.24}$$

$$u + e^- \rightarrow d + \nu_e \tag{1.25}$$

Contrary to the case of β decay, the neutrino emission is mono-energetic for this two-body process. The electron capture decay creates a vacancy in an atomic shell that produces a cascade of X-rays and Auger electron emissions.

1.3.4 De-excitation processes

Following the discovery of X-rays by Wilhelm Röntgen in 1895 and of radioactivity in 1896, many nuclear and atomic de-excitation processes resulting from the disintegration of a radionuclide have been identified by physicists: the discovery of γ radiation by Paul Villard in 1900; the study of the Auger electron emission phenomenon by Lise Meitner and Pierre Auger in 1922 and 1923; the explanation of the internal conversion mechanism by Lise Meitner and Otto Hahn in 1924; or the observation of the Coster-Kronig transition by Dirk Coster and Ralph Kronig in 1935.

The de-excitation processes can be separated into two main categories: γ transitions and atomic relaxation.

1.3.4.1 γ transitions

In the electromagnetic spectrum, γ-rays are the most energetic radiations. Resulting from the de-excitation of an unstable nucleus, they are distinguished from X-rays (of atomic origin) on the basis of their nuclear origin [57]. As a consequence of radioactive decay, the daughter nucleus can be in an excited or ground state. Each energy level of the nucleus has a total angular momentum with quantum number J and a parity, which corresponds to the nucleon configuration inside the nucleus. When the nucleus de-excites to a lower energy level, its configuration changes and it looses a certain amount of energy. This energy can be carried away in the form of photon emission (a γ-ray). The emitted energy corresponds approximately to the difference between the initial E_i and final E_f energy level of the transition[4]. Each excited level of a nucleus has a certain lifetime, which can vary from less than 10^{-20} s to many years for an isomeric state.

When the energy is not released by a γ-ray, an electron in an atomic shell acquires directly the energy of the transition and is ejected from the atom with a kinetic energy that accounts for its binding energy in the atomic shell. This phenomenon is called internal conversion. There is a third process of nuclear de-excitation, called internal pair production, which is possible only when the transition energy is greater than twice the rest mass of an electron (1022 keV). However, in most cases, the probability of occurrence is negligible compared to γ emission or internal conversion.

1.3.4.2 Atomic relaxation

By performing studies on cathode rays, Joseph John Thompson experimentally proved in 1897 the existence of a negatively charged particle called an electron, whose existence had been postulated in 1874 by George Johnston Stoney [58, 59]. In 1911, after performing the famous "gold foil experiment", Ernest Rutherford postulated an atomic structure similar to the

[4]The recoil energy of the nucleus is often negligible, of the order of magnitude of few eV.

solar system in which the electrons orbit around a positively charged nucleus [60]. In 1913, Niels Bohr combined the concept of quanta, established a few years earlier by Max Planck, with the Rutherford atomic model and claimed that electrons are "balls" that can occupy particular orbits with fixed angular momentum and energy, and that their distance from the nucleus is proportional to their energy [61]. Later, in 1924, Louis de Broglie postulated "wave-particle" duality which motivated Erwin Schrödinger to explore a better explanation, and in 1926, he came up with the idea of an electron as a wave function rather than a particle in his "Schrödinger's equation", for which he was awarded the Nobel Prize in physics in 1933 [62–64]. From this time, the electron is no longer considered as a ball but as a "cloud of probability" surrounding the nucleus.

In atomic physics, the electron is today modelled as a wave function, and it no longer occupies an orbit, but a certain volume around the nucleus. Although the term "orbital" does not reflect reality, it is still used to describe the energetic distribution of electrons within the electron cloud of an atom. Thus, the electron occupies different orbitals, also called electron shells, whose energy levels are discrete. These shells are described by four quantum numbers:

1. The main quantum number n, associated with a main electron shell;
2. The azimuthal quantum number l (with $l \leq n - 1$), which corresponds to the orbital angular momentum L of the electron, associated with an electron subshell: s for $l = 0$, p for $l = 1$, d for $l = 2$, etc.;
3. The magnetic quantum number m (where $-l \leq m \leq l$), which corresponds to the magnetic moment of the electron associated with an electron orbital;
4. And the electron spin s ($= \pm 1/2$).

Another historical notation exists, the Siegbahn notation which was simplified by the International Union of Pure and Applied Chemistry (IUPAC) and is largely used in X-ray spectroscopy [65–67]. In this notation, a letter is associated to the main quantum number n: K for $n = 1$, L for $n = 2$, M for $n = 3$, etc. The subshell names of electron shells are associated with the values of n and l: 1s for the K shell, 2s and 2p for the L shell, 3s, 3p and 3d for the M shell, etc. The K shell does not have any subshell, but in this notation, the shells of higher energy have three or more subshells. The subshell 2s corresponds to the subshell L_1 and 2p to the subshells L_2 and L_3. The subshell 3s corresponds to the subshell M_1, 3p to the subshells M_2 and M_3 and 3d to the subshells M_4 and M_5; and so on for the higher energy shells. In this notation, each subshell is associated with the binding energy of its electron.

When a vacancy in an inner shell of an atom is created, an electron from a higher energy level will fill this vacancy, releasing a certain amount of energy. This de-excitation (or relaxation) is accompanied by the emission of an Auger electron or an X-ray. The emission resulting from the de-excitation process is then mono-energetic.

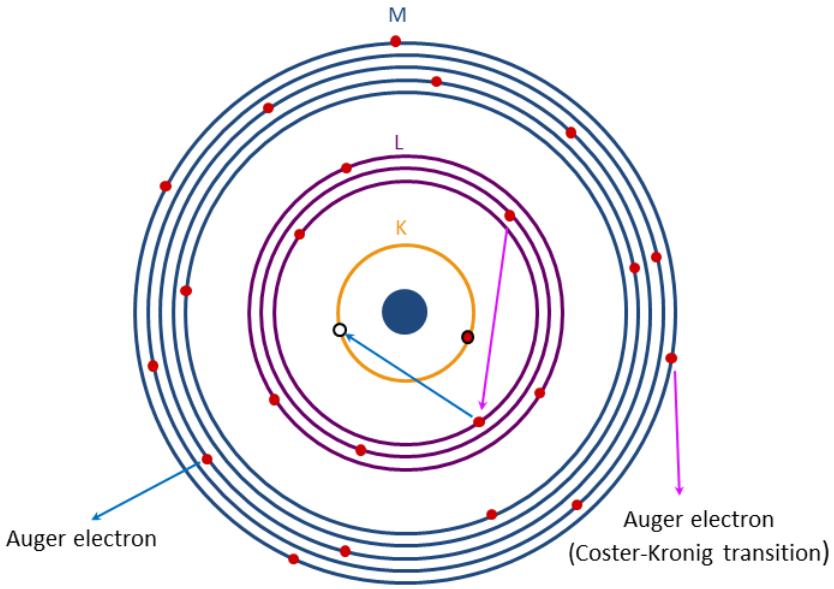

Figure 1.7 – Examples of relaxation processes by: (a) KL_1M_3 Auger transition (blue arrow); (b) $L_1L_2M_5$ Coster-Kronig transition (pink arrow).

The atomic energy can also be released by ejecting another electron from another subshell: this process is called the Auger effect, and the ejected electron is called an Auger electron. The Auger electron has a notation according to the transition. Figure 1.7 shows an example of the emission of a KL_1M_3 Auger electron. The energy of the Auger electron is the difference between the binding energies of the electron shells involved in the transition, minus a correction that accounts for the difference in electron binding energies between the atom in an excited state and its ground state. In some cases, the electronic transition occurs between two electronic subshells. In this case, this emission is called a Coster-Kronig transition and leads to the emission of, e.g. an $L_1L_2M_5$ Auger electron (Figure 1.7).

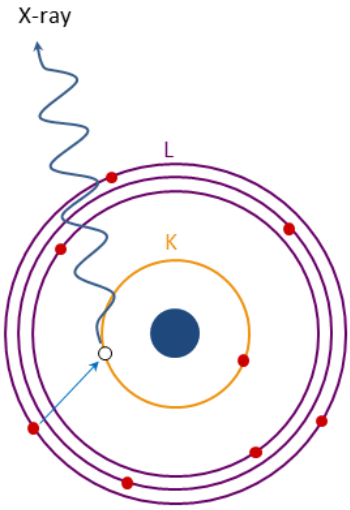

Figure 1.8 – Example of an atomic relaxation process by X-ray emission from K-L_3 electron transition ($K\alpha_1$).

When the atom is in an excited state, and it releases its energy in the form of mono-energetic radiation, it is called X-ray emission. Then, the energy of the X-ray simply depends on the energy difference between the binding energies of the electron shells involved in the transition. The notation of the emitted X-ray corresponds to the initial and final shells. Figure 1.8 provides an example of a K-L_3 X-ray, also called Kα_1 in the Siegbahn notation.

1.4 Electron and photon interactions with matter

After being emitted subsequently to radioactive decay, photons and electrons have a certain probability of interacting in matter. The measurement of β emission spectra depends on the interaction of electrons with matter (e.g. in a crystal used as a detector). Therefore, it is important to introduce the main interactions of electrons in matter, but also radiation-matter interactions, since it can have a major impact on the interpretation of our experiments.

1.4.1 Electron-matter interactions

Different electron-matter interactions exist and they are classified into elastic and inelastic interactions.

1.4.1.1 Elastic interactions

During an elastic interaction, the primary electron can be scattered either by the Coulomb field of an atomic electron or by the nucleus. The primary electron does not loose any energy in such a process or, in practice, only a negligible amount of energy. The elastic scattering by the Coulomb field of atomic electrons is most probable for low energy electrons. The probability of elastic scattering with a nucleus increases with the scattering angle. In this case, there is no photon emitted, and no nuclear excitation occurs because no kinetic energy from the primary electron is transferred to the atomic electron cloud or the nucleus (see Figure 1.9).

1.4.1.2 Inelastic interactions

In inelastic interactions, the incoming electrons can interact with the atomic electrons of the target and excite or ionise the atom. The primary electrons can also interact with the Coulomb field of the nucleus, which will change their path and can decelerate them. Thus, it leads to electromagnetic radiation emission, known as *bremsstrahlung*, which means braking radiation. An electron most rarely deposits its full energy after only one interaction. Therefore, when electrons of a certain energy pass through matter, the energy spectrum becomes wider and asymmetric, with a clear tail at low energy. Depending on the distance between the electron and the nucleus, the photon is created with the kinetic energy of the electron which is transferred to the Coulomb field of the nucleus.

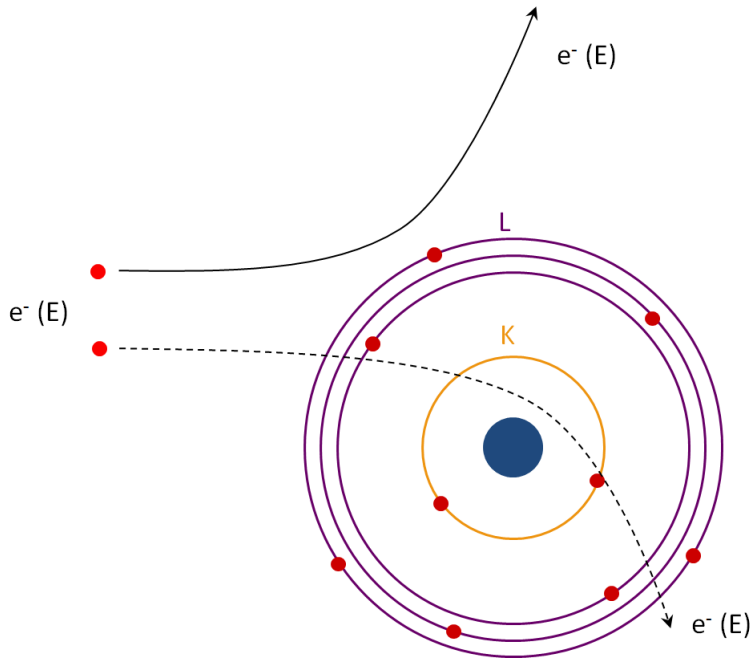

Figure 1.9 – Elastic scattering on the atomic electrons (plain arrow); elastic scattering on the nucleus (dashed arrow).

For a mono-energetic electron that interact by an inelastic collision with a nucleus of a given material, the energy spectrum of the bremsstrahlung photons will be continuous with a maximum energy equal to the kinetic energy of the electron. The "Stopping power" represents the mean energy lost by an electron per unit of distance travelled through the material, written as $-(dE/dx)$. The full stopping power has two contributions, the collisional stopping power $-(dE/dx)_{col}$ due to inelastic collisions and the radiative stopping power $-(dE/dx)_{rad}$ due to the emission of bremsstrahlung. Figure 1.10 shows a summary of inelastic interactions.

Inelastic collisions and energy loss As discussed above, inelastic scattering is the process by which an electron interacts with an atom and transfers energy, especially if the electron energy is below 1 MeV. There are two possibilities for an inelastic collision to occur, leaving the atom in an excited state or an ionised state. In the case of an excitation, an electron from one of its shells acquires the necessary energy to be promoted to a higher energy shell that is not already filled by an atomic electron (because of the Pauli exclusion principle). Then, it will be followed by the emission of X-rays or Auger electrons, according to atomic relaxation processes (see section 1.3.4.2). For ionisation, an electron from an inner shell is ejected. This incident electron loses a more significant part of its energy than in the case of excitation. However, the probability of an ionisation is very low, even if the primary electron energy is very high. This implies the mean energy lost by an electron per collision is very low, and a very high number of collisions will occur until it stops in the matter.

The energy loss due to inelastic collision, $-(dE/dx)_{col}$, was first quantified by Bohr. Then,

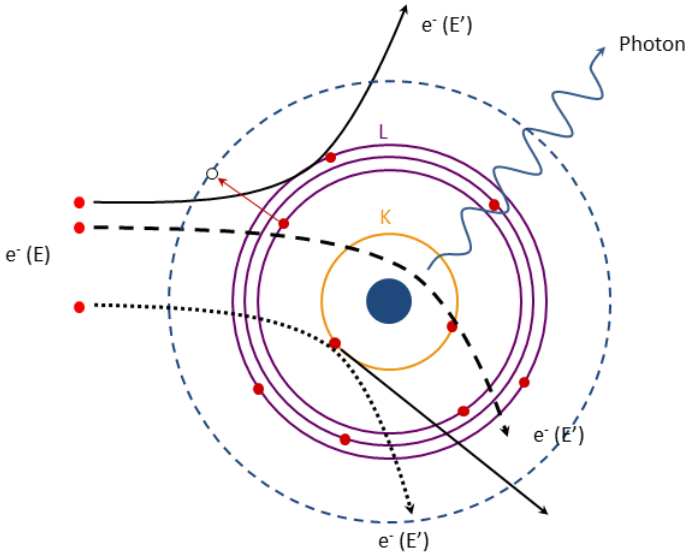

Figure 1.10 – Inelastic scattering by the atomic electrons with excitation (plain arrow), on the nucleus with bremsstrahlung (dashed arrow), and by the nucleus with ionisation (dotted arrow).

with the advancement of quantum mechanics, this concept was developed in particular for light and relativistic particles by Mott, Bethe, Möller and Bloch. The details of these calculations and formulas can be found in [68].

Bremsstrahlung and energy loss From the electromagnetism theory, we know that when a charged particle is deviated from its path or accelerated due to an electric or magnetic field, there is a probability of emission of electromagnetic radiation. If an electron is accelerated, it will "radiate" energy. Bremsstrahlung is the process of energy loss of electrons due to their deceleration in the Coulomb field of a nucleus. The energy loss due to radiative interactions, $-(dE/dx)_{rad}$, was developed by Heitler [69]. The collisional stopping power increases logarithmically with the energy E of the electron, while the radiative stopping power increases proportionally to E. The ratio of both stopping powers for high-energy electrons (i.e. relativistic energies) is given by:

$$\frac{\left(\frac{dE}{dx}\right)_{\text{rad}}}{\left(\frac{dE}{dx}\right)_{\text{col}}} = \frac{(E + m_e c^2)\ Z}{1600\, m_e c^2} \tag{1.26}$$

with $m_e c^2$ the rest mass energy of the electron and Z the atomic number of the material. With the example of silicon, for a kinetic energy of 1 MeV, the loss due to radiative interactions is around 1.6% of the energy loss due to collisional interactions, as shown in Figure 1.11. Generally, below 1 MeV, the radiative energy loss is neglected.

The total energy loss is the sum of the energy loss due to inelastic collisions (ionisation or excitation) and the energy loss due to bremsstrahlung:

$$\left(\frac{dE}{dx}\right)_{\text{tot}} = \left(\frac{dE}{dx}\right)_{\text{col}} + \left(\frac{dE}{dx}\right)_{\text{rad}} \tag{1.27}$$

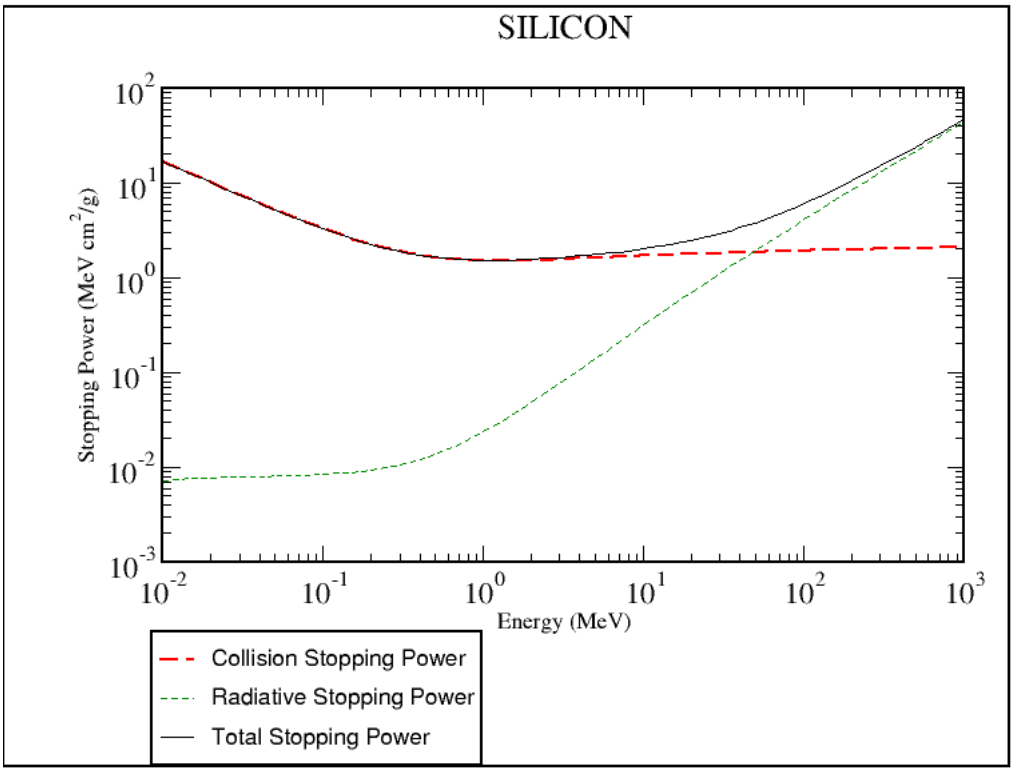

Figure 1.11 – Illustration of the total, collision and radiative stopping powers in silicon as a function of the kinetic energy of the electrons. The Figure was obtained with the ESTAR program, NIST [70].

Before being stopped in a material, an electron will have a great number of interactions and thus changes of directions. Therefore, the length of the path in a material is much greater than the mean distance of penetration. Two parameters can be identified:

– **The range *R*:** It corresponds to the true length of the path. According to Møller, Rossi and Greisen [71], the range can be calculated as:

$$R = \int_0^E \left(\frac{dE}{dx}\right)^{-1} dE \tag{1.28}$$

with R expressed in cm;

– **The practical range** R_p: Since the range does not express the actual depth reached by an electron in matter, it corresponds to the practical range (see Figure 1.12). Theoretical calculation of this quantity is very complicated, but semi-empirical formulas exist. For silicon, it is based on the measurements from Katz and Penfold [72]:

$$\begin{cases} R_p = 0.412\, E^{1.265-0.0954\,\ln E} & 0.01 < E < 3\ MeV \\ R_p = 0.530\, E - 0.106 & E > 3\ MeV \end{cases} \tag{1.29}$$

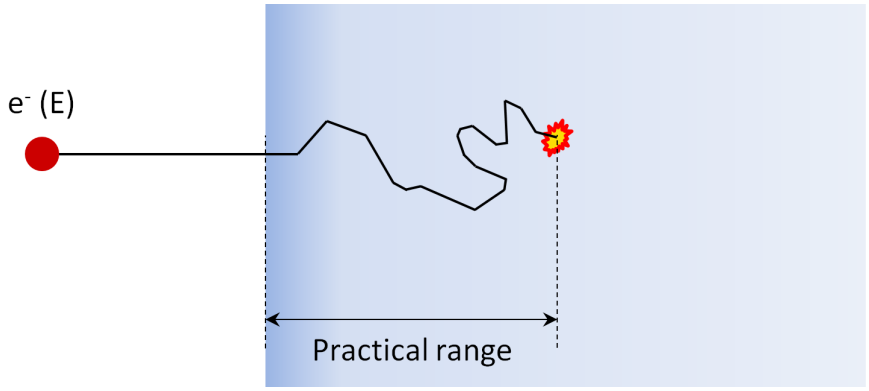

Figure 1.12 – The path of an electron of energy E in a material (in blue). The black line represents the actual range compared to the practical range.

1.4.2 Photon-matter interactions

Following the discovery of the photovoltaic effect by Alexandre Edmond Becquerel in 1839 [73] and the direct observation of the photoelectric effect by Heinrich Hertz in 1887, Albert Einstein was the first to propose in 1905 an explanation of this phenomenon using the concept of a photon and the quantum of energy previously proposed by Max Planck in 1900 during his studies on black-body radiations [74]. He was awarded Nobel Prize in physics in 1921 for the discovery of the law of the photoelectric effect[5].

In 1859, while performing a diffusion experiment on nanoscopic particles, John Tyndall noticed that the light was faintly blue-tinted. After publishing two articles in 1871, highlighting the same effect observed by John Tyndall, Lord Rayleigh demonstrated in 1881 that his equations follow the laws of electromagnetism established earlier by James Clerk Maxwell. This effect was called the Rayleigh effect, a kind of coherent scattering of photons in matter. Later, in 1908, Gustav Mie proposed a more general theory of coherent scattering of electromagnetic radiation on spherical particles, which is known as Mie scattering [75, 76].

In 1906, John Joseph Thomson proposed a theory of coherent scattering of electromagnetic radiations on free electrons. While investigating the change in wavelength of X-rays scattering in the matter, Arthur Compton initially believed that this phenomenon was related to fluorescence radiation combined with a Doppler effect. He performed new experiments in 1922 and revised his judgment by considering light in its corpuscular aspect, with an energy quantum $h\nu$ and colliding with a free electron. Thus, Arthur Compton provided experimental evidence of the wave-particle duality of light, introduced by Max Planck and then used by Albert Einstein for the photoelectric effect, and discovered a new kind of scattering that now bears his name, Compton scattering. Thomson scattering is the limit for low energy photons of Compton scattering [77].

[5] https://www.nobelprize.org/prizes/physics/1921/summary/

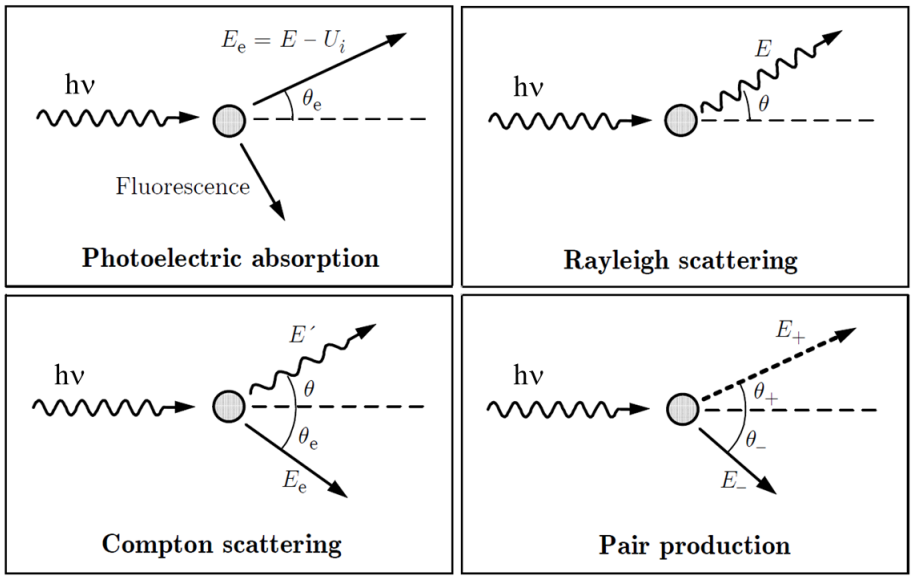

Figure 1.13 – The different kinds of photon-matter interactions.

Patrick Blackett in 1933 was the first to experimentally observe in a counter-controlled cloud chamber the pair production process. A while later in 1933, Francis Perrin proposed the first theory of pair production in the vicinity of an electron [78].

There are four main types of photon-matter interactions: *photoelectric effect*, *coherent scattering*, *incoherent scattering* and *pair production*. Figure 1.13 shows a summary of the different kinds of photon-matter interactions.

1.4.2.1 Photoelectric effect

When an incoming photon interacts with matter, it is absorbed by an atom and, as a result, an electron is ejected from one of its orbitals. In this process, called the photoelectric effect, the photon energy absorbed by the atom is transferred to an atomic electron. The kinetic energy of this ejected electron is equal to the difference of the energy of the photon and the binding energy of the electron:

$$E_e = h\nu - E_X \tag{1.30}$$

with $h\nu$ the initial energy of the photon absorbed, and E_X the binding energy of the ejected electron. The vacancy created by the electron is then followed by a cascade of rearrangement in the atomic shells, i.e. the atomic relaxation described in section 1.3.4.2.

1.4.2.2 Coherent scattering

As explained earlier, there are different kinds of coherent scattering such as Thomson scattering, Rayleigh scattering, Mie scattering or Delbrück scattering. Thomson scattering is a particular case of Compton scattering of a photon on a free electron. It is a very low energy limit of Compton scattering. It means that when the photon energy is lower than the mass

energy of the electron (511 keV), the Thomson model is sufficient to describe the scattering process. For higher energies, the Compton model applies for the photon scattering on free electrons.

In Rayleigh scattering, the photon is scattered by bound atomic electrons without ionising or exciting the target atom, which means that the energies of the incident photons are identical to the scattered ones. For this model of coherent scattering, the electromagnetic radiation must be considered in a waveform. All electrons of the atom follow the oscillating field of the incoming (incident) wave and thus re-emit the oscillation energy in the form of a wave with the same wavelength, but in a different direction. Rayleigh scattering occurs when the wavelength of the electromagnetic radiation is greater than the size of the target object.

The Rayleigh model is a limit of Mie scattering, which is a more general model of coherent scattering on particles, molecules, etc. when the size of the target is very small compared to the wavelength. For low energy photons (below 30 keV), the Rayleigh model is applied. When the energy of photons increases, the transition between coherent and incoherent scattering is progressive, and the Compton model of scattering has to be considered.

1.4.2.3 Incoherent scattering

There are different kinds of incoherent scattering for electromagnetic radiations, here we discuss Compton scattering.

Compton scattering process describes the interaction of a photon with an electron of absorbent material. The incoming photon gets deflected from its original direction by an angle θ and transfers a part of its energy to the electron, called "recoil electron". This electron can be scattered with any angle θ_e and thus its kinetic energy varies from null energy to a fraction of the incident photon energy. Considering a collision of a photon with a free electron, then according to the conservation of energy and momentum, the energy of the scattered photon is:

$$h\nu' = \frac{h\nu}{1 + \frac{h\nu}{m_e c^2}(1 - \cos\theta)} \tag{1.31}$$

with $h\nu'$ the energy of the scattered photon, $h\nu$ the energy of the incident electron, $m_e c^2$ the electron rest mass energy.

1.4.2.4 Pair production

In pair production, the photon interacts with the Coulomb field of the nucleus and is converted into an electron-positron pair. Pair production is possible when the incident photon energy is at least twice the rest mass energy of the electron (or the positron), i.e. 1022 keV. The resulting electron and positron share the excess energy of the photon. During this interaction, the positron looses its energy in surrounding matter and interacts with an atomic electron with which it annihilates and produces two photons of 511 keV each, as shown in Figure 1.13.

1.4.2.5 Interaction cross-sections

The interaction cross-section represents the probability of a photon to interact in the matter. For a photon beam, the mass (μ/ρ) and linear (μ) attenuation coefficients are used to represent the probability of the beam attenuation in a material. The unit of the cross-section is barn, 10^{-24} cm^2, the unit of the mass attenuation coefficient is cm^2·g^{-1}, the unit of the linear attenuation coefficient is cm^{-1}.

- **Photoelectric effect:** The interaction cross-section τ of the photoelectric effect is proportional to the atomic number Z and inversely proportional to the energy of the incoming photon E. It is assumed that the cross-section is highly dependent on Z and less dependent on E. To maximise this effect, it is preferable to use a high Z material. The photoelectric effect is the dominant interaction for low energy photons, as shown in Figure 1.14.
- **Coherent scattering:** The interaction cross-section σ_{coh} of coherent scattering is a complicated function of the atomic number Z and the scattering angle θ. The cross-section is dependent on the atomic form factor, a measure of the scattering amplitude of a wave by an isolated atom, and on the Thomson differential cross-section, which is the interaction cross-section of a coherent photon scattering on a free electron [79]. The coherent scattering is a non-negligible effect of photons at low energy, below 30 keV.
- **Incoherent scattering:** The interaction cross-section σ_{KN} by Compton scattering on a free electron is only dependent on the energy of the incoming electron E. However, when we consider an atom in a material, it is surrounded by many other atoms and hence many electrons. It is necessary to take into account the atomic number Z of the material. The incoherent scattering cross-section σ_{incoh} depends on the incoherent scattering function and on the differential cross-section of Klein-Nishina, σ_{KN}. Basically, σ_{incoh} is considered as directly proportional to Z and inversely proportional to E. Compton scattering is the dominant interaction for intermediate energy photons, as shown in Figure 1.14.
- **Pair production:** The interaction cross-section κ for pair production increases as the energy E increases and as the square of the atomic number Z. This function increases continuously from the energy threshold at 1022 keV. Thus, pair production is the dominant interaction mechanism of high energy photons, as can be seen in Figure 1.14.

The total linear attenuation coefficient μ is defined from the partial attenuation coefficients as:

$$\mu = \mu_\tau + \mu_{\sigma_{coh}} + \mu_{\sigma_{incoh}} + \mu_\kappa \tag{1.32}$$

The total mass attenuation coefficient μ/ρ is most commonly used to determine the attenuation of a photon beam with an energy E in a material:

$$\frac{\mu}{\rho} = \frac{N_A}{A}\,(\tau + \sigma_{coh} + \sigma_{incoh} + \kappa) \tag{1.33}$$

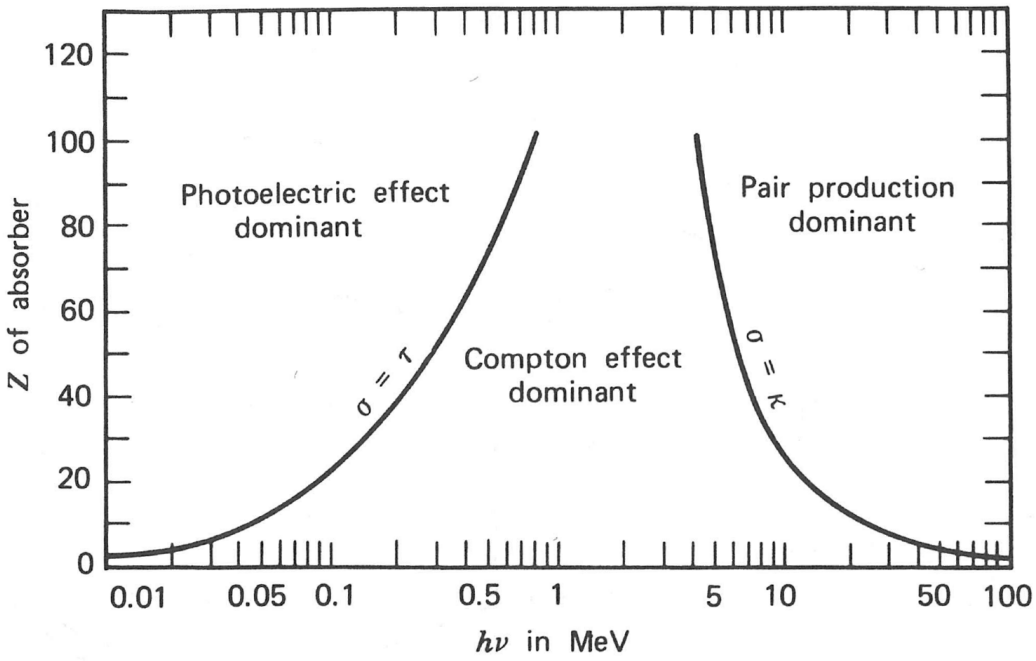

Figure 1.14 – Predominance of each type of interaction in the matter as a function of the energy of the incident photon and the atomic number of the target material [80].

with ρ the density of the material, N_A the Avogadro constant and A the mass number of the material.

1.5 Techniques used for beta spectra measurement

As seen above, there are several phenomena by which electrons can loose their kinetic energy. Therefore, the full absorption of electron energy is not simple, explaining that the precise measurement of the shape of a β spectrum is challenging. The entire detection system must be designed to minimise particle diffusion and backscattering. An ideal "detector" should be chosen with the following characteristics:

- A very low energy threshold with good energy resolution;
- A 100% detection efficiency, i.e. all emitted primary particles are detected, and all the energy is absorbed in the detection volume;
- A linear energy response of the detectors for the entire energy range of the measurement;
- A fast response time in order to detect each interaction, even if this criterion is less important with a good dead time acquisition system.

Ideal measurement of β spectra means the absorption of β-particles as much as possible with the best possible energy resolution. These characteristics depends on the type of detector used

for the measurement. Several techniques have been used for the measurement of β spectra since the 1950s. In the following, we start from the very first measurements performed for the shape of β spectra, and we continue with the evolution of the measurement techniques along with the advancements of nuclear instrumentation. Although the techniques look efficient, none is perfectly suitable for β spectrum measurements. Eventually, we describe how silicon detectors were applied in the past to β spectrometry, as it is the chosen technique for the present work.

1.5.1 Magnetic and electrostatic spectrometry

The measurement of the energies of β-particles was first carried out by their deflection in a magnetic field by Baeyer and Hahn in 1910. In this "direct deflection method", they recorded the β rays emitted from a radioactive wire, which was passing through a narrow slit, on a photographic plate placed at a chosen distance, facing the slit and the radioactive wire. The magnetic field deflection was perpendicular to the rays [71]. Later, Baeyer discovered the presence of definite lines in the β spectrum. As the rays were not focused, the resolving power was very poor. In 1912, Danysz built a new magnetic focusing device [81] based on a semi-focusing principle, which became later the most used device in β spectroscopy. Further, there were several developments in this technique that was very well described by Siegbahn [71].

The basic principle of a magnetic spectrometer is as follows. If an electron of charge e with velocity v is moving in a homogeneous magnetic field B perpendicular to its plane, the centrifugal force exerted moves the electron in a circular path with a radius r. The equation of motion, according to the Lorentz force, can be established as:

$$Bev = \frac{mv^2}{r} \qquad \text{where} \qquad m = \frac{m_e}{\sqrt{1 - \frac{v^2}{c^2}}} \tag{1.34}$$

The momentum is directly proportional to the magnetic field:

$$p = mv = eBr \tag{1.35}$$

The magnetic spectrometer thus determines the distribution of β particles as a function of momentum. The detector counts the number of particles detected for each value of the magnetic field during a constant time interval. These detectors can be of any type, for example, a photographic plate, a photomultiplier tube, etc.

In another kind of spectrometer, called an electrostatic spectrometer, the distribution of β particles as a function of energy is determined by applying a high-voltage. Their main advantage is a low energy threshold, but they are limited by the accessible high voltages, which restricts their application to low energy spectra. A well-known experiment called KATRIN (Karlsruhe Tritium Neutrino Experiment) aims at measuring the tritium β spectrum in order to determine the neutrino mass accurately and is based on the principle of an electrostatic

Figure 1.15 – The KATRIN spectrometer, built to measure the mass of the antineutrino particle with sub-eV precision by measuring the β spectrum of tritium, being moved to the Karlsruhe Institute of Technology (KIT).

spectrometer. This experiment was first started in 2001 and since then, has been contributing to a range of innovative research using this experimental facility [82, 83]. The details of this huge experimental facility can be found on the collaboration website[6]. The KATRIN facility (Figure 1.15) is currently set-up at Karlsruhe Institute of Technology (KIT), Germany.

Magnetic and electrostatic spectrometers have an excellent resolving power (few eV), which makes them suitable for β spectrometry. However, these devices have a small solid angle that significantly reduces the counting rate. Consequently, high activity sources are necessary, resulting in a thick source volume and significant self-absorption of β particles that distorts the measured spectrum. The major drawbacks of this technique are the size of the facility and the time duration of the measurements.

1.5.2 Liquid scintillation

The measurement of the light radiation produced by the transport of ionising particles in some materials is one of the oldest detection techniques [84]. The basic principle of liquid scintillation is based on the interaction of ionising radiation with "scintillating" molecules diluted in an organic solvent [12]. In the sparkling cocktail of liquid scintillation, the solvent is the main component absorbing the energy of ionising particles emitted by the radionuclide. This absorbed energy is transferred in the form of ionisation or excitation, drifts from one solvent molecule to another until it is transformed into heat or trapped by a fluorescent solute molecule.

[6] `https://www.katrin.kit.edu`

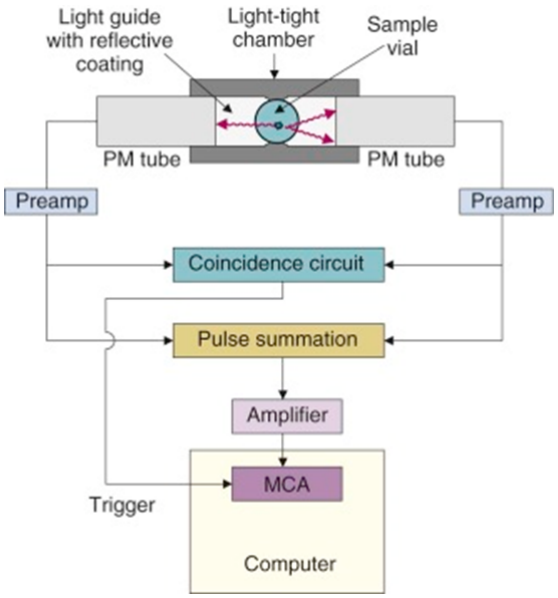

Figure 1.16 – A schematic diagram of a liquid scintillation counter. Figure from [85].

Light from fluorescence is detected utilising photomultiplier tubes (PMT, see Figure 1.16). The photomultipliers are placed face to face in order to detect photons in coincidence and eliminate the background noise of photomultipliers. The major advantages of this technique are an easy implementation, a relatively small duration measurement, and a 4π detection since the radionuclide is mixed with the sparkling cocktail. The light output of this technique is low because it takes about 1 keV of electron energy to produce some photoelectrons in photomultipliers. There are statistical fluctuations in the number of photoelectrons that leads to very poor energy resolution. Thus, even if liquid scintillation is an efficient technique for activity measurement of radionuclides, it is not suitable for β spectrometry.

1.5.3 Cryogenic detectors

The metallic magnetic calorimeters (MMC) have been applied for β spectrum measurement over the past few years. This method was developed at LNHB in collaboration with the University of Heidelberg. Metallic magnetic calorimeters are a particular type of cryogenic detectors, with an operating temperature around 10 mK. They have an excellent linear response, the best among all current cryogenic detectors. It is a well-suited technique for high-precision β spectrometry. The detection system is mainly composed of three modules: a radiation absorber, a thermal sensor and a link which connects either the absorber or the sensor to a cold source (see Figure 1.17).

The radionuclide is enclosed in an absorber usually made of gold, and all the energy emitted by the radionuclide is absorbed. The energy released by the electrons results in an elevation of the temperature, which is directly proportional to the deposited energy and inversely proportional to the heat capacity of the detector. The sensor is made of a paramagnetic material,

gold-erbium (Au:Er). This sensor is exposed to a magnetic field in strong thermal contact with the absorber. The magnetic moment of the sensor changes according to the rise of temperature. The magnetic flux variation of the sensor is measured by a Superconducting Quantum Interference Device (SQUID) magnetometer, characterised by an excellent sensitivity and a very low noise level. The energy deposited by the incident radiation in the absorber is directly proportional to the variation of the magnetic flux measured by the SQUID. The relationship between the variation of the magnetic flux $\delta\phi$ and the deposited energy δE is given by:

$$\delta\phi = \mu_0 \frac{G}{r} \left(\frac{C_s}{C_s + C_\alpha} \right) \frac{\delta E}{B} \tag{1.36}$$

where μ_0 is the permeability of vacuum,
G is a coupling constant between the variation of magnetic moment and the flux measured by the magnetometer,
r is the radius of the magnetometer sensitive loop,
C_s and C_α are the heat capacitances of the sensor and absorber respectively,
B is the external magnetic field.

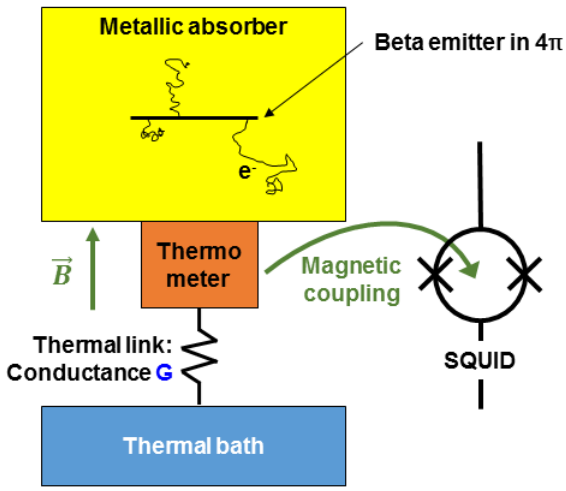

Figure 1.17 – A schematic diagram of a metallic magnetic calorimeter (MMC) device.

There is a weak thermal bond between the detector and a cryostat bath, which brings the detector back to an equilibrium temperature after the interaction. The equilibrium time constant must be large enough not to dissipate heat before it is read by the sensor and small enough to be able to differentiate between each radiation-absorber interaction.

The heat capacity of the detector must be minimised in order to increase the signal, which is achieved by cooling down the detector to cryogenic temperatures. In the case of β spectrometry, the radioactive source is embedded in the absorber itself, allowing a 4π detection geometry. In addition, for a pure β transition, if the absorber is well sized to stop all the emitted electrons, the detection efficiency can reach 100%, and the total energy of the β particles can be absorbed.

The energy threshold is very low since the slightest interaction of radiation with matter causes a release of heat. The limit of the theoretical intrinsic resolution is set by thermodynamic fluctuations, which are very low at very low temperatures. Beta spectrometry with MMCs fulfils the criterion for measuring β spectra of excellent quality. However, there are some limitations to this technique that must be highlighted.

The absorber must be dimensioned in order to absorb all the released energy, from both primary and secondary particles, and care must be taken to limit the radiative phenomena that lead to photons escaping from the absorber. These two points limit the application of MMCs to low-energy β emitters ($E_{max} < 500$ keV). As the time to restore equilibrium is of a few milliseconds, the activity of the source must necessarily be low, typically about 10 Bq, in order to avoid a high detection dead time. Consequently, in order to have sufficient statistics, the acquisition time is typically for several weeks. In addition, to reach the temperature required for the detector, one needs specialised equipment that is very complicated. At LNHB, a dilution cryostat using a ^{3}He - ^{4}He mixture is used.

MMCs remain a very "demanding" and promising technique, very efficient to measure low energy spectra. They allow examination of very fine effects due to atomic structure that is not achievable with traditional techniques. However, for energies higher than 500 keV, one needs to find another technique.

1.5.4 Semi-conductor detectors

Semi-conductor materials have been in use since the 1960s in many fields. They became even more popular in nuclear physics when the nuclear physicists found the semi-conductor detectors better than the well-known gas chamber at that time. The most important difference was the higher energy resolution in semi-conductor detectors, ten times better than the gas chamber.

Silicon (Si) and germanium (Ge) detectors are the most commonly used. Silicon detectors are preferred for charged particle detection, whereas germanium detectors have a finer energy resolution and are generally used for γ-ray spectroscopy.

Commercial Ge detectors are ultra pure and packed under vacuum in a sealed cylinder to protect the Ge crystal. This cylinder has a front face window made of a beryllium foil of hundreds μm thickness. Such an entrance window can absorb electrons of energies up to 120 keV, which makes Ge detectors unsuitable for the measurement of β particles.

Si detectors are an excellent choice for electron detection and have been used since the 1960s. Their backscatter factor on the detector surface is lower than for Ge as this phenomenon is dependent on the atomic number Z of the material. When Z is high and the energy of the electron is low, this phenomenon is more probable. As the atomic number of silicon ($Z = 14$) is lower than that of germanium ($Z = 32$), the electrons tend to scatter much less on the surface

of a silicon detector.

Measurements of β spectral shape have been carried out using Si detectors in the 1960s and the 1970's [86–89]. Some of these implemented devices have also been improved by adding NaI(Tl) detectors in order to perform β-γ coincidence measurements for the β emitters with multiple transitions. The results obtained showed the efficiency of this simple detection technique, which can be used for the study of β decay energy spectra.

However, there are few measurements available in the literature compared with the 20 000 β transitions present in the ENSDF database. A recent compilation of all the experimental shape factors [2] of single transitions highlighted that among 130 experimental shape factors in total, 36 are from allowed transitions, 25 are from first forbidden unique transitions and 53 are from first forbidden non-unique transitions. These experimental shape factors were not measured in the entire energy range of the spectrum [90–92]. The shape factors available in the literature for ^{99}Tc, a second forbidden non-unique transition, are shown in Table 1.2 as an example. As can be seen, most of the measurements were performed in the 1960s and the shape factors are not consistent with each other.

Shape factor	Method of measurement	Energy range	Reference(s)
$p^2 + q^2$	Magnetic spectrometer	$>$ 140 keV	Taimuty (1951)
$(0.5 \pm 0.13)\, p^2 + q^2$ or $p^2 + 2q^2$	Magnetic spectrometer	$>$ 50 keV	Feldman and Wu (1952), Wu (1955), Behrens and Szybisz (1976)
$(0.49 \pm 0.04)\, p^2 + q^2$ or $p^2 + 2.05q^2$	Plastic scintillator detector	$>$ 50 keV	Snyder and Beard (1966)
$q^2 + 0.54\, p^2$	4π Si(Li)	$>$ 50 keV to 250 keV	Reich and Schüpferling (1974)

Table 1.2 – Shape-factor functions for ^{99}Tc as derived from several references.

The spectra, based on these factors, shown in Figure 1.18, show the discrepancy in the shape of the spectra. The detailed literature survey shows that these measured spectra require some corrections such as self-absorption, scattering and backscattering, etc., in order to extract precisely the initially emitted spectrum [90]. However, those corrections were not always taken into account in the results, which leads to the conclusion that new measurements are essential.

The spectra of ^{36}Cl decay from all the experimental shape factors available in the literature are shown in Figure 1.19, showing the discrepancy in the different shape factors again. Generally, in the literature, information such as radioactive source preparation, detector dead layers, etc. is not detailed. However, we will see in the next chapter that the corrections due to physical phenomena (self-absorption, scattering, backscattering, etc.) cannot be neglected and have a significant impact on the shape of a β spectrum. Moreover, it has already been observed that even a small distortion in the β spectrum can have a significant impact on applications [1]. This

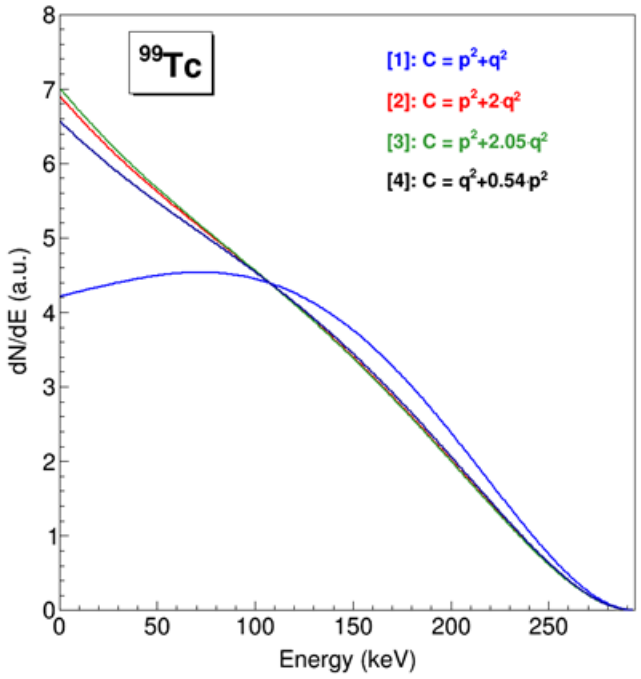

Figure 1.18 – Comparison of the experimental shape factors of ^{99}Tc decay, a second forbidden non-unique transition. The references correspond to the ones in Table 1.2 [90, 93–95].

clearly shows the need for new precise measurements in order to extract accurate information on the β spectral shapes. This would allow us to improve our experimental and theoretical knowledge of β decays.

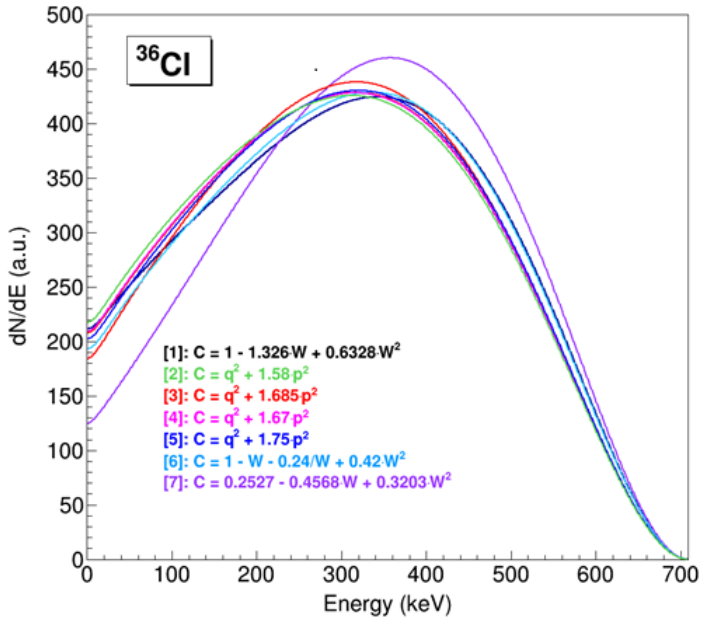

Figure 1.19 – Comparison of the experimental shape factors of ^{36}Cl decay, a second forbidden non-unique transition. The references correspond to [86, 90–92, 95–98]

At LNHB, the β spectrometry studies are conducted with two detection techniques: cryogenic detection technique (Metallic Magnetic Calorimetry) and Si detectors. The measurements performed with MMC detectors are very precise, but there are some limitations ($E_{max} < 500$ keV) as already discussed. Besides, MMC measurements also need good comparison with precise measurements from different techniques. To perform measurements at higher energies, there is a need for another technique. This is why a spectrometer based on a single Si detector was developed in 2011 [4]. However, the measurements showed significant distortion, and their correction introduced a large uncertainty, a critical point for a metrological study of β decays. In order to reduce the uncertainty on the measurement, it is vital to measure the β spectra as close as possible to the initially emitted spectra.

The main objective of this doctoral thesis is to develop a 4π β spectrometer with two Si detectors (Passivated Implanted Planar Silicon or Silicon-Lithium). This will also allow us to compare the measurements performed with Si detectors and high-precision measurements performed with MMC in a common energy range. Furthermore, MMCs do not allow to measure high statistics, something possible with Si detectors.

"You can't solve a problem on the same level that it was created.
You have to rise above it to the next level."
- Albert Einstein

Chapter 2

Experimental studies on the detection system

Beta spectrometry consists of the study of the shape of β spectra, which is the energy distribution of β particles resulting from a radioactive β decay. When a β particle interacts in the detector volume, the output signal is processed by the electronic system to measure the signal amplitude and to increment the histogram channel according to this amplitude value. For a silicon detector, since the amplitude of the signal is directly proportional to the deposited energy, the measured histogram is the characteristic energy spectrum of the measured radionuclide. Beforehand, it is necessary to determine the correlation between the channel number and the energy, which is performed by measuring mono-energetic lines from well-known radionuclides. This step is known as the energy calibration of the detector.

In β spectrometry, the measured spectrum can differ largely from the initially emitted spectrum. Indeed, the shape of the measured spectrum can be distorted by:

- The detector characteristics: the active volume, the energy resolution and the thickness of the dead layer on the silicon crystal.
- Physical phenomena: the electron scattering and backscattering on materials of the detection system, the bremsstrahlung phenomenon which creates an additional component on β spectrum, or the self-absorption of radiations within the radioactive source.

This chapter presents the developments performed on the β spectrometer during this thesis and its design based on the specific needs of β spectrometry.

At LNHB, β spectrometry had already been started in the past. The aim of current work is to rethink and rebuild the former experimental set-up in order to perform more accurate measurements to reach lower uncertainties on the shape factor of β spectra. In this chapter, the former experimental set-up is briefly discussed. A part of this set-up has been reused in its original form, and later modified according to the new requirements. All the different elements associated with the measurement system are discussed in detail.

2.1 Former developments

An experimental device, based on single silicon (Si) semi-conductor detector was developed in the past at LNHB by C. Bisch [4]. The device was designed after taking into account certain physical phenomena (diffusion and scattering of electrons, self-absorption in the source). The measurements were performed using a Si detector of 500 μm thickness and 450 cm^2 surface area. The position of the source was precisely controlled with a translation feedthrough, and the detection geometry was thus less than 2π. This set-up was optimised using GEANT4 Monte Carlo simulations [4]. The operational system is shown in Figure 2.1. A schematic 3D diagram is shown in Figure 2.2. The components associated with the device are as follows:

(i) On the top of the detection chamber, the flange was connected to a BNC connector. Two copper wires (from the connector) were connected to the detector located at the centre of the detection chamber. Outside the detection chamber, a preamplifier was directly connected to the flange *via* a BNC connector.

(ii) The flange at the back of the cube allowed the connection of a vacuum gauge to measure the pressure within the detection chamber.

(iii) The left and bottom flanges were connected to the valve system that isolated the detection chamber and maintained the vacuum during the change of the source.

(iv) The flange on the right was connected to a copper finger plugged in an external Dewar in order to extract heat from the detector outside the chamber. The detector was placed in a copper holder that was attached to the cold finger utilising a clamp.

(v) Finally, the flange at the front of the cube was blank. It allowed easy access to the interior of the chamber.

In a preliminary study, the β spectrum distortion in the detection chamber (under vacuum) was analysed according to the materials and dimensions chosen [99]. The study highlighted that the larger the area of the chamber, the easier it is to obtain good vacuum, thus limiting the scattering phenomenon. However, the vacuum pump used at that time was not sufficiently powerful and emptying a large volume was taking a long time. Taking into account this constraint, the vacuum chamber was finally manufactured with aluminium in a cubical form whose side is 170 mm.

Another study was dedicated to the cooling system. Indeed, the main difficulty was to connect the stainless steel tube surrounding the cold copper finger from the Dewar with the vacuum chamber. After several attempts, the copper finger, surrounded by a stainless steel tube outside the chamber was joint to the copper rod also shielded by stainless steel tube *via*

Figure 2.1 – Experimental set-up for β spectrometry, developed at LNHB in 2012.

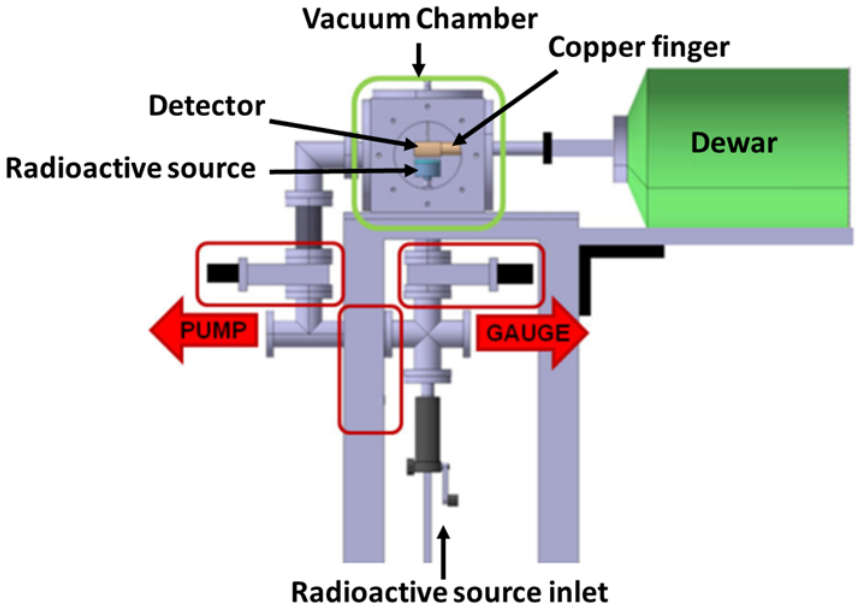

Figure 2.2 – Diagram of the experimental device developed by C. Bisch with a silicon detector precisely positioned in a dedicated vacuum chamber, the radioactive source being inserted by means of a translation feedthrough.

KF40[1] joint (see Figure 2.3). A specific glue was used to maintain the copper finger within the stainless steel tube from the chamber to the KF40 connection. In order to reach a good vacuum around the copper finger throughout, there was an additional valve opening on the Dewar side. This allowed pumping from both sides and reaching a good vacuum. This opening is a stainless steel tube with a 6 mm diameter, welded to the stainless steel tube. In this configuration, the pressure reached inside the chamber was 10^{-6} mbar [4].

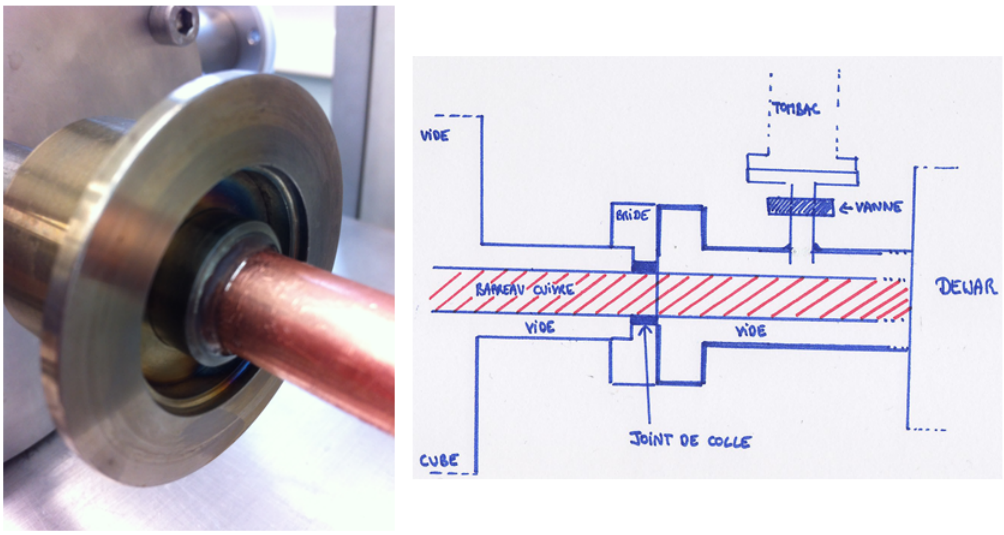

Figure 2.3 – Left: The glue joint seals the detection chamber. The edge visible in the picture is a KF40 joint. Right: Diagram of the area between the detection chamber and the Dewar [4].

2.2 The new 4π geometry of the detection system

The most important part of this measurement system is the detection geometry. The previous configuration was ideal for easily changing the source to measure. However, the solid angle was less than 2π, leading to a strong distortion of the measured spectrum due to the backscattering of the β particles (this is illustrated below on Figure 2.9).

In order to improve the absorption of β particles, it is needed to have a 4π detection geometry. Therefore, a two-detector system has been very carefully designed by studying its geometry using PENELOPE Monte Carlo simulations (see section 2.6) and placed inside the vacuum chamber. At LNHB, four silicon detectors are dedicated to β spectrometry: two Passivated Implanted Planar Silicon (PIPS®) detectors and two silicon-lithium [Si(Li)] detectors.

For a very precise measurement, especially in the case of β particles, it is preferable to have a detector with the thinnest possible entrance window in order to minimise the energy loss within the dead layer of the detector. The ion implantation technique has the great advantage

[1]KF stands for Klein Flange, which is a flange for vacuum available in different dimensions. Here, the diameter is 40 mm.

of providing a maximum thickness of 50 nm equivalent silicon for the PIPS® entrance window, which corresponds to stopping electrons with 1.3 keV kinetic energy. The first measurement device is designed for the detection of electrons of maximum energy 850 keV. This configuration consists of two identical PIPS® detectors fully depleted, each of 1 mm thickness and 300 mm^2 surface area. In the active volume of 1 mm thick Si detector, electrons of energy up to 850 keV can have full energy deposition [70].

The ideal configuration for a 4π geometry is a sandwich of two detectors with a radioactive source in the middle. However, a direct sandwich of a radioactive source would contaminate the detectors and the detector holders, which of course has to be avoided. Moreover, the two standard PIPS®, manufactured by Mirion Technologies, are encapsulated in a metal housing with a 0.9 mm distance between the metal surface and the silicon surface. Consequently, the aim was to find the best compromise according to the requirements and the constraints.

The detection system was designed using 3D CAD (Computer Aided Design) SOLIDWORKS software. These pieces were first printed using a plastic 3D printer available at LNHB (see Figure 2). The whole holder configuration allows a compact geometry and consists of four pieces: two pieces to place the detectors and two closing plates. In the centre part of both detector holders, there is a dedicated design to place a radioactive source ring (see Figure 2b), which ensures a reproducible placement of the source. Furthermore, the semi-cylindrical structure for each detector holder appearing (see Figure 2a,b) is designed to fix the assembled detection system on the copper finger in the detection chamber. Apart from this, there is a small hole at the centre dedicated as a chimney to facilitate the vacuum around the radioactive source. Figure 2 shows the prototype of the 3D printed pieces and tested by placing detectors inside.

After this first approach, some further modifications were performed in the design (see Figure 2.5). One of them was the inclusion of a copper plate to hold the preamplifiers, to get them as close as possible to the detectors. The advantage of this short distance between a detector and its corresponding preamplifier is discussed further in detail in section 2.4.

With this compact geometry, the distance between the silicon surfaces of the detectors was minimised to 3 mm, with the radioactive source in the middle. This configuration allowed us to obtain a quasi-4π detection geometry with the available detectors. In the end, the device is mounted on the copper finger inside the vacuum chamber (see Figure 2.6).

The second measurement device in an almost 4π geometry has been designed for two Si(Li) detectors in the same configuration as for the PIPS® detection system (Figure 4). Furthermore, we managed to obtain a distance of 2.4 mm between the detector surfaces, thanks to the manufacturing team. A Monte Carlo study has been performed for a β spectrum of end-point energy of 2278.5 (16) keV using this Si(Li) device geometry and is discussed in section 2.6.

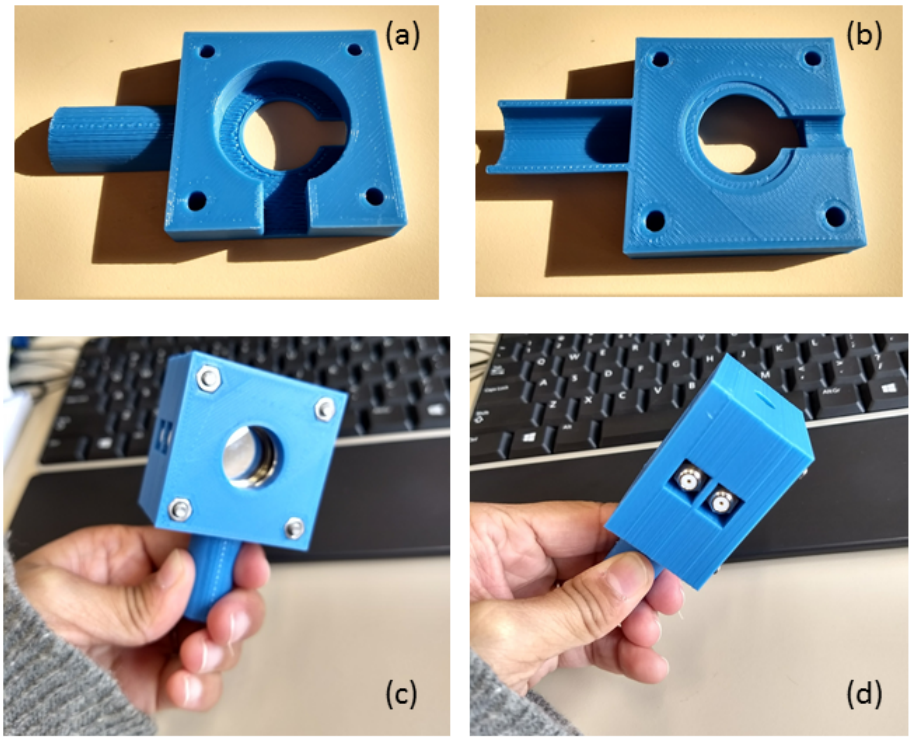

Figure 2.4 – Detector holders printed in plastic using 3D printer for the optimisation and test. Up (a,b) are the holders of each detector. Bottom (c,d) the plastic detection system after placing the detectors.

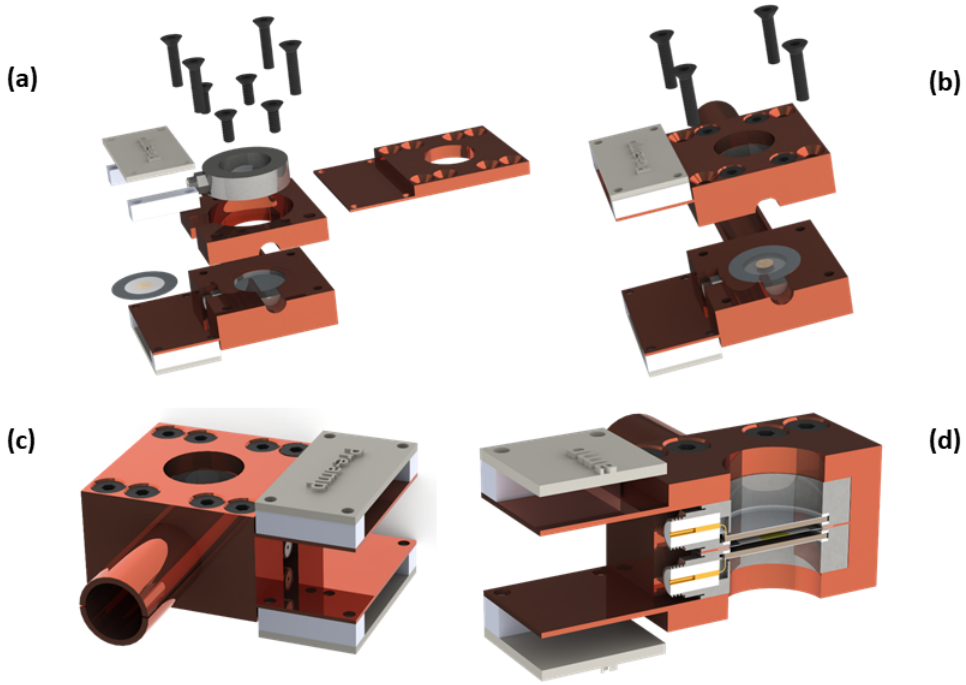

Figure 2.5 – Final 3D picture of the detection system. (a) An exploded view of the pieces of the detection system. (b) Two detectors in their respective detector holder. (c) The whole detection system in measurement configuration. (d) A cut view in the middle of the detection system.

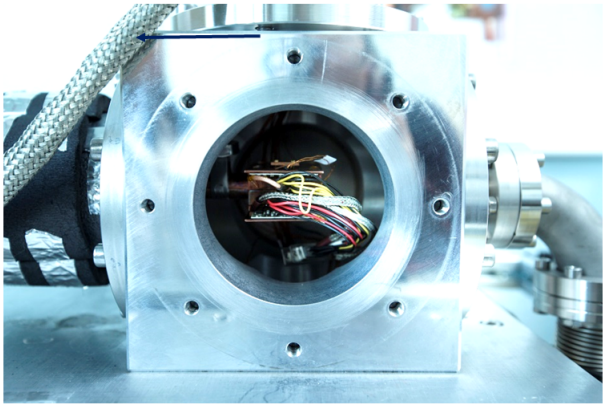

Figure 2.6 – The assembled device mounted on the cold finger inside the detection chamber.

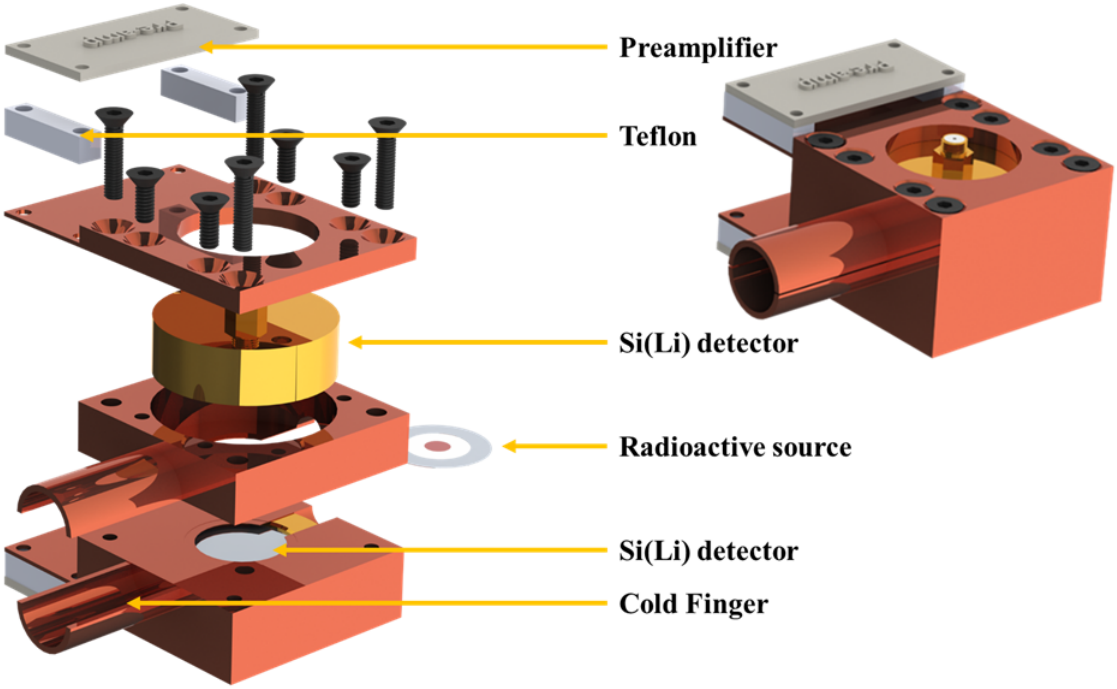

Figure 2.7 – 3D picture of the detection system with Si(Li) detectors. The distance between the detectors is 2.4 mm in the measurement configuration (right).

2.2.1 Passivated Implanted Planar Silicon detectors

As discussed in chapter 1, the properties of silicon semi-conductors are particularly well adapted to the requirements of β spectrometry.

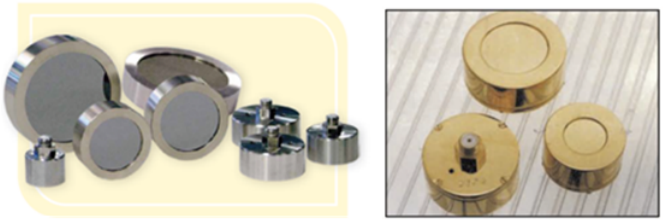

Figure 2.8 – Left: PIPS®. Right: Si(Li) detectors. Figure from [100].

There are different types of silicon semi-conductors (see Figure 2.8). The operating principle of semi-conductors is very well-known and explained in detail in [80].

PIPS® detectors have been chosen because of their particular fabrication technique, which provides an advantage over other silicon detectors. The ion implantation technique allows introducing doping impurities at the surface of a semi-conductor detector by exposing it to an ion beam, produced by an accelerator [101]. Nowadays, the manufacturing of Si detectors is a combination of ion implantation technique and passivation of silicon junction detectors [102].

When a β particle interacts in the silicon detector, it creates an equal number of electron-hole pairs whose origin and mobility are explained by band theory [103]. This interaction corresponds to the deposited energy in the detector. However, it is not directly measurable and requires an acquisition chain to obtain an equivalent energy spectrum [80]. This will be discussed in section 2.4. When the high voltage is applied to the electrodes, an electric field is created in the semi-conductor. This field drifts the charges (electrons and holes) towards the anode and the cathode, which induces a current between the detector terminals. There is some finite conductivity in the detectors, even without any ionising radiation, in the form of leakage current.

The leakage current can add to the electronic noise. However, it is deficient in PIPS because the edges of the junction are enclosed within the volume of the silicon crystal. Besides, crystal doping is performed by ion implantation, which reduces the dead layer thickness of the entrance window to about a hundred of nanometers SiO_2 equivalent [100]. Since the electrons loose energy in this dead layer, it is important to have it as thin as possible. The surfaces are aluminised to create the ohmic contacts on the front and the back of the detector, which makes it robust and prevents from external damage [100]. The only disadvantage of these detectors for β spectrometry is that their manufacturing is limited to an active volume of 1 mm thickness, equivalent to electron energy of 850 keV. This thickness is not sufficient to measure β spectra of a few MeV maximum energy. It is, therefore, necessary to use another type of silicon detector

with thicker volume.

2.2.2 Silicon-Lithium detectors

Silicon Lithium detectors, commonly known as Si(Li), are manufactured using lithium-drift technology. These detectors are commercially available in a wide range of thickness from 2 to 10 mm. Generally, the manufacturers of Si(Li) detectors recommend to maintain them at liquid nitrogen temperature to avoid the redistribution of lithium drift with temperature fluctuations [80]. In addition, due to their large thickness, leakage currents can contribute significantly to noise at room temperature. It is, therefore, necessary to handle these detectors carefully and operate with cooling at liquid nitrogen temperature. The manufacturing process of Si(Li) involves a dead layer thickness at the detector entrance window of 200 nm SiO_2 or silicon equivalent, which corresponds to stopping electrons of 5.3 keV kinetic energy. The silicon crystal of Si(Li) detectors used in this work has a thickness of 5 mm with 500 mm^2 surface area.

2.3 Optimisation of the detection chamber

As already mentioned, the measured spectrum resulting from a β decay can be distorted by several factors. The distortion due to physical phenomena can clearly be seen on the shape of the ^{14}C measured spectrum in Figure 2.9. In principle, a measured spectrum can be unfolded with several different methods using the response function of the detection system. However, the larger the correction, the larger the uncertainty from the unfolding process.

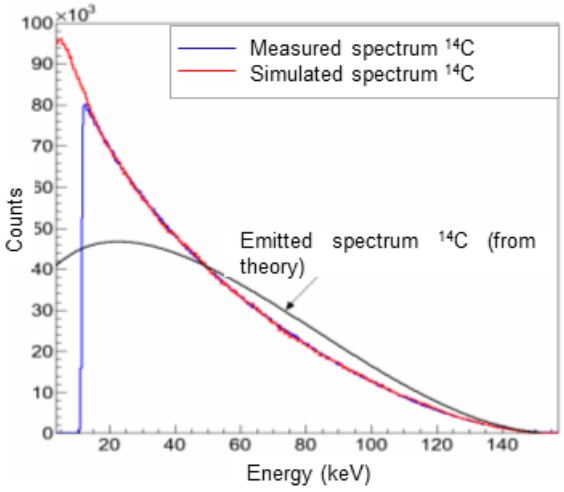

Figure 2.9 – Measured spectrum of ^{14}C decay (blue) compared with the simulated (red) and theoretical (black) spectra using a Si detector in a less than 2π configuration [4].

To reduce this uncertainty, it is necessary to absorb the maximum number of electrons in the detection system. Then, it should be feasible to be as close as possible to the initially

emitted spectrum. In order to limit the distortions of the β spectrum, new geometry for the detection system has been designed. The configuration involves two Si detectors, positioned in front of each other, resulting in an almost 4π geometry. The detectors are cooled down using a liquid nitrogen system, and the detection chamber is operated under ultra-high vacuum (UHV). The operation of detectors under UHV limits the electron scattering and prevents moisture developments due to the condensation on the cold surface of the silicon. However, the continuous operation of the vacuum pump generates vibrations during the measurement, which degrades the signal-to-noise ratio of the detector. These vibrations have been attenuated very efficiently in this measurement system as detailed below. The complete experimental set-up was designed using the SOLIDWORKS software (see Figure 5).

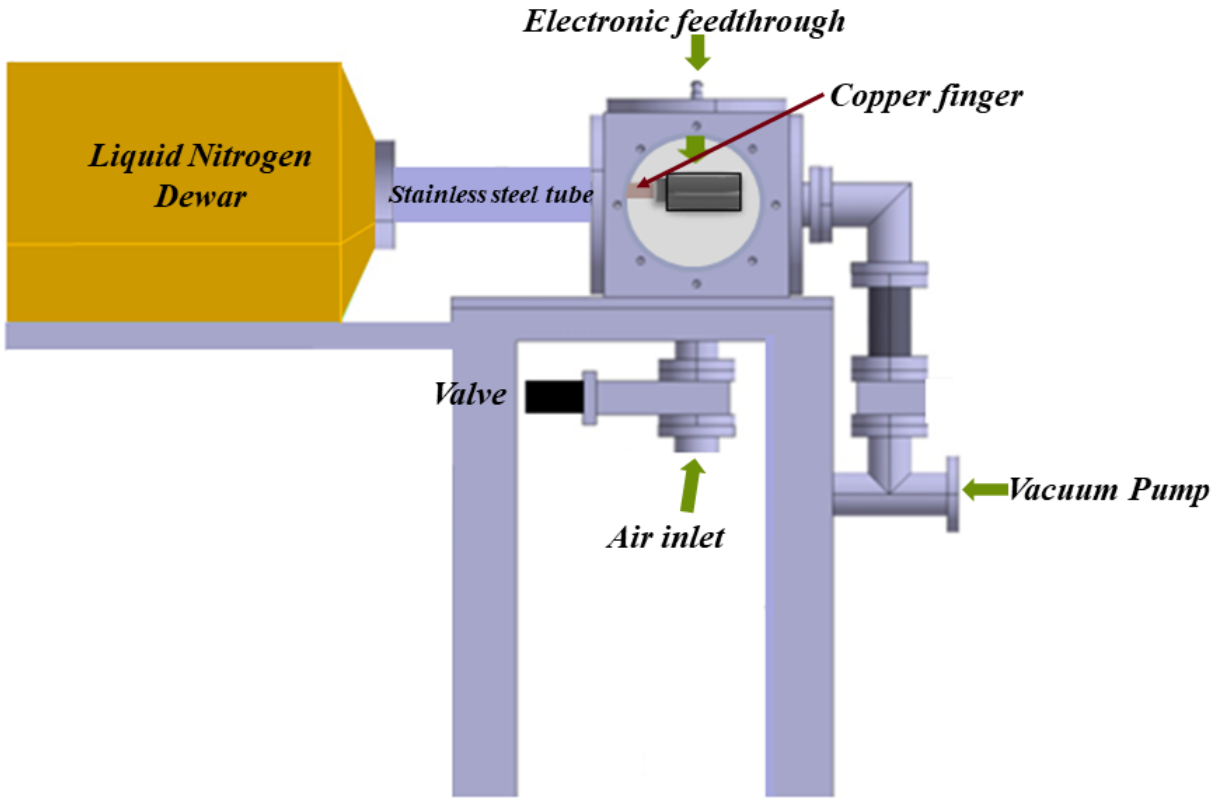

Figure 2.10 – Diagram of the β spectrometer developed at LNHB in this work. The black frame represents the detection chamber and the other components are labelled in black colour.

The detection chamber (in a black frame in Figure 5) was already existing [4]. This part of the measurement system is the only major component used from the previous developments. It is a 170-mm cube, made from an aluminium alloy (duraluminum). The six sides of the chamber are closed with *DN 100 ISO* flanges. Each of them has a specific flange customisation, as explained below:

(i) On the top side of the detection chamber, the flange contains a vacuum passage with a CF40 flange[2], which is specialised for an electronic feedthrough (see section 2.4).

[2]CF stands for ConFlat flange which uses a copper o-ring to achieve ultra-high vacuum. CF40 is with 40 mm

(ii) On the backside of the chamber, which does not appear in Figure 5, a vacuum gauge has been connected in order to measure the pressure within the detection chamber.

(iii) The flange placed on the left side of the chamber is connected to a liquid nitrogen Dewar *via* a copper rod surrounded by a stainless steel tube, as shown in Figure 6. However, this connection has been improved, as detailed in section 2.3.2.

(iv) On the right side of the chamber, a vacuum pump is connected *via* a long vacuum tube. There is a sandbox placed between the vacuum pump and the detection chamber: the vacuum tube is going throughout the sand in order to attenuate the vibrations (see Figure 6).

(v) The flange placed at the bottom of the chamber is connected to a valve with a tiny filtered opening, which allows a fine air inlet in order to break the vacuum "gently".

(vi) The flange at the front side of the chamber has been kept a solid blank flange. It provides easy access inside the chamber, which is particularly needed for the manipulations.

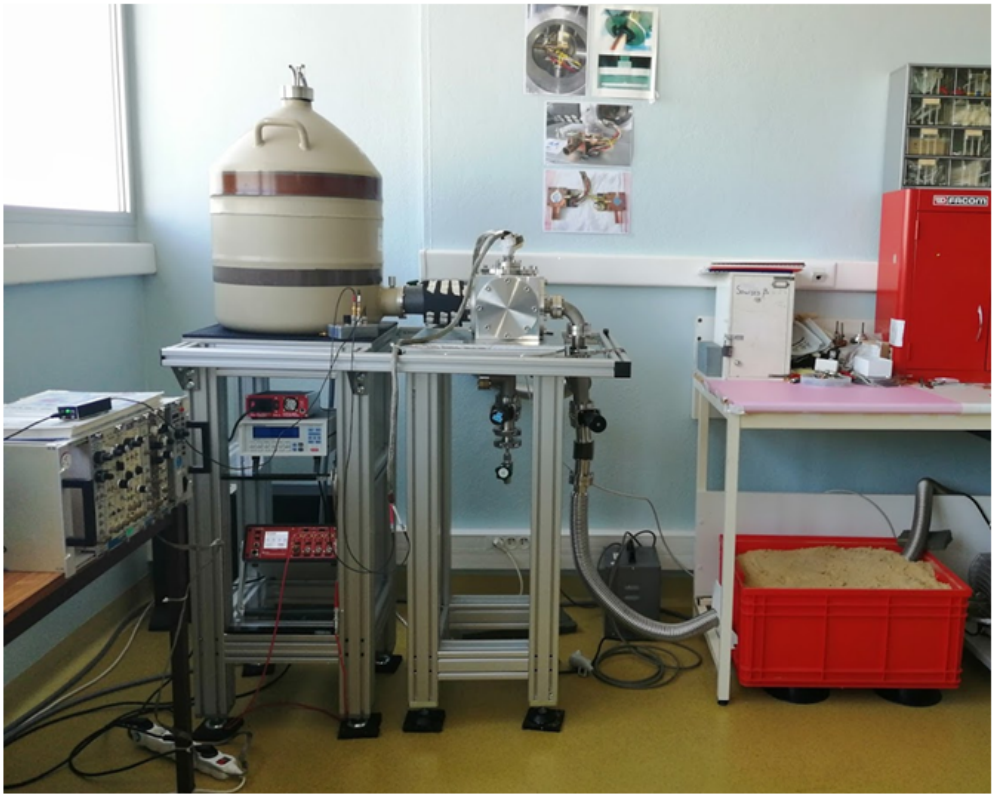

Figure 2.11 – Picture of the new experimental set-up of β spectrometry.

diameter. The CF40 feedthrough used for the vacuum passage is model “Mil-C-26482 CF40” from FULLVAC.

2.3.1 Vacuum system

Electrons being the lightest particles, they scatter very easily in any medium. Their scattering results in a partial energy deposition and distorts the measured energy spectrum [4] significantly. In order to minimise the interaction of electrons within the detection chamber, the detectors are operated under vacuum. Furthermore, while cooling the detectors at low temperature, the water vapours in the air condense on the coldest spot, which acts as a dead layer at the entrance window of the detector. An additional dead layer is undesirable in particular for electron measurements. In order to avoid this, the detectors are operated under an ultra-high vacuum, between 10^{-6} and 10^{-8} mbar. All the vacuum components, the vacuum pump, the valves and the flanges have been chosen accordingly.

The vacuum gauge Edwards WRG-S-NW25 is used to read the pressure inside the chamber. It was chosen on purpose in previous work, and we are using the same. A new, more powerful vacuum pump has been tested and used, EDWARDS TIC pumping station. This pump features are integrated to TIC turbo and instrument controller, which offers full control of the pump functionalities *via* a simple interface. The speed of the turbomolecular pump is ranging from 47 to 400 L.s^{-1}. The gauge is connected to the pump *via* an Ethernet cable. The primary pump evacuates air from the chamber up to 10^{-2} mbar, and then, the turbopump starts immediately. This system allows us to reach up to 10^{-5} mbar at room temperature within 1.5 hours for our chamber.

2.3.2 Cooling system

PIPS detectors are operational at room temperature; however, in these conditions, the leakage current contributes significantly to noise and degrade the energy resolution of the detectors [80, 104]. This can be improved by cooling the detectors at lower temperatures. Our detectors are cooled by liquid nitrogen (77 K) which reduces the leakage currents between 10^{-9} and 10^{-12} A [100].

The vacuum chamber connected with liquid nitrogen Dewar was used as it was designed in the previous developments (see Figure 6). The black protection appearing around the stainless steel tube was used to insulate the tube from the environment to reduce thermal leakage because condensation on the stainless steel tube was observed. The use of the glue, mentioned in the section 2.1, is indeed creating a contact between the copper finger and the stainless steel tube, causing a thermal leakage. Considering this may not be negligible, we decided to use a temperature sensor in order to get accurate information about the temperature of the detectors and to control its stability during the acquisition. This measurement allowed to learn that they were only cooled down to 255 K. In the previous work, the temperature was not monitored, so the actual status of cooling was not known. The temperature of 255 K is still sufficient for the operation of PIPS® detectors. However, a cooling at 110 K would allow reaching a better energy

resolution of the detection system [80]. In addition, the detection system has been modelled to be adaptable for Silicon-Lithium [Si(Li)] detectors, which request perfect cooling (100 K).

In order to design a new cooling system, the connection between the Dewar and the chamber was opened. The connection between the copper finger from Dewar and the copper finger from the chamber was achieved using another piece of copper. These two copper fingers were inserted on both ends without clamping. This bad thermal contact along with the use of glue perfectly explains why it was not possible to reach a temperature of less than 255 K.

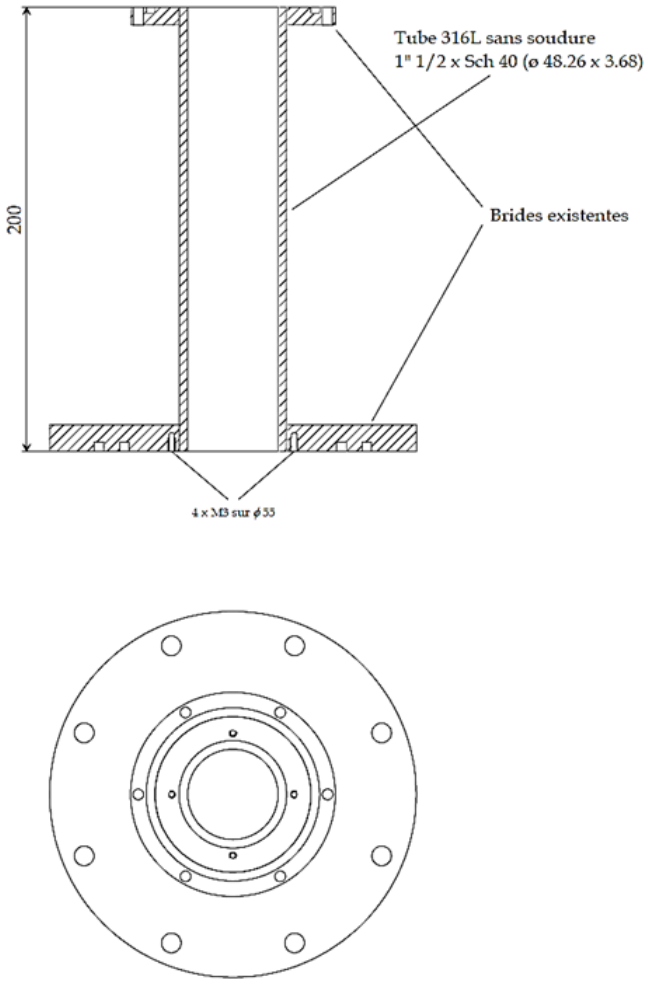

Figure 2.12 – Sketch of the new cold finger connection from the liquid nitrogen Dewar to the chamber along with the flanges.

A specific vacuum component has been designed in order to minimise the thermal leakage and to ensure high vacuum quality. In this new configuration, only one copper rod connects the liquid nitrogen Dewar to the detection chamber (see Figure 2.12). Individual pieces were manufactured to clamp this copper rod with the Dewar copper finger to ensure good thermal contact (see Figure 2.13). Several tests were performed in order to verify the cooling system. The results demonstrated that the temperature reached by the detectors is 102 K. Meanwhile, the pressure in the chamber was found to be less than 10^{-7} mbar, thanks to this new cooling

system.

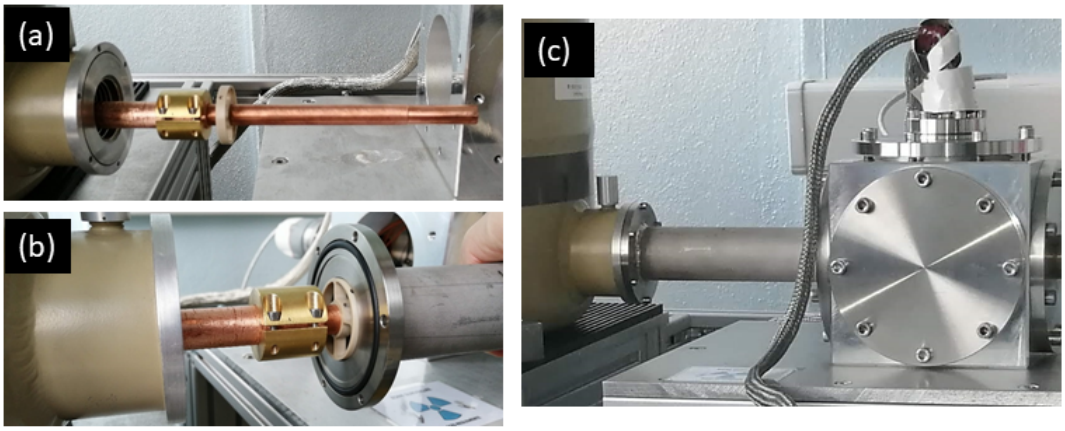

Figure 2.13 – (a) The copper finger attached to the Dewar's finger with a brass clamp. (b) The copper finger inserted in the stainless steel tube and a ring manufactured in PEEK is used in order to maintain the copper rod centred inside the stainless steel tube. (c) Finally, the copper finger is plunged into the chamber and is surrounded by a stainless steel tube.

2.4 Electronic chain

The energy deposited in the detector results in the form of a signal and requires an electronic chain to process it. The basic electronics for the measurements consist of a preamplifier, an amplifier and a multichannel analyser (MCA). The electronics measure the signal amplitude and convert it in a histogram, with the channel number on the x-axis and the number of counts on the y-axis. It is further retrieved *via* an acquisition software in the form of a characteristic spectrum of the measured radioactive source.

Customised feedthrough has been made for the detector electronics (see Figure 2.14). All the connections are made in-house (see Figure 2.15). CF40 feedthrough in the sealed passage for vacuum is used. It provides a connector of 19-pins, which is divided into several connectors as per the requirement.

Another feedthrough has been designed in order to improve the quality of signals. This includes a new flange *DN 100 ISO* with coaxial connections throughout the flange (see Figure 2.16) with the following connectors:

- two SHV male connectors for high voltage supply;
- four SMA female connectors for the output signal;
- two 15-pins Sub D male connectors to be adapted for the temperature sensor, heater, etc.

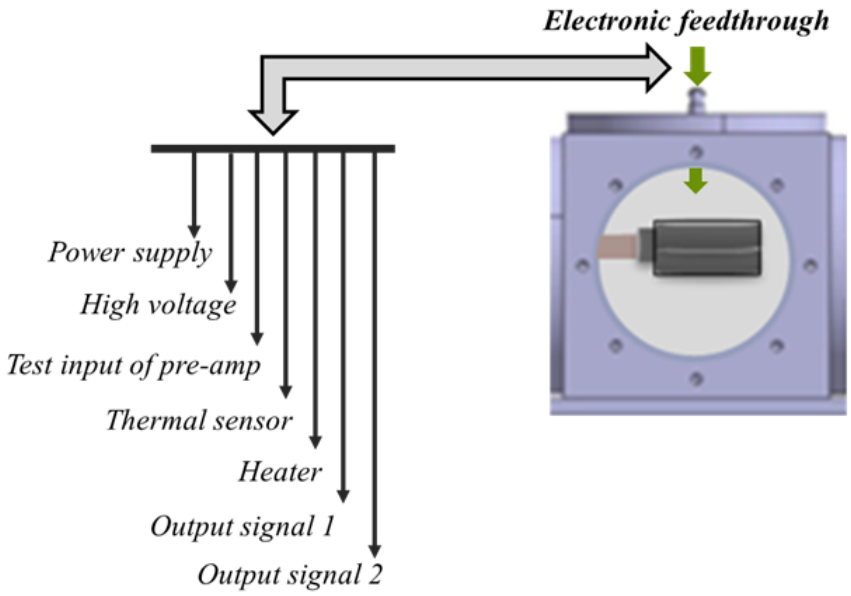

Figure 2.14 – Schematic diagram of the electronic feedthrough.

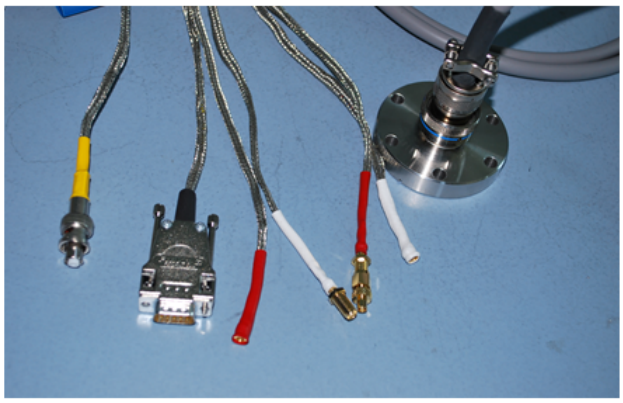

Figure 2.15 – Customised electronic feedthrough with CF40 passage.

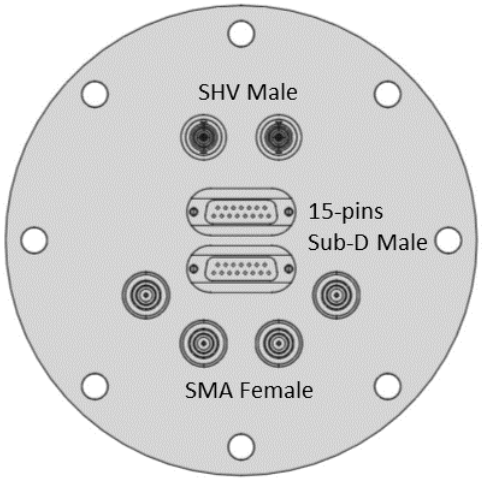

Figure 2.16 – Scheme of the electronic feedthrough on a *DN 100 ISO* flange with coaxial connectors.

This flange has been received but remains to be tested. Measurements performed with this feedthrough are not included in this work. By splitting physically, even more, the different cables, we expect to obtain smaller electronic noise.

2.4.1 High-voltage

An electric field is required to drift the charges in the detector and is created by supplying the high voltage (Figure 2.17). Every detector has a specific value of optimum voltage, usually given by the manufacturer. It can vary from a few tens to several thousand volts depending on the detector volume. The recommended bias voltage is 200 V for the 1 mm thick PIPS® and 500 V for the 5 mm thick Si(Li).

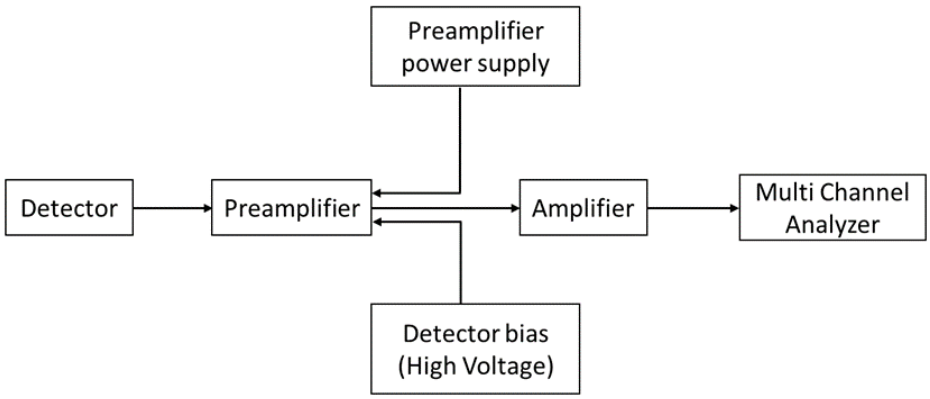

Figure 2.17 – Scheme of the electronics for measurement of deposited energy in semi-conductor detector.

The high voltage increases the volume of the depletion region and the mobility of the charge carriers in the detector. On the other hand, if the voltage is too high, it can cause a very rapid increase in the current (electronic breakdown), damaging the crystal. A high-voltage power supply must meet the following conditions:

- being adjustable for the voltages required by the detectors with suitable ramping;
- maintaining the maximum current;
- having a very low noise level;
- being stabilised so as not to drift over time.

To supply the high voltage to the detectors, a desktop module DT1419ET from CAEN is used. This is a stable module that has already been used as a high voltage supplier at LNHB for PIPS® detectors. A visual interface is provided to monitor the ramp of the voltage and its stabilisation over time. This is why this particular module was chosen for our measurement. In

our acquisition system, and most of the cases, the high voltage is supplied to the preamplifier that feeds the detector voltage to minimise noise.

2.4.2 Preamplifiers

A preamplifier is the first stage of an acquisition system. The signal amplitude at the detector output is low and requires an amplification. Generally, the preamplifier is placed as close as possible to the detector in order to reduce the capacitance. It serves as an interface between the detector and the rest of the electronics system. The two main functions of a preamplifier are to adapt the high impedance of the detector in order to preserve the signal throughout the cable and to maximise the signal-to-noise ratio [105].

There are two types of preamplifiers available for spectrometry: charge-sensitive preamplifiers and "reset" preamplifiers. Charge-sensitive preamplifiers are used in this work. A charge-sensitive preamplifier consists of a voltage amplifier (a so-called loop circuit) to which feedback is applied between the input and output terminals (Figure 2.18).

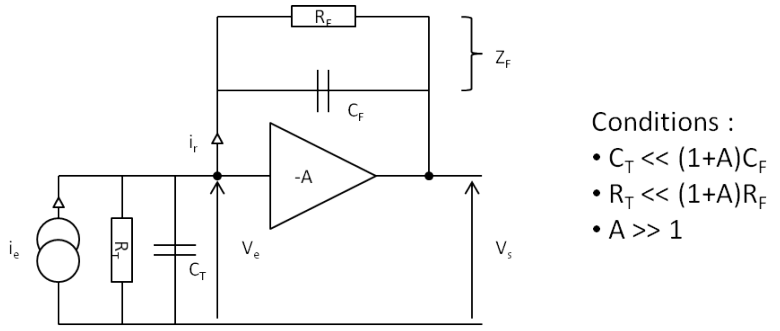

Figure 2.18 – Diagram of a charge-sensitive preamplifier. C_T is the equivalent input capacitance including the detector, preamplifier element and wiring. R_T is the equivalent input resistance including the bias and preamplifier input.

The open-loop assembly must have:

– the highest possible input impedance so as not to disturb the input signal and adapt the high impedance of the detector;

– the lowest possible output impedance to minimise signal loss;

– a high gain.

The advantage of feedback is to make the output voltage independent of any change in the detector capacity during an event.

A CAEN A1422H preamplifier has been chosen for this work, which is a Low-Noise-Fast-Rise-Time-Charge-Sensitive Preamplifier of F2 type, suitable for capacitance up to 200 pF with

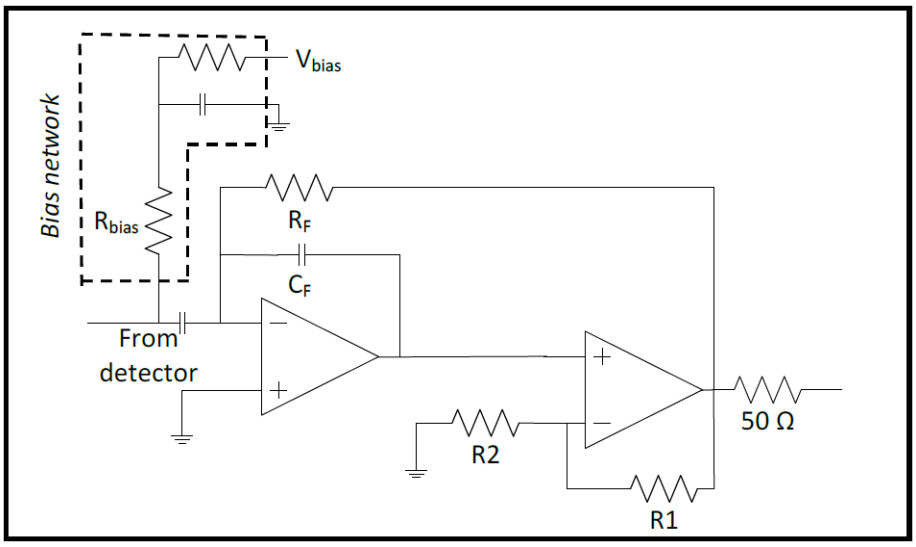

Figure 2.19 – Circuit diagram of the A1422H charge-sensitive preamplifier manufactured by CAEN, used for the measurement.

a sensitivity of 90 mV/MeV. The circuit diagram provided by the manufacturer is shown in Figure 2.19.

The detector capacitance, which is a crucial component of the total equivalent input capacitance and therefore of the noise, is fixed by the surface of the silicon crystal and calculated by using the operating principle of PIPS® [100]. The number of electron-hole pairs created in the detector can be written as:

$$N = \frac{E}{\epsilon} \tag{2.1}$$

where E is the kinetic energy of the particle and ϵ is the energy required to create an electron-hole pair, 3.61 eV for Si. The thickness of the depletion region depends on the high voltage applied and can be calculated as:

$$W = 0.562\sqrt{\rho V} \tag{2.2}$$

where ρ is the electrical resistivity in ohm.cm and V is the applied voltage in volts. With this, the capacitance (in pF) can be simply calculated as:

$$C = 1.05\frac{A}{W} \tag{2.3}$$

where A is the area of the detector (in cm^2), W is the thickness of detector (in cm) and 1.05 is the product of vacuum permittivity and the dielectric constant of Si with unit pF·cm^{-1}. With $A = 3$ cm^2 and $W = 0.1$ cm, we obtain $C = 31.5$ pF.

We have used two identical preamplifiers, one for each detector (Figure 2.20). As requested, we have placed the preamplifiers close to the detectors. They are fixed on the dedicated copper plates using Stycast® Epoxy, a specialised glue for cryogenic applications. The preamplifiers are connected to a 15 pin-SubD connector (Figure 2.20).

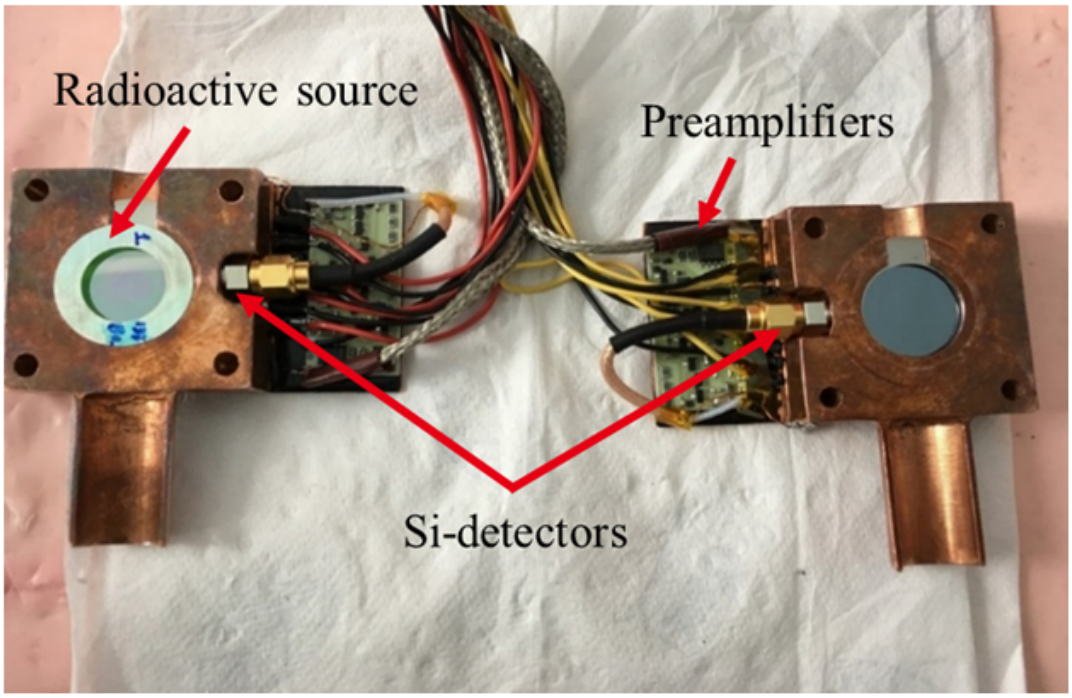

Figure 2.20 – Experimental set-up with two PIPS® detectors (300 mm^2) in a configuration close to 4π geometry and preamplifiers fixed with Stycast® Epoxy glue.

2.4.3 Shaping of signal

For several years, digital signal processing has been developed in nuclear physics experiments. The Field Programmable Gate Array (FPGA) programming techniques with increased sampling speeds have facilitated the development of digital acquisition systems. These digital systems perform on a single board the various processes (shaping, amplification, signal processing) that were initially carried out by different analogue circuits such as spectroscopy amplifiers, constant fraction discriminators, analogue-to-digital converter (ADC), etc. This series of modules are now being replaced by single ones that are commercially available. These fast speed and compact systems allow the connection of several detectors on a single acquisition module. They include a high-voltage power supply, an amplifier and an MCA module. They are widely used in nuclear physics measurements.

In order to analyse a signal resulting from the detector, different filters can be applied to change its shape. In this work, trapezoidal shaping is used. The signal goes through the preamplifier and is next converted to a trapezoidal shape. This shaping is useful in particular when the charge collection varies with the position of radiation interaction in the detector. Any shaping of the signal requires the mastering of important parameters:

– Pole-zero cancellation (P/Z): The pulse from a charge-sensitive preamplifier has a long falling tail that is finite. This shows a slight undershoot of the pulse which remains for a long time as the decay time of the preamplifier pulse is of the order of 50 μs. If there is another pulse arriving in that time interval, its amplitude estimate will be biased. The

pole-zero cancellation is used to restore the signal output without any undershoot.

– Base-line restorer (BLR): In radiation measurements, pulses occur in a sequence with many other pulses, leading to a problem with the baseline shift. This corresponds to the depression of the baseline below zero. However, in nuclear-measuring systems, the pulse amplitude carries most of the information, which is determined with the true zero baselines. If there exists a baseline shift, the amplitude reading will be reduced. This is why all spectrometry module has a BLR to correct for the baseline shift.

First, a CAEN desktop digitiser module available at LNHB was used. However, we discovered some bugs in this acquisition module, as explained in section 2.4.4. Finally, an efficient and quick solution was found by using a very compact acquisition module, *nanoMCA* developed by *labZY*, also based on FPGA technology, which is presented in detail in section 2.4.5.

2.4.4 CAEN digitiser

The CAEN digitiser DT5724 was used in this work. This module provides access to a waveform acquisition and to online algorithms, called Digital Pulse Processing (DPP), with an acquisition window. The acquired data are read by an ADC with a 14-bit resolution. This module is applicable to several detectors such as silicon detectors, high-purity germanium detectors or inorganic scintillators coupled with charge-sensitive preamplifiers. The acquisition is possible for each independent channel and with a coincidence/anticoincidence logic among different channels [106].

In the case of DPP, data can be saved in list mode[3]. The acquisition is handled by the *CoMPASS* or the *MC2Analyzer* software, which can manage the various algorithm parameters to generate the plots and to save the energy spectra. To access the waveform of the signal, *CAENScope* or *WaveDump* software are used.

We used *MC2Analyzer* software to control the waveform and acquisition of the data. To achieve the coincidences of interest, we used the "neighbourhood trigger" mode in which one of the channel triggers and all the channels are acquired with a time-stamp (Figure 2.21). The aim is to get the sum of the energies deposited in both detectors.

Each time-stamp represents the occurrence of an event and the corresponding energy deposition. In order to get the sum of energies deposited in both detectors, the data were analysed, and we found that some events in the two detectors were missing (Figure 2.21). It appeared to be energy-dependent, thus with an influence on the spectrum shape. As a consequence, this module could not be used for the measurement and was replaced by a *nanoMCA* acquisition module.

[3]The analogue-to-digital converter stores the value with a time-stamp for each event.

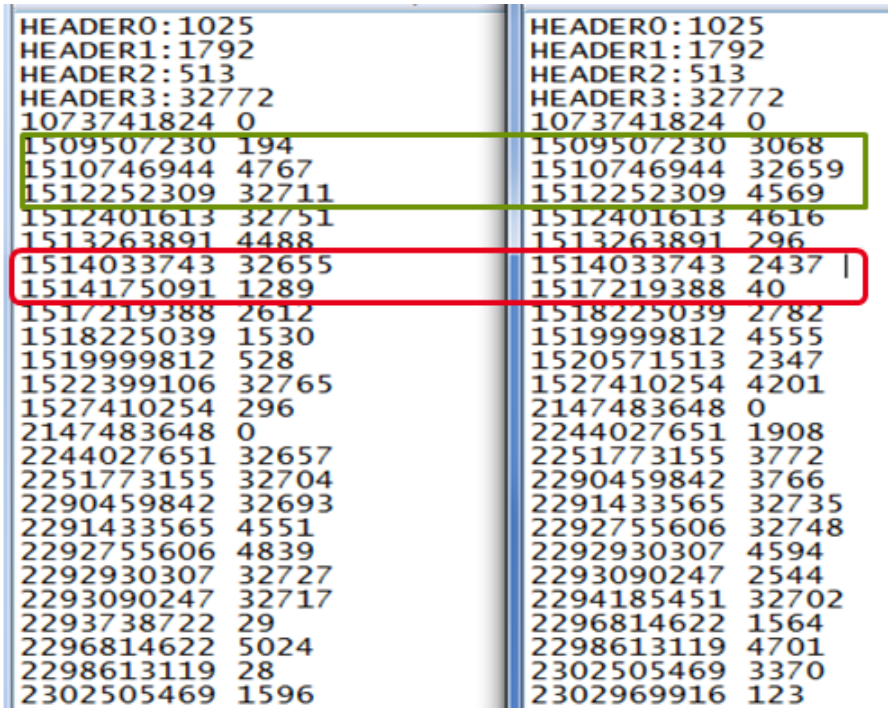

Figure 2.21 – The output file structure of the measurements obtained by using CAEN digitiser as acquisition system. The green frame highlights the time-stamp of each detector and the corresponding channel number. The red frame indicates the missing of events.

2.4.5 The nanoMCA digital module from labZY

The *nanoMCA* module from *labZY* is a high-performance Multi-Channel Analyser (MCA) [107]. It is based on Digital Pulse Processing (DPP) technology. The nanoMCA can easily be adapted to specific radiation measurement applications. The DPP algorithms are in-system programmable, and *labZY* provides standard DPP designs that support a variety of detectors such as HPGe, Silicon drift detectors, or LaBr scintillators.

2.4.5.1 Overview of the module

The *nanoMCA* module is a small, compact package measuring 92 x 38 x 25 mm^3 (Figure 2.22), comprising the amplifier and the signal shaping.

The front panel of nanoMCA (Figure 2.23, left) shows:

- Two USB connectors: IO and PWR. The first serves as a connection and power supply between the computer and the module. The second can be used as an independent power supply for the nanoMCA.
- A button to switch on/off the power supply of the module.
- A green or red LED indicating the status of the module.

The rear panel of nanoMCA (Figure 2.23, right) has four inputs:

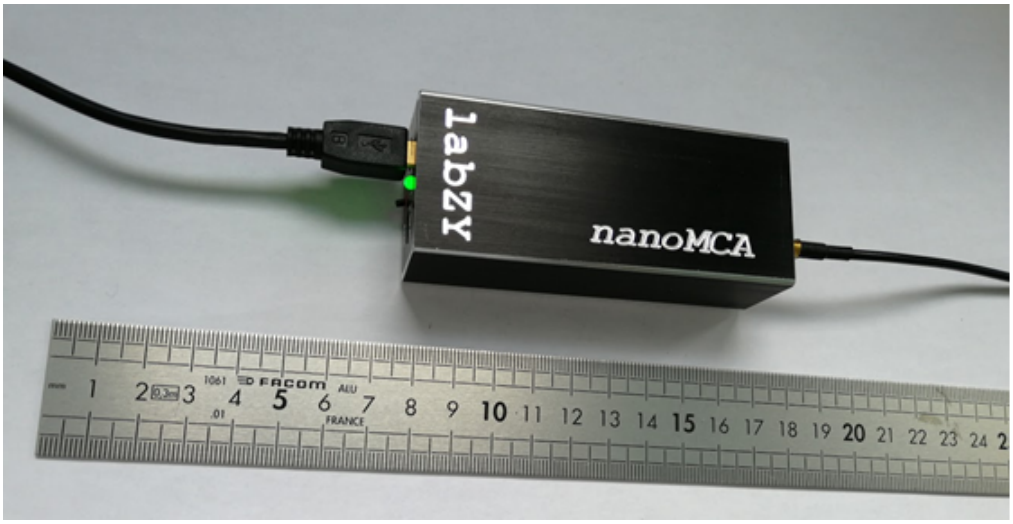

Figure 2.22 – The nanoMCA module from *labZY*.

Figure 2.23 – Front (left) and back (right) panels of the nanoMCA module.

- Input A receives the signal from a preamplifier, either a reset or charge-sensitive feedback preamplifier.
- Input B receives an already shaped signal, by using a traditional analogue amplifier, for example.
- Inputs C and D are digital or analogue/digital inputs with different functions (inhibit signals, input to a 12-bit ADC, etc.).

In our case, we used input A.

2.4.5.2 Signal processing

The *nanoMCA* module provides trapezoidal or triangular shaping synthesised with a Rise Time, a Fall Time (= Rise Time) and a Flat Top. This module is configured with a software called *labZY*-MCA (Figure 2.24) that adjusts the shaping parameters.

In the *labZY nanoMCA* module, two shaping parameters have to be adjusted: the Slow Shaper that accounts for the main shaping of the signal coming from the detector; and the Fast

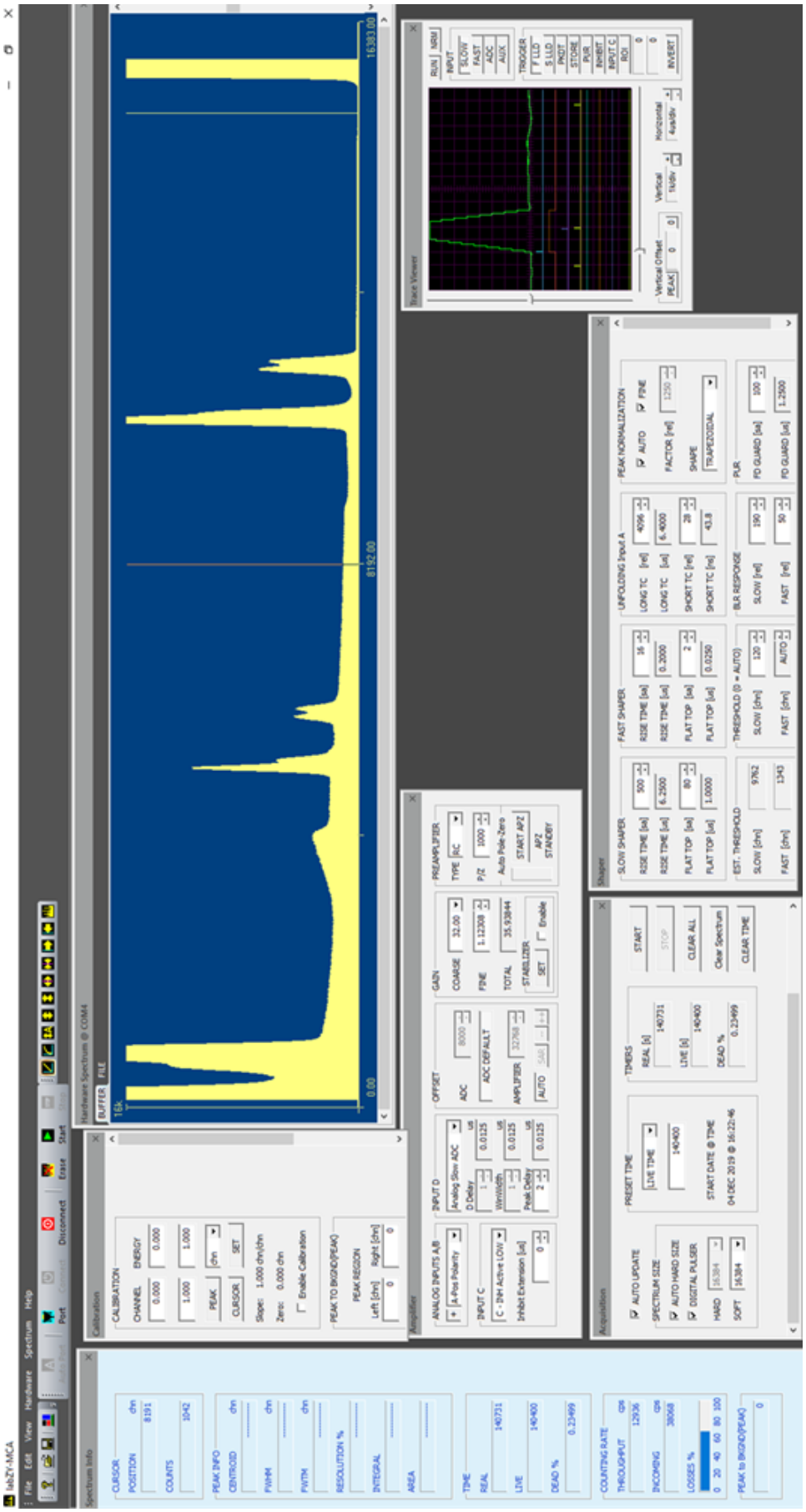

Figure 2.24 – The control panel software of *labZY* nanoMCA.

Shaper used for the identification of events, which accounts for the pile-up rejection. Therefore, the Rise Time (RT) and Flat Top (FT) are required to be set for both shapers [107].

The module provides its own software that allows the basic processing of the spectra. The output files (the energy spectra) are saved with a specific extension: "`.lzs`". The main settings to be adjusted in the software are:

- The settings for the spectrum acquisition, such as the number of channels (maximum 16 384), gain and real-time of acquisition. It also provides the live time of the acquisition after dead time correction.
- The digital pulser, which is provided to trigger and generate a Gaussian between channels 15 000 and 16 383. This pulser is very useful for adjusting the digital shaping of the signal from the detector in order to obtain a Gaussian shape with no tail on the left or right. It also helps to determine the electronic contribution to the noise over the spectrum.
- The type of preamplifier of the detector, charge-sensitive for this work.
- Different settings that are specific to the inputs A, B, C or D. In our case, we used input A with the positive polarity of the pulses.
- The shaping parameters of the trapezoid: RT and FT for Slow and Fast Shapers, Short and Long Time Constants (TC), pole-zero (P/Z), BLR Response (baseline restoration), FD Guard (pile-up) and the Slow and Fast thresholds in the different channels.
- The module also provides an oscilloscope visualisation, which allows observing the signal according to the change of parameters. It is particularly useful to adjust the values of the pole-zero, Fast Shaper and BLR (see Figure 2.24).

As discussed above, in the nanoMCA module, only a single input can accept a signal from a preamplifier, which means only one of the detectors in our case. As our set-up consists of two detectors, we need to sum the signals from both detectors to be able to use the *labZY* acquisition module. We have two identical detectors and preamplifiers; however, the signal analysis on oscilloscope showed a slight difference of gain between the signals for an identical energy peak. Gain adjustment is then required in order to sum the signals precisely. A small in-house passive module, including a potentiometer, was built. It allows gain adjustment and the signal sum up (Figure 2.25). As a passive module, it does not add any additional noise to the signal, but the sum contains the noise of each signal. It is the main drawback of this method. The gain adjustment was performed very accurately by measuring the conversion electron peaks at 481 keV and 975 keV from the decay of ^{207}Bi. Finally, the output signal is sent to the input A of the nanoMCA module.

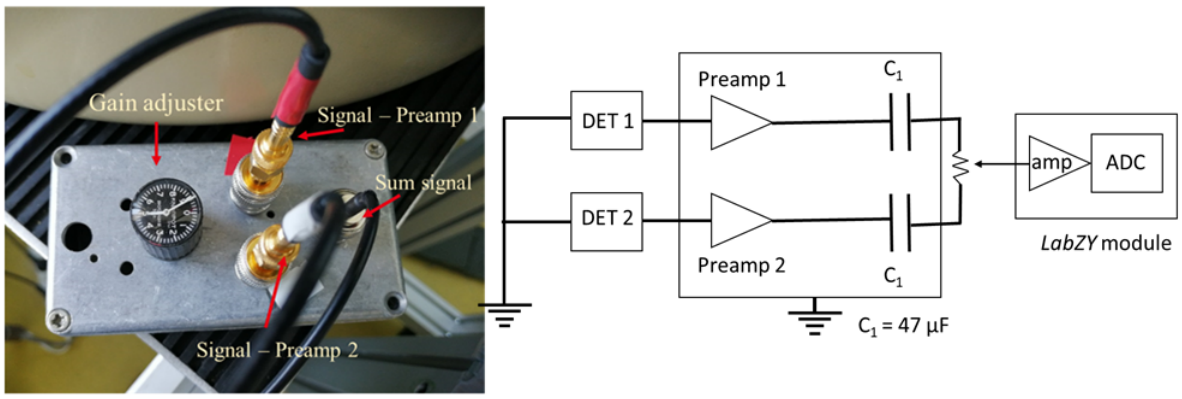

Figure 2.25 – The passive module made to adjust the gain of the signals from preamplifiers.

The first tests performed showed too much noise in the signals In order to improve the quality of the signal from the detector, several developments have been implemented that includes decoupling of the ground loops with the help of a transformer, and double shielding of cables to prevent electromagnetic crosstalk. The final experimental set-up fixed after all modifications and improvements for β spectrometry is shown in Figure 2.26.

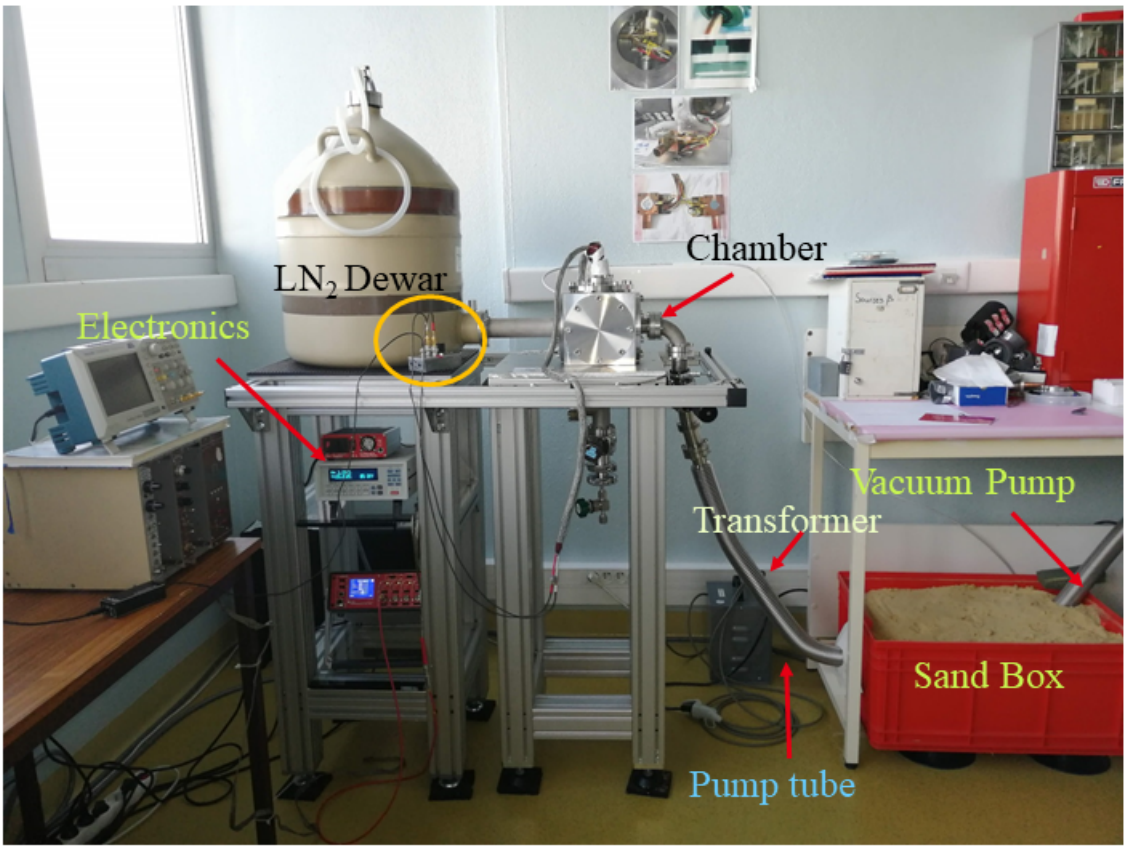

Figure 2.26 – The final experimental set-up at LNHB.

2.5 Radioactive source preparation

The experimental device has been designed and optimised along with an efficient acquisition system in order to minimise sources of β spectra distortions. Apart from this, the radioactive source preparation plays a major role in a precise measurement of the electron energy spectrum. Its quality can significantly distort the shape of β spectra [108]. First, the requirements of a radioactive source for β spectrum measurements are discussed. Next, the process of radioactive source preparation using VYNS films and Mylar® films as support and the shielding of radioactive sources is presented in detail.

2.5.1 Radioactive sources for β spectrometry

A solid radioactive source is prepared by employing a radioactive deposit, which is a distribution of a certain number of radioactive atoms on a deposit area of support. In order to ensure that the spectrum emerging from the source is as close as possible to the real emission spectrum, it is necessary to limit physical phenomena induced by the support as well as by the radioactive deposit itself.

2.5.1.1 Backscattering and self-absorption phenomena

Electrons emitted by the radioactive source may backscatter on the support. This phenomenon is dependent on the atomic number of the support material. Its probability increases with the atomic number and the thickness of the support [80], which must be chosen with a low atomic number (Z) and the lowest possible thickness.

The self-absorption of electrons within the radioactive source is also very critical. The resulting energy loss of the particles induces a higher energy threshold of the detection system and shifts the measured energy to a lower one, thus distorting the spectrum. It is highly dependent on the crystallisation of the radioactive deposit in the radioactive solution.

Therefore, the material choice for the source support is of concern and the crystallisation of the radioactive deposit has to be controlled.

2.5.1.2 Crystallisation of the radioactive deposit

When a radioactive drop is deposited on source support, it is followed by a drying process. During this step, the crystallisation of the radioactive solution takes place in two steps: nucleation and growth. Nucleation is the phenomenon in which the first nuclei of a crystal appears in a solid phase. These nuclei also called as seeds form a crystalline structure by arranging themselves in a particular order. The addition of nuclei in the layer increases the size of the crystals, and this process is called growth. If there are many seeds, it will result in many small crystals. On the contrary, if there are less seeds, it will result in large size crystals. The

self-absorption phenomenon will be weaker in smaller and homogeneously distributed crystals. Consequently, for β spectrometry, a homogeneous radioactive source with small size crystals is desirable in order to minimise the absorption of electrons.

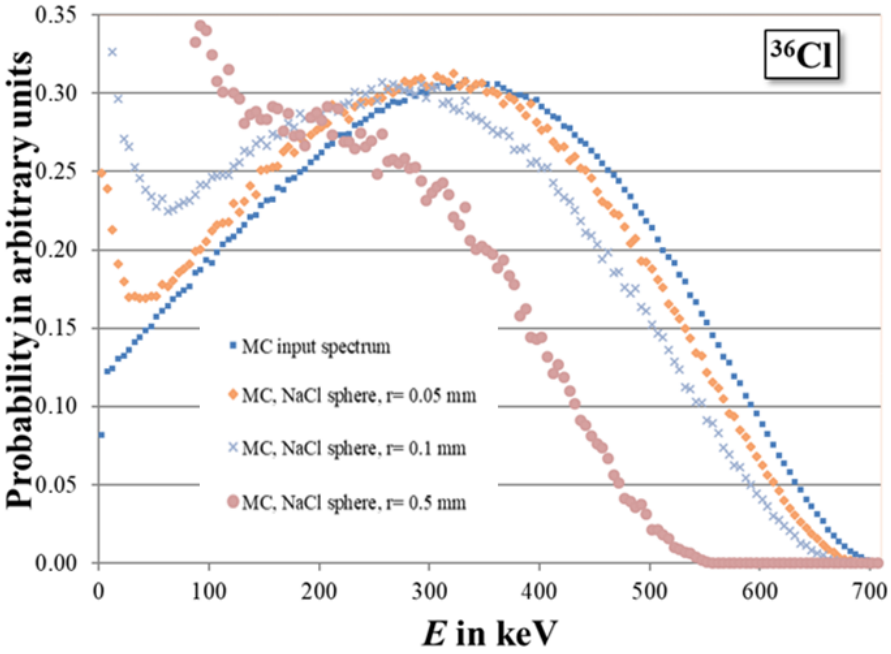

Figure 2.27 – Effect of the crystallisation on the shape of ^{36}Cl β spectrum. "MC input" refers to the Monte Carlo input spectrum, that has been taken from [96].

The effect of the crystal size on the shape of the β spectrum was studied by M. Paulsen at PTB[4], Germany, in the framework of the European EMPIR project MetroBeta (Figure 2.27). Monte Carlo simulations were performed for ^{36}Cl decay where the crystals of NaCl were considered in sphere shape. It clearly demonstrated the increasing self-absorption of electrons in the spheres with increasing size. The crystallisation of a radioactive deposit can be improved by modifying the physical properties of the surface of the support or by controlling the drying step [109, 110].

Considering the requirements, the radioactive source preparation follows mainly four steps:

1. The preparation of the source support;
2. The deposition of a seeding agent to increase the wettability of the film (in our case: latex microspheres);
3. The deposition of the radioactive drop;
4. The drying process.

[4]Physikalisch-Technische Bundesanstalt, Germany.

In our case, the supports are VYNS and Mylar® films. We discuss below the procedure to prepare a source with a VYNS film and finally, the choice of using a Mylar® film.

2.5.2 VYNS film sources

Polyvinyl chloride acetate copolymer, also called VYNS, is a solution with 15% of polyvinyl acetate and 85% of polyvinyl chloride. The density of VYNS is 1.28 g.cm^{-3}. These films are prepared to deposit latex microspheres, on which a radioactive deposition is done afterwards. They have a thickness of 0.05 to 1 μm depending on the concentration of the solution and are made of a low Z material, which makes them perfectly suitable for β spectra measurements. Radioactive sources on VYNS films were used and fabricated in the past at LNHB to perform activity measurements with proportional counters and β spectrometry. The step by step procedure (see Figure 2.28) to prepare VYNS film is:

1. The white powder form of VYNS is mixed with an organic solvent, such as cyclohexanone. The concentration of VYNS in the solution is critical because it determines the thickness of the film. The solution used for our study presents the content of 8% of VYNS.

2. A glass plate, cleaned with ethanol and isopropanol (this helps to spread the VYNS solution smoothly), is placed at the centre of the spin base of the dedicated device at LNHB.

3. 200 μl of VYNS solution is deposited on the glass plate with a pipette and then, spread on the surface of the glass by spin coating at a rate of 3 000 rotations per minute during 1 minute.

4. The film is resized to 2 cm^2 by scraping off the excess with a utility knife.

5. The film is then delicately removed from the glass. This process is called "fishing": the glass plate is fixed on a holder with an angle of 45° to the surface of the water and immersed slowly inside the water at (20 ± 2) °C. The film leaves the surface of the glass and floats on water.

6. Once the film is floating on the water surface, the stainless steel ring (ϕ_{ext} = 25 mm, ϕ_{int} = 15 mm, thickness = 0.15 mm) is dipped in water, with the help of fine tweezers. Then, it is taken below the floating film to be taken out of the water, following the film diagonally. Afterwards, the film is stuck on the stainless steel support, placed in the holder and let dry for at least 12 hours at room temperature. The films that are not tightly stretched over the stainless steel ring after the drying process cannot be used. Indeed, a radioactive source on a curled VYNS film will not be homogeneous. A well-stretched VYNS film is shown in Figure 2.29.

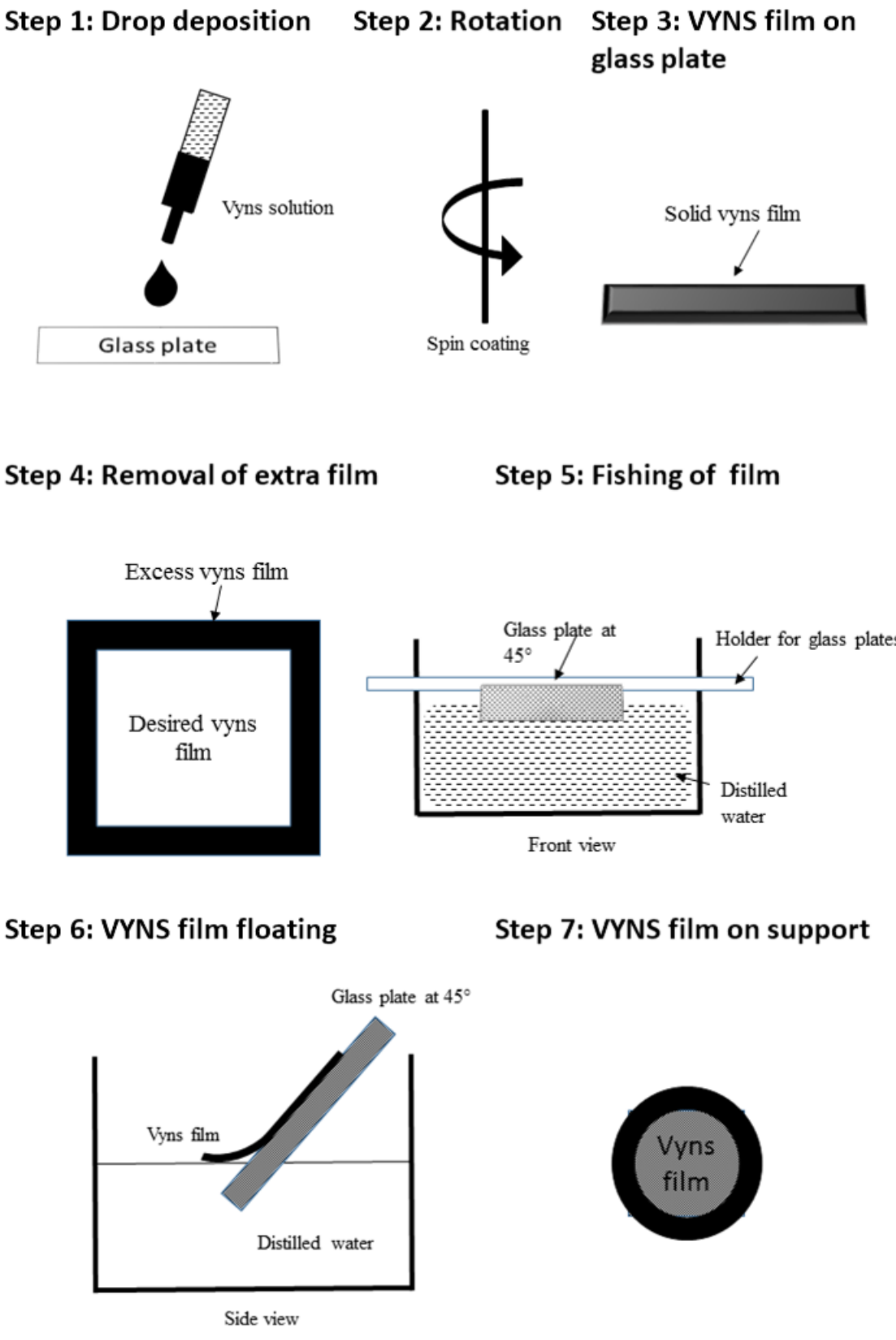

Figure 2.28 – Schematic representation of the different steps for VYNS film preparation procedure.

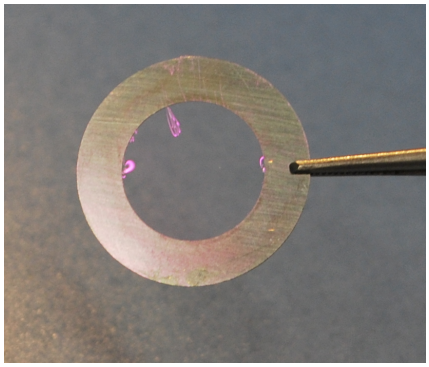

Figure 2.29 – A well-stretched VYNS film on its stainless steel support.

The 0.5 μm VYNS films are highly suitable for β spectra measurements. However, they are very fragile and stretch over time. They cannot be stored and used more than four months after preparation.

2.5.2.1 Radioactive deposit on VYNS film

A radioactive source can be prepared by depositing a drop of radioactive solution on the surface of VYNS film, but the crystallisation of the residual element is not homogeneous. The autoradiography of this type of source shows a ring-shaped crystallisation. In addition, the heterogeneity of the sources and the quantity of residual salts significantly increase the self-absorption phenomenon. Therefore, deposition of a seeding agent is required, which has the following advantages:

- It ensures the wettability of the film by reducing the surface tension of the drop of a radioactive solution;

- It provides crystallisation nuclei for the deposit in the drying process.

An alcoholic suspension of mono-dispersed polystyrene-latex spheres with a diameter of 0.07 μm, deposited by electrospraying method, is used as a seeding agent. The thickness of the deposit is estimated to be around 0.07 μm for a single layer, which corresponds to a mass deposit of about 0.7 $\mu g \cdot cm^{-2}$. However, the deposit is visible by naked eyes (see Figure 2.31) and, since the thickness had not been characterised, it led us to believe that it could be much higher than the estimated value. We used a high-precision balance to weigh the film before and after electrospraying the latex microspheres. The difference in the weight of the film was found to be less than 1 μg, which is the balance precision limit. The actual volume of the deposit area is the volume paved with spheres. Keeping the volume, we deduced an effective thickness of 8 nm for an equivalent plain layer. The latex deposit is of hydrophilic nature, which increases the porosity of the film and decreases its surface tension.

2.5.2.2 Electrospraying procedure

Electrospraying, originally proposed by Carswell and Milsted [111], is an efficient method used to generate a fine jet of droplets of a solution by means of an electric field. It is a process to generate fine aerosols from a liquid. It is used in several fields such as fluid physics, biomedical applications, polymer physics, etc. [112–114]. This efficient process has been recommended for the fabrication of homogenous radioactive sources for β spectrometry [115].

This mechanism is simply based on the dispersion of "particles" in the presence of an electric field. The electrospray device consists of a capillary tube with a tank at the top containing the solution to be sprayed (polystyrene-latex in our case). As shown on Figure 2.30, the spray electrode is placed inside the capillary tube, which is slightly projected at the bottom (≈ 1 mm). The positive terminal of a high voltage is linked to an electrode, which is connected to the top of the capillary. The spraying is directed to a conductive film, connected to the negative pole of the power supply *via* metallic support. The distance between the tip of the electrode and the film is 2.3 cm. When the high voltage of 7.5 kV is applied, the latex liquid is dispersed from the capillary in extremely fine droplets forming a cone shape. The film undergoes a random circular motion during the sputtering process so that the deposit is homogeneous. A 10 mm diameter aperture is placed above the film in order to constrain the diameter of the deposit.

As the VYNS film is non-conducting, a flash of gold is generally plated for regular production of sources at LNHB, with a thickness of a few hundred nanometres. As gold is a high Z material, its use would increase self-absorption and bremsstrahlung, which is undesirable for β spectrometry. Consequently, a silver disc was used between the support of electrospray and the VYNS film, which sticks well by electrostatic contact. On top of the film, a second stainless steel ring with an outer diameter greater than the diameter of the VYNS film ring was added. It encapsulates the film and ensures the conductance of VYNS film. This method allows us to make a good connection between cathode and anode and to form a good cone of spray without a gold spray. Finally, the whitish deposit is visible on the VYNS film (Figure 2.31). Removing the film from the silver base is highly critical because the film sticks very well to it with electrostatic contact and VYNS film is very fragile. Therefore, it has to be performed very carefully in order to keep its integrity.

2.5.2.3 Radioactive deposit

The radioactive deposit is very critical for any radioactive source. In order to obtain a deposit as small as possible, a special pipette with a very thin tip is prepared (see Figure 2.32). A typical amount dispensed is 20 mg for ~ 50 kBq/g activity concentration of the solution due to dead time considerations.

Indeed, the detector signal processed by the acquisition system takes a while, which is called dead time. Basically, the events occurring in that dead time are lost. This dead time

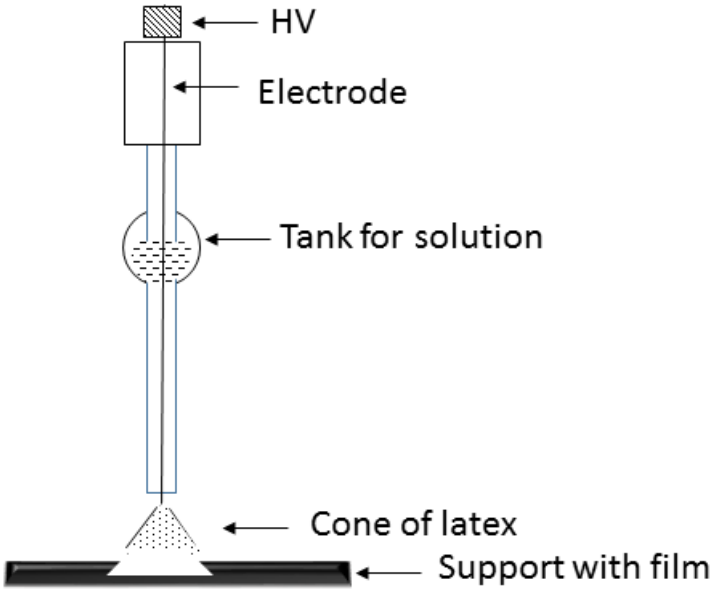

Figure 2.30 – Diagram of the basic principle of electrospray.

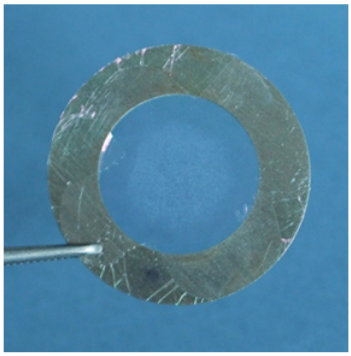

Figure 2.31 – The VYNS film after the electrospray of latex micropsheres.

also depends on the count rate of signals, the higher the count rate, the more the loss of events. In addition, the higher the count rate, the more the probability of pile-up events. Considering the decay constant of our signal, which is around 50 μs, the radioactive sources are prepared with a typical activity of 1 kBq.

2.5.2.4 Drying of source

The drying step of the radioactive deposit plays an important role in the crystallisation process. Two drying methods are used in the laboratory:

1. Oven-drying: It is a dehydration process implemented in an oven. The source support after the drop deposition of a radioactive solution, stored in a holder, is placed inside an oven operated at a temperature of 60°C at atmospheric pressure. This process takes about 30 min and after that, the radioactive source is placed aside to cool down at room temperature.

2. Freeze-drying: It is a low-temperature dehydration process that includes drying of a frozen product by sublimation under reduced pressure. In this case, the sample does not undergo significant change in shape during drying [116]. In this method, the aqueous components contained in the radioactive solution freeze by rapidly cooling the deposit down to -85°C. The parameters to be controlled during the process are the pressure (5 Pa) and the temperature. The freezing speed is an important parameter: the slower, the larger the size of the crystals. The whole process takes about 1 h. A complete description of the vacuum freeze-drying procedure and the commercial apparatus used to manufacture the sources is given in [116, 117].

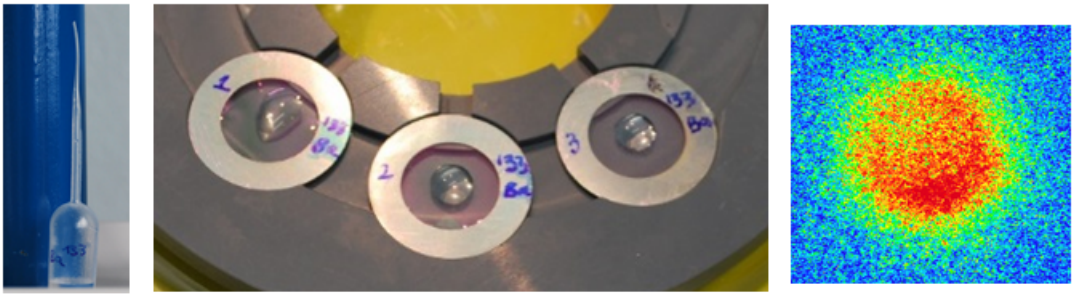

Figure 2.32 – (1): Pipette used for a radioactive drop deposition. (2): Radioactive drop deposition of ^{133}Ba. (3): Autoradiography of a source dried in oven.

During the first tests, only the oven-drying method was used. The autoradiography of ^{133}Ba source (Figure 2.32) shows that the source can be considered as sufficiently homogenous. However, after performing certain measurements and analysis, we observed a significant disagreement below 60 keV between our measurement of ^{99}Tc decay and the high-precision one performed with a Metallic Magnetic Calorimeter (MMC) at LNHB. This led us to think about the self-absorption in the source of ^{99}Tc. Indeed, a comparison between oven-dried and freeze-dried sources showed a definite improvement in electron detection efficiency with freeze-dried sources [116]. In order to compare the influence of different preparation techniques, we prepared new radioactive sources with and without freeze-drying. The systematic comparison of results is discussed in the next chapter.

2.5.3 Mylar® film sources

As the radioactive source prepared on VYNS are not long-lasting, we chose to give priority to sources using a thin Mylar® film, made of polyethylene terephthalate, which has a wide range of properties such as electric/thermal insulation, transparency, high tensile strength, chemical stability, reflectivity, gas barrier and odour barrier. This film is more robust than VYNS film and commercially available. However, Mylar® film of very low thickness is very recent on the market. We have used Mylar® film of 0.7 μm thickness, the lowest thickness available at that

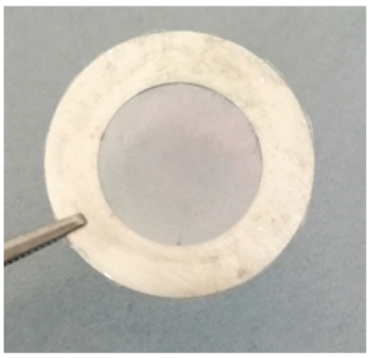

Figure 2.33 – A Mylar® film source support with electrosprayed latex microspheres.

time, which is comparable with the thickness of VYNS film used. As the film is ready for use, the radioactive source preparation is faster than with VYNS films.

The whole process of preparation remains almost the same, i.e.:

(i) Preparation of film support on a stainless steel ring;

(ii) Electrospraying of latex microspheres;

(iii) Radioactive drop deposition;

(iv) Drying.

To prepare the Mylar® film support, we have used "SuperGlue" (Cyanoacrylates), which is widely used in electronics, forensics, medical, etc. The Mylar® film is glued on the stainless steel ring (Figure 2.33). As we are operating radioactive sources under vacuum, we performed some tests for Mylar® film support. At 10^{-7} mbar pressure the film had no damage, which demonstrated its robustness. We also tested the performance of Mylar® film at liquid nitrogen temperature by dipping it inside a Dewar and no damage was observed at 77 K. This ensured the choice of using this film as radioactive source support.

2.5.4 Shielding of sources

At the beginning of measurements, non-shielded radioactive sources were used in order to minimise the energy loss within the source. This configuration appeared to be delicate. Indeed, during the measurement of ^{14}C, contamination occurred on the detector placed on top. This contamination was challenging to deal with; attempts were made to clean the detector. After a while, an additional noise in the detector was observed. The origin was the detector itself due to too many manipulations of the connector. Eventually, new detectors were ordered. To avoid contamination, the radioactive deposit was sandwiched between two Mylar® films of 0.7 μm thickness.

As this operation was performed at atmospheric pressure, while these radioactive sources have to be operated under vacuum, we performed some tests to investigate their behaviour

in real conditions. In principle, the best would be to test with a blank source without any radioactivity, but all the sources are not prepared at once, so atmospheric pressure, temperature and humidity are not always the same. We thus decided to test all the radioactive sources with an unused chamber, connected to an old primary vacuum pump. Eventually, no damage or unusual behaviour was observed with the tested sources, and we could use it in our detection system.

2.6 Optimisation of the detection system using Monte Carlo simulations

The measurement of β spectra faces a major challenge: measured spectra can be distorted due to the interactions of β particles in different elements of the detection system. In order to obtain the initially emitted spectrum of a given transition and to reach the smaller uncertainties, the physical processes that lead to spectrum distortions must be minimised.

To study the origins of the spectrum distortions and other phenomena, the transport codes of particles in matter using the Monte Carlo method are very useful. However, the results obtained with transport codes must be validated by experimental results. In this section, we briefly describe the Monte Carlo methods and then the PENELOPE code that has been chosen in this work over other Monte Carlo simulation codes. Finally, we discuss the various studies carried out for the optimisation of the detection system.

2.6.1 Monte Carlo methods

The term Monte Carlo (MC) method refers to a class of algorithms implemented to calculate a numerical value for an unknown parameter by a sampling of random numbers. This method was invented by Stanislaw Ulam, a mathematician in the 1940s [118], as part of his contribution to the Manhattan project for the development of the atomic bomb. Monte Carlo methods have a wide range of applications in different fields such as physics, game theory, and finance. Our interest in Monte Carlo methods is the transport of fundamental particles in materials. The most known Monte Carlo codes used to simulate particle transport in the matter are PENELOPE [119], GEANT4 [120], MCNP [121], EGSnrc [122], etc. Originally, these codes were developed for specific objectives, for example, GEANT4 for high-energy physics, MCNP for neutron transport for the atomic bomb and reactor physics, EGSnrc for medical physics and PENELOPE were initially focused on the electron and positron transport for low energy. Nowadays, all these codes have a much more general outlook and all are capable of simulating the transport of the two types of particles that concern us in this work: electrons and photons.

In order to obtain the origin of distortions, a detailed track of interaction of the particles is required. As discussed in chapter 1, the average number of events per interaction of photons is low, making their transport simulation simpler than for electrons. The detailed simulation

of photon interactions by the photoelectric effect, or a pair production or a few Compton interactions (from the order of ten) is relatively easy with today's computing power.

For electrons and positrons, the situation is much more complicated. As already discussed in section 1.4.1, the average energy loss per interaction for an electron is low, of the order of a few tens of eV. Therefore, the high-energy electrons undergo a large number of interactions before being absorbed in the detector. A detailed simulation of electron or positron interactions with matter is only feasible when the average number of collisions per particle is not too large, typically a few hundred. A small number of collisions is only possible for elementary geometry. However, multiple scattering theory implemented in the transport codes makes it possible to simulate even a complicated geometry in detail.

2.6.2 PENELOPE

PENELOPE is a Monte Carlo code that was originally designed to handle the transport of electrons and positrons in the matter, for an energy range from a few hundred eV to 1 GeV [119]. PENELOPE stands for **PEN**etration and **E**nergy **LO**ss of **P**ositrons and **E**lectrons. It has been developed by the University of Barcelona and distributed by the Nuclear Energy Agency (NEA) of the OECD. Since then, it has been completed by the addition of photon transport, for an energy range from 100 eV to 1 GeV.

The simulation of electrons and positrons transport is performed by means of a combined process. The interactions for which the transfer of energy W or the scattering angle θ is greater than a predefined value (so-called hard collisions) are processed with condensed soft events in detail. It uses small cutoff values so that the soft collisions have a minimal effect on the detailed simulation. An accurate simulation of soft events is possible with the multiple scattering approach. However, the simulation of hard events affects the generation of secondary particles, which are important to consider in a detailed simulation. This is performed by adding small cutoff values; even though it increases the computation time, it gives detailed simulation tracks. Since the PENELOPE code uses a mixture of different methods and thus gives accurate results, it is considered as the reference code for the transport of electrons and positrons in the matter.

PENELOPE also simulates the emission of photons due to the fluorescence phenomenon and electrons subsequently to a vacancy in an electronic shell of an atom. The atomic relaxation due to this vacancy is continued until all the inner shells are filled.

PENELOPE is programmed in FORTRAN77 language; the code does not allow object-oriented programming. It is separated into several subroutines assigned to the geometry, the physics modelling, etc. It can be started from two main programs: *pencyl* and *penmain*. Generally, the geometry of PENELOPE allows quite complex quadric constructions. The main difference between *pencyl* and *penmain* is the geometry to be simulated. *Pencyl* allows only

cylindrical geometries, whereas *penmain* allows a more comprehensive set of three-dimensional surfaces. The *penmain* program is used in this work.

The two main files required to begin with simulation are a geometry file and an input file. A geometry file, with extension `.geo`, contains the geometry of the experimental set-up implemented. The material files used in the geometry are created from another dedicated program that uses a list of materials already registered in PENELOPE. It contains all the physical data on each material, including the tables of the physical properties (mean excitation energy, density, etc.), the interaction cross-sections, the atomic relaxation data, etc. A material absent of the predefined list can be created by entering its physical properties.

The input file, with the extension `.in`, is the main file where all the parameters are mentioned:

- Information on the type of particles to be simulated: electron, photon or positron;
- Initial energy for a monoenergetic source, or a spectrum with energy and total probability (in our case beta spectrum);
- Spatial coordinates, volumes, body numbers in geometry, etc.;
- The name of the material files used for the simulation accordingly with geometry and the corresponding parameters: absorption energies, cutoff parameters, etc.;
- The name of the geometry file;
- The detector information as an active body with energy range and number of bins;
- The names of the output files;
- The duration of the simulation in seconds or the total number of events to be simulated;
- The seed of the random number generator.

The output file generated after the simulation is the energy deposited in the detectors and its corresponding probability density, in 1/(eV*particle). However, in our case, we are interested in the energy deposited in each detector event-by-event in order to get the sum of the energies deposited in each of them. Therefore, we have implemented some modifications in the *penmain* PENELOPE code to obtain this information. The two detector energies are summed up to get the total energy deposition in the detection system for each event, a conventional coincidence procedure. The emitted primary energy for each event is also printed in this output file (Figure 2.34). This allows verifying the initial spectrum given as an input of the simulation.

```
#  Results from PENMAIN. Output from impact detector #
#
#  1st column: primary energy
#  2nd column: particle energy (KeV), 1st detector.
#  3rd column: particle energy (KeV), 2nd detector.
#  4th column: SUM energy (KeV).,
```

1.	124.785513213262249	0.000000000000000	0.000000000000000	0.000000000000000
2.	11.634660903339356	6.340657245133319	0.000000000000000	6.340657245133319
3.	77.704644358667906	13.995604868735485	49.483545586037081	63.479150454772565
4.	0.286832225919114	0.000000000000000	0.000000000000000	0.000000000000000
5.	45.373375135351388	0.000000000000000	1.915245959404593	1.915245959404593
6.	55.361201370461892	0.000000000000000	54.856540438933017	54.856540438933017
7.	29.442406615291052	23.013677021827451	0.000000000000000	23.013677021827451
8.	95.148398968676986	94.793284756869909	0.000000000000000	94.793284756869909
9.	53.948823082097789	23.731761227975625	26.503015500719723	50.234776728695351
10.	31.107052747439354	0.000000000000000	23.387308201488153	23.387308201488153
11.	33.957479531590721	0.000000000000000	21.249572267237163	21.249572267237163
12.	40.865095452886592	32.567044424594847	0.000000000000000	32.567044424594847
13.	45.796995891837710	27.885009384551179	12.767107840905229	40.652117225456408
14.	130.988265246386874	130.698034513146297	0.000000000000000	130.698034513146297
15.	18.128638377848205	0.000000000000000	3.823939079072771	3.823939079072771
16.	42.826762439112557	2.371750598019629	33.016592581094798	35.388343179114429
17.	89.023659954784023	88.400248681824237	0.000000000000000	88.400248681824237
18.	69.828660706726907	20.539643557753845	46.190169763706059	66.729813321459901
19.	8.446494024457406	0.000000000000000	0.000000000000000	0.000000000000000
20.	84.497807580425246	83.100711518286431	0.000000000000000	83.100711518286431

Figure 2.34 – Output of the simulation after the modification of the *penmain* PENELOPE code. The green rectangle highlights for an event the primary energy emitted in the source, the energy deposited in one detector, the energy deposited in the second detector and the sum of the energies deposited in both detectors, respectively.

2.6.3 Experimental developments

As already presented, the measurement geometry is highly crucial for the metrological study of the shape of β spectra. This geometry has to be designed very accurately to minimise the sources of distortion. We thus studied the influence of the distance between the two entrance windows of the detectors using PENELOPE simulations. The simple geometry of two face to face Si detectors surrounding a radioactive source was simulated. The study was performed for ^{14}C decay, which is an allowed transition with end-point energy of 156.476 (4) keV [123].

The ^{14}C beta spectrum calculated by the BetaShape program was used as an input of the simulation. The distance between the active layers of the detectors has a significant influence on the shape of the aggregate beta spectrum (Figure 2.35). The improvement with the new system, i.e. two detectors instead of a single one, in the absorption of electrons can clearly be observed. It is also clearly visible that there is still a remaining distortion at 1 mm distance that needs to be corrected. The distance between the detectors in the actual detection configuration is 3 mm. The simulation result clearly shows that it would be needed to decrease even more this distance in order to obtain a measured spectrum as close as possible to the emitted spectrum. Considering that minimising the distance below 3 mm is practically not feasible, the remaining distortion must be corrected by an unfolding procedure (see chapter 4).

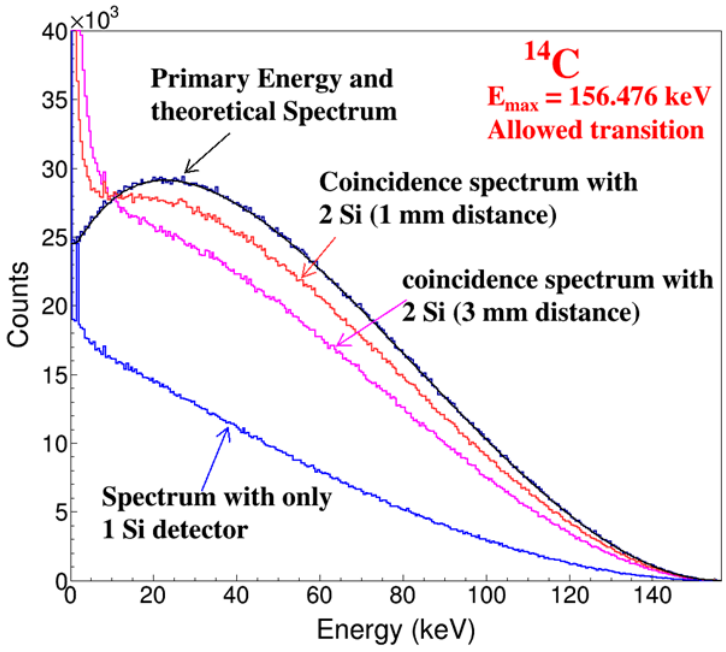

Figure 2.35 – The Monte Carlo study showing the influence of the distance between the detectors. This distance is of 3 mm as defined in the actual set-up configuration.

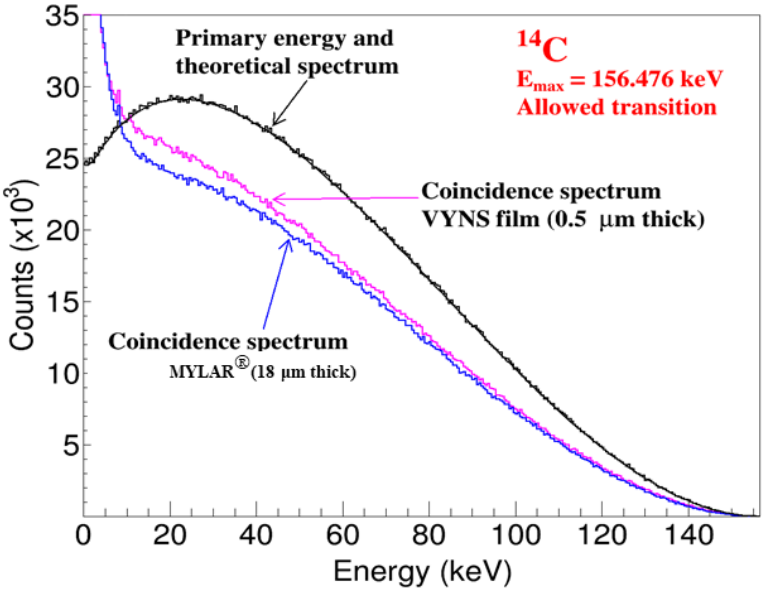

Figure 2.36 – ^{14}C spectra obtained with Monte Carlo simulation for VYNS (0.5 μm thick) and Mylar® (18 μm thick) films as source supports, illustrating the self-absorption phenomenon in the actual measurement system.

2.6.4 Radioactive sources

After limiting the distortion due to detection geometry, it is important to study the influence of different types of source support on the shape of beta spectra. The same geometry has been implemented as above, and two realistic thin films have been considered: a 0.5 μm thick VYNS and an 18 μm thick Mylar® film.

The effect of the thickness of the source support is clearly shown in Figure 2.36. The self-

absorption in the 0.5 μm VYNS film is less than in the 18 μm Mylar® film and this effect is more significant at low energies. As a result, we first used 0.5 μm thick VYNS films as the source support material. Then, as explained in section 2.5.3, the Mylar® film with 0.7 μm thickness had been made commercially available. As it is more robust than VYNS film, it has been preferred in a second time. In order to confirm our choice, we compared the results of the simulations for a 0.5 μm thick VYNS and a 0.7 μm Mylar® films (see Figure 2.37). The result shows that it is an excellent compromise to use Mylar® shielded source as the distortion will be corrected for the final extraction of the spectrum.

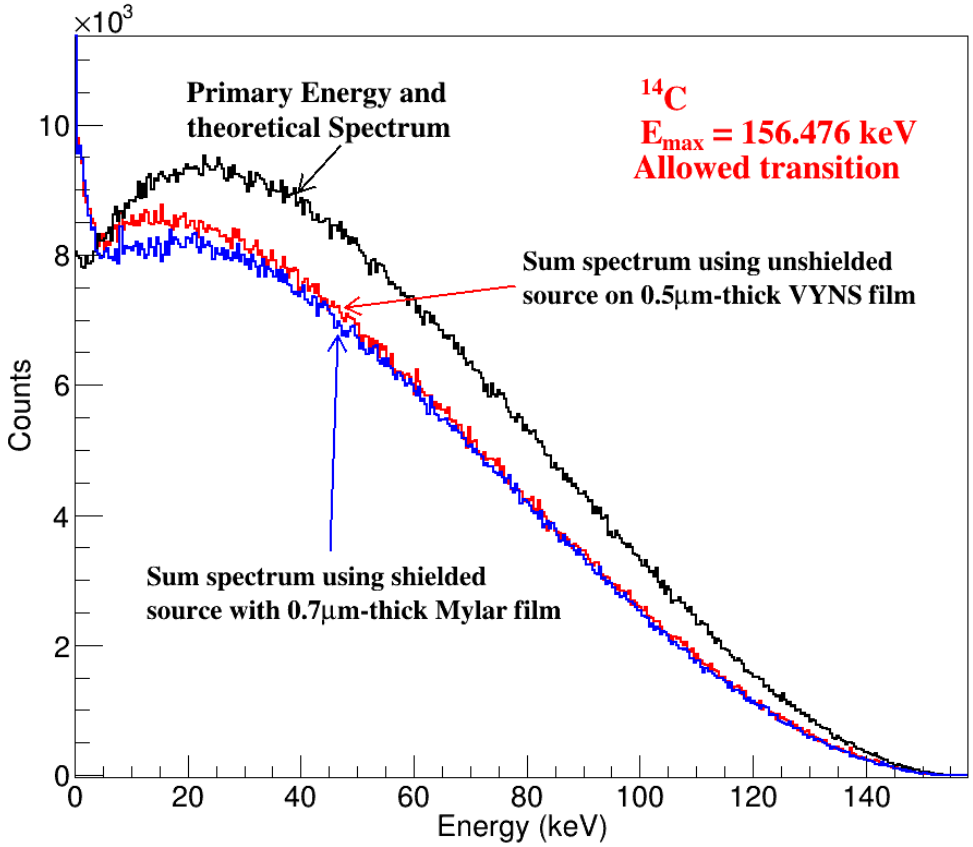

Figure 2.37 – Comparison of self-absorption phenomenon in radioactive sources with different source supports using Monte Carlo simulations. The red curve represents the spectrum obtained with the actual geometry for a radioactive source on a 0.5 μm thick VYNS film without shielding. The blue curve represents the spectrum obtained for a radioactive source prepared on a 0.7 μm Mylar® film and shielded with an identical Mylar® film.

2.6.5 Silicon-Lithium device

A Monte Carlo study has been performed for ^{90}Y decay, whose end-point energy is 2278.5 (16) keV [123]. The theoretical spectrum given by the Betashape program was used as an input of the simulation. The almost 4π detection geometry with 2.4 mm distance between the detectors (see section 4.1.3.3) and a shielded radioactive source on Mylar® film has been implemented in PENELOPE. Figure 2.38 shows the beta spectrum of ^{90}Y obtained with simulation. The main difference observed between the initially emitted spectrum and the "measured" spec-

trum comes from the bremsstrahlung process. Indeed, electrons loose some energy due to this process, and the emitted photons are only partially detected in the Si(Li) detectors.

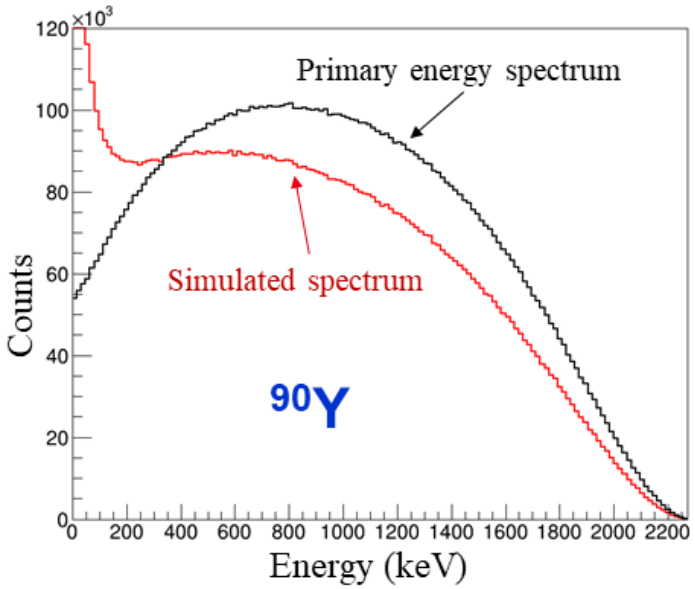

Figure 2.38 – Monte Carlo simulation for ^{90}Y using the actual Si(Li) detection geometry. The black curve represents a theoretical spectrum from Betashape as an input of simulation. The red curve shows the simulated spectrum using our almost 4π geometry.

Conclusion

In this chapter, a new experimental set-up developed for β spectrometry has been presented with the following main characteristics:

- Physical processes such as backscattering and self-absorption on the shape of beta spectra have been studied and limited as much as possible.

- The detection system has been designed by taking into account the requirements and constraints. It includes an almost 4π detection geometry with a sandwich of two silicon detectors and a radioactive source. The distance between the detectors has been minimised to 3 mm for PIPS device and 2.4 mm for Si(Li) device.

- The preamplifiers are placed at 3 cm distance from the detectors. Different acquisition systems have been tested, and finally, the *nanoMCA* module from *labZY* has been used.

- The radioactive sources are prepared with VYNS and Mylar® films. However, considering the disadvantages of VYNS film and commercial availability of 0.7 μm Mylar® film, the latter was preferred.

– The self-absorption effect due to the crystallisation of the radioactive solution has been reduced as much as possible by considering different drying methods: freeze and oven drying.

– The experimental set-up has been optimised using PENELOPE Monte Carlo simulations. One of the studies highlighted the influence of the distance between the detectors on the shape of the beta spectrum. The shorter the distance between the detectors, the closer the resulting spectrum to the initially emitted spectrum. Another study showed the self-absorption effect in the source support material by using two films of different thicknesses. Indeed the thinner the thickness, the lower the self-absorption. The set-up has been improved with new components based on several measurement tests performed.

We will see in the next chapter that the described set-up is only a first version. The measurements performed motivated us to improve it in different aspects in order to reach the best possible accuracy.

"What I love about science is that as you learn, you don't really get answers. You just get better questions."

- John Green

Chapter 3

Results and Analysis

The influence of different parameters on the spectrum shape has been studied in the previous chapter. The geometry of the detection system was thus optimised in order to limit the distortion of spectra. This chapter presents all the complementary studies: characterisation of the experimental set-up including energy calibration, analysis of the measured β spectra, and comparison with Monte Carlo simulations. The measurements are described in three steps:

1. Tests of the detection system in its first implementation;
2. After improvements of the detection system, without cooling;
3. Final configuration with cooling, and influence of the radioactive sources preparation on the measured spectrum shape.

The geometry and input files of the simulations are explained in detail.

3.1 Methods and analysis

The measurements are acquired in the form of spectra. Then, it is necessary to analyse them to obtain usable information. Several means have been used to achieve this, one of them being the PENELOPE code. Analysis and comparison of both simulated and measured spectra have been performed with the help of dedicated routines developed using the ROOT environment [124]. In this section, the implementation of the experimental geometry for the Monte Carlo simulations, the input β spectra, other simulation parameters, and the method to characterise the detectors are discussed in detail.

3.1.1 Monte Carlo simulations using PENELOPE

The detection system has been developed to minimise the physical phenomena that distort the measured spectrum, as discussed in chapter 2. However, all these phenomena still contribute to some spectral distortion without being totally eliminated. The response of the detection

system must be determined precisely to extract accurate information from the acquired spectrum. As explained in chapter 2, each component associated with the detection system has been designed or purchased on purpose. Therefore their dimensions are accurately known. Subsequently, the experimental geometry has been implemented in PENELOPE to perform the simulations.

3.1.1.1 Model of geometry

In PENELOPE, PENGEOM is the dedicated interface to build geometries. The close geometry of the two Si detectors with radioactive source in the middle has been created (see Figure 3.1). The PIPS® detectors are modelled as a 1 mm thick Si active volume, with a 50 nm thick dead layer of equivalent Si and an active surface area of 300 mm^2. These detectors are enclosed in copper holders. The entrance windows are at 3 mm distance from each other. The radioactive source is modelled as a 0.7 μm thick Mylar® film supported by a stainless steel ring, as described in the previous chapter (see Figure 3.2).

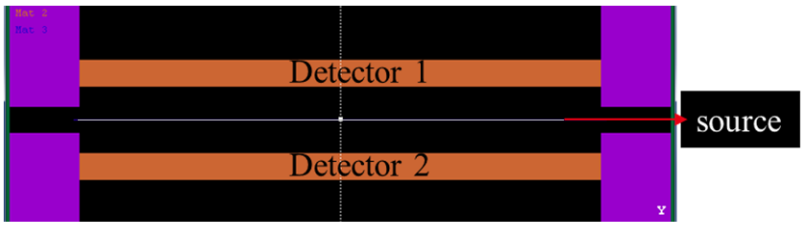

Figure 3.1 – Diagram of the detection system geometry implemented in PENGEOM (PENELOPE). The pink colour represents the detector holders in copper material. PIPS® detectors, 1 mm thick including 50 nm thick dead layer (equivalent Si), are in orange and the radioactive source is the thin white line in the middle of the detectors.

The radioactive deposit is modelled as a volume of air at a pressure of 10^{-7} mbar (10 mm diameter and 10 nm thickness) on the top of an 8 nm thick plain latex layer. In order to have more accurate simulations, this deposit has been modified by the actual material: $TlCl_3$ for ^{99}Tc, NaCl for ^{36}Cl, etc. The layer of latex models the electrosprayed microspheres, whose (actual) diameter is 70 nm. As explained in chapter 2, we deduced that we effectively deposited a monolayer of microspheres by weighing the films before and after electrospraying. The actual volume of latex is the deposit area paved with spheres, represented here by a plain layer of equivalent thickness containing the same quantity of material (see Figure 3.3). Finally, the source shielding is taken into account with an additional 0.7 μm thick Mylar® film.

When the radioactive sources have been prepared on a VYNS film of 0.5 μm thickness, the modelling of the geometry has been implemented accordingly.

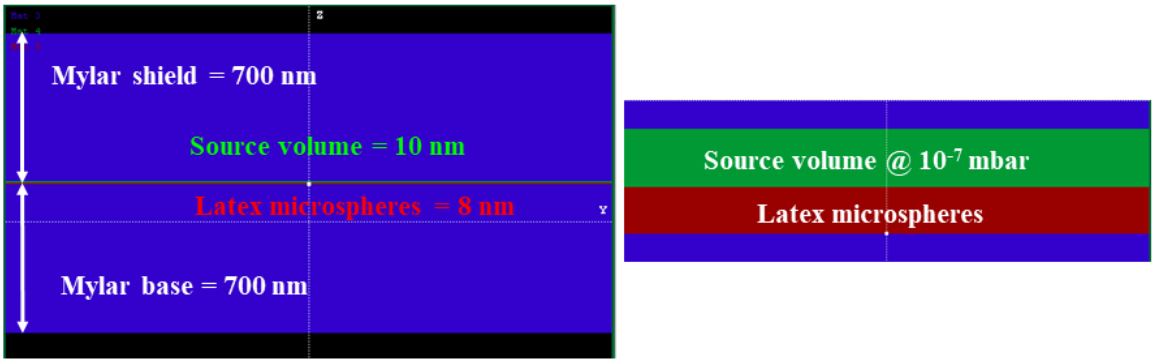

Figure 3.2 – Scheme of the radioactive source geometry implemented in PENELOPE. Left: the thicknesses are at the same scale : 700 nm Mylar® film with 8 nm latex body and 10 nm radioactive deposit. Right: a zoom of left picture.

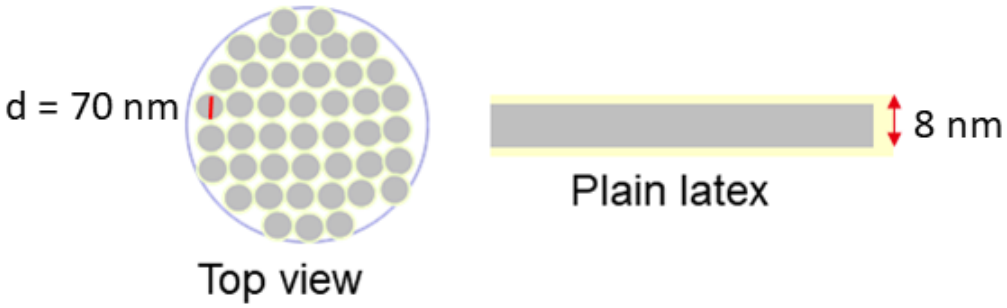

Figure 3.3 – Scheme of the latex microspheres (70 nm diameter) paved on the radioactive deposit area and the equivalent plain latex (8 nm depth). The same volume of latex in both cases.

3.1.1.2 Input of the simulation

The input of the simulation is used for the generation of the primary particles, namely the emission spectrum. In our case, it is a β spectrum provided by the BetaShape program based either on experimental shape factors, if any available, or on a theoretically calculated spectrum. In order to verify the characterisation of the detection system, we performed simulations of the radionuclides used for energy calibration based on their decay schemes, which are from the nuclear decay data evaluated by the DDEP. This will be further discussed in detail.

3.1.1.3 Other input parameters

In the previous chapter, we described the importance of the multiple scattering theory used in Monte Carlo simulations. In PENELOPE, they are controlled by some input parameters:

- absorption energy E_{abs};
- constants C_1 and C_2;

- the cutoff energies W_{cc} and W_{cr}.

The *absorption energy* corresponds to the minimum value of energy absorbed in the material, which should be greater than 50 eV in PENELOPE because of the interaction databases.

The parameter C_1 defines the mean free path between the hard collision events. It should be small enough to ensure reliable results.

The parameter C_2 gives the average fractional energy loss between two hard collision events [119].

The cutoff energies W_{cc} and W_{cr} correspond to the cutoff energies of hard inelastic collisions and hard bremsstrahlung emission, respectively. They influence the simulated energy distribution. By using larger cutoff energies, simulation speed can be enhanced. However, using too large values may distort the simulated distribution because of the missing information. In practice, the simulated energy distributions are observed to be quite insensitive to the exact values of these cutoff parameters. Still, they must be chosen according to the requested precision of the simulation.

In our case, parameters E_{abs}, C_1, C_2, W_{cc} and W_{cr} were varied to see the influence on the β spectrum shape of ^{14}C decay. Tests were performed for cutoff energies of 250 eV and 1 keV, and one can see in Figure 3.4 that the resulting spectra almost overlap. Residuals between the two simulated spectra, given in Figure 3.5, show that the impact of higher energy cutoff is less than 0.07%, which matches well our aimed precision and speeds up the simulation by 60%.

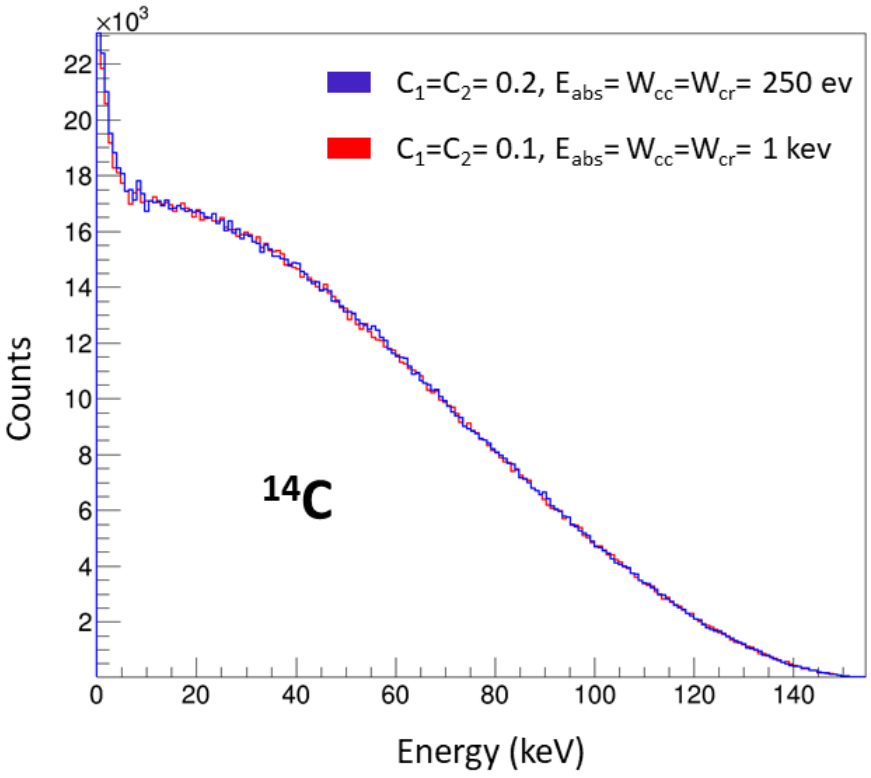

Figure 3.4 – Comparison of different input parameters using the almost 4π geometry, with the example of ^{14}C decay.

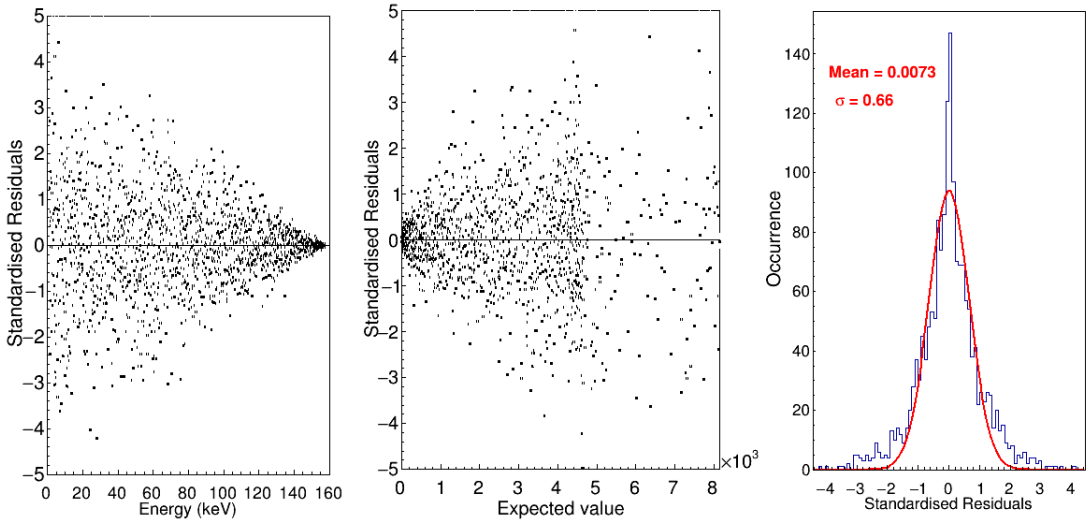

Figure 3.5 – Residuals of the comparison of different input parameters in Figure 3.4: The red curve is a Gaussian fit that shows residuals are distributed around zero.

The definition of residuals can be found in section 3.1.5. It is noteworthy that even at low energy (below 10 keV), the residuals are uniformly distributed, and no distortion is observed: the Gaussian fit of the residuals (red curve in third Figure 3.5) clearly demonstrates that the 1 keV energy cut can be safely used. Finally, the parameters used to obtain the red curve in Figure 3.4 (1 keV) are kept for the simulations.

Apart from these input parameters, the use of a source box is crucial to define the radioactive source dimensions. Even though the source body has to be declared in the input file, its dimensions and homogeneity are determined by its intersection with the source box, whose dimensions are provided by the user. Generally, this should be scaled twice the size of the source body in order to ensure the actual source dimensions.

3.1.2 Nuclear and atomic databases for Monte Carlo simulations

The simulation of multiple particle emissions requires a specific procedure to sample the decay pathways. Even for nuclei with simple decay schemes, the measured spectra can have some additional structures due to time-correlated emissions, which influences the coincidence measurements [125]. Random decay simulations require nuclear decay data, for example, from ENSDF files in GEANT4 simulations. The evaluated data from DDEP are recommended by the BIPM for their reliability and are, therefore, the reference data in radionuclide metrology.

The PenNuc module uses these data for the simulation of random decay pathways. This module automatically manages the nuclear decay and the atomic relaxation of a given radionuclide. It generates the emitted energies of the photons, electrons and positrons[1]. Each transition is then followed either by the emission of electrons or photons (β or γ transitions) or

[1]Alpha particles, and heavy ions in general, are not simulated in PENELOPE.

by a vacancy in the inner shell (internal conversion process in a gamma transition, or electron capture). The subsequent atomic relaxation is simulated by using the database of transition probabilities and energies from [126]. The DDEP decay scheme of a radionuclide is available on LNHB website[2] in a specific text file with a format adapted to PenNuc. The file for ^{207}Bi decay and the parameters are described in ANNEX I 4.1.3.3.

3.1.3 Energy calibration

When electrons interact in a detector, the deposited energy is determined from the electric signal and stored in the form of channel numbers. In order to obtain the measured spectrum in terms of energy, an energy calibration is required. In practice, this is performed by measuring well-studied radionuclides with well-known energy lines as reference. By measuring electron lines, one can establish a relationship between an energy and a channel number. The calibration curve is obtained using a polynomial relationship:

$$E(\text{keV}) = E_0 + G_1\, C + G_2\, C^2 + G_3\, C^3 + ... \tag{3.1}$$

where C is the channel number, E_0 is the energy at channel 0 and G_i is the gain of the channel energy [57]. Silicon semiconductors are known for their almost linear energy response, and a linear adjustment is generally sufficient. Thus, it is possible to fit the data using a linear curve $y = ax + b$ where the parameters are determined by the least-squares method, which minimises the difference between the observed data (y_i) and the fitted points:

$$\sum_{i=1}^{n} [y_i - (a + bx_i)]^2 \tag{3.2}$$

The curve is fitted using the Microsoft Office Excel software, and the corresponding fit quality is given by the parameter "R^2". Its value ranges from 0 to 1, the better the fit, the closer to 1. The determination coefficient R^2 is the square of the correlation coefficient "r" defined as the ratio of the covariance between the variables x and y to the product of their standard deviations.

The energy calibration is determined from the centroid position of the peaks, obtained using the COLEGRAM software [127] developed at LNHB. The procedure consists of fitting mathematical functions to the experimental data points in order to describe at best the different peaks of the spectrum. The adjustment of the mathematical function is made using the Marquardt-Levenberg algorithm according to the least-squares or χ^2 methods.

3.1.4 Energy resolution

The performance of a detector is characterised in particular by its energy resolution. The number of electron-hole pairs created during the interaction of an electron in the detector is not

[2] `http://www.lnhb.fr/nuclear-data/nuclear-data-table/`

constant, and as the charges drift to the electrodes, they may recombine or produce new pairs. As a result, the peak induced by a beam of a mono-energetic electron does not correspond to a Dirac function in the energy spectrum. Still, it has a certain width, usually close to a Gaussian distribution. Besides, the noise of the electronic chain contributes to this peak width. The energy resolution, or Full Width at Half Maximum (FWHM), is generally approximated by the following relationship:

$$W_T^2 = W_P^2 + W_C^2 + W_E^2 \tag{3.3}$$

The first term W_P^2 is the fluctuation of the number of charges created in the detector and is given by:

$$W_P^2 = (2\sqrt{2\ln 2})^2 F\epsilon E \tag{3.4}$$

where ϵ is the average energy to create an electron-hole pair (3.76 eV for Si at 77 K), E is the energy of the incident photon, and F is the Fano factor. The presence of the last factor is explained by the fact that the pair creation statistic does not exactly follow a Poisson's law, in which events are independent of each other. The Fano factor [128, 129] is the ratio of the observed variance of the number of created pairs to the variance according to Poisson's law. Any theoretical prediction is tough to perform because it depends on the quality of the detector crystal. It is usually measured, and its value is typically 0.1 for silicon and germanium detectors [80].

The term W_C^2 corresponds to the charge collection statistic, and it varies as the square of the energy of the incident electron. The effects of an incomplete charge collection are linearly dependent on energy. As the energy increases, the number of charge carriers created in the detector increases, and thus, the charge collection may be incomplete. This effect also increases with the dimensions of the detector crystal. The recombination phenomena probabilities increase when the distance between the electron-hole pair creation increases, allowing a greater collection.

The electronic noise W_E^2 is highly dependent on the detector capacitance and the electronic components of the acquisition system. Its contribution to the FWHM is energy independent.

Since the values of any of these terms cannot be determined independently without experimental study, the analysis for the FWHM evaluation was performed using a Gaussian function and is expressed by:

$$\text{FWHM} = 2\sqrt{2\ln 2} \times \sigma \tag{3.5}$$

where σ is the standard deviation of the Gaussian distribution. It is determined experimentally from the peaks used for the energy calibration. PENELOPE does not take into account these effects of charge collection and electronic noise, which in reality, degrade the intrinsic resolution of the detector. Therefore, the simulated spectra need to be convoluted with a realistic Gaussian distribution to account for the energy resolution of the detection system.

During a simulation, all the energy deposited in the detection volume is stored in a file event-by-event. After the end of simulation, it produces a `.dat` file. This file is then processed by a ROOT macro to fill in a tree event-by-event, and finally, a histogram of counts as a function of energy is created. To take into account the resolution of the detector, the deposited energy is spread in a Gaussian distribution centred on the stored energy with the experimental FWHM.

3.1.5 Validation of simulations

The measured spectrum of each radionuclide has been compared with the corresponding simulation. To analyse the two spectra, they must be normalised, which is done by integration in a given energy range.

The agreement of the spectra can be qualitatively explained by visual interpretation. However, to be accurate, a quantitative assessment is necessary.

Here, the coefficient of determination R^2 introduced previously, can also be used. If we consider a set of n measurements "y_i" and a model resulting in n predictions "y_i^{th}", one has:

$$R^2 = 1 - \frac{\mathrm{var}(\hat{e}_i)}{\mathrm{var}(y_i)} \quad \text{with} \quad \hat{e}_i = y_i - y_i^{th}. \tag{3.6}$$

This definition is valid for $n >> 1$ for any type of model. Again, a value close to unity indicates good agreement between the prediction and the experiment. The error of the model is defined by $\hat{e}_i$ and the unbiased variance estimates are:

$$\mathrm{var}(y_i) = \sum_{i=1}^{n} \frac{(y_i - \overline{y})^2}{n-1} \quad \text{and} \quad \mathrm{var}(\hat{e}_i) = \sum_{i=1}^{n} \frac{(\hat{e}_i)^2}{n-p-1} \tag{3.7}$$

with $\overline{y}$ the average of the measurements and p the number of parameters of the model. For β spectra, two parameters constrain the model: the maximum energy $E_{\max}$ and the normalisation parameter of the simulated data to the experimental data. Hence, R^2 is determined with these two parameters and it defines the global disagreement between the measured and the simulated spectra. We have also considered the standardised distribution of residuals:

$$r_i = \frac{\hat{e}_i}{\sqrt{\mathrm{var}(\hat{\mathrm{e}}_\mathrm{i})}} \tag{3.8}$$

If the predicted value (from simulation, calculation, or fit) is relevant, 99.7% of the standardised residuals must fall within [-3,3], 95.4% within [-2,2] and 68.3% within [-1,1]. Three different ways of residuals are considered, firstly, standardised residuals as function of energy showing their non-linearity. Secondly, standardised residuals as function of the expected value (simulation or calculation) presenting how the prediction reproduces the observed. Thirdly, by projecting the residuals on the Y-axis we obtain the histogram of the residuals, showing their probability distribution, where a Gaussian can be fitted. The variance of the Gaussian provides us a second criterion to assess the quality of comparison.

3.2 First test of the measurement system

The first implementation of the detection system was characterised by measuring the conversion electron lines from a ^{133}Ba source. The corresponding Monte Carlo simulation has also been performed using the PenNuc module. The comparison between measurement and simulation is discussed below. The analysis of ^{36}Cl decay has also been carried out and is described.

3.2.1 Characterisation of detectors with ^{133}Ba decay

The ^{133}Ba radionuclide is widely used for energy calibration, providing a large number of X-rays, γ-rays, and conversion electrons. The energy calibration of our detection system has been determined by measuring the conversion electron peaks. The response of the detection system was found to be linear from 35 keV to 350 keV, as can be seen in Figure 3.6 and from the R^2 coefficient. The FWHM was observed to be 16 keV for the electron peak of ^{133}Ba at 80 keV.

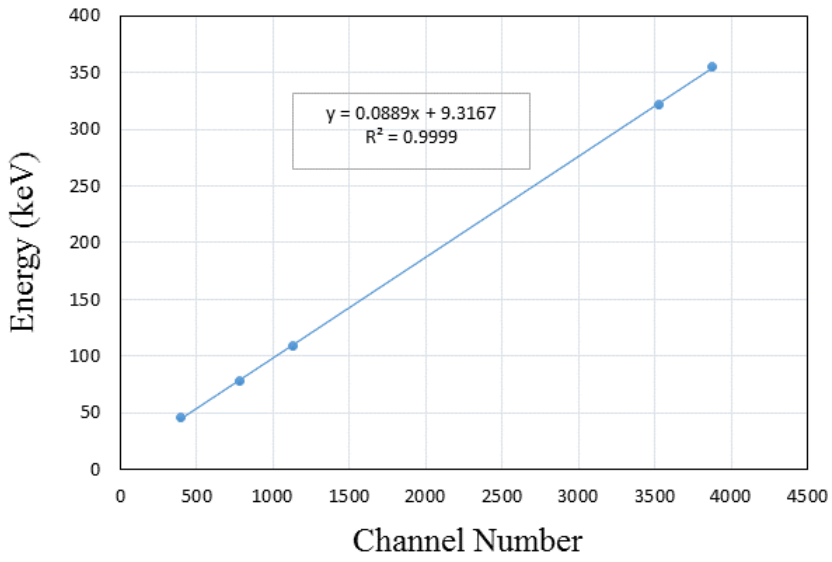

Figure 3.6 – Preliminary energy calibration curve of electron energy as a function of channel number, performed with the conversion electron lines from ^{133}Ba decay.

The measured spectrum of ^{133}Ba decay has been compared to the corresponding simulation (see Figure 3.7), which has been convoluted with a Gaussian distribution using the experimentally observed standard deviation. The spectra look to be in fair agreement. But, as the disagreement parameter $(1 - R^2)$ between 35 keV and 550 keV is of 23.5%, it cannot be considered as sufficiently good for our purpose, particularly between 100 keV to 250 keV. The analysis of ^{133}Ba is complicated due to the emission of conversion electrons and Auger electrons. As, the energies are very close to each other, the separation of the peaks is difficult because of

the energy resolution of our detection system. The disagreement between the spectra emerges from both measured and simulated. The measurement is preliminary and is thus not perfect, and the simulation is based on decay data library, whose inconsistency for ^{133}Ba has already been observed in [130]. In addition, the electron peaks are not measured but based on the γ-rays and Internal Conversion Coefficients (ICC) values. From the measurement side, one can also think about the self-absorption effect on the spectrum, which is observed for other radionuclides and discussed in section 4.1.3.3. However, it is evident that both the energy resolution and the threshold can be improved, what we will see in the following sections.

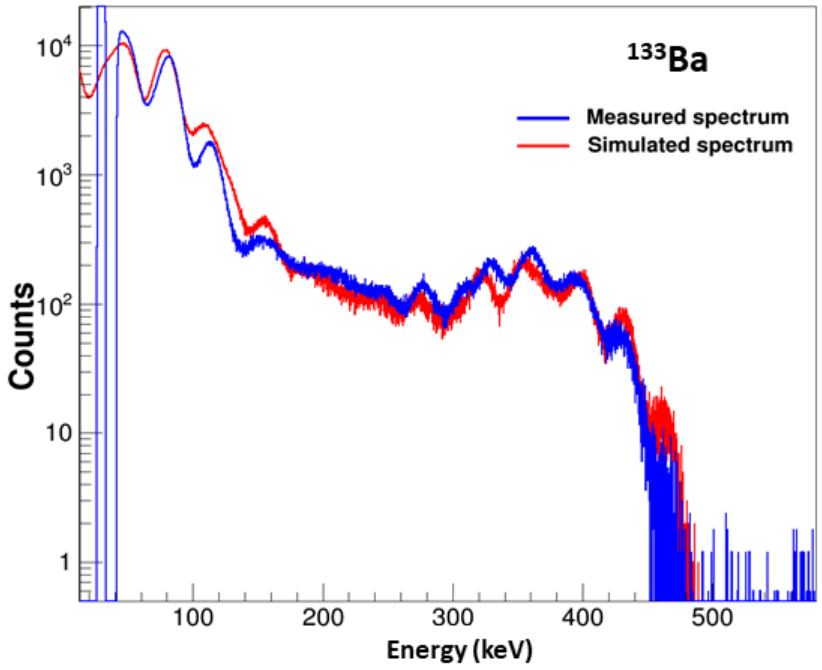

Figure 3.7 – Comparison of measured spectrum (blue) and simulated spectrum (red) using the PenNuc module for ^{133}Ba decay.

3.2.2 Beta spectrum measurement of ^{36}Cl decay

The first β spectrum measurement has been performed for ^{36}Cl decay. With maximum energy of 709.53 (4) keV [123], an emitted β particle should be stopped within the thickness of our Si detectors (1 mm). The ^{36}Cl source was prepared on a VYNS film (0.5 μm thick), and the corresponding experimental geometry has been simulated in PENELOPE. The transition is second forbidden non-unique; its spectrum shape is thus sensitive to the structure of the nuclear states involved, making difficult any accurate theoretical prediction. Therefore, the input spectrum was generated using the experimentally extracted shape factor from Rotzinger [96]. This measurement was carried out with metallic magnetic calorimeters (MMC) with an energy resolution of 700 eV at 122.1 keV [96]. As the MMC measurements are known for their preciseness, it is reliable as input for our simulation.

The energy calibration curve determined from the ^{133}Ba measurement has been applied to the ^{36}Cl measurement, assuming a linear response beyond 400 keV, which is reasonable for Si detectors. The spectra have been normalised by integration between 200 keV and 300 keV (Figure 3.8). Above 35 keV, good agreement between the measured and simulated spectra has been observed with a disagreement parameter $(1 - R^2)$ equals to 1.8%. However, it is still not a sufficiently good agreement for the main objective of our study, and the measurement needs to be improved to reach better accuracy.

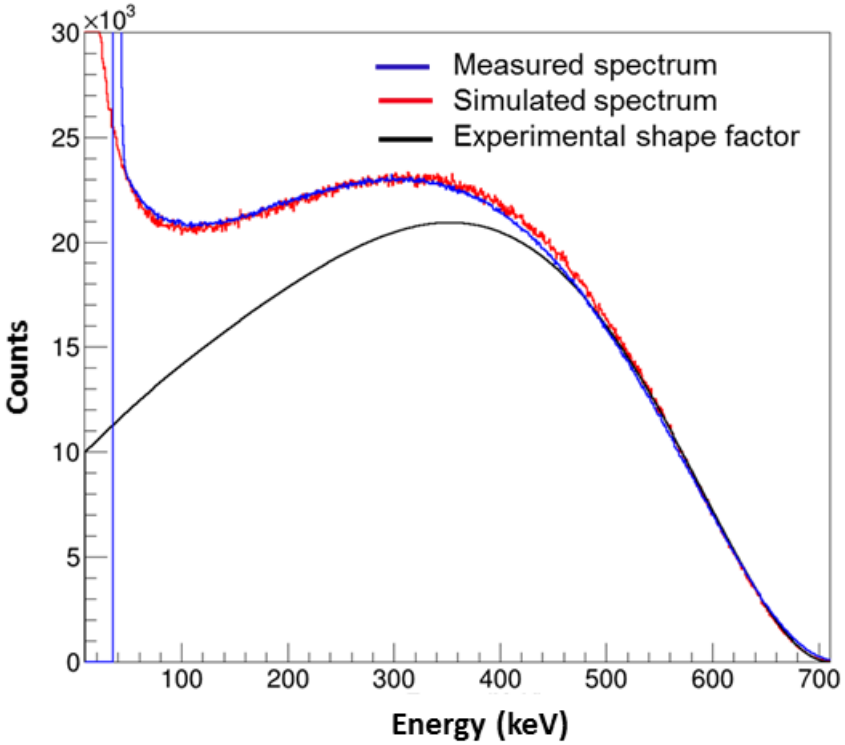

Figure 3.8 – Comparison between measured spectrum (blue), simulated spectrum (red) and the spectrum from the experimental shape factor (black) extracted from Rotzinger [96] for ^{36}Cl decay (2^{nd} forbidden non-unique transition).

3.2.3 Conclusion of the first test

The preliminary measurements have been achieved with sources prepared on purpose for ^{133}Ba and ^{36}Cl radionuclides to test the system. The results clearly demonstrate the relevance of measuring β spectra with the current technique, in 4π geometry.

However, the first measurements performed after the set-up implementation showed an energy threshold of 35 keV and an energy resolution of 16 keV at 80 keV.

The current experimental set-up aims to measure precisely the shape of β spectra with the lowest energy threshold possible and better energy resolution, which is not accomplished. Hence, the set-up requires further improvements to access more accurate information.

3.3 Measurements with improved set-up without cooling

Preliminary results in the above section showed a need for improvement in the experimental set-up. Many attempts were made to improve the signal-to-noise ratio. One of the significant advancements was the settlement of ground loops. All the cables connected to different electronic modules have been upgraded by single and double shielding. A transformer has been used to decouple the ground of the vacuum pump with other electronics. By identifying noise and contamination of ^{14}C in the detector itself, the PIPS detectors have been replaced (see chapter 2). These changes improved the signal-to-noise ratio and will be seen in this section.

In this section, the characterisation of this new implementation of the detection system and the β spectrum measurements will be discussed. These measurements have been performed at room temperature.

3.3.1 Characterisation of detectors

The energy calibration has been extracted by measuring the particles emitted in ^{109}Cd and ^{207}Bi decays, which provide a wide range of well-defined energies.

^{109}*Cd decay*

The measurement of ^{109}Cd decay has been chosen in particular to test the energy threshold. The radioactive source was prepared on a 0.7 μm thick Mylar® film. The peaks have been analysed with the COLEGRAM software and fitted using Gaussian functions (Figure 3.9). The energy threshold of 22 keV has been obtained. By employing the reference peak energies from the decay of ^{109}Cd and ^{207}Bi, an energy calibration has been extracted (see Figure 3.13). The energy resolution (FWHM) extracted from 62 keV peak was found to be 12 keV. By applying this calibration curve, the energy is observed with a slight shift towards low energy (see Table 3.1). The discrepancy seems to originate from the energy loss within the radioactive source and the dead layers. The electrons are passing through the 0.7 μm Mylar® film, loosing an energy of 0.5 keV for a 62.5 keV electron according to ESTAR [70].

^{207}*Bi decay*

The second measurement was performed for the ^{207}Bi decay. The radioactive source was also prepared on a 0.7 μm thick Mylar® film. The peaks fitted in the energy range 450 keV - 580 keV and 950 keV - 1100 keV are shown in Figures 3.10 and 3.11. The fitted peaks used for energy calibration (see Table 3.1) show a relative difference in energies of about 0.2%. The shoulder of peak at 482 keV is not very well resolved; however, the fit shows the energy of about 493 keV. There is no direct electron emission at this energy, but the probability of Auger

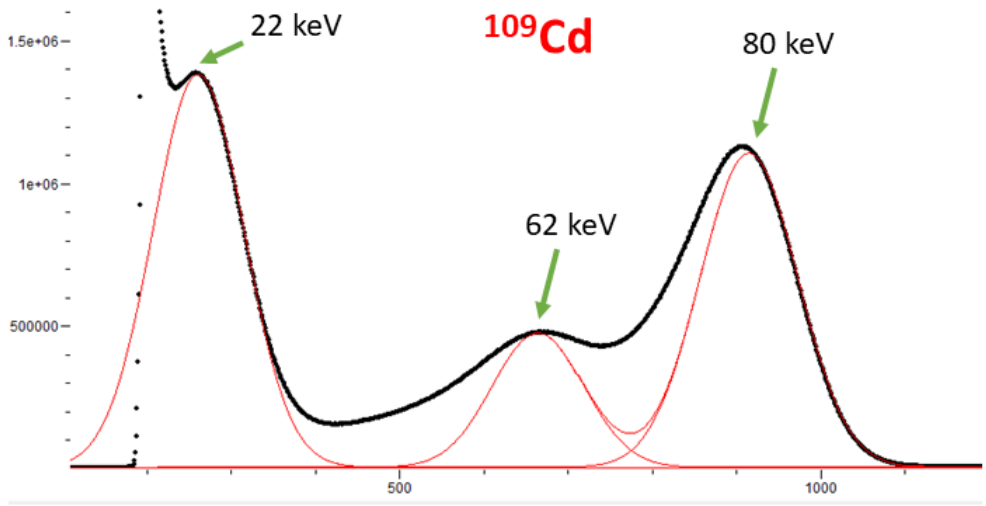

Figure 3.9 – The analysis of ^{109}Cd spectrum by using COLEGRAM software. The peaks are fitted with Gaussian functions.

electron emissions between 5.2 - 15.7 keV is very high (54.8%). The origin of the second peak seems then to originate from coincidence events in which conversion electrons at 481.6 keV and Auger electrons deposit their energy. The same structure is observed for the 553 keV and 975 keV peaks.

The measured spectrum of ^{207}Bi has been compared with a Monte Carlo simulation (10 million events) using the PenNuc module to verify the observed structures (see Figure 3.12). The simulation was convoluted with the observed FWHM of the detection system. The spectra were normalised by integration between 300 keV and 500 keV. Good agreement was obtained between the measured and the simulated spectra, with a disagreement parameter $(1 - R^2)$ equals to 5.3%. This value seems rather high and is due to the statistics of simulation and to the poor accuracy of the atomic data used for Auger electron emission. Nevertheless, it still validates the characterisation of the detection system.

Radionuclide	Nature	Expected energy (keV)	Channel number	Measured energy (keV)	$\lvert\Delta E\rvert$
^{109}Cd	$ec_{1,0\ K}$	62.5	665	61.787	2.17%
^{207}Bi	$ec_{1,0\ K}$	481.6	5391	482.162	0.24%
	$ec_{1,0\ L}$	553.6	6200	554.22	0.22%
	$ec_{3,1\ K}$	975.65	10923	974.95	0.004%
	$ec_{3,1\ M}$	1061.74	11865	1058.86	0.107%

Table 3.1 – The conversion electron energies from the decay of ^{109}Cd and ^{207}Bi used for the energy calibration. Expected energies are from the decay data evaluations [9].

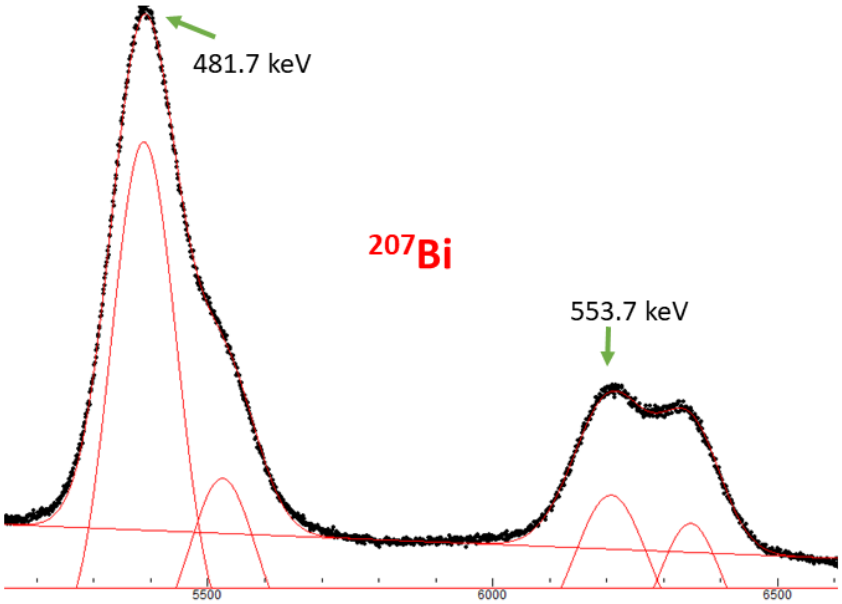

Figure 3.10 – Analysis of the ^{207}Bi conversion electron lines with the COLEGRAM software.

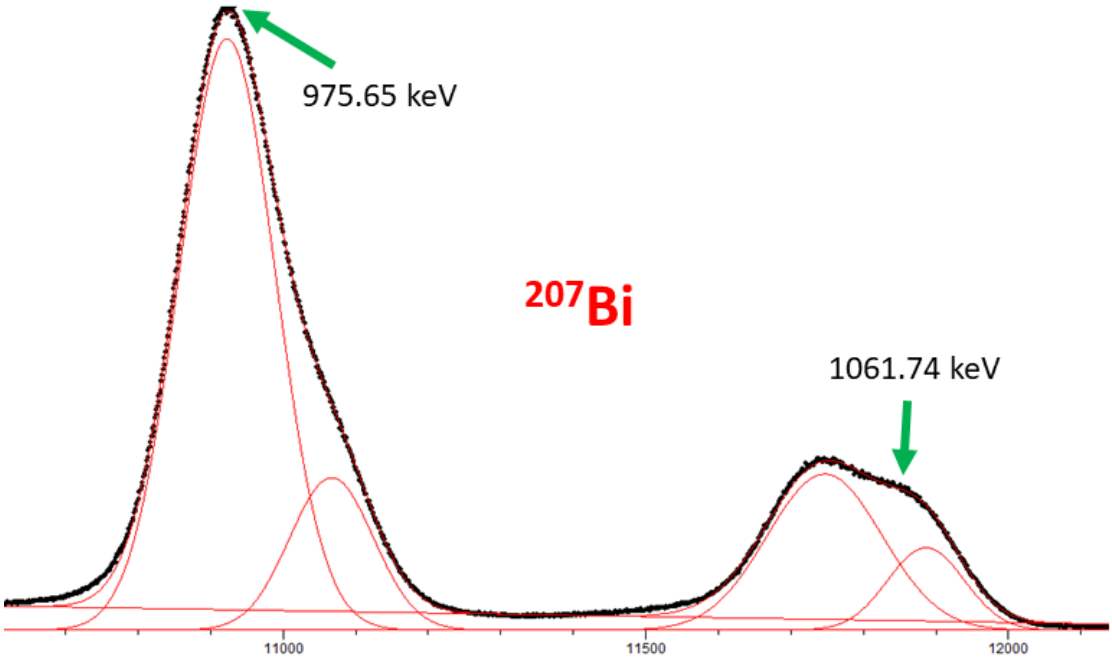

Figure 3.11 – Analysis of the ^{207}Bi conversion electron lines at higher energies with the COLEGRAM software.

3.3.2 Beta spectrum measurements

After the characterisation of the detection system, β spectra have been measured for the decays of ^{14}C, ^{36}Cl, ^{99}Tc and ^{204}Tl. All the β spectra are discussed below in detail. Systematic background measurements have been performed to verify that there is no radioactive contamination of detection system due to potential material leakage from the sources. All the measured

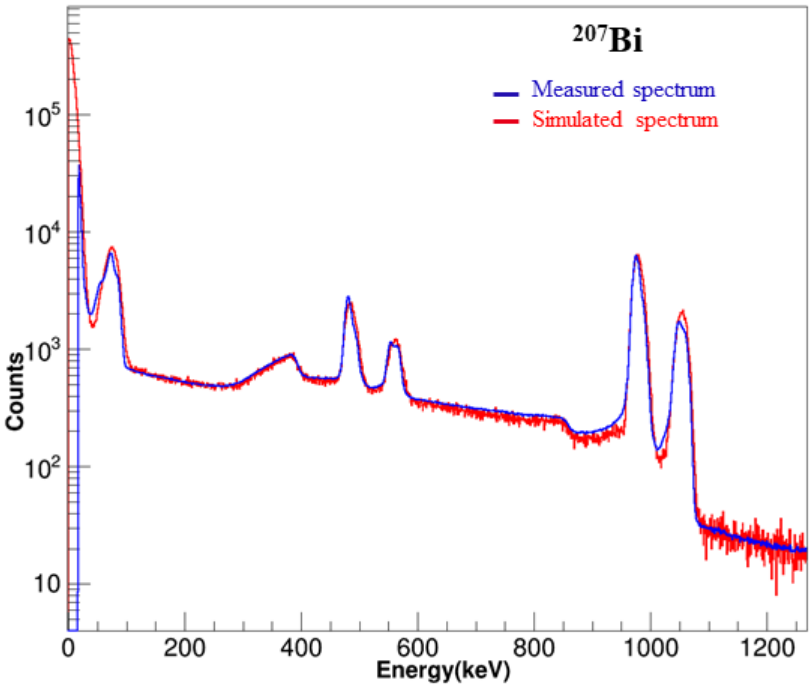

Figure 3.12 – Comparison of measurement (blue) and simulation (red) for ^{207}Bi decay.

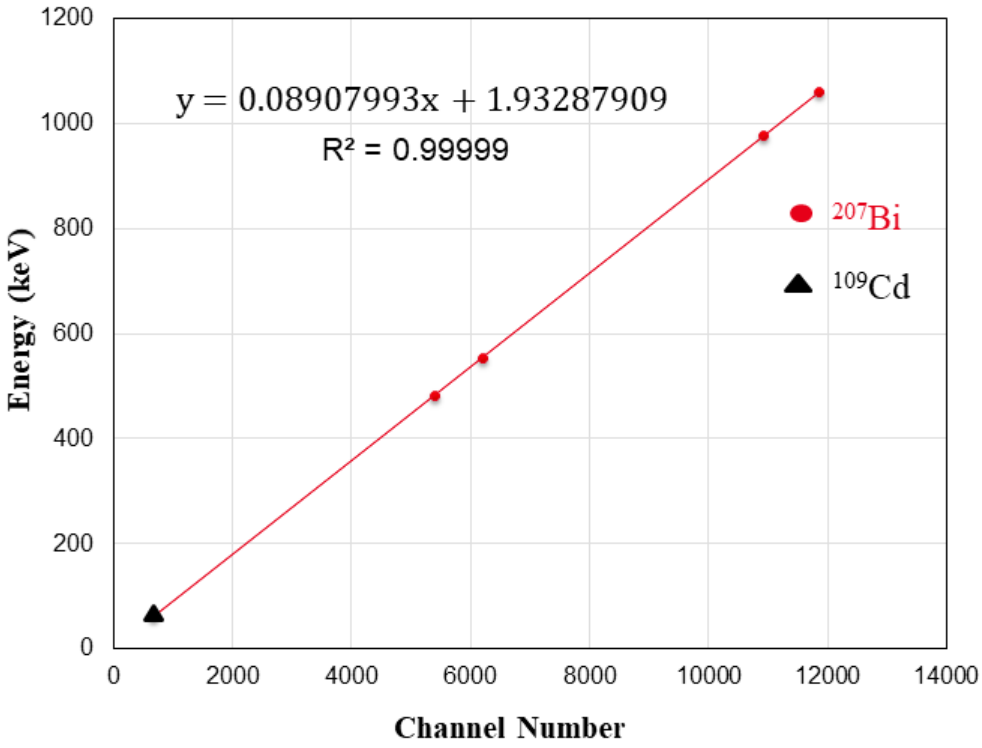

Figure 3.13 – The energy calibration curve extracted using the conversion electron peaks from ^{207}Bi and ^{109}Cd decays.

spectra presented are after applying background subtraction.

3.3.2.1 Carbon-14 decay

Carbon-14 is a pure β emitter that decays as an allowed transition with $E_{\max} = 156.476$ keV [131]. A shielded radioactive source prepared with a 0.7 μm thick Mylar® film and dried with the "oven-dried method" was used for the measurement. The measured spectrum was compared with PENELOPE simulations (Figure 3.14).

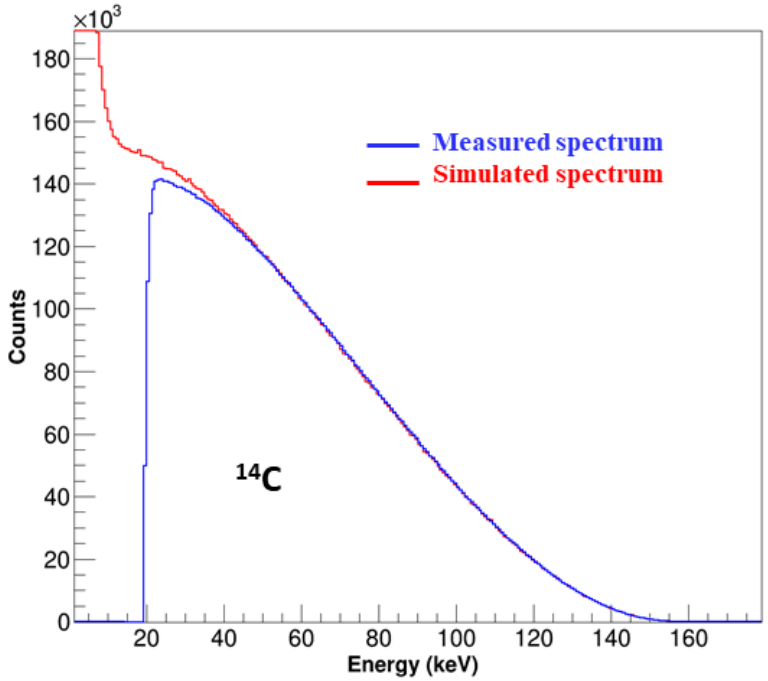

Figure 3.14 – Comparison of measured (blue) and simulated spectra (red) for the allowed decay of ^{14}C. The input of the simulation is a theoretical calculation from the BetaShape code.

The measured spectrum (in blue) is the background-subtracted spectrum. For simulation, the β spectrum was calculated as an allowed transition using the BetaShape code to be used as an input. The spectra have been normalised by integration between 40 keV and 90 keV. Excellent agreement over the energy range from 40 keV to $E_{\max}$ has been obtained. A slight disagreement can be seen below 40 keV, that can be due either to the measurement, with a real distortion of the initially emitted spectrum, or to the simulation, with too many electrons depositing only a part of their energy because of an inaccurate geometry. Nevertheless, the quantity $(1 - R^2)$ defining the disagreement is 0.086% between 22 keV and $E_{\max}$ and 0.036% between 40 keV and $E_{\max}$, showing the quality of simulations performed. We will see in the next section that the slight disagreement can be explained.

3.3.2.2 Chlorine-36 decay

Chlorine-36 measurement has already been discussed previously. For this new measurement, the same radioactive source was employed. The same experimental shape factor from Rotzinger [96] was used as input of the simulation. The simulated spectrum was normalised to the measured one by integration between 550 keV and 650 keV (see Figure 3.15). The agreement between the two spectra can only be seen between 550 keV and $E_{\max}$. The observed difference seems to be due to the energy loss in the radioactive source. The properties of the source are simulated; except, the existence of large crystals in the dried deposit, which can induce strong distortion due to the self-absorption process. It is discussed in detail in the section 4.1.3.3.

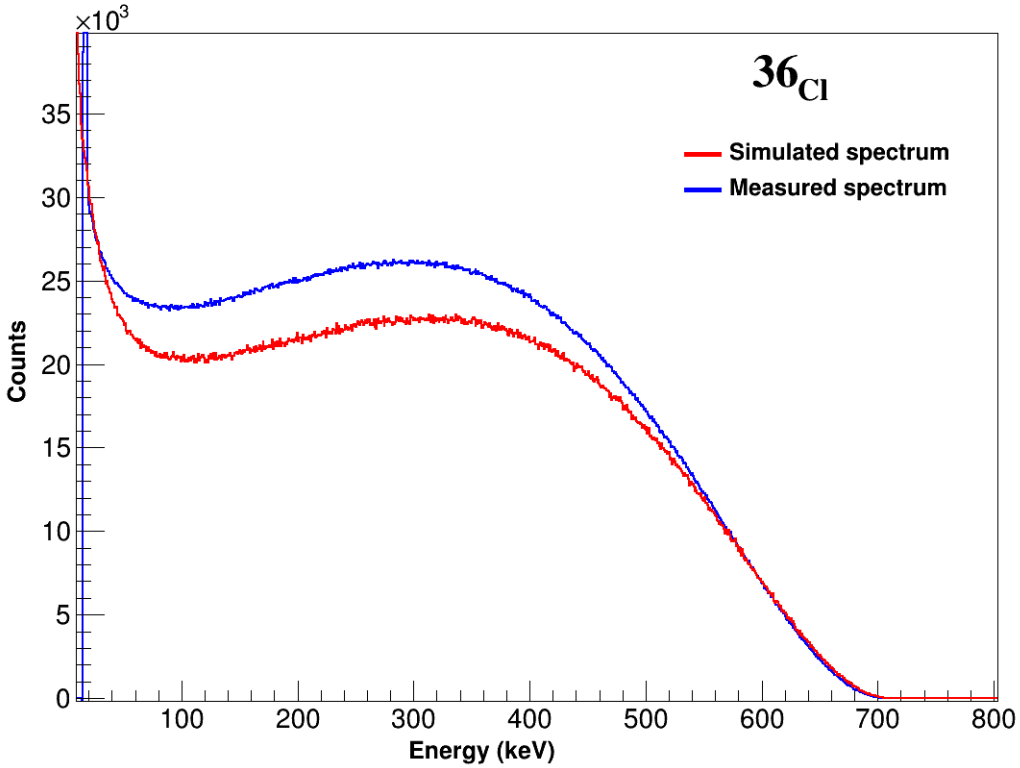

Figure 3.15 – Comparison of measured spectrum (blue) and simulated spectrum (red) for ^{36}Cl decay.

3.3.2.3 Technetium-99 decay

Technetium-99 decay is a second forbidden non-unique transition with a maximum energy of 297.5 keV [123]. The ^{99}Tc source was prepared on a 0.7 μm thick Mylar® film and dried with "oven-dried method". A precise theoretical prediction is difficult due to the influence of the nuclear structure involved in the decay, as for any forbidden non-unique transition. A spectrum built on the experimental shape factor from Reich [95] was thus preferred as an input of the simulation. The measured spectrum has been compared to this simulated spectrum (Figure 3.16). The spectra have been normalised by integration between 200 keV and 250 keV.

Excellent agreement is found above 100 keV. However, significant disagreement is observed below this energy. The disagreement $(1-R^2)$ is 1.35% if determined between 22 keV and $E_{\max}$, while it is only 0.677% if determined between 100 keV and $E_{\max}$.

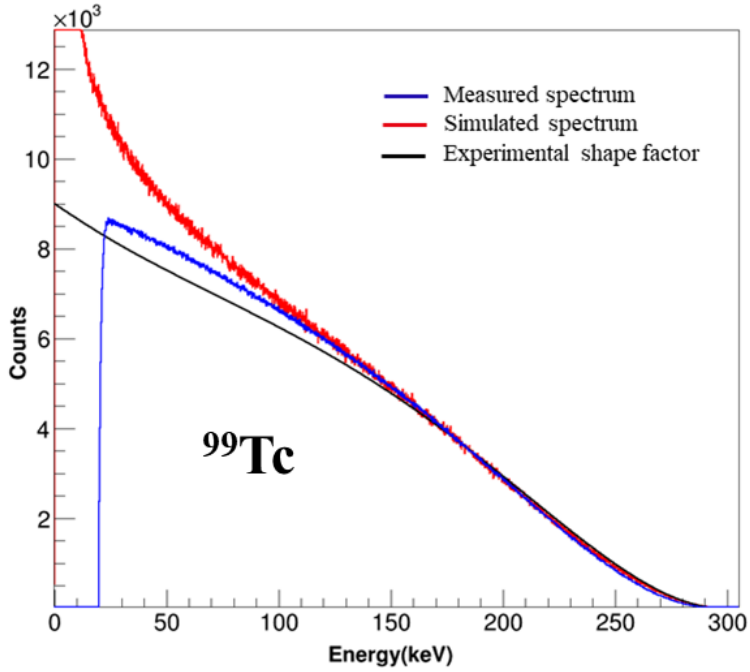

Figure 3.16 – Comparison between the measured (blue) and the simulated (red) spectra for ^{99}Tc decay. The Reich spectrum (black), used as input of the simulation, is given here to show the influence of the detection system on the measured shape.

The disagreement at low energy has been investigated. The input of the simulation is based on an experimental shape factor measured between 55 and 250 keV [95] and extrapolated outside this energy range by the BetaShape code. This could explain the large discrepancy below 60 keV; but it has to be verified. During the EMPIR project MetroBeta[3], ^{99}Tc decay has been measured at LNHB very recently by metallic magnetic calorimetry (MMC). Results are still preliminary[4]; however, a significant decrease of the emission probability is observed in the energy range 30 - 80 keV compared with Reich's measurement and a sharp increase also visible below 20 keV that is typical of atomic effects. Therefore, the MMC measured spectrum of ^{99}Tc has been considered as direct input of the simulation (see Figure 3.17).

Excellent agreement is then obtained with our measured spectrum above 60 keV, while a significant discrepancy can still be observed below. The disagreement $(1-R^2)$ is 1.48% in our measured energy range while goes down to 0.24% between 50 and 250 keV. The studies performed to solve this disagreement between both measurement techniques below 60 keV are detailed in section 4.1.3.3.

[3] `http://metrobeta-empir.eu/`
[4] A draft is being written at the time of writing.

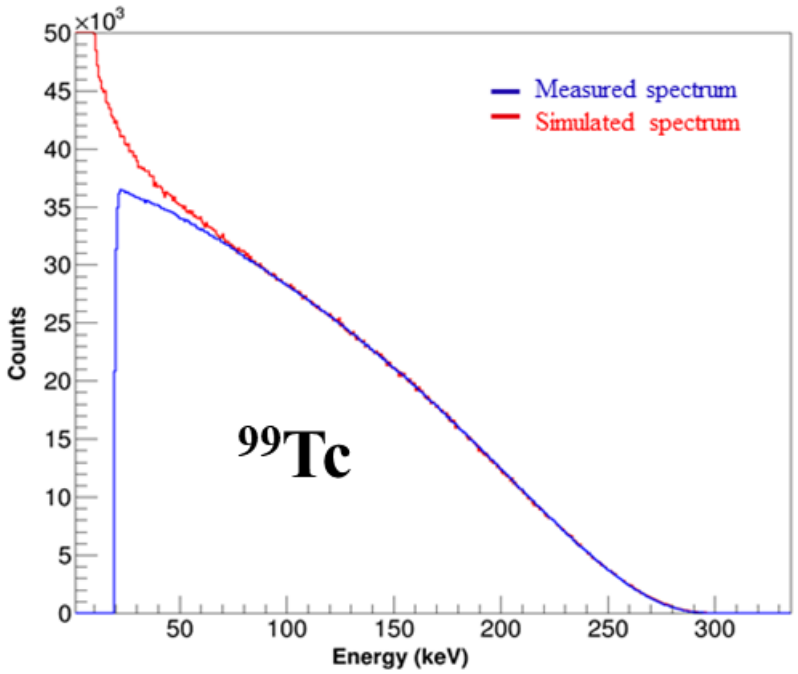

Figure 3.17 – Comparison between the measured spectrum (blue) of the second forbidden non-unique transition in ^{99}Tc decay and the PENELOPE simulated spectrum (red) performed by using MMC spectrum as an input (see text for details).

3.3.2.4 Thallium-204 decay

Thallium-204 decays through a first forbidden unique transition with available energy of 763.2 keV [123]. A shielded radioactive source prepared on a 0.7 μm thick Mylar® film, dried with the "oven-dried method", was used for the measurement. A theoretically calculated spectrum by the BetaShape code was given as input of the simulation. The comparison between the measured and simulated spectra is shown in Figure 3.18. The spectra are normalised by integration between 200 keV and 300 keV, showing a good agreement above 70 keV. However, a slight disagreement has been observed below this energy. The coefficient $(1 - R^2)$ is 0.205% between 25 keV and the E_{max} while it goes down to 0.16% between 70 keV and the E_{max}. The discrepancy at low energy is arising from the lack of preciseness associated with the experimental geometry and will be explained in the next section.

3.3.3 Analysis of the distance between the detectors

As described in chapter 2, the detection system has been designed and built with a 3 mm distance between the detectors. However, the disagreement observed at low energy for ^{14}C, ^{99}Tc and ^{204}Tl spectra led us to re-think about this distance between the detectors. Indeed, this gap can influence the spectrum shape because of the escape of particles, which then deposit only a partial amount of their kinetic energy, something that was also observed in Figure 2.35.

We investigated the discrepancy by adjusting the distance parameter in our simulations,

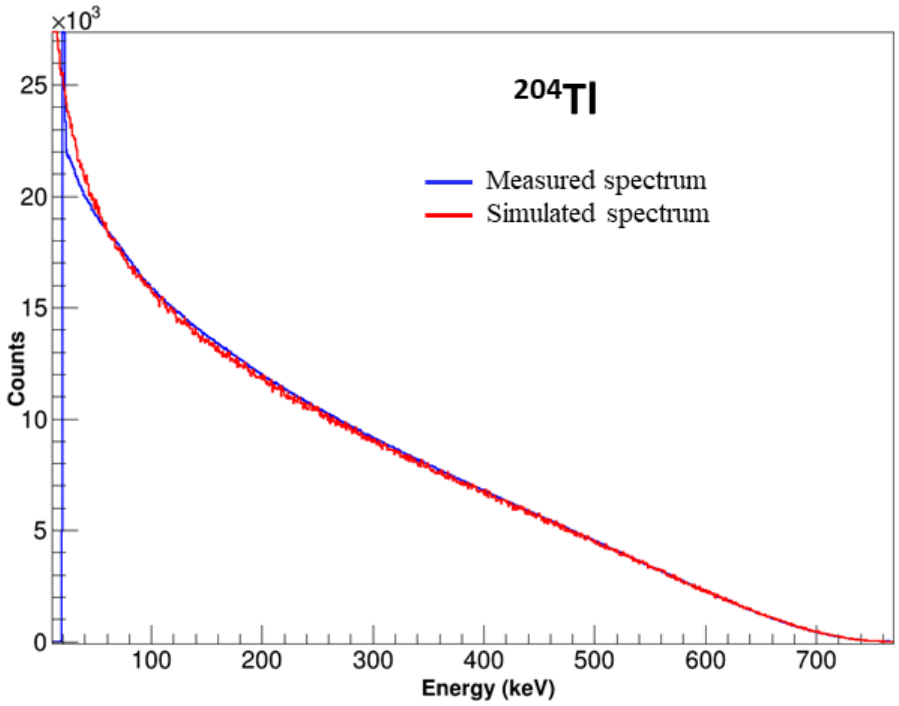

Figure 3.18 – Comparison between the measured spectrum (blue) of the first forbidden unique transition in ^{204}Tl decay with the simulated spectrum (red).

varying it from 2.4 mm to 3 mm with 0.1 mm step in our PENELOPE geometry, all other parameters remaining identical. The complete analysis concluded that the actual distance between the detectors is 2.5 mm, showing excellent agreement between the measurements and the simulations. The comparison between measurement and simulation was done for ^{14}C, ^{99}Tc and ^{204}Tl spectra, and also for ^{207}Bi (Table 3.2).

Radionuclide	Energy range (keV)	1-R^2 (%)	
		3 mm	2.5 mm
^{14}C	22 - 156.47	0.086	0.005
^{99}Tc	22 - 297.3	1.35	0.57
^{204}Tl	25 - 763.2	0.205	0.09
^{207}Bi	22 - 1090	5.35	4.3

Table 3.2 – The (1-R^2) parameters from the comparison between the measurements and simulations with 3 mm and 2.5 mm distance between the detectors.

In the case of ^{14}C, the distortion below 40 keV disappears considering 2.5 mm distance (see Figure 3.19) and the residual analysis given in Figure 3.20 are flatter with 2.5 mm distance than with 3 mm distance.

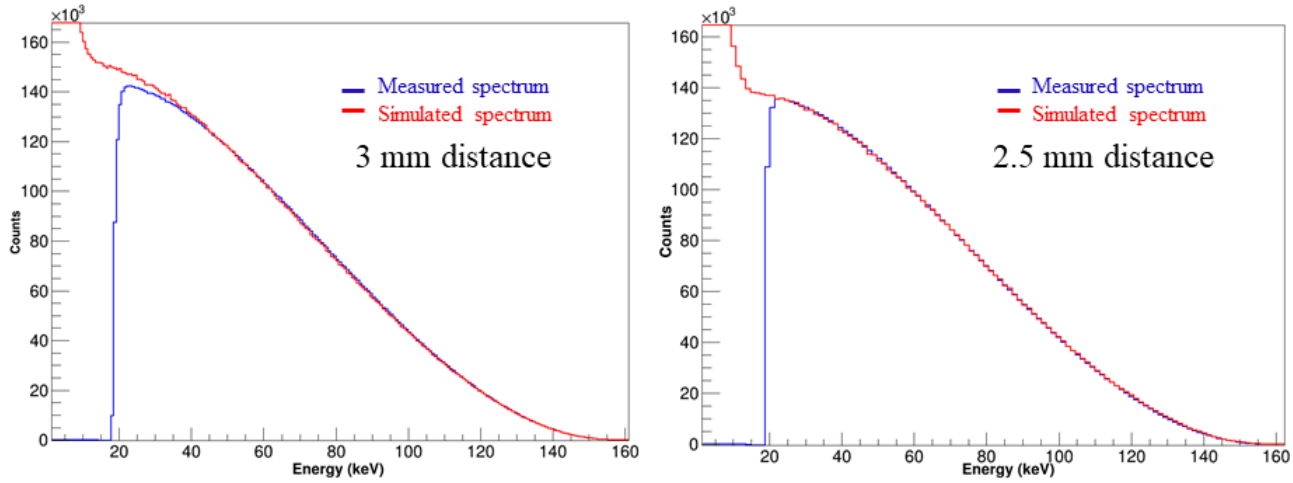

Figure 3.19 – Comparison between the measurement and the simulation of ^{14}C decay with a distance between the detectors of 3 mm (left) and 2.5 mm (right).

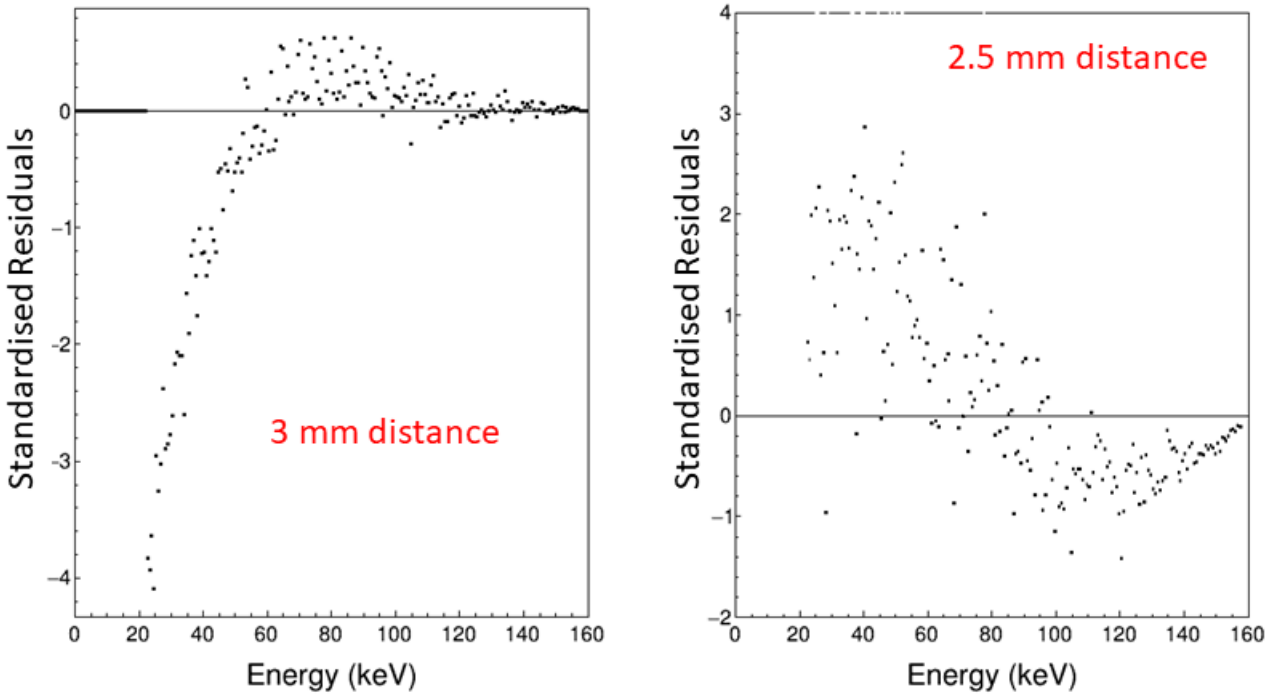

Figure 3.20 – Residuals between measurement and simulation of ^{14}C decay with a distance between the detectors of 3 mm (left) and 2.5 mm (right).

Similar effect is observed in the case of ^{99}Tc spectra, (see Figure 3.21 and 3.22).

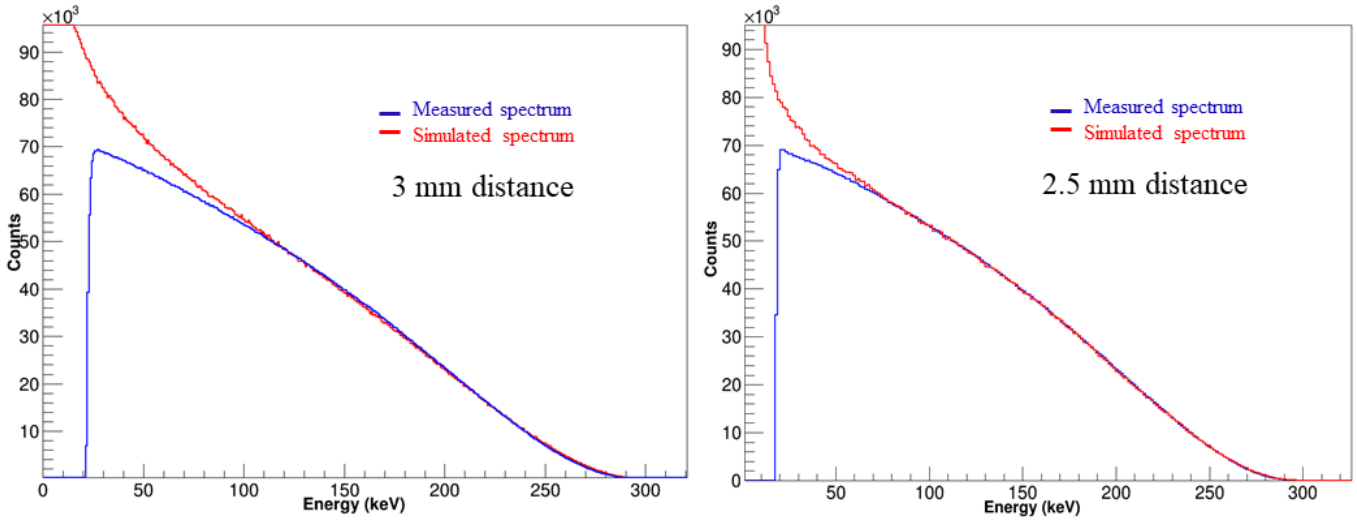

Figure 3.21 – Comparison between the measurement and the simulation of ^{99}Tc decay with a distance between the detectors of 3 mm (left) and 2.5 mm (right).

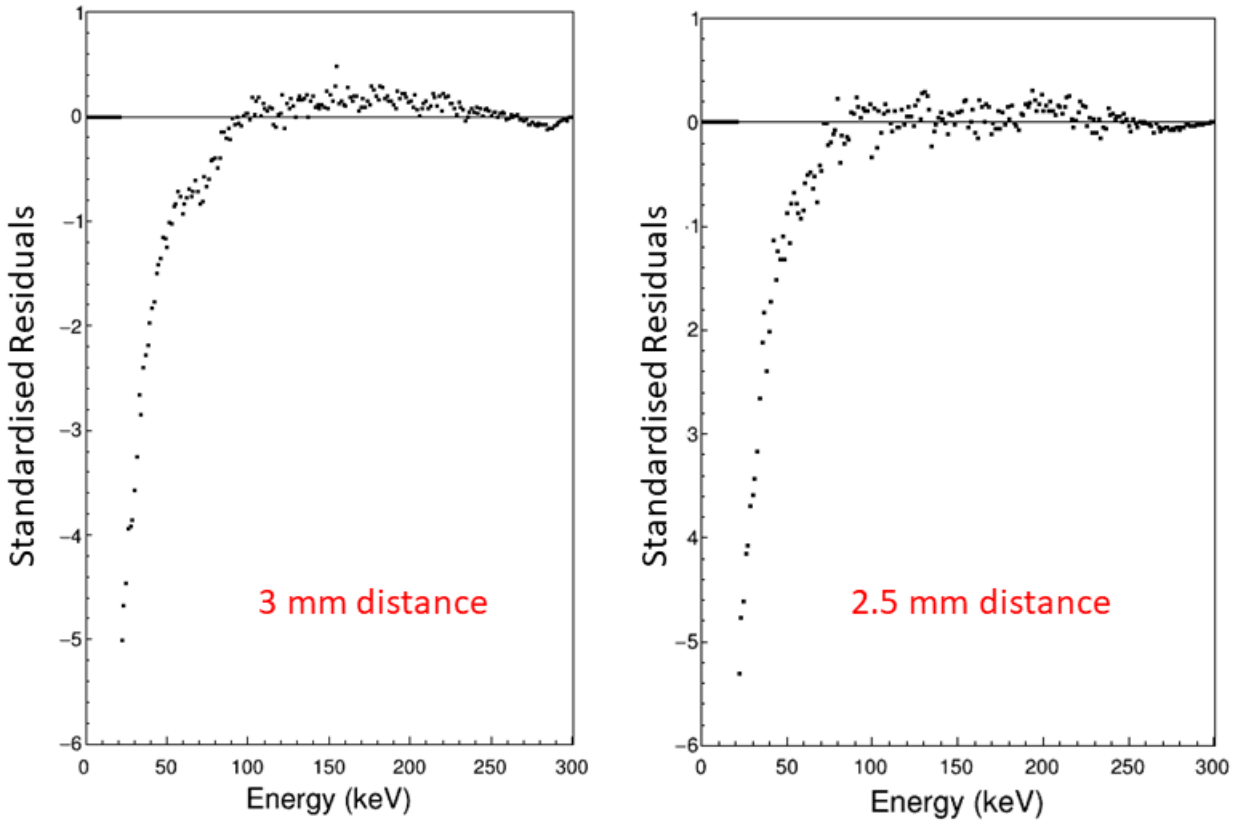

Figure 3.22 – Residuals between measurement and simulation of ^{99}Tc decay with a distance between the detectors of 3 mm (left) and 2.5 mm (right).

In the case of ^{204}Tl spectra, the distortion at low energy is small with 2.5 mm. However, one can see a slight disagreement between 40 and 120 keV (see Figure 3.23 and 3.24), which is originating due to the presence of electron capture branch and will be discussed in the section 3.4.3.3.

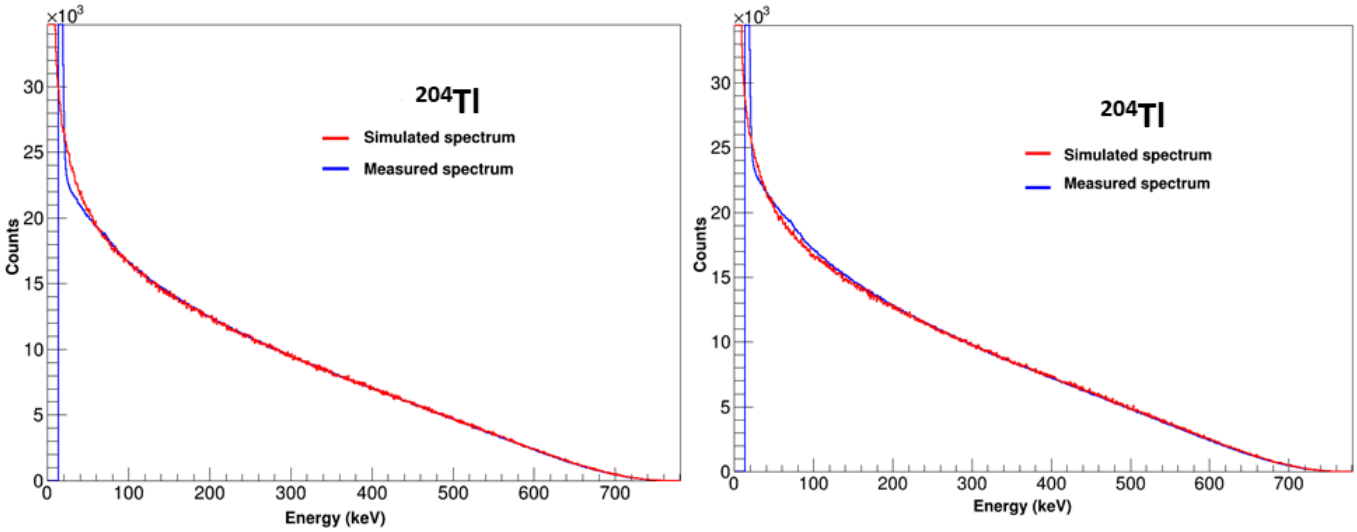

Figure 3.23 – Comparison between the measurement and the simulation of ^{204}Tl decay with a distance between the detectors of 3 mm (left) and 2.5 mm (right).

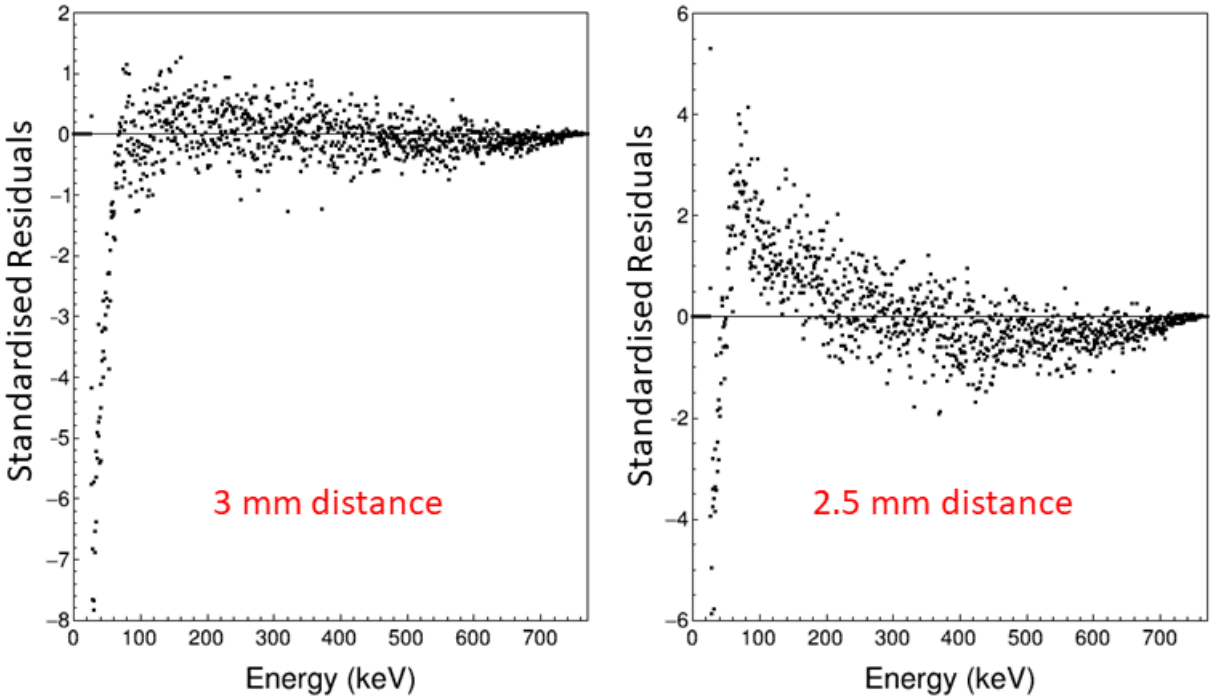

Figure 3.24 – Residuals between measurement and simulation of ^{204}Tl decay with a distance between the detectors of 3 mm (left) and 2.5 mm (right).

The agreement is better between the measurement and simulation even in the case of ^{207}Bi spectra (see Figure 3.25).

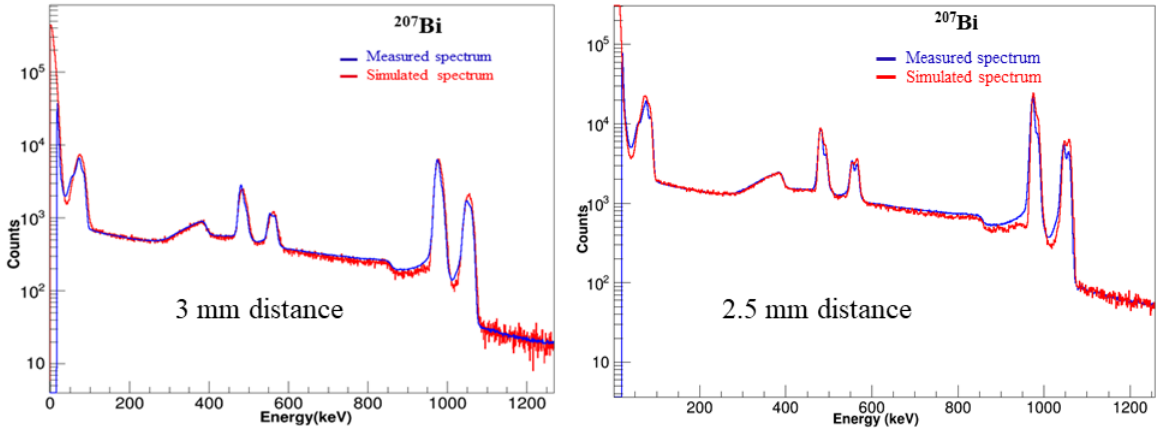

Figure 3.25 – The comparison between the measurement and the simulation of ^{207}Bi decay with a distance between the detectors of 3 mm (left) and 2.5 mm (right).

In the design of our detector holders, the centre part (ring) holding the radioactive source is made of a copper layer of 500 μm thickness. The thickness may have been reduced due to mechanical constraints that eventually reduce the distance between the detectors. Copper is a soft metal with Mohs scale hardness of 3, as the detector holders are assembled with screws, every radioactive source manipulation can deteriorate the material. However, we discussed with the manufacturing team, and they mentioned that the machine used to build the pieces was new and so not totally mastered and finely tuned. So, while at the beginning, it was considered that built design would be accurate. It appeared that the precision of such small thickness (500 μm) is questionable.

We thus checked the actual dimensions of the copper pieces. A direct measurement of the centre thickness (detector holder) was performed with a laser, which provided a value of 350 μm. Twice this thickness (700 μm) plus twice the distance due to PIPS encapsulation (900 μm for each detector) gives 2.5 mm, consistent with the simulation results.

Finally, it shows conclusively that the actual distance between the detectors is 2.5 mm. The consistency obtained between the measurements and the corresponding simulations is excellent. The direct measurement also proves the precision of simulations. Thus, 2.5 mm is kept for all the simulations presented in the rest of this work.

3.3.4 Conclusion for measurements without cooling

The quality of the measurements has been improved with further developments in the detection system. In this section, the measurements performed with the almost 4π detection system at room temperature have been discussed.

The characterisation of the detection system using ^{207}Bi and ^{109}Cd has shown a linear response from 63 keV to 1060 keV and is still linear down to the energy threshold of 22 keV.

The β spectra have been measured for the decays of ^{14}C, ^{36}Cl, ^{99}Tc and ^{204}Tl.

The questions raised by the discrepancy at low energy led us examining the parameter of geometry.

While at the beginning of the work, the geometry was considered to be as designed, our simulations led the conclusion that the discrepancy is arising from the distance between the detectors, which was found to be 2.5 mm, a value confirmed by direct measurement. With this new geometry, an excellent consistency is obtained between the measurements and the simulations.

The discrepancy of ^{99}Tc measurement below 60 keV remains unexplained at this stage of the analysis and will be explored in the section.

3.4 Measurements with final set-up with cooling

The performance of silicon detectors especially in terms of their energy resolution can be improved by cooling them at low temperatures, as discussed in chapter 2. The measurements of ^{109}Cd, ^{207}Bi, ^{14}C, ^{36}Cl, ^{99}Tc and ^{204}Tl have been performed again by cooling the detectors at liquid nitrogen temperature. It allowed us to compare the response of the detection system with and without cooling. In this section, we first describe the characterisation of the detection system with cooling, and the β spectrum measurements are then illustrated with their analysis.

3.4.1 Characterisation of detectors

The detection system has been re-characterised by measuring the decay of ^{109}Cd and ^{207}Bi with the same procedure as before. The measurements and analysis are discussed below.

Cadmium-109 decay

The re-measurement of ^{109}Cd allowed to characterise the performance of detectors with cooling at the low energy scale. The energy threshold is found to be 15 keV, and the peak at 22 keV is clearly separated from noise (Figure 3.26). The cooling system has thus a significant impact on the energy resolution of the detectors. The FWHM of the detectors has found to be 9 keV at 62.5 keV. The new calibration has been extracted from the reference peaks of ^{109}Cd and ^{207}Bi (see Figure 3.31). By applying this curve, the observed energies are listed in the Table 3.3. The relative difference between the observed energy and the data is significant, around 2%. It is even more important for the peak at 22.5 keV, with a shift of 7.5%. The peak at 62.5 keV has the same measured energy as in the Table 3.1, for the detection system

operating at room temperature. These results clearly question the linearity of the detectors at low energy, which is quite unexpected for silicon detectors with such a magnitude.

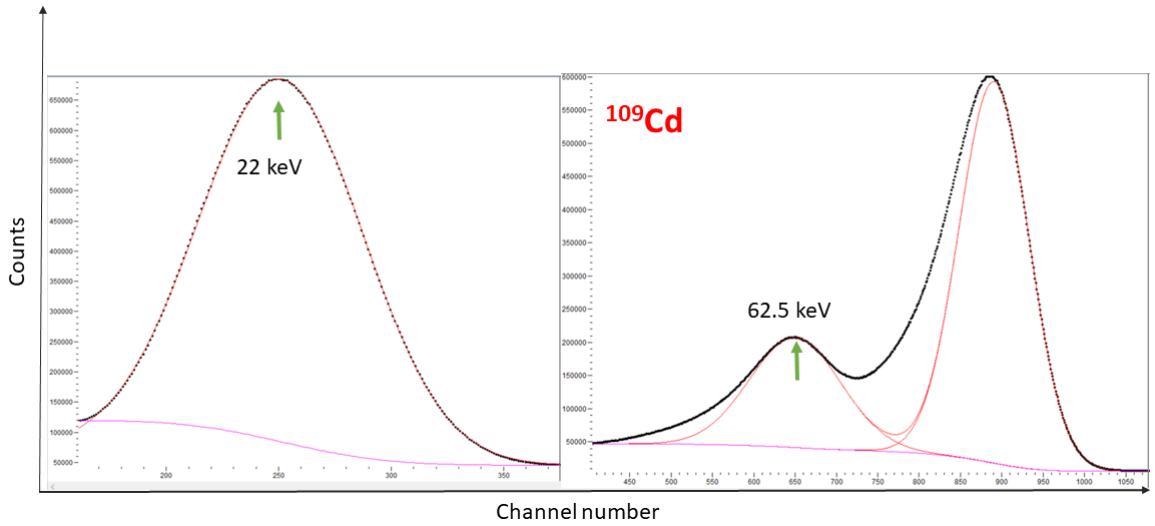

Figure 3.26 – The analysis of ^{109}Cd spectrum with the COLEGRAM software. Peaks are fitted with Gaussian functions at 22 keV (left) and at 62.5 and 86.7 keV (right).

Radionuclide	Nature	Expected energy (keV)	Channel number	Measured energy (keV)	$\|\Delta E\|$
^{109}Cd	e_{AK}	22.5	251	24.7	7.51%
	$ec_{1,0\ K}$	62.5	651	61.78	2.17%
	$ec_{1,0\ L}$	86.7	891	84.35	2.71%
^{207}Bi	$ec_{1,0\ K}$	481.6	5115	481.36	0.07%
	$ec_{1,0\ L}$	553.6	5889	554.10	0.20%
	$ec_{3,1\ K}$	975.65	10360	974.33	0.12%
	$ec_{3,1\ M}$	1061.74	11132	1058.86	0.2%

Table 3.3 – The conversion electron energies from the decay of ^{109}Cd and ^{207}Bi used for the energy calibration. Expected energies are from the decay data evaluation [9].

As we know, there are still some energy loss due to the radioactive source materials, detector dead layer, etc., the measured energy is not the true one. In order to extract the actual energies, the spectrum has to be unfolded. For deconvolution of the measured spectrum, response function of the detection system has been implemented and whole process is explained in the chapter 4. The spectrum after deconvolution is shown in Figure 3.27. The energies after unfolding were found to be closer to the DDEP data [11] (see Table 3.4). The relative difference between the energies of the unfolded peaks is about 1%.

The peak at 22.5 keV has a difference of about 11%. This peak is coming from K Auger electron (e_{AK}) emission. Besides, there are also L Auger electron (e_{AL}) emissions between

1.8 keV and 3.8 keV with a probability of 167%. The mean energy for those emissions gives 2.8 keV. As the solid angle of our system is almost 4π, the detection of Auger electrons from both K and L shells is highly probable, implying that we observe the sum of e_{AK} and e_{AL} electrons, i.e. 25.3 keV. The observed energy (after unfolding) is 25.1 keV, which very close to 25.3 keV (0.8% difference).

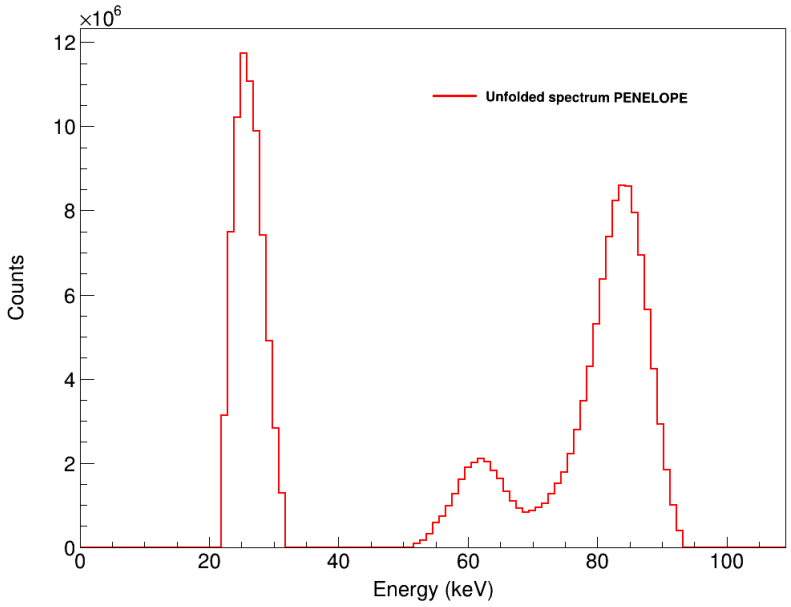

Figure 3.27 – Unfolded ^{109}Cd measured spectrum with PENELOPE.

Nature	Energy (keV)	Measured Energy (keV)	Unfolded Energy (keV)	Diff (Energy - Unfolded energy)
e_{AK}	22.5	24.7	25.1	11.5%
$ec_{1,0\ K}$	62.5	61.8	62.25	0.4%
$ec_{1,0\ L}$	83.7	84.4	84.6	1.7%

Table 3.4 – The energies of the conversion electron peaks from the decay of ^{109}Cd after the unfolding process.

Bismuth-207 decay

The re-measurement of ^{207}Bi was carried out with the same radioactive source as before (oven-dried) and analysed with the COLEGRAM software (Figures 3.28 and 3.29). The energies obtained by applying the calibration curve are within 0.2% of the expected values (see Table 3.3). These energies are consistent with the one obtained in the Table 3.1.

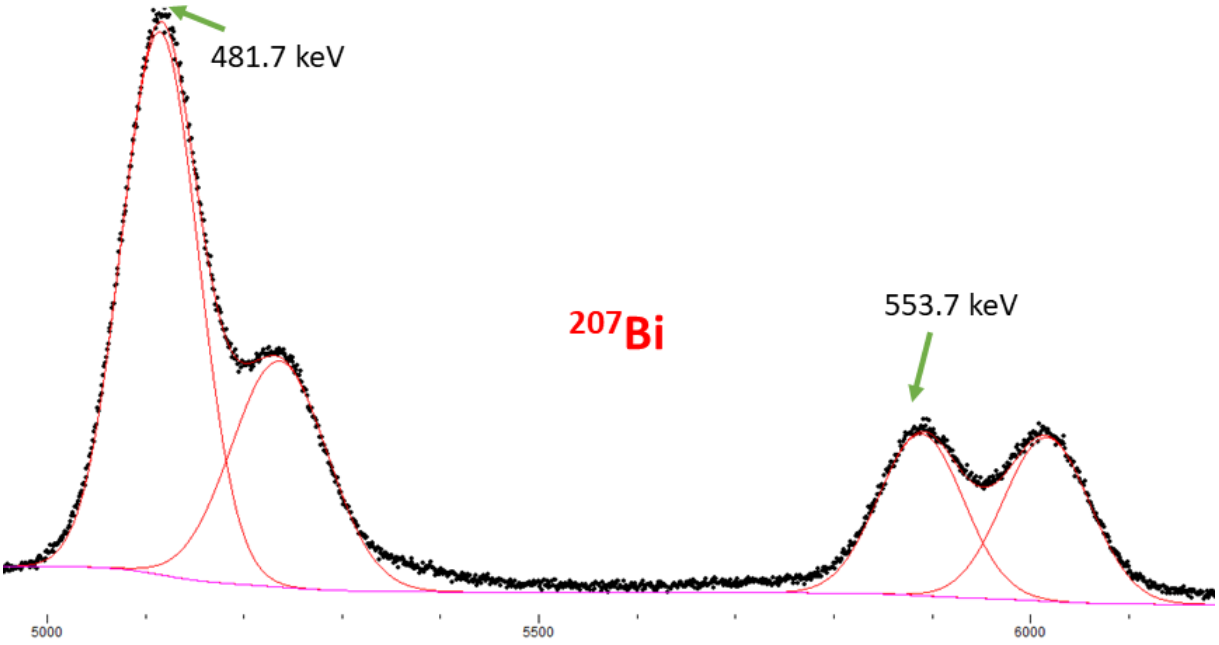

Figure 3.28 – The analysis of ^{207}Bi spectrum with COLEGRAM software. The peaks are fitted with Gaussian function.

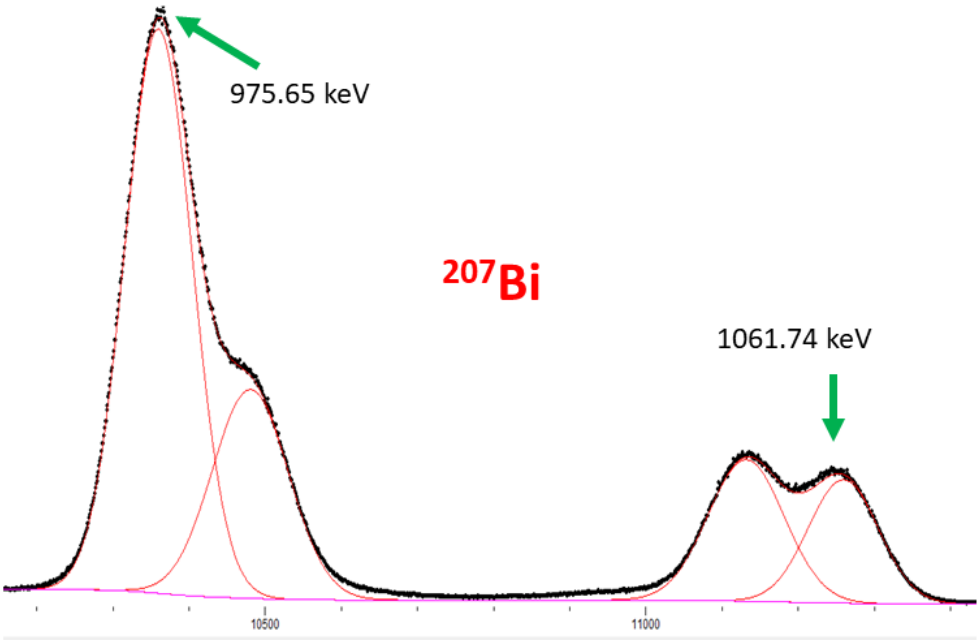

Figure 3.29 – The analysis of ^{207}Bi spectrum at higher energies with COLEGRAM software. The peaks are fitted with Gaussian function.

The true values of these energies are extracted after the unfolding process same as in the case of ^{109}Cd (Figure 3.30). The peak energies after unfolding the measured spectrum are observed to be less than 0.3% different from the DDEP data [10] (see Table 3.5).

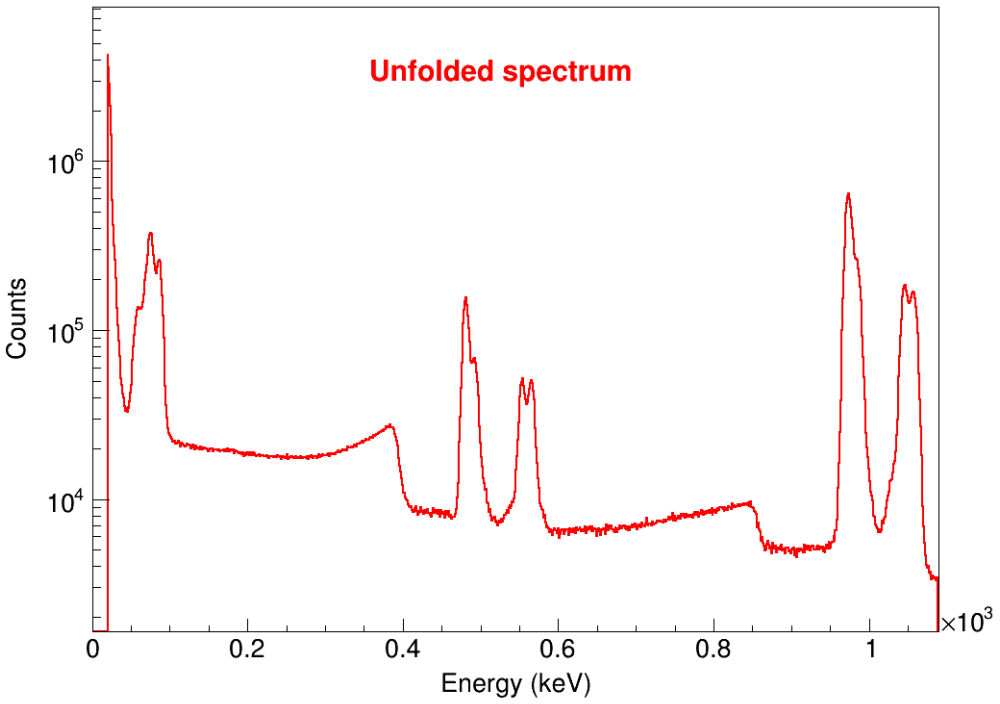

Figure 3.30 – Unfolded ^{207} Bi measured spectrum with PENELOPE.

Nature	Energy (keV)	Measured Energy (keV)	Unfolded Energy (keV)	Diff (Energy - Unfolded energy)
$ec_{1,0\ K}$	481.6	481.35918	481.07	0.1%
$ec_{1,0\ L}$	553.6	554.10	553.7	0.02%
$ec_{3,1\ K}$	975.65	974.33	973.9	0.2%
$ec_{3,1\ M}$	1061.74	1058.86	1058.547	0.3%

Table 3.5 – The energies of the conversion electron peaks from the decay of ^{207}Bi after the unfolding process.

The final energy calibration curve has been extracted using the peaks listed in Table 3.3 and was found to be linear from 25 keV to 1060 keV (see Figure 3.31). The linear equation of calibration is:

$$Y = 0.0939X + 0.7706 \tag{3.9}$$

with a coefficient of determination (R^2) equals to unity.

The energy calibration has been applied to the measurement of ^{207}Bi and compared with the corresponding simulation using the PenNuc module. The simulated spectrum has been convoluted with a Gaussian distribution having an FWHM of 9 keV, as experimentally determined. The spectra have been normalised between 500 and 700 keV. Excellent agreement is obtained

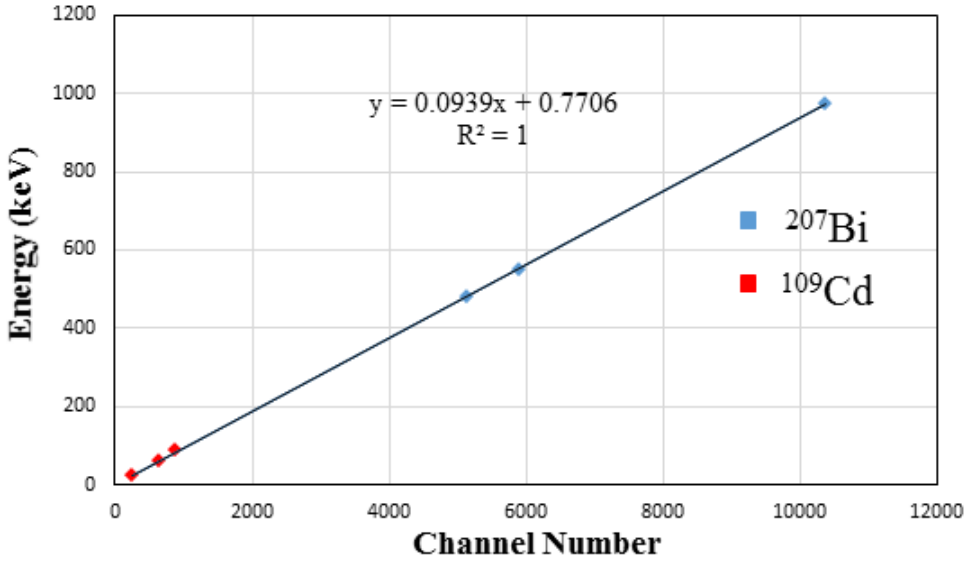

Figure 3.31 – The energy calibration curve obtained from the conversion electron peaks of ^{109}Cd and ^{207}Bi (see Table 3.3) for the final set-up with cooling.

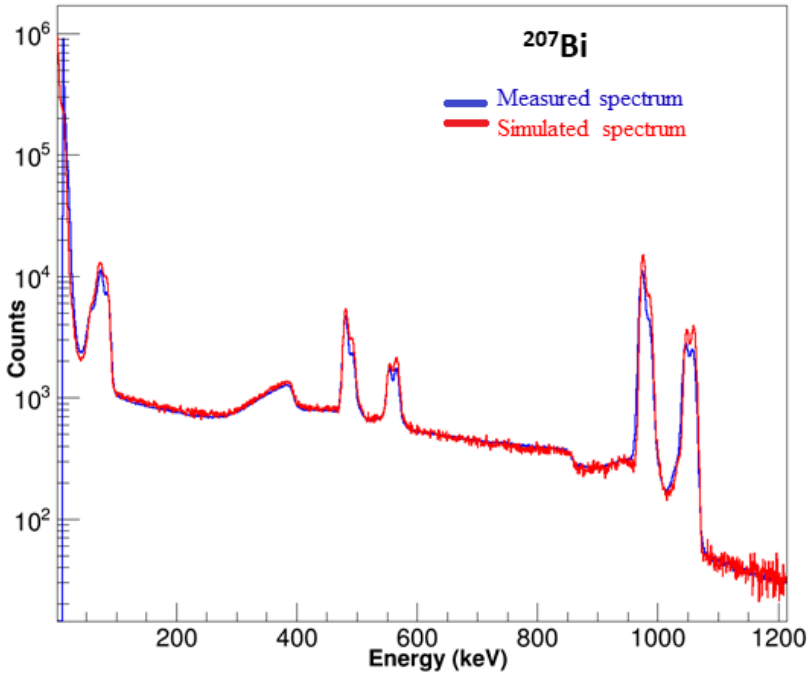

Figure 3.32 – Comparison between the simulated spectrum and the measured spectrum of ^{207}Bi obtained with the final set-up with cooling.

between the measured and the simulated spectra (Figure 3.32), with disagreement parameter $(1 - R^2)$ equals to 3.2%. Still, the value is higher due to the small disagreement in the peak intensities. As the simulation is based on the decay data library, and electrons energies usually not measured but calculated, a slight difference with measurements can be considered as reasonable.

3.4.2 Influence of source preparation on the shape of β spectra

After the last improvements of the detection system and the modifications in our Monte Carlo simulations, a discrepancy still remains between measured and simulated spectra for ^{99}Tc and ^{36}Cl decays. Investigating in details all the causes of remaining distortions, the only consistent, realistic possibility was considered to be the self-absorption phenomenon in the radioactive source. As already discussed in chapter 2, radioactive sources nature is crucial for β spectrometry. To test this last hypothesis, new radioactive sources are prepared with the freeze-drying method (see section 2.5.2.4) to control the crystallisation of the deposit. In this section, we describe the influence of radioactive sources preparation methods on the shape of β spectra from ^{99}Tc and ^{36}Cl decays.

3.4.2.1 Technetium-99 decay

For this study, radioactive solutions with and without carrier salt (NH_4TcO_4) were used. The presence of carrier salt in the solution promotes the size of crystals in the drying process. Furthermore, the drying process of the radioactive deposit is highly responsible for the crystal growth. The oven drying process is the usual process of drying at LNHB and was then used for the first preparation. As it has already been discussed that the freeze-drying process reduces the size of crystals and hence the self-absorption [116], a comparison was decided between the two drying processes.

Consequently, new radioactive sources have been prepared with two types of radioactive solution: a solution containing a carrier salt and another one free of carrier salt. These sources have been dried with two drying methods: freeze-drying and oven drying. Each measurement has been compared with the simulated spectrum, still keeping the MMC measured spectrum as input. The spectra have been normalised by integration between 200 keV and 250 keV. The analysis led to the following conclusions:

- Radioactive source with carrier salt, oven-dried (Figure 8) This source has been prepared following the same preparation technique as before (previous measurements) with the same radioactive solution. It is therefore with no surprise that the measured spectrum exhibits an identical distortion at low energy as we observed in Figures 3.16 and 3.17.

- Radioactive source with carrier salt, freeze-dried (Figure 9) The measured spectrum is clearly closer to the simulated spectrum compared with the previous test, highlighting the strong impact of the drying process. The residuals distribution given in Figure 10 emphasizes a small distortion at low energy (30 - 60 keV), even if the disagreement parameter $(1 - R^2)$ is only 0.041% between 22 keV and $E_{\max}$. This result can be explained by the presence of the carrier salt, which creates larger crystals in the radioactive source. Indeed, the larger the concentration of carrier salt in the solution, the larger the number

of inactive crystals and the larger the size of the crystals in the radioactive source. The effect of self-absorption is critical at low energy.

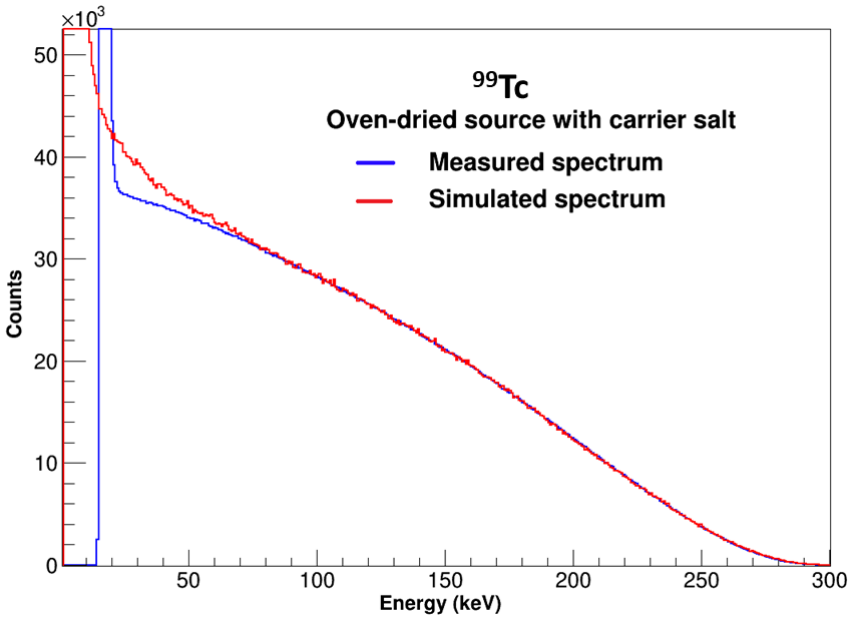

Figure 3.33 – Comparison between the measured spectrum of ^{99}Tc with a radioactive solution with carrier salt dried with oven-drying method and simulation using MMC spectrum as an input.

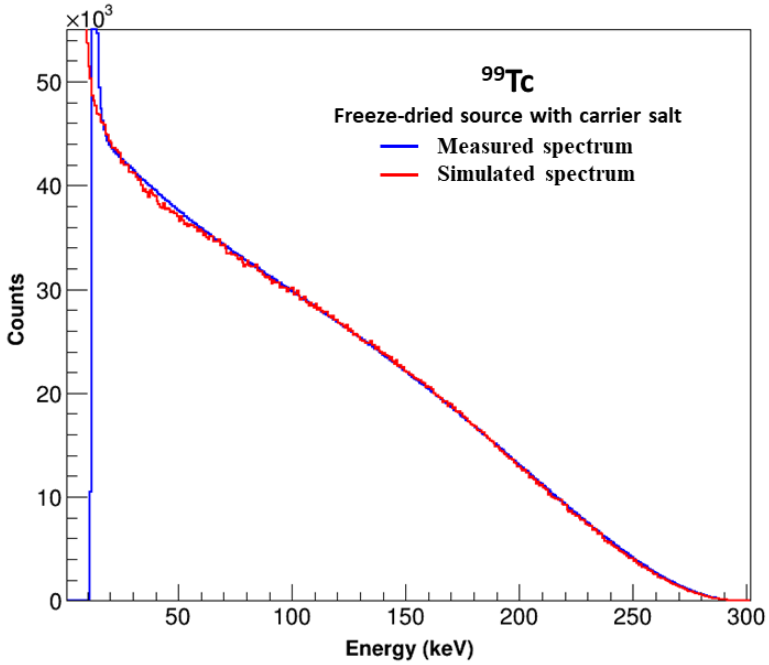

Figure 3.34 – Comparison between the measured spectrum of ^{99}Tc with a radioactive solution with carrier salt dried with freeze-drying method and simulation using MMC spectrum as an input.

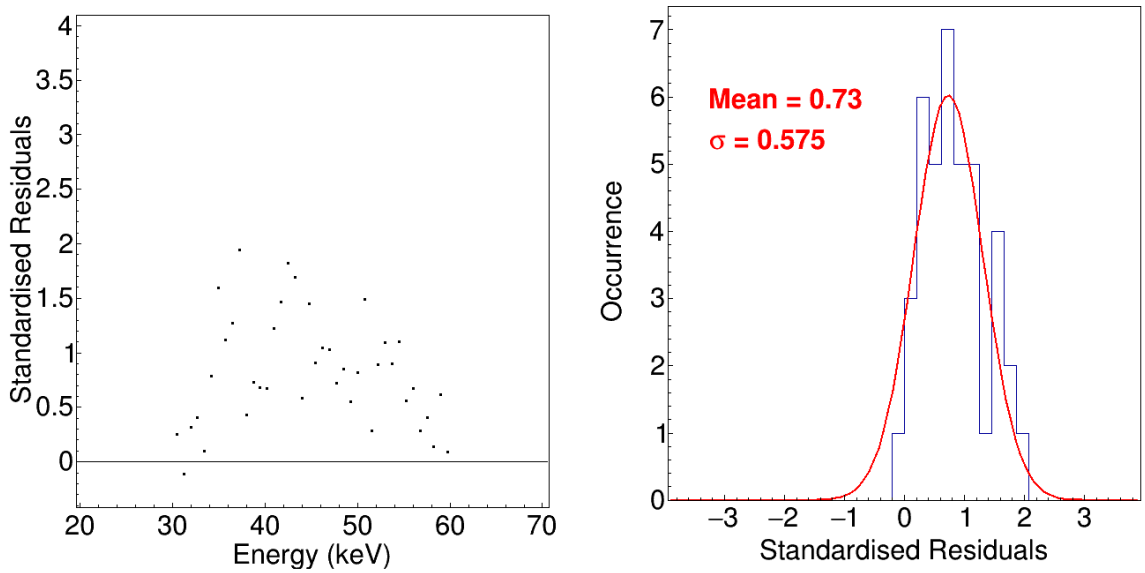

Figure 3.35 – Residuals of spectra obtained by the comparison between the measured spectrum of source with radioactive solution with carrier salt dried with freeze-drying method (Figure 9) and the simulated spectrum using MMC spectrum as input for ^{99}Tc decay.

– Radioactive source without carrier salt, oven-dried (Figure 11) The corresponding measured spectrum exhibits an identical distortion at low energy as the one for the source prepared with a solution containing carrier salt and oven-dried. It leads to the conclusion that for ^{99}Tc, the source preparation technique, especially the drying process, is more important than the radioactive solution by itself.

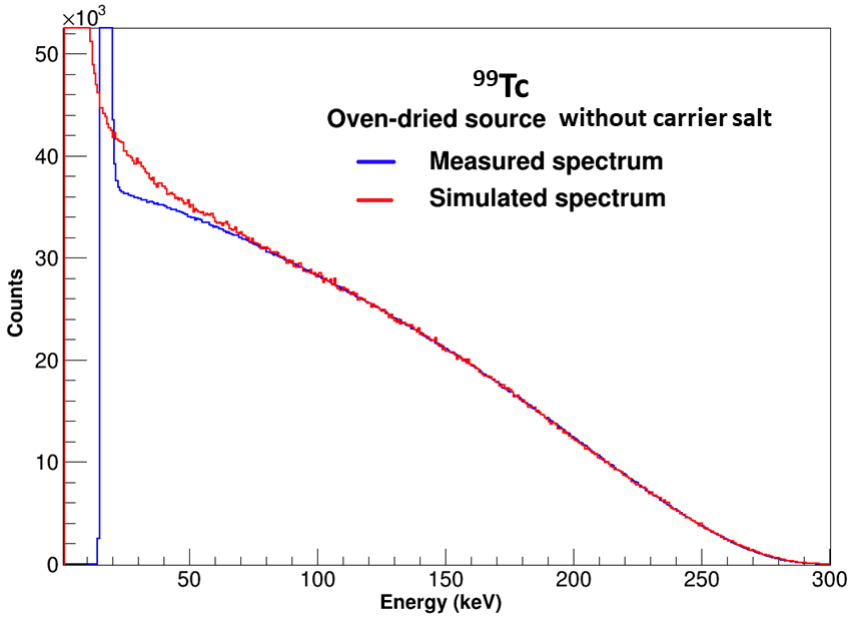

Figure 3.36 – Comparison between the measured spectrum of ^{99}Tc with a radioactive solution without carrier salt dried with oven-drying method and simulation using MMC spectrum as an input.

– Radioactive source without carrier salt, freeze-dried (Figure 12) The measured spectrum is found to be in excellent agreement with the simulation down to 20 keV. The residuals between 30 - 60 keV are shown in Figure 13, showing less distortion in comparison with Figure 10. It demonstrates a small but existing influence of the choice of the radioactive solution on the crystal growth. The disagreement parameter (1-R^2) is 0.035% between 22 keV and E_{max}, to be compared with 1.47% in the previous measurement (oven-dried with salt carrier solution 3.3.2.3). The remaining disagreement between the measurement and the simulation seems to come from the input of simulation, which is the MMC measured spectrum. The MMC measured spectrum (at LNHB) was compared with another measurement of ^{99}Tc also performed with MMC facility, recently developed at PTB Germany [132], and a small difference in the same energy range is observed. However, this difference is not very clear due to the poor statistics of PTB measurement[5].

  Nevertheless, the freeze-drying procedure, along with the carrier free solution, has showed a strong influence on the shape of β spectrum.

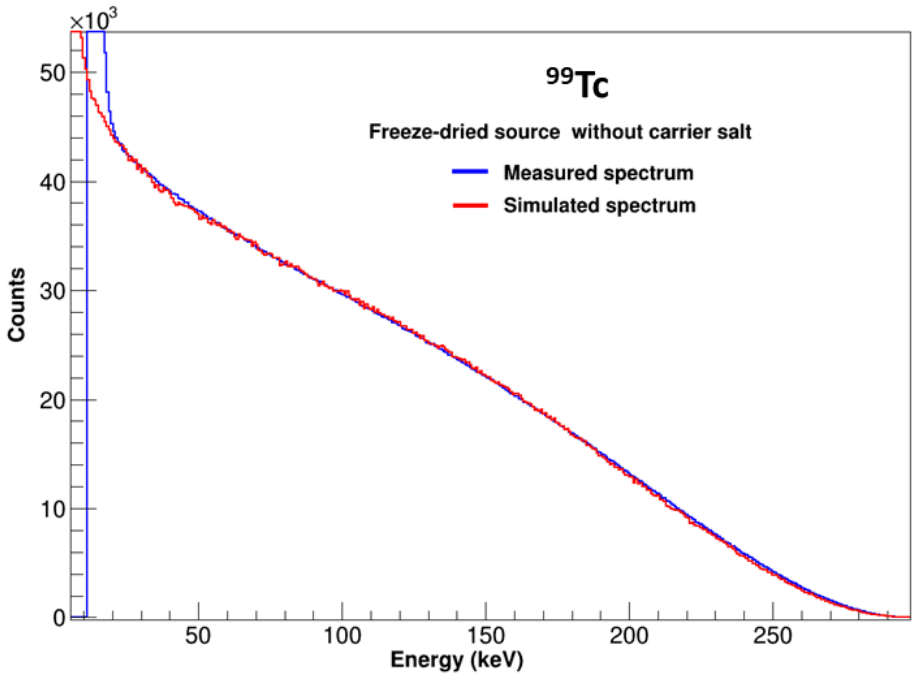

Figure 3.37 – Comparison between the measured spectrum of ^{99}Tc source with radioactive solution without carrier salt dried with freeze-drying method and simulation using MMC spectrum as an input.

This study leads to a whole picture of the situation that is consistent and logical. We demonstrated that the self-absorption phenomenon was the leading cause of the discrepancy observed previously in ^{99}Tc spectra below 60 keV between simulation and measurement. The oven-drying method seems to produce large crystals in which the emitted β particles loose

[5]New measurement with more statistics is in progress at PTB and a comparison of ^{99}Tc measurements from MMC at LNHB, PTB, and Si detector measurement (this work) will be performed.

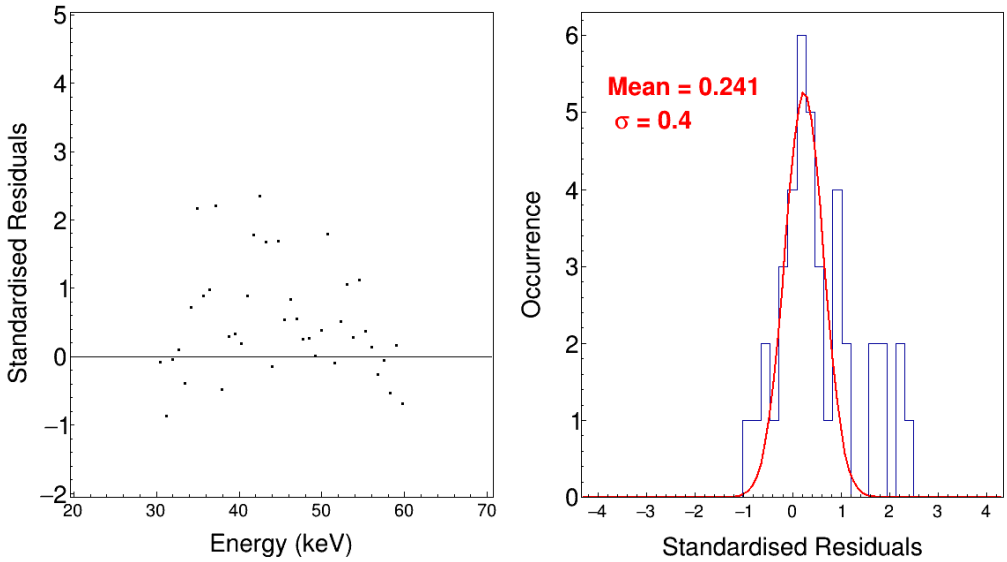

Figure 3.38 – Residuals of spectra obtained by the comparison between the measured sectrum of radioactive source prepared without salt and freeze drying method (Figure 12) and the simulated spectrum using MMC spectrum as input for ^{99}Tc decay.

a significant amount of their kinetic energy. The freeze-drying process appears to produce crystals of smaller size, reducing the self-absorption phenomenon. Besides, it was observed that the radioactive solution without carrier salt leads to minimum distortion in the measured spectrum, and should thus be preferable for an exact study.

3.4.2.2 Chlorine-36 decay

Similar tests have been performed for the influence of drying methods on the measurements of ^{36}Cl spectrum. The radioactive source prepared for ^{36}Cl was on a VYNS film in the previous measurements. For these measurements, shielded radioactive sources have been prepared on 0.7 μm thick Mylar® films applying the two drying methods, freeze-drying and oven-drying. These measurements have been compared with the corresponding Monte Carlo simulations (Figures 3.39 and 3.40). The spectra have been normalised by integration between 550 keV and 650 keV. The measured spectra are in good agreement with the simulation only at high energy, above 500 keV for oven-drying and above 450 keV for freeze-drying. However, a significant distortion is visible below these energies. Even if strong disagreement remains between simulations and measurements, the same conclusion can be made as for ^{99}Tc: the measured spectrum of ^{36}Cl is significantly less distorted with a freeze-dried source than with an oven-dried source. This shows the existence of different sizes of crystals in the radioactive source that is not well controlled in the preparation process. A carrier free radioactive solution of ^{36}Cl was not available at LNHB and so it was not possible to study this effect.

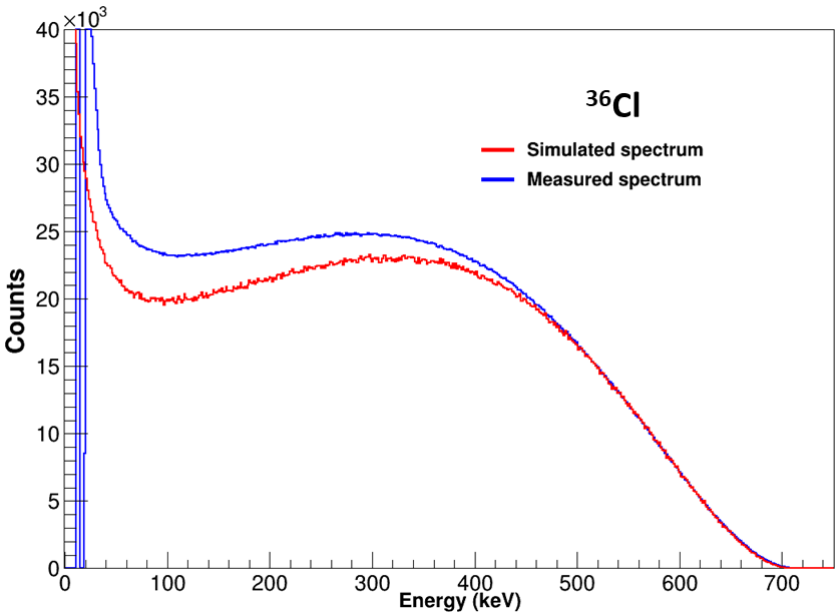

Figure 3.39 – Comparison between the measured spectrum of ^{36}Cl with radioactive source dried with freeze-drying method and the simulation.

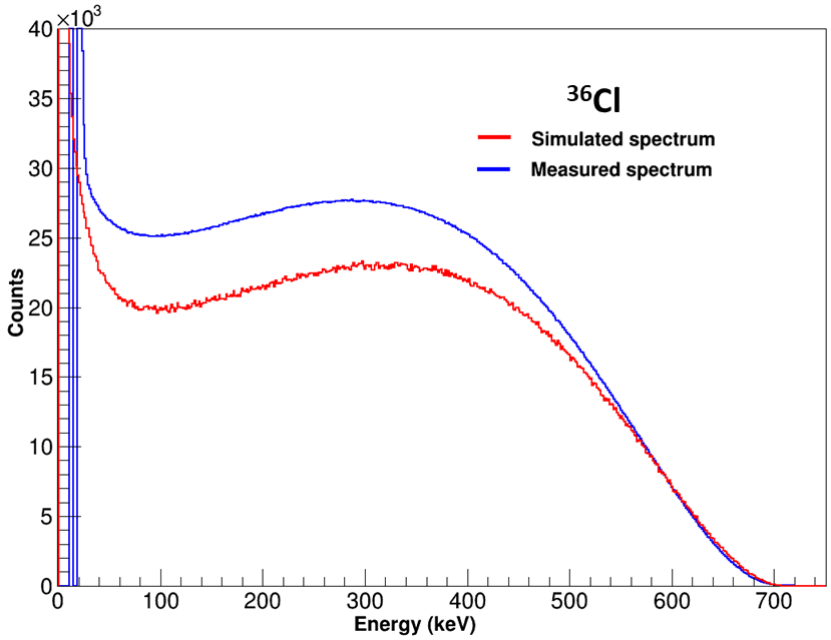

Figure 3.40 – Comparison between the measured spectrum of ^{36}Cl with radioactive source dried with oven-drying method and the simulation.

Imaging the radioactive source would have been ideal for estimating the possible mean size of the crystals present on the source support. However, laboratories which have adequate apparatus are very cautious and do not want to risk any radioactive contamination. Lack of time prevents us from preparing inactive source supports.Therefore, we chose to perform Monte Carlo simulations (10 million events) considering different sizes of crystals in the radioactive source. As for the simulation of latex microspheres (see section 3.1.1.1), we studied an active layer of NaCl on a surface of 1 cm^2 which thickness was varied from 1 μm to 8 μm with 1 μm step, corresponding to 0.079 to 0.6 μm radii of spherical crystals (see Figure 3.41). It is undoubtedly a crude approximation as the real length of material across which electrons go through is of high importance, and the actual size of crystals is most probably not uniform over the source surface. A similar effect has already been discussed in chapter 2 and has been observed in [108]. It is clear, with this study, that another radioactive source preparation technique is required for ^{36}Cl in order to reduce the self-absorption effect.

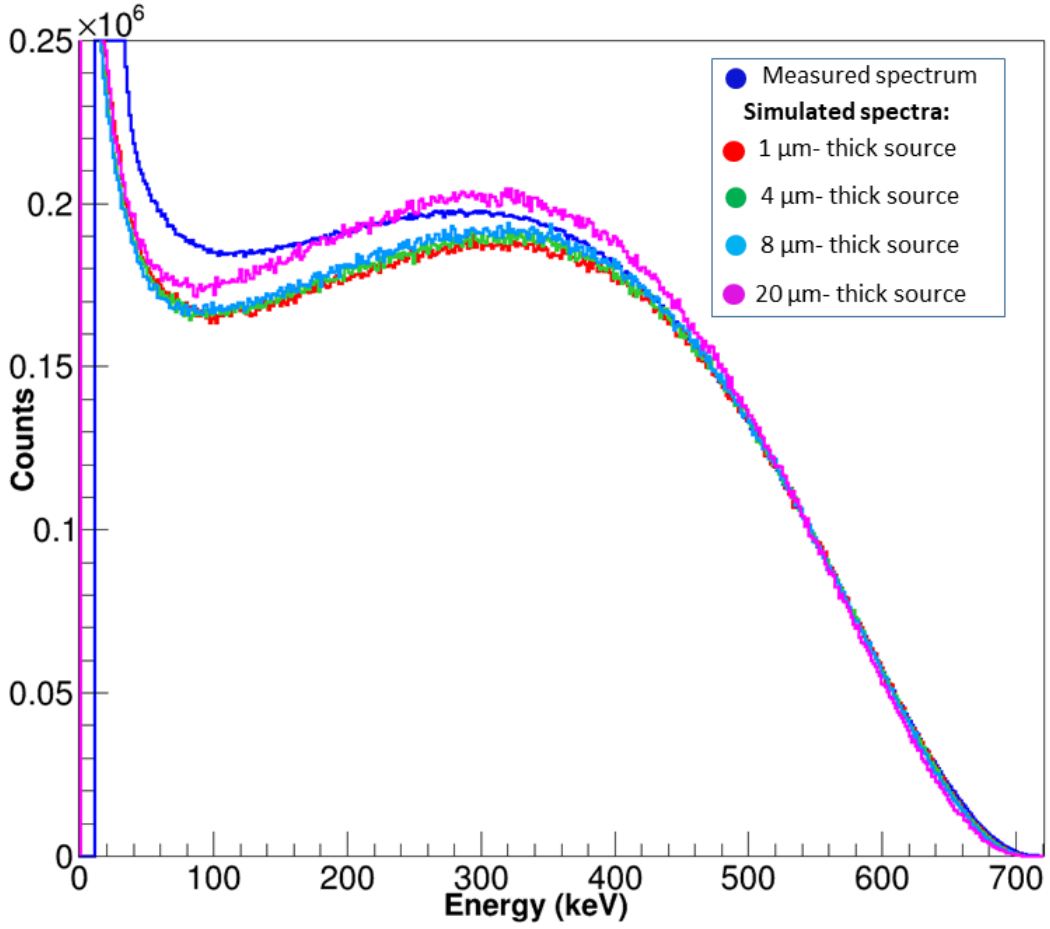

Figure 3.41 – Influence of the size of NaCl crystals on the shape of our measured spectrum. The dark blue curve is for the measured spectrum. The other curves have been obtained for crystals simulated as a NaCl film of different effective thicknesses in the source: 1 μm (red); 4 μm (green); 8 μm (blue); 20 μm (pink).

3.4.3 Final beta spectrum measurements

After the improvements of the measurement conditions, by modification in the experimental set-up and the optimisation of source preparation, final measurements for the decays of ^{14}C, ^{36}Cl, ^{99}Tc and ^{204}Tl are discussed in this section. The distance between detectors is kept at 2.5 mm for simulations as established previously. Shielded radioactive sources were prepared with 0.7 μm thick Mylar® films.

3.4.3.1 Carbon-14 decay

The final measurement of ^{14}C was carried out by cooling the detectors with the same radioactive source as for the without cooling measurement. The spectra were normalised by integration between 40 keV and 90 keV. Excellent agreement between the simulation and the measured spectrum over the energy range from 30 keV to $E_{\max}$ has been obtained (Figure 3.42). The spectra are in good agreement with a disagreement parameter $(1 - R^2)$ equal to 0.021%. One of the important effects to be noted is the residuals around the end-point, which are certainly more uniform thanks to the improved energy resolution. However, the Gaussian fit of the residuals shows a small distortion on the measured shape (Figure 3.43) compared to simulated one using an allowed spectrum. This distortion probably arises from the emitted spectrum indicating that the ^{14}C spectrum does not have a perfect allowed shape. This is consistent with the results available in the literature from Kuzminov and Bisch [4, 133]. The extraction of the experimental shape factor requires a deconvolution process that is detailed in the next chapter.

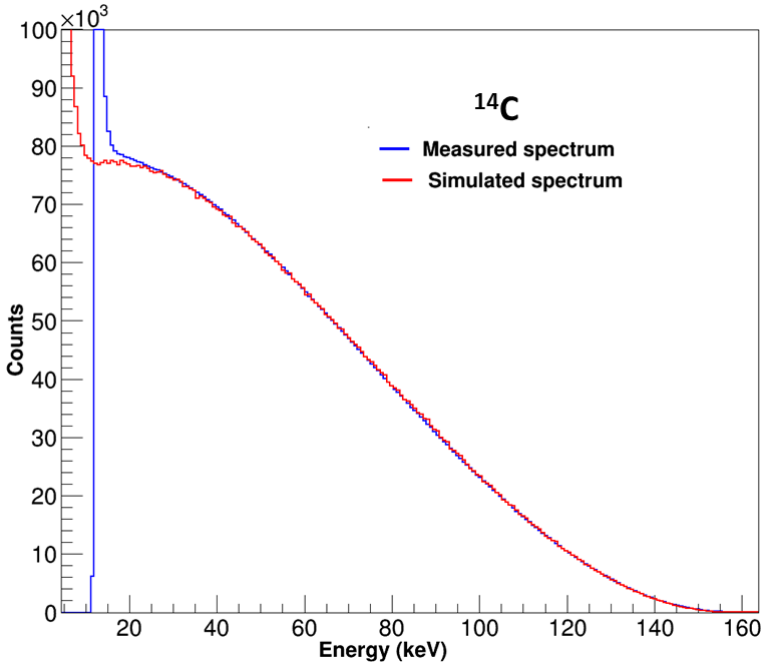

Figure 3.42 – Comparison between the measured (blue) and simulated (red) spectra of ^{14}C decay with cooling of the detectors.

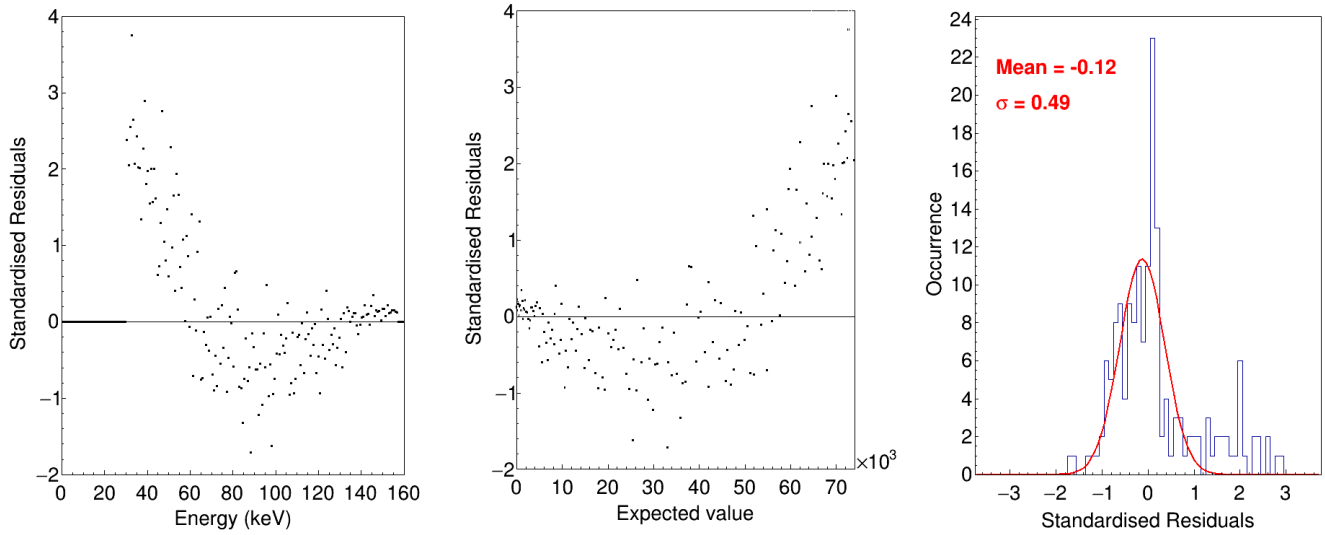

Figure 3.43 – Residuals between the measured and simulated spectra of ^{14}C decay with cooling of the detectors. The red curve is a Gaussian fit of the residuals distribution.

3.4.3.2 Technetium-99 decay

The final measurement of ^{99}Tc decay is processed with the freeze-dried source prepared with a carrier-free radioactive solution. The spectra with the residuals have already been shown earlier in Figures 12 and 13. Its analysis has already been discussed in the section 4.1.3.3. Measurement and simulation using the MMC spectrum as input are in good agreement. Extracting an experimental shape factor requires a deconvolution procedure, that is discussed in the next chapter.

3.4.3.3 Thallium-204 decay

The measurement of ^{204}Tl decay carried out with cooling is compared with the simulated spectrum in Figure 3.44. The spectra have been normalised by integration between 100 keV and 750 keV. Good agreement between the measurement and the simulation is obtained above 120 keV. Certain distortion is observed below this energy. This distortion could be related to self-absorption in the source, which has not been analysed further.

It is a surprising result, as the same source was used for the measurements without cooling, where good agreement with the simulation was found down to 50 keV. Nevertheless, the disagreement parameter $(1 - R^2)$ equals to 0.33% and the distribution of the residuals highlights the inconsistency with the simulation below 120 keV (see Figure 3.45).

A possible explanation of this discrepancy is the electron capture branch present in ^{204}Tl decay, with a branching ratio of 2.92(13)% [7]. The capture process creates vacancies in the atomic cloud of ^{204}Hg and leads to Auger electron emissions between 53 and 83 keV. Taking into account the 9 keV energy resolution of our detection system, this could explain the additional counts observed below 100 keV. This contribution was unresolved in the previous measurement

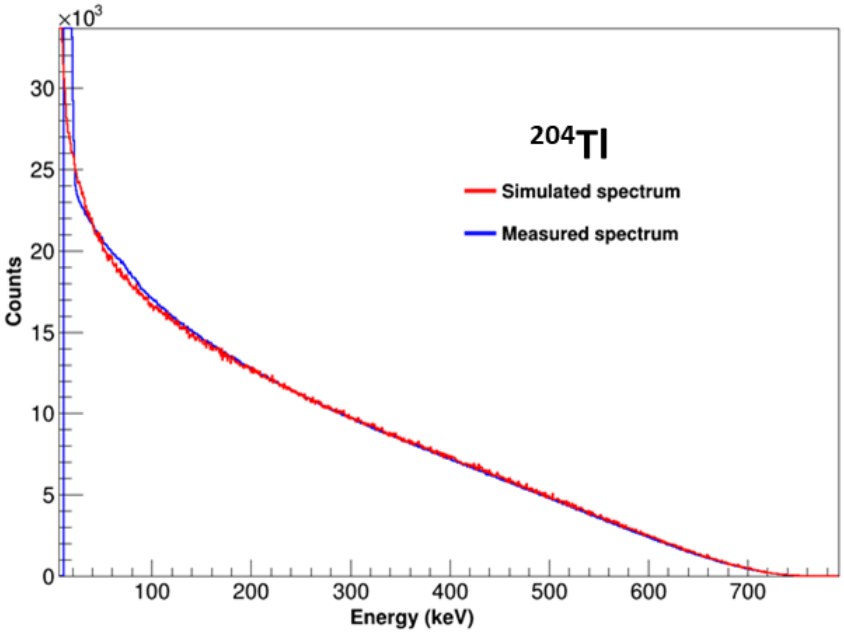

Figure 3.44 – Comparison of the measured spectrum (blue) of ^{204}Tl with the simulated spectrum (red). The input of the simulation is the theoretical spectrum calculated from BetaShape.

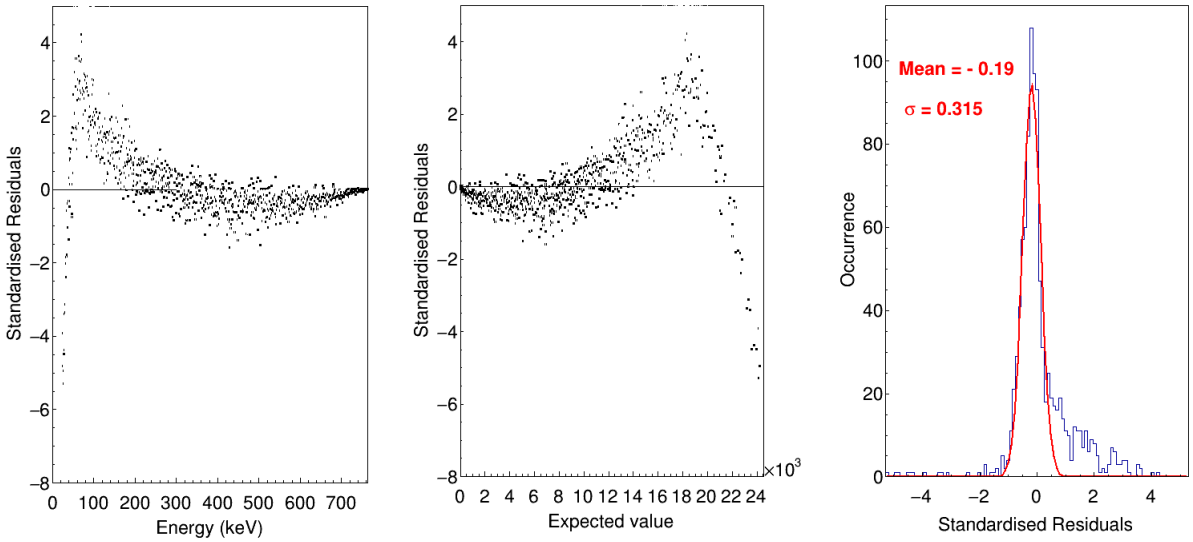

Figure 3.45 – Residuals of the spectra in Figure 3.44.

due to a worse energy resolution.

Using the PenNuc module, the capture branch has been introduced in the simulation together with the β branch, the atomic relaxation contribution subsequent to the capture process being automatically managed by the module. The PenNuc module contains a ^{204}Tl β spectrum of less accuracy, and we modified its code to use a more accurate spectrum given by the BetaShape program.

The result of this simulation (Figure 3.46) shows an excellent agreement from 40 keV to the end-point energy with the measured spectrum. The spectral residuals (Figure 3.47) are found to

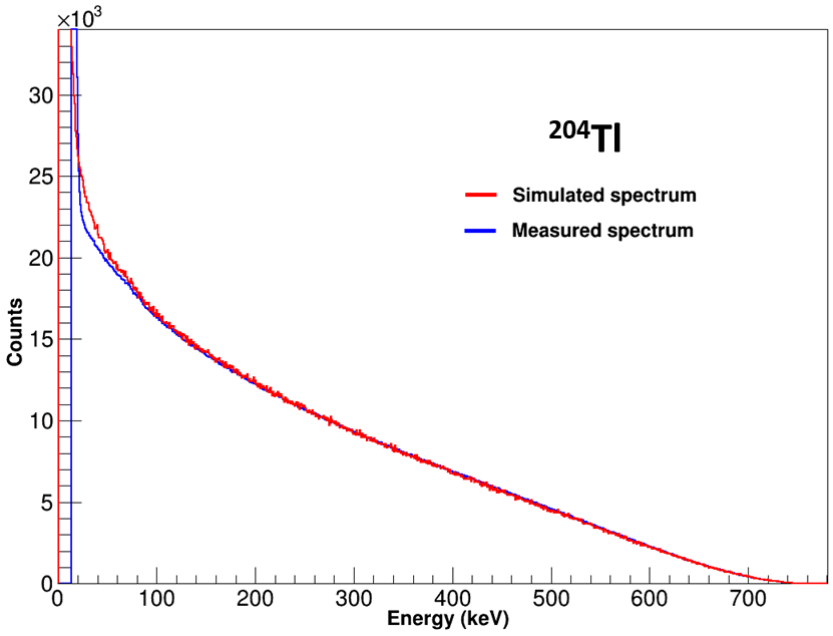

Figure 3.46 – Comparison of the measured spectrum (blue) of ^{204}Tl with the new simulated spectrum (red) using the PenNuc module and the spectrum given by BetaShape.

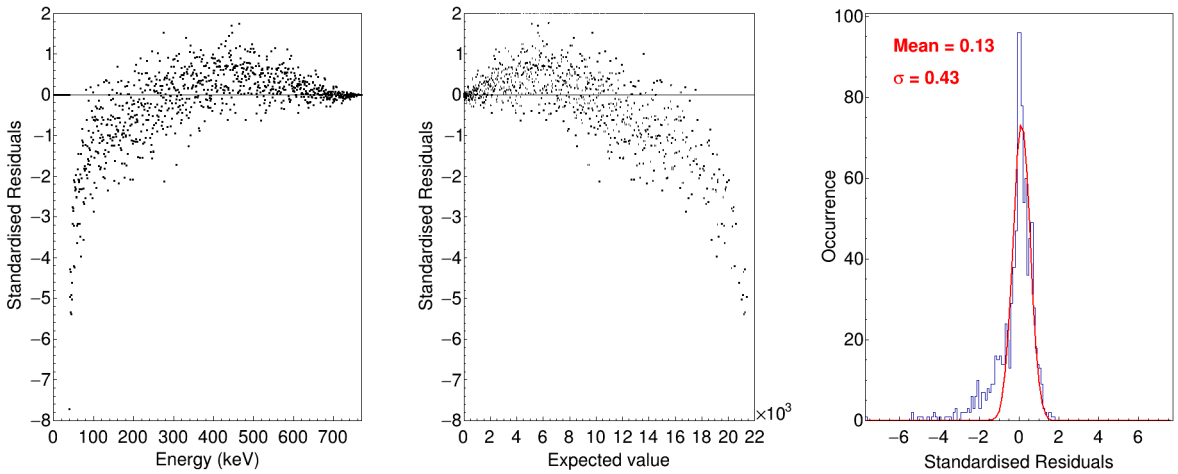

Figure 3.47 – Residuals of the spectra in Figure 3.46.

be uniformly distributed between 40 keV and $E_{\max}$, the distribution of residuals shows a small distortion. The parameter $(1-R^2)$ equals to 0.3% between 20 keV and $E_{\max}$ but is only of 0.2% starting from 40 keV. As the simulation is performed using first forbidden unique transition shape in addition with EC branch, the remaining distortion at this point, seems to originate from the emitted spectrum. For the further analysis of β spectrum, the contributed of EC branch must be removed. Therefore, in the specific case of ^{204}Tl decay, an accurate description of the decay scheme is of importance for an accurate description of our measurement.

3.4.3.4 Chlorine-36 decay

The measurement of ^{36}Cl decay has already been discussed in the section 4.1.3.3. The measured spectrum has significant energy loss due to the presence of large size crystals. The final measurement would require a new radioactive source based on different techniques. However, such a source is still subject to ongoing work. Therefore, the final measurement in this work is kept as the one with the freeze-dried radioactive source (see Figure 3.39).

Conclusion

In this section, we have described the final characterisation of the detection system. The β spectrum of ^{14}C, ^{36}Cl, ^{99}Tc and ^{204}Tl decays were measured. The influence of the source preparation on ^{99}Tc shape has been studied by preparing sources with different radioactive solutions, with and without a carrier salt, followed by a freeze or an oven-drying method. Finally, measurements performed with the freeze-dried sources, which have been demonstrated to minimise self-absorption, are adopted as the final results.

The measurement of ^{36}Cl β spectrum still exhibits substantial distortion that is most probably due to self-absorption in the radioactive source.

The final results along with the experimental system are improved at each step of measurements by eliminating the distortions (Table 3.6.)

	First test	Measurement without cooling	Measurement with cooling
Energy threshold (keV)	35	22	15
Energy resolution (keV)	16 at 80 keV	12 at 62.5 keV	9 at 62.5 keV
Linearity	35 - 350 keV	62 - 1090 keV	25 - 1090 keV

Table 3.6 – The improvement in the energy threshold, energy resolution and linearity of detection system at the three stages of experiments.

The measurements carried out in this work still have some remaining distortions and even if their contribution to the spectrum shape has been minimised, it is still necessary to correct them. For this purpose, an unfolding or deconvolution method has been developed in order to obtain the initially emitted spectrum, free of the distortions introduced by the detection system. The method developed and the extraction of the experimental shape factors are discussed in detail in the next chapter.

"Mathematics reveals its secrets only to those who approach it with pure love, for its own beauty."

- Archimedes

Chapter 4

Deconvolution of spectra

The beta spectrum measured with our detection system does not entirely correspond to the initially emitted spectrum. Indeed, it is distorted due to several factors such as the detector dead layer, the distance between the detectors, the radioactive source, etc. However, the work aims to determine accurately the initially emitted spectrum. In order to achieve this, the remaining distortions have to be removed, which requires an unfolding (deconvolution) procedure. The corrections can only be introduced if the response of the detection system is accurately known. In this work, the response function has been built from Monte Carlo simulations, and a mathematical algorithm has been implemented to unfold the measured spectra. First, this procedure is discussed below. Then, the extraction of shape factors from the corrected spectra and their analysis are presented.

4.1 Deconvolution process

The measured spectrum results from the convolution of the initially emitted spectrum with the response of the detection system. In order to extract the spectrum free of distortion, it is necessary to determine the response function and to unfold the measured spectrum. The method developed in this work is based on the matrix inversion method, which has already been applied in several works [134–137]. The idea has mainly been inspired from [134] and the detailed mathematical justifications can be found in this article. The step-by-step process of unfolding is presented in the following subsections.

4.1.1 Method of unfolding process

The proposed procedure is an exact solution as long as the problem is not mathematically ill-posed. The main objective is to determine how the content of a given energy bin $[E_i, E_{i+1}[$ is spread over the other bins. It is done using mono-energetic simulations, one for each bin. It is then possible to build a response matrix of the detection system that is independent of the

knowledge of the beta spectrum. Further, applying the inverse of this matrix to the measured spectrum will provide the unfolded spectrum.

It is noteworthy that such a deconvolution relies on reliable Monte Carlo simulations. Thanks to the refined work we performed that has been detailed in previous chapters, we can be confident about the accuracy of our simulations and thus about the response function. In addition, the quasi-4π geometry dramatically reduces the magnitude of the correction from the deconvolution and therefore, its contribution to the final uncertainty.

The method has also been applied as a test to the spectra acquired in the past in 2π geometry at LNHB [4]. The beta spectra were measured using a single PIPS detector (ultra-vacuum, very thin sources, cooled down). In that work, the GEANT4 code was used for the simulations and analysis. Hence, we used this implementation to build the corresponding response function. The same geometry has also been implemented in PENELOPE in order to compare the response using two different Monte Carlo codes. The simulation result has then been treated by the following procedure.

4.1.1.1 Energy binning

The first step is to fix the energy binning and to treat the spectra accordingly. The same binning has to be defined for all the procedures based on considerations about the measurements (see Figure 4.1). In this work, a binning of $\Delta E = 1$ keV has been chosen and we thus consider intervals $[E_i,E_{i+1}[$ with $(E_{i+1}\text{-}E_i) = \Delta E$, starting from $E_0 = 0$ keV. Each energy spectrum in the procedure was binned according to a simple algorithm:

- Measured spectrum - The original binning has to be smaller than ΔE. The loop goes from the first original bin to the last original bin. If the total current original bin is included in $[E_i,E_{i+1}[$, its content is added to this bin. If it overlaps with another bin going beyond (E_{i+1}), its content is spread between the two bins $[E_i,E_{i+1}[$ and $[E_{i+1},E_{i+2}[$ with a weight which depends on the overlap of the bins.

- Simulated spectrum - The result of the simulation is a deposited energy, event-by-event. Therefore, it is only necessary to build the spectrum by adding one event in the corresponding final bin, event-by-event.

The first bins in the measured spectrum are generally empty due to the threshold applied to avoid the acquisition of electronic noise. In addition, a maximum threshold has to be chosen, where it is reasonable to consider that there is nothing beyond that energy. These considerations fix the dimension of the vectors (measured and emitted spectra) and the matrix (response function).

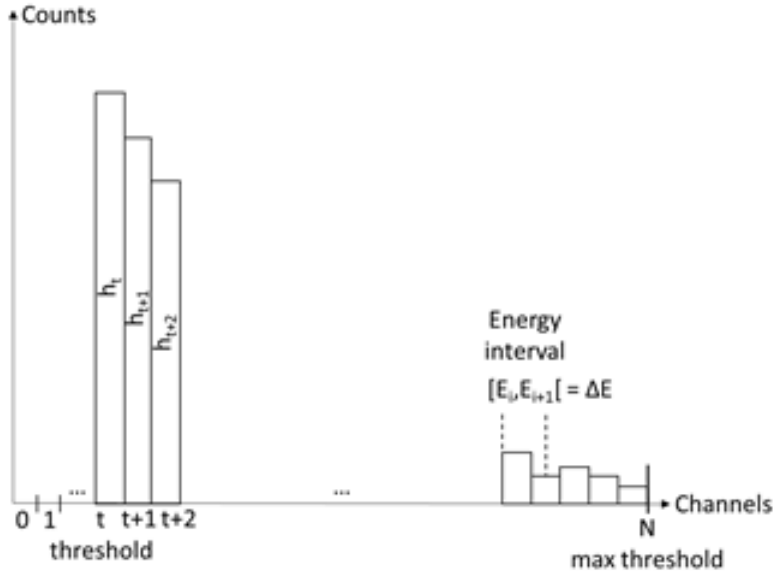

Figure 4.1 – Binning definition and its application to the measured spectrum.

4.1.1.2 Response Function

The binning having been fixed, the response function can now be defined as a square matrix (a rectangular matrix is not invertible). The measured spectrum $M(E_i)$ then results from the multiplication of the response matrix $R(E_i + \Delta E, E_i)$ of the detection system by the initial spectrum $S(E_i)$:

$$\begin{pmatrix} M(E_0) \\ \vdots \\ \vdots \\ \vdots \\ M(E_N) \end{pmatrix} = \begin{pmatrix} R(E_0+\Delta E, E_0) & \cdots & R(E_N+\Delta E, E_0) \\ \vdots & & \vdots \\ \vdots & \ddots & \vdots \\ \vdots & & \vdots \\ R(E_0+\Delta E, E_N) & \cdots & R(E_N+\Delta E, E_N) \end{pmatrix} \times \begin{pmatrix} S(E_0) \\ \vdots \\ \vdots \\ \vdots \\ S(E_N) \end{pmatrix} \tag{4.1}$$

Each column of the response matrix quantifies how the content of one energy bin is distributed over the other bins (see Figure 4.2). The initially emitted particles with energy in the interval $[E_i, E_{i+1}[$ fall in the corresponding bin $S(E_i)$. They partly contribute to the measured number of counts in all the bins with a weight determined by the response matrix elements, obtained from Monte Carlo pulse simulations (*i.e.* with mono-energetic primary events). It is noteworthy that in the case of electrons, there is always a small amount of energy lost in the detector dead layers, preventing full-energy deposition. Therefore, only the bins with an energy lower than the primary pulse energy E_p have a non-null content (see Figures 4.2 and 4.3).

Consequently, the response matrix is triangular by construction: all the matrix elements below the diagonal are null, and all the diagonal elements are strictly positive. In this case, the matrix determinant is the product of the diagonal elements, thus always non-null, which ensures that the matrix is invertible. In addition, each column of the matrix has to be normalised (*i.e.*

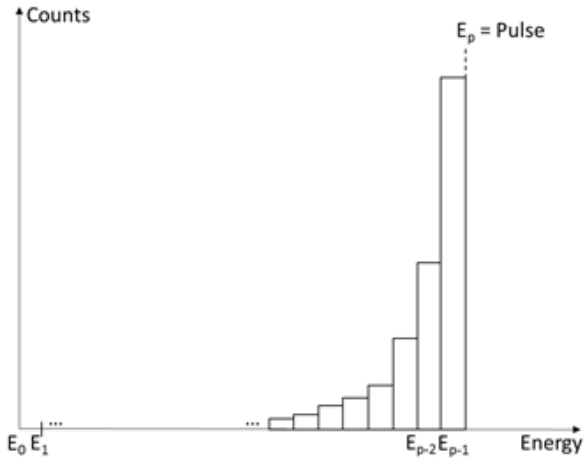

Figure 4.2 – Typical histogram resulting from a mono-energetic (E_p) electron pulse simulation.

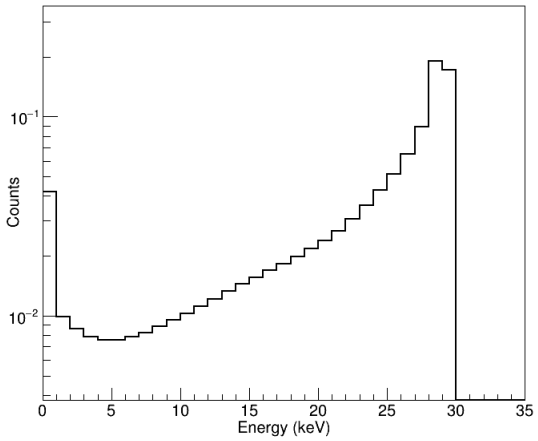

Figure 4.3 – Normalised histogram resulting from a mono-energetic electron pulse simulation for 30 keV.

the sum of the bin contents equal to unity) in order to keep the information about the absolute number of counts.

Many tools already exist to manipulate vectors and matrices. We use in the present work the linear algebra package from ROOT, which includes efficient functions to determine the inverse matrix.

4.1.1.3 The ^{14}C spectrum with a single silicon detector

For the measurements performed by C. Bisch with a single PIPS detector [4], we have used the GEANT4 simulations she developed to build the response matrix in order to test the method. First, we rerun the simulations in order to reproduce the measured spectrum. GEANT4 simulations have been performed using the Low Energy Electromagnetic Physics model, with a range cut of 10 nm and an energy threshold of 250 eV (minimum of the tables) for all particles, and switching on the fluorescence, Auger and PIXE atomic processes. The full

beta spectrum has been considered as an input of the simulation with the latest Q-value, *i.e.* $E_{\max} = 156.476$ keV [123].

The ^{14}C decay is known to be an allowed transition that exhibits a very long half-life, a typical effect due to specific nuclear structure. This can have an influence on the shape of its β spectrum and some experimental shape factors are available in the literature [133, 138–148]. The most recent and precise result is from Kuzminov [133] and has been used as an input of the simulations; a usual allowed shape has also been considered.

The simulations have been performed with the 2π geometry for 60 million primary events. The spectra have been convoluted with a Gaussian distribution (FWHM = 4.4 keV, taken from [4]) to take into account the energy resolution of the detection system. As can be seen in Figure 4.4, the simulated spectra are close to the measured spectrum. Good agreement is found for both input shapes, the allowed shape being better below 40 keV and Kuzminov's shape being better above.

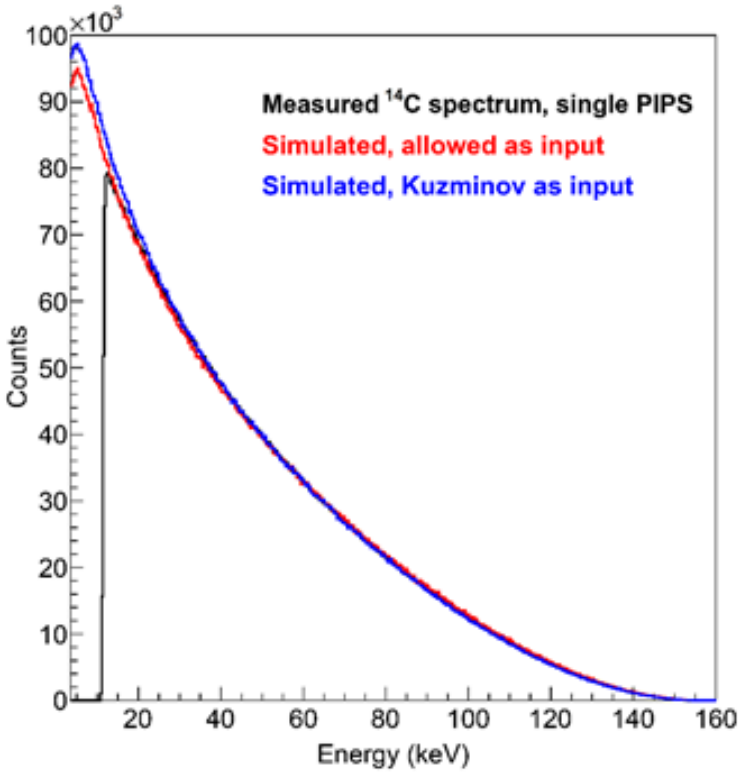

Figure 4.4 – Comparison of the measured ^{14}C β spectrum (black) with GEANT4 simulations using as an input: *i*) a spectrum calculated as a regular allowed transition (red); and *ii*) a spectrum (blue)built from the experimental shape factor determined by Kuzminov [133].

The same geometry has been implemented to perform PENELOPE simulations, with identical considerations as described in previous chapters, in order to see the influence of the Monte Carlo code. A comparison of the GEANT4 and PENELOPE spectra can be seen in Figure 4.5 and the corresponding residuals in Figure 4.6. The spectra are in excellent agreement down to 10 keV with a disagreement parameter (1-R^2) equal to 0.02%. However, one can see a small distortion

in the energy distribution of the residuals. This difference is thought to come from the multiple scattering model for electron transport that is included in PENELOPE but not in GEANT4. PENELOPE should provide more accurate and reliable results and has thus been preferred for the unfolding process applied to our measured spectra.

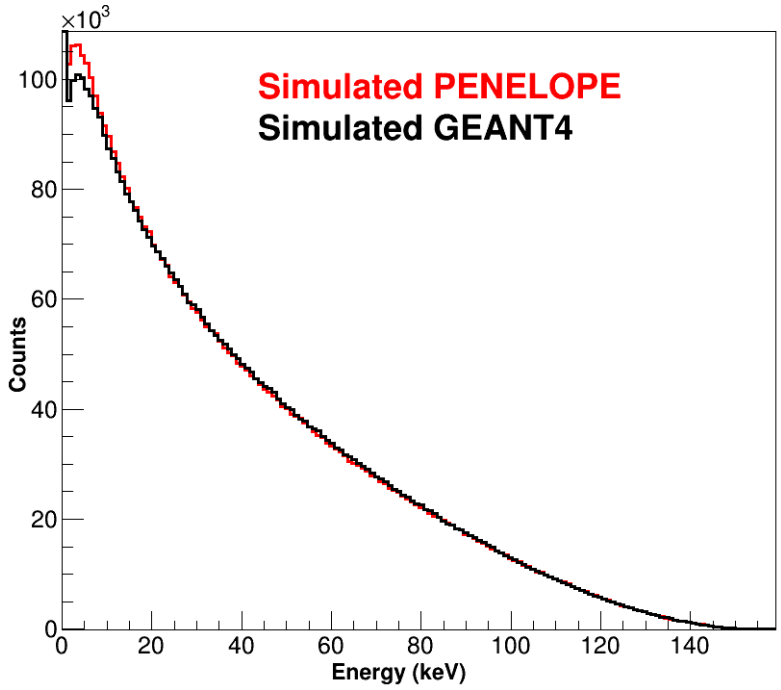

Figure 4.5 – Comparison of the simulated ^{14}C β spectrum with GEANT4 and PENELOPE simulations for a 2π geometry, using as an input the spectrum of a regular allowed transition.

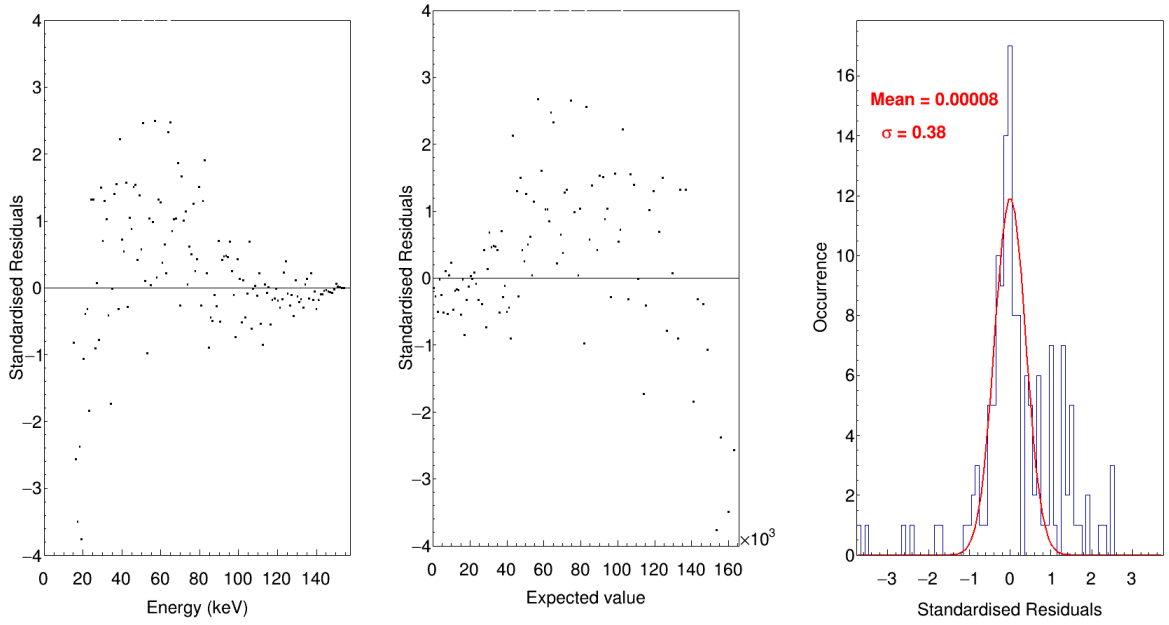

Figure 4.6 – Residuals between the ^{14}C β spectra simulated with GEANT4 and PENELOPE shown in Figure 4.5.

4.1.1.4 Validation of the method

Following the procedure described in the previous sections, the response matrices have been created from the mono-energetic pulse simulations, with 5 million primary events for each energy bin. In order to validate the method, we applied the unfolding process to different spectra obtained by simulation and we verified if we could retrieve the original input spectra. This exercise was done for both GEANT4 and PENELOPE codes.

We first considered the simulated spectrum of ^{14}C with 2π geometry generated from the allowed spectrum calculated by the BetaShape program. The initial β spectrum (input of simulation) has been retrieved by deconvolution down to at least 10 keV (see Figure 4.7). The result is similar if a spectrum built on Kuzminov's shape factor is considered. In addition, the response functions built using GEANT4 and PENELOPE codes have led to identical results down to 10 keV (see Figure 4.8). As the threshold of the measurement is above 10 keV, this unfolding process can be safely applied.

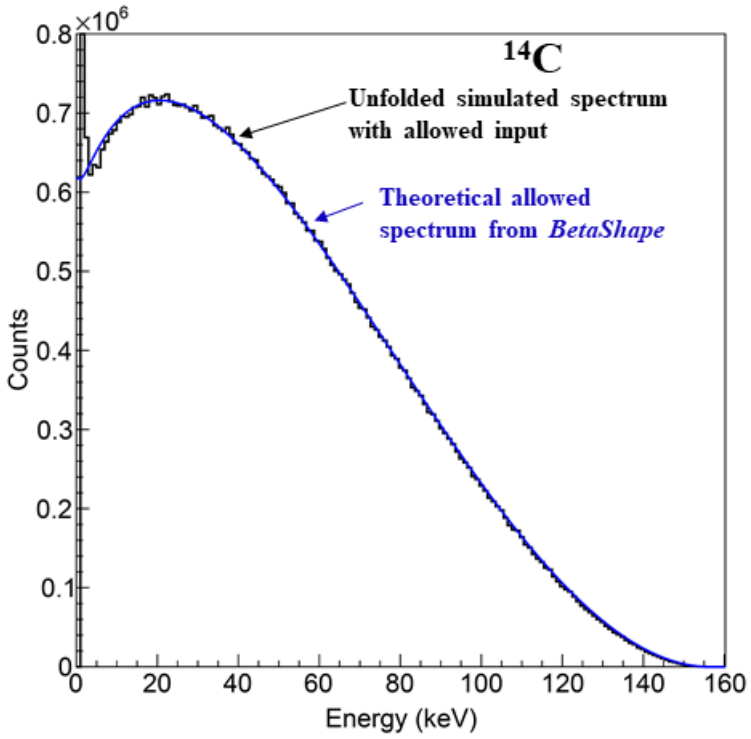

Figure 4.7 – Unfolded ^{14}C simulated spectrum, with GEANT4. The input allowed spectrum has been retrieved at least down to 10 keV. Result is similar when using the experimental shape factor determined by Kuzminov [133], which validates the implementation of the unfolding process.

The method was also applied to the simulated spectrum of ^{99}Tc considering a quasi-4π geometry. A β spectrum built from Reich's shape factor was used as the input [95] of the PENELOPE simulation. The initial spectrum could be retrieved by deconvolution down to at least 10 keV (see Figure 4.9). The same study was performed for the 2π geometry with GEANT4, and the result is similar.

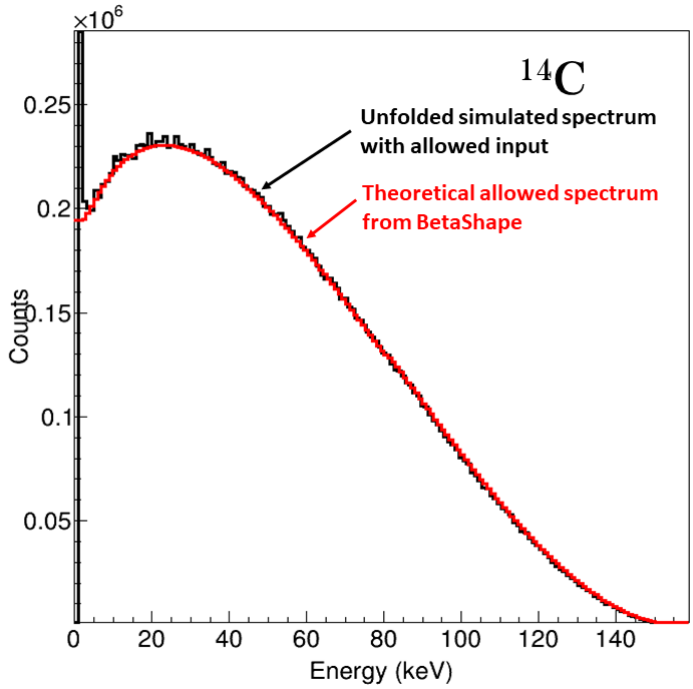

Figure 4.8 – Unfolded ^{14}C simulated spectrum, with PENELOPE. The input allowed spectrum has been retrieved at least down to 10 keV. Result is similar when using the experimental shape factor determined by Kuzminov [133].

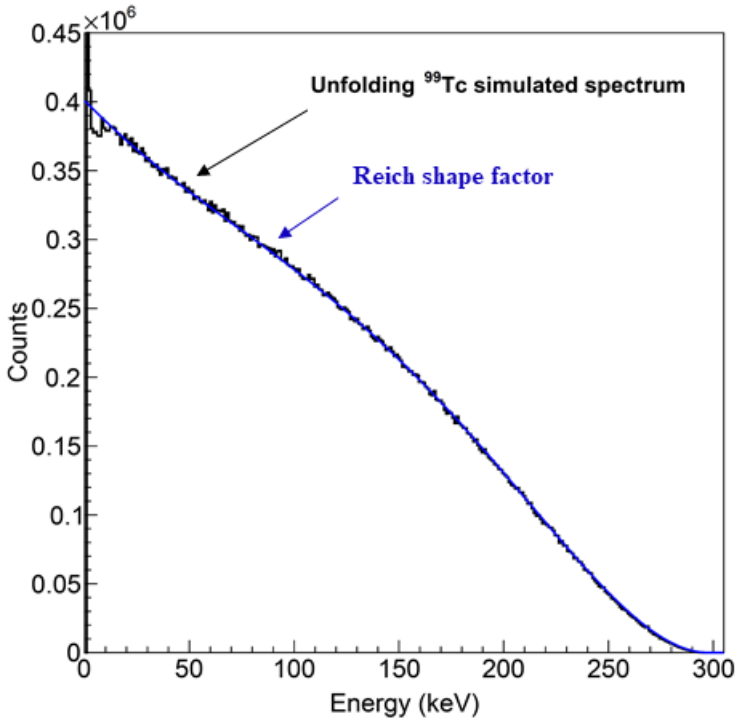

Figure 4.9 – Unfolded ^{99}Tc simulated spectrum, with PENELOPE. The input spectrum, built using Reich's shape factor [95], has been retrieved at least down to 10 keV.

4.1.2 Unfolded beta spectra

After validation, the unfolding process has been applied to the measured spectra of the previous study by C. Bisch (2π geometry) and those obtained in this work with the quasi-4π detection system. All the unfolded spectra are discussed in detail in the following sections.

4.1.2.1 Carbon-14 decay

The spectrum of ^{14}C measured with the quasi-4π detection system presented in section 3.4.3.1 has been unfolded. The resulting spectrum is found to be close to an allowed shape (see Figure 14) and not to Kuzminov's shape. The spectra have been normalised by integration between 40 and 150 keV. The disagreement parameter $(1 - R^2)$ between unfolded spectrum and Kuzminov shape is 0.28% between 22 keV and $E_{\max}$, while, with allowed shape it is 0.04% between 22 keV and $E_{\max}$.

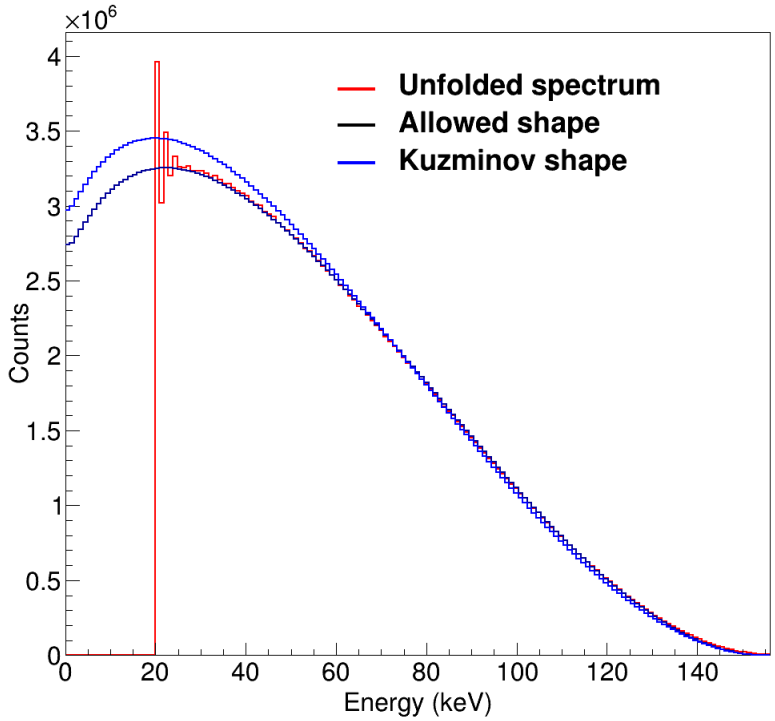

Figure 4.10 – Unfolded spectrum of ^{14}C (red), the allowed spectrum (black) and Kuzminov spectrum (blue).

Some fluctuations appear below 30 keV that could be due to the unfolding process itself, because of insufficient statistics for the pulse simulations or a too large binning so close to the energy threshold. Such a study would require many more simulations and has not been tested yet. Remarkably, the disagreement parameter goes down to 0.008% for allowed spectrum between 26 keV and $E_{\max}$.

The comparison between the final spectrum (unfolded) with the MMC measured spectrum, given in Figure 15, shows an excellent agreement down to 26 keV with a disagreement parameter

$(1 - R^2)$ equal to 0.05%, which validates the quality of our measurement. The corresponding residuals are uniformly distributed within 2σ (Figure 16). The peaks at low energy in the MMC spectrum are due to energy calibration sources.

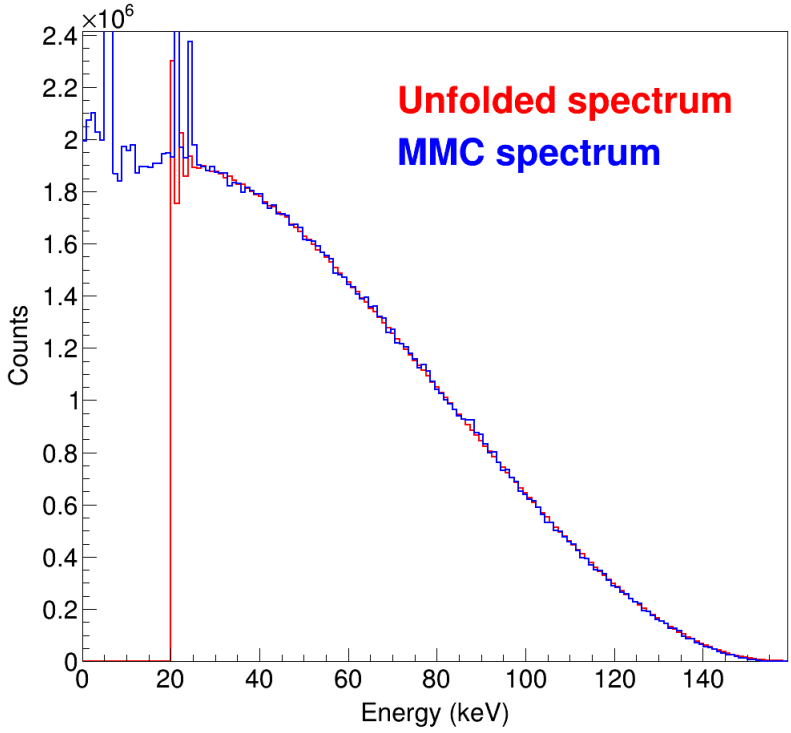

Figure 4.11 – Unfolded spectrum of ^{14}C (red curve) and the MMC measured spectrum (blue curve).

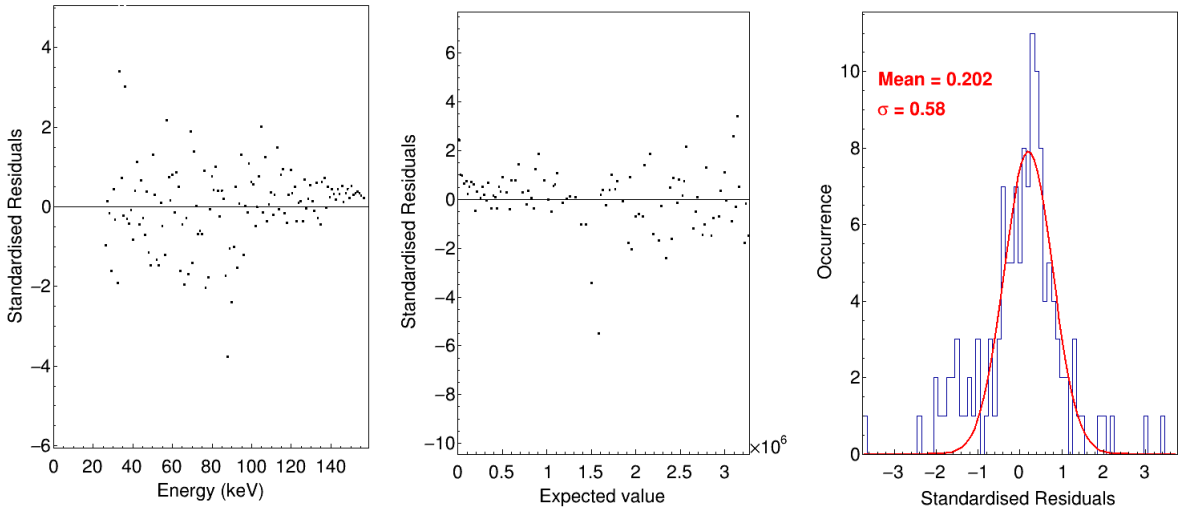

Figure 4.12 – Residuals between the unfolded spectrum of ^{14}C and the MMC measured spectrum.

The quasi- 4π unfolded spectrum is also compared with the unfolded spectrum from 2π measurement in Figure 4.13. The spectra are in overall good agreement above 60 keV, and a significant difference can be seen below this energy. The backscattering effect is very large

in the 2π measurement, which leads to a strong unfolding correction. In addition, the 2π measurement was performed with a thicker source, prepared by contamination of 18 μm thick Mylar® film. These differences can explain the discrepancy at low energy. Nevertheless, the shape factor extraction is still required to complete the analysis and will be discussed in detail in section 4.1.3.

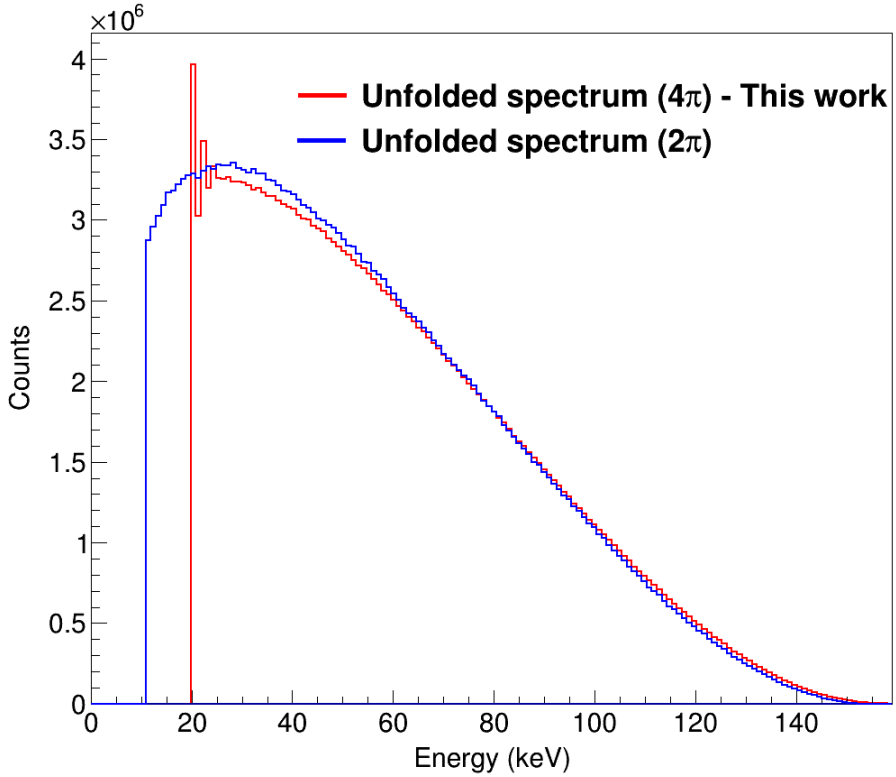

Figure 4.13 – Comparison of unfolded ^{14}C spectra measured in 2π and quasi-4π geometries.

4.1.2.2 Technetium-99 decay

The spectrum of ^{99}Tc measured with quasi-4π detection system presented in section 3.4.3.2 has been unfolded. The unfolded spectrum is found to be in excellent agreement with the MMC measurement at LNHB (see Figure 17). The spectra have been normalised by integration between 40 and 290 keV. The disagreement parameter $(1-R^2)$ is equal to 3.63% between 22 keV and $E_{\max}$ whereas its value decreases to 0.06% between 26 keV and $E_{\max}$. The residuals are distributed within 2σ (Figure 18), showing excellent agreement between the two measurements. However, a small tendency can still be observed in the energy distribution of the residuals, which might be originating from both measurements.

The spectrum has also been compared with the Reich shape and the unfolded spectrum from 2π measurement (see Figure 19). Our spectrum is in good agreement with all the spectra above 120 keV. The Reich's shape factor was measured between 55 keV and 250 keV. The corresponding spectrum in Figure 19 is built applying this shape factor over the full energy range, which explains the inconsistency with our measurement and the MMC measurement

below this energy. The same reasons as for ^{14}C spectrum, namely strong backscattering effect to correct and a different source preparation, can explain the difference between the 2π spectrum and the two other spectra.

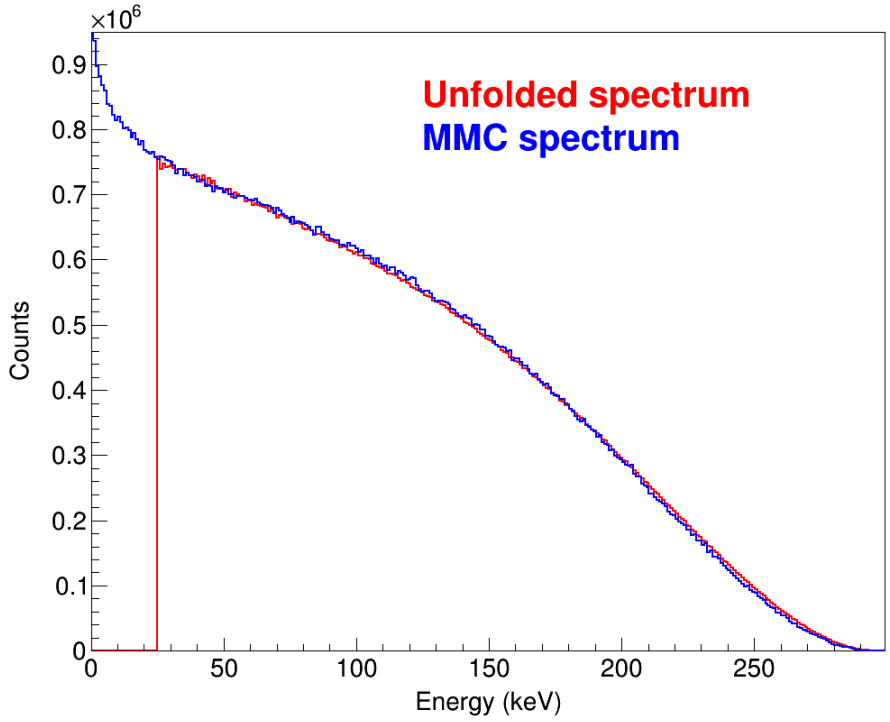

Figure 4.14 – Unfolded spectrum of ^{99}Tc (red curve) and the MMC spectrum (blue curve).

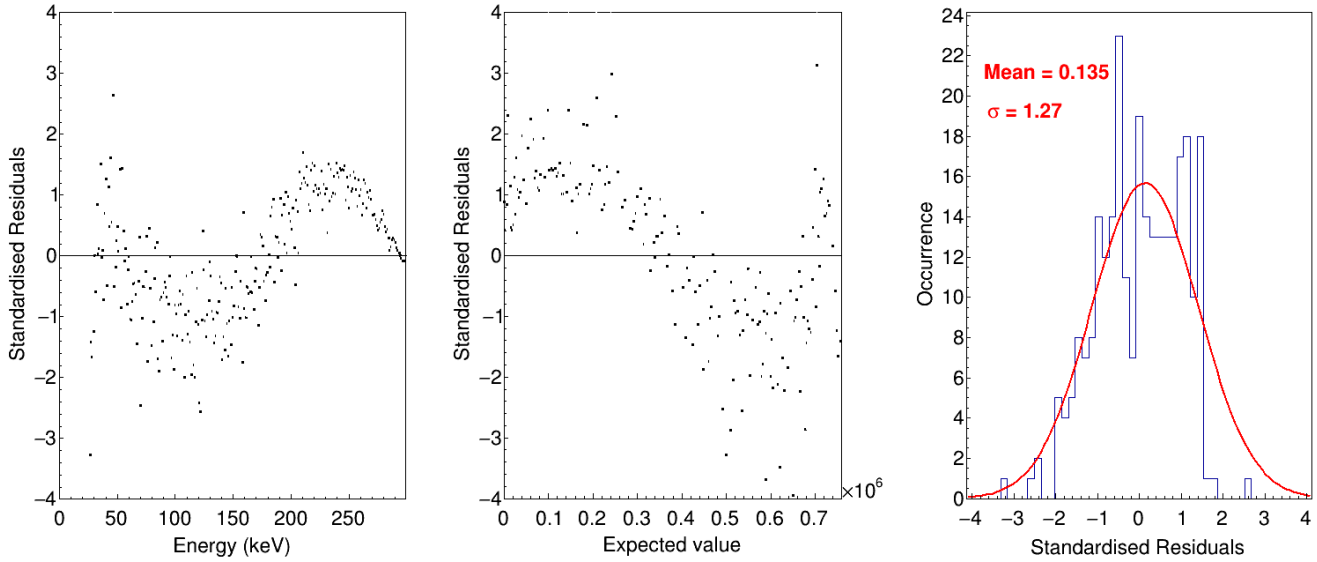

Figure 4.15 – Residuals between the unfolded spectrum of ^{99}Tc and the MMC spectrum showed in Figure 17.

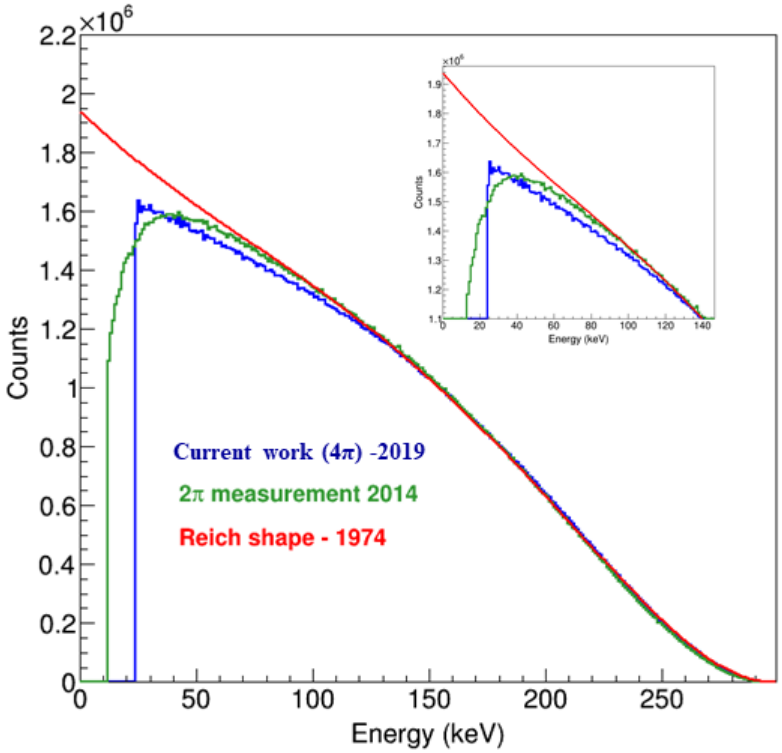

Figure 4.16 – Comparison of the unfolded ^{99}Tc spectra from measurements in 2π and quasi-4π geometries with a spectrum based on the experimental shape factor from Reich [95].

4.1.2.3 Thallium-204 decay

The final spectrum of ^{204}Tl measured with quasi-4π detection system discussed in the section 3.4.3.3 has been unfolded. It is compared with the theoretical spectrum calculated by the BetaShape program for this first forbidden unique transition in Figure 4.17. The discrepancy between the measured and the simulated spectrum has already been discussed in chapter 3. The calculated spectrum is also very close to an experimental spectrum measured by Flothmann with a 4π Si(Li) β spectrometer between 190 keV and 675 keV [149]. The spectra are in good agreement above 120 keV, and a significant disagreement can be seen below, due to the contribution of the electron capture branch (EC) as discussed in chapter 3.

Further analysis has been processed in order to remove the contribution of the EC branch from the measured spectrum and then unfold the resultant. As we cannot distinguish between the events from EC and β decays in our measurement, the EC branch in the decay scheme (see Figure 4.18) has been simulated together with the β branch using the PenNuc module with a statistics close to the total number of counts in the measurement. We processed as follows:

1. The simulation of the total spectrum with the complete decay scheme using the PenNuc module was performed for 100 million events.

2. The simulation with only the EC branch was performed for 100 million events.

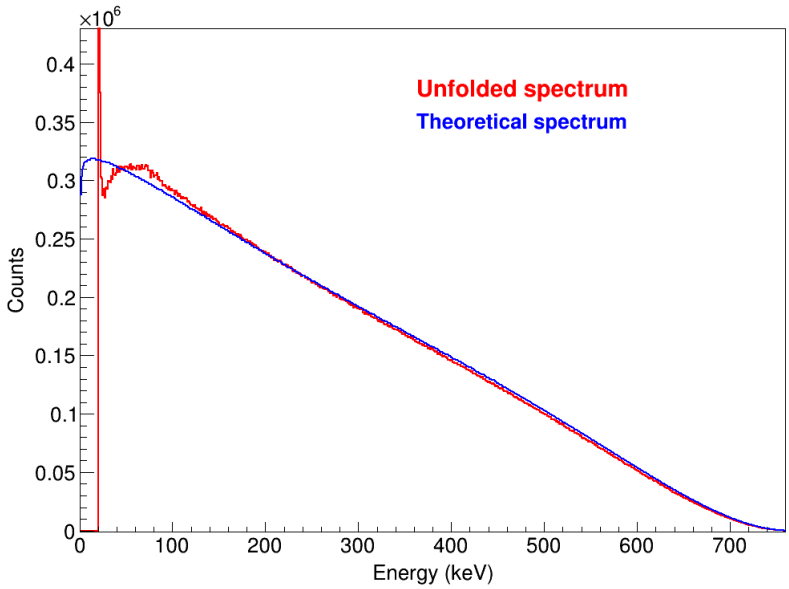

Figure 4.17 – Comparison of the unfolded ^{204}Tl spectrum measured in quasi-4π geometry with the theoretical spectrum calculated by BetaShape.

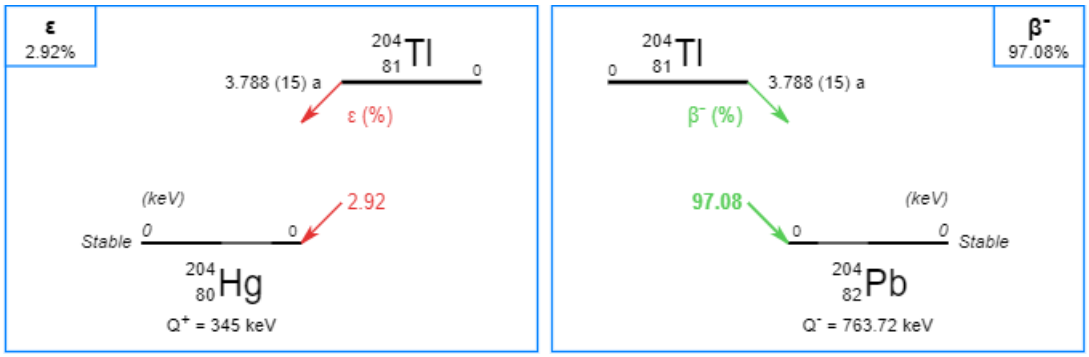

Figure 4.18 – Decay scheme of ^{204}Tl.

3. The simulation of only the β^- branch was performed for 100 million events, again with the PenNuc module. As a reminder, the input spectrum is the accurate spectrum calculated by the BetaShape code after some modifications in the PenNuc module, as discussed in chapter 3.

4. The spectra were normalised with their branching ratios: 2.92 (13)% for the EC branch and 97.08 (13)% for the β^- branch [7].

5. The simulated β^- branch spectrum has to be equal to the total simulated spectrum minus the normalised EC spectrum (see Figure 4.19). The resultant is the corrected beta spectrum.

6. The corrected spectrum was unfolded and the input β spectrum was retrieved, as shown in Figure 4.20. The disagreement parameter $(1 - R^2)$ is equal to 0.3% between 30 keV and $E_{\max}$.

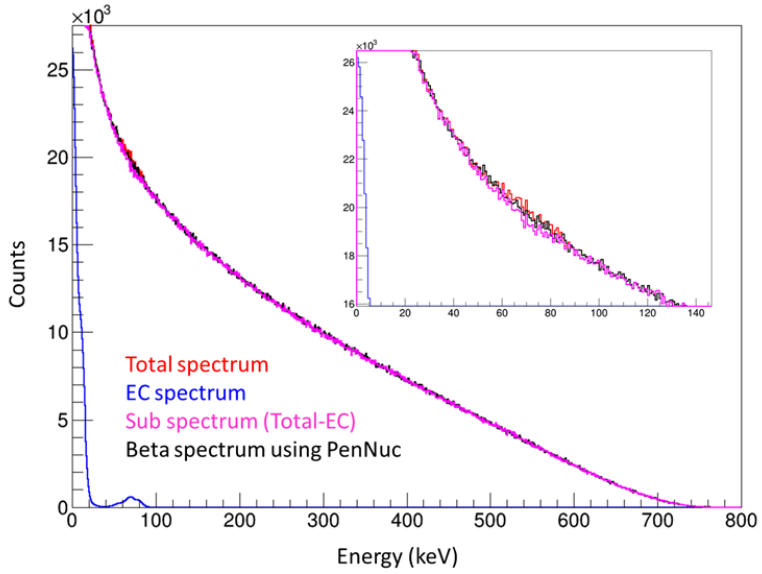

Figure 4.19 – Simulated spectra of ^{204}Tl with total decay scheme (red), EC branch (blue), subtracted spectrum of total minus EC branch (pink) and the beta spectrum (black).

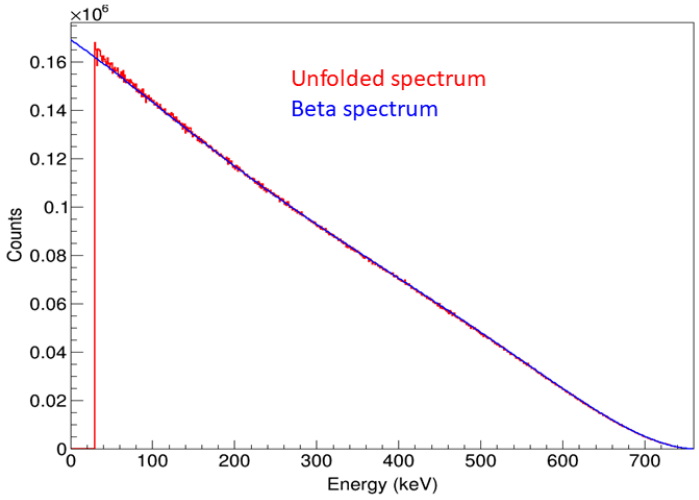

Figure 4.20 – Unfolded simulated spectrum (total spectrum - EC branch) of ^{204}Tl.

This study performed on simulated spectra validates the approach. We can now move to the next step by applying it to the measured spectrum. The measured spectrum (background subtracted) has been fitted between 40 keV and 120 keV in order to determine the number of counts due to the EC branch (see Figure 4.21). The β spectrum has been fitted with a second-order polynomial. Five Gaussian functions were found to be necessary in order to reproduce the measured spectrum accurately. The Gaussian integral in the fit shows the number of events due to the EC branch in the total measured spectrum, which has then been used to normalise the simulated spectrum of the EC branch. The normalised EC spectrum has next been subtracted from the measured spectrum, providing the corrected spectrum. Finally, the corrected spectrum has been unfolded and compared with the theoretically calculated spectrum by the BetaShape program (see Figure 4.22). The spectra are in the excellent agreement above 200 keV, and a slight distortion can be seen below.

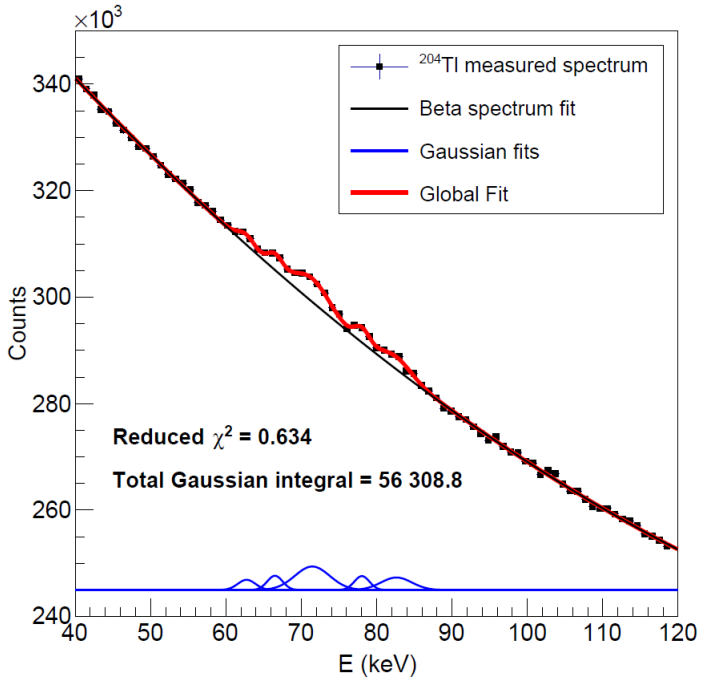

Figure 4.21 – Fit of the measured spectrum (background subtracted) of ^{204}Tl decay between 40 and 120 keV.

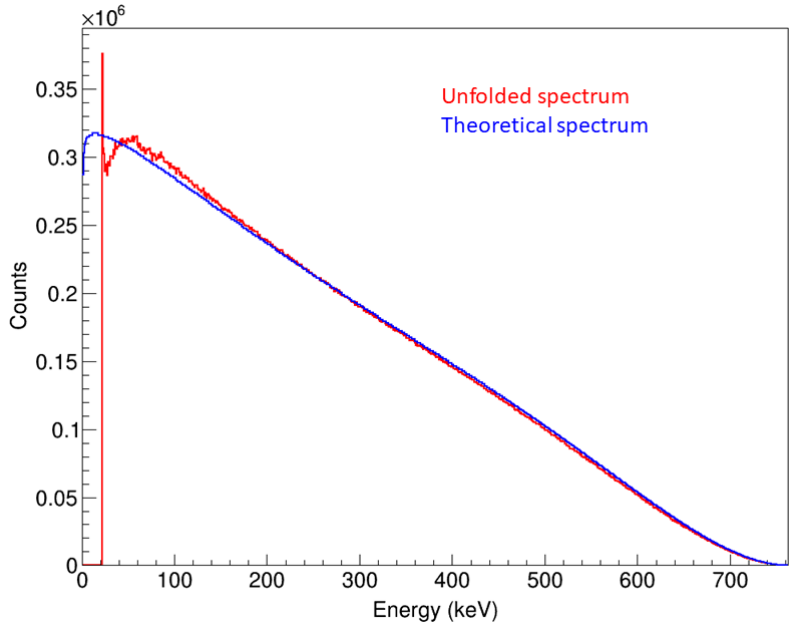

Figure 4.22 – Unfolded spectrum (red) of ^{204}Tl compared with a theoretical spectrum (blue) from the BetaShape code.

The unfolded spectrum has then been compared to the spectrum built on the experimental shape factor taken from [149] (see Figure 4.23). Provided that this experimental shape factor was obtained between 190 keV and 675 keV, an excellent agreement has been found in the common energy range of measurement with $(1 - R^2)$ equal to 0.03%. The residuals are given in Figure 4.24.

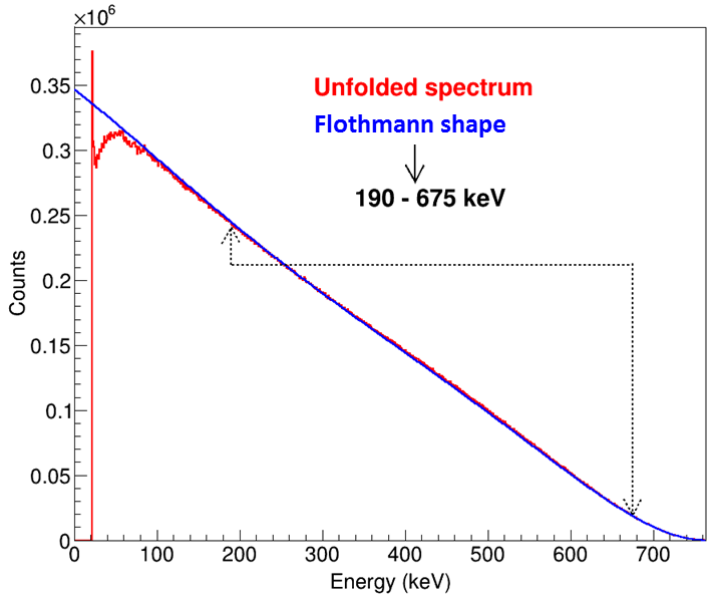

Figure 4.23 – Unfolded spectrum (red) of ^{204}Tl compared with a spectrum (blue) from the BetaShape code based on the experimental shape factor given in [149], whose range of measurement is between 190 keV and 675 keV.

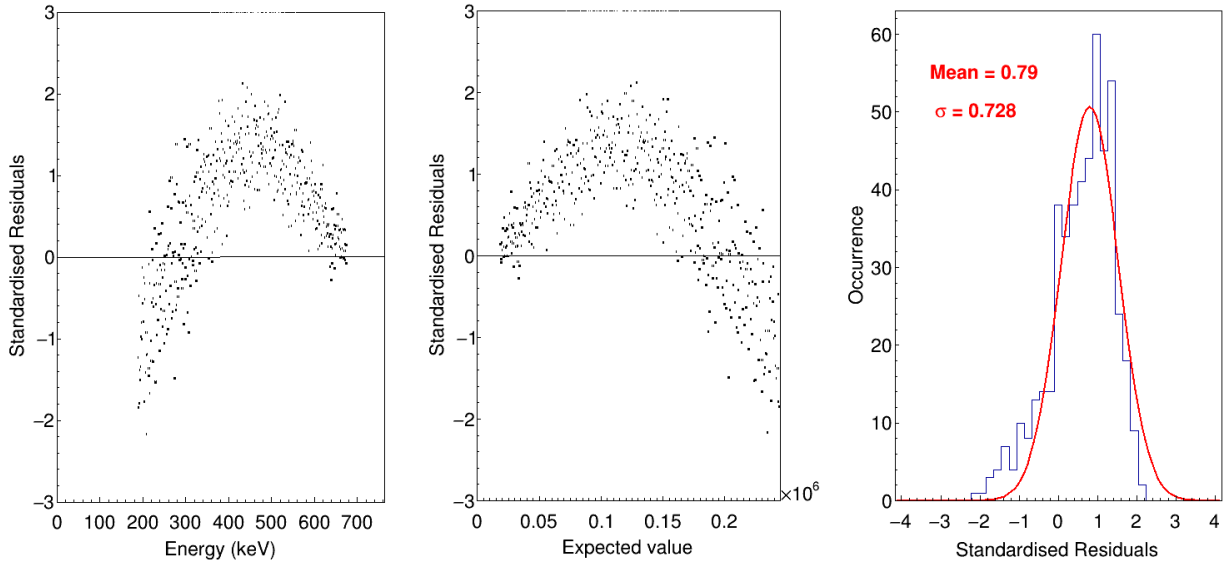

Figure 4.24 – Residuals of the spectra in Figure 4.23 for ^{204}Tl.

In order to understand the discrepancy in Figure 4.22, the unfolded spectrum has been compared with a theoretical spectrum determined with more elaborated modelling, which precisely takes into account the atomic screening and exchange effects (see Figure 4.25) [150]. In this case, the spectra are in good agreement between 40 keV and $E_{\max}$ with $(1-R^2)$ equal to 0.04% while it was 0.08% with the theoretically calculated spectrum from BetaShape (Figure 4.26). It shows that measurement is precise enough to be sensitive to atomic effects.

Strange behaviour with a deficit of counts below 40 keV can be seen in the spectrum. One of the possible origins is the binning of pulse simulations for the construction of response function; with smaller bins (less than 1 keV), this effect may be mitigated.

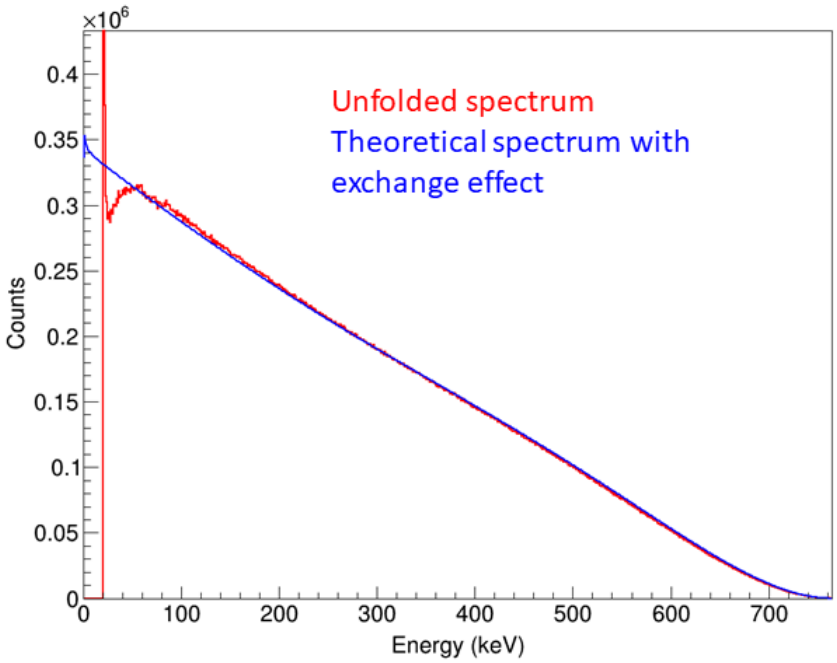

Figure 4.25 – Unfolded spectrum (red) of ^{204}Tl compared with a theoretical spectrum that precisely accounts for atomic screening and exchange effects (blue).

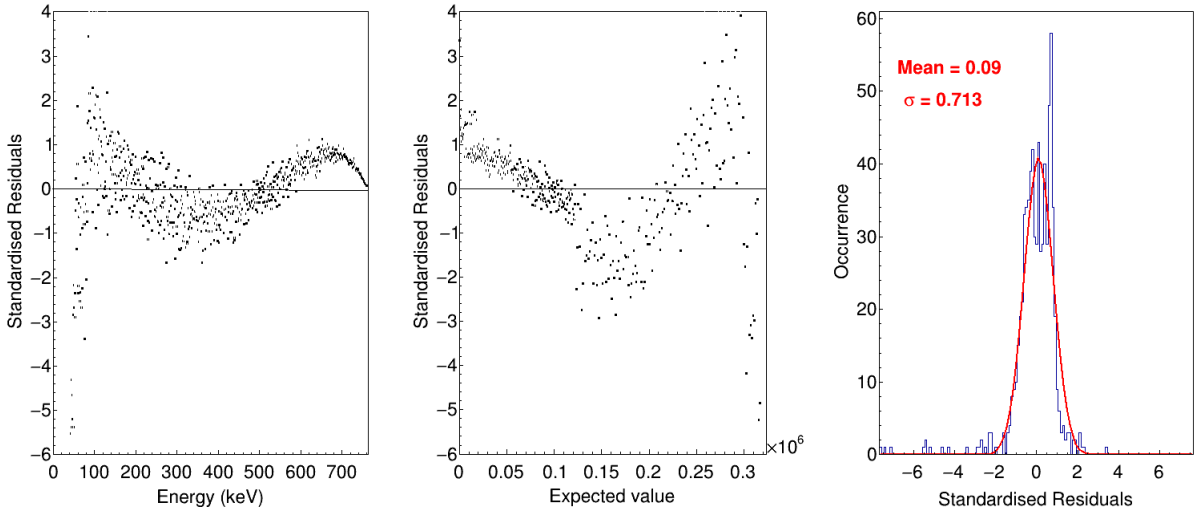

Figure 4.26 – Residuals of the spectra in Figure 4.25 for ^{204}Tl.

4.1.3 Extraction of shape factors

As discussed in chapter 1, a shape factor can be extracted from a measured beta spectrum. We have retrieved accurate spectra and our measurements for ^{14}C, ^{99}Tc and ^{204}Tl decays have been found to be in excellent agreement with MMC spectra and other results available in the literature in the common energy range of the measurements. In this section, the shape factors are extracted considering three cases: silicon measurements in quasi-4π and 2π geometries, and MMC measurements. As a reminder, the quasi-4π and 2π spectra are considered after having been unfolded of the response of the detection system.

4.1.3.1 Carbon-14 decay

Carbon-14 shape is of interest due to its unusual long half-life (5 700 years) for an allowed transition. This is a clear sign of an accidental cancellation of the nuclear matrix elements that are generally dominant in such a transition. It is then necessary to consider forbidden terms, i.e. next-to-leading order terms in the multipole expansion of the nuclear current. As the forbidden transitions can be particularly sensitive to nuclear structure, the question arises about how much ^{14}C spectrum shape is influenced. It has been a subject of investigation over the past 70 years [138, 140, 148, 148, 151, 152]; however, its precise shape is still unknown. Some studies claimed that ^{14}C spectrum exhibits an allowed shape down to 50 keV but diverges below.

In this work, the shape of the measured ^{14}C spectrum was found to be closer to the allowed shape than to Kuzminov's shape [133], as discussed above in the unfolding section (see Figure 14). In order to extract the experimental shape factor, the parameterisation given by Kuzminov has been employed:

$$C(E) = 1 + \beta(E_{\max} - E) \tag{4.2}$$

In [133], both $E_{\max}$ and β parameters were adjusted, with $E_{\max} = 156.27$ (3) keV and $\beta = 1.24$ (4) X 10^{-3}. It is noteworthy that this endpoint energy disagrees with the current Q-value of 156.476 (4) keV given in [123].

In our fitting procedure, the initial shape is considered as for an allowed transition, which means in the present case $C(E) = 1$, and the fit parameters are adjusted by χ^2 minimisation in order to reach the experimental spectrum. The energy range was fixed between 26 keV and 140 keV, where excellent agreement with MMC measurement is observed, and the maximum energy was fixed to the current Q-value from [123]. The fitting procedure is quite sensitive to the starting values of the parameters, β and a global normalisation in the present case.

After several iterative attempts to get both a realistic shape and a good χ^2 value, the best adjustment led to a normalisation parameter equal to 0.955 and β equal to 0.492 (see Figure 4.27). The residuals show good adjustment (Figure 4.28) with a disagreement parameter (1-R^2) of 0.007% between the adjusted spectrum and the measured spectrum.

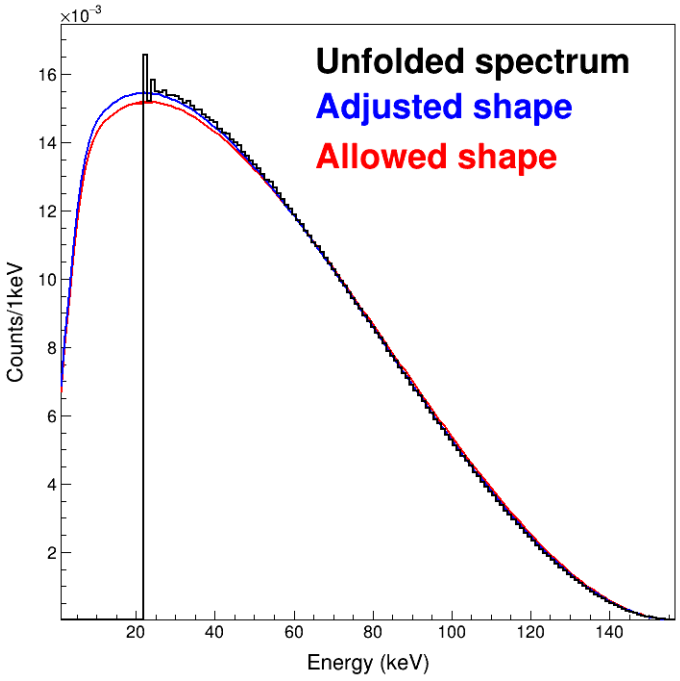

Figure 4.27 – Extraction of ^{14}C experimental shape factor from the unfolded quasi-4π spectrum. The allowed shape (red) gives the starting spectrum of the fitting procedure; the adjusted shape (blue) gives the final spectrum.

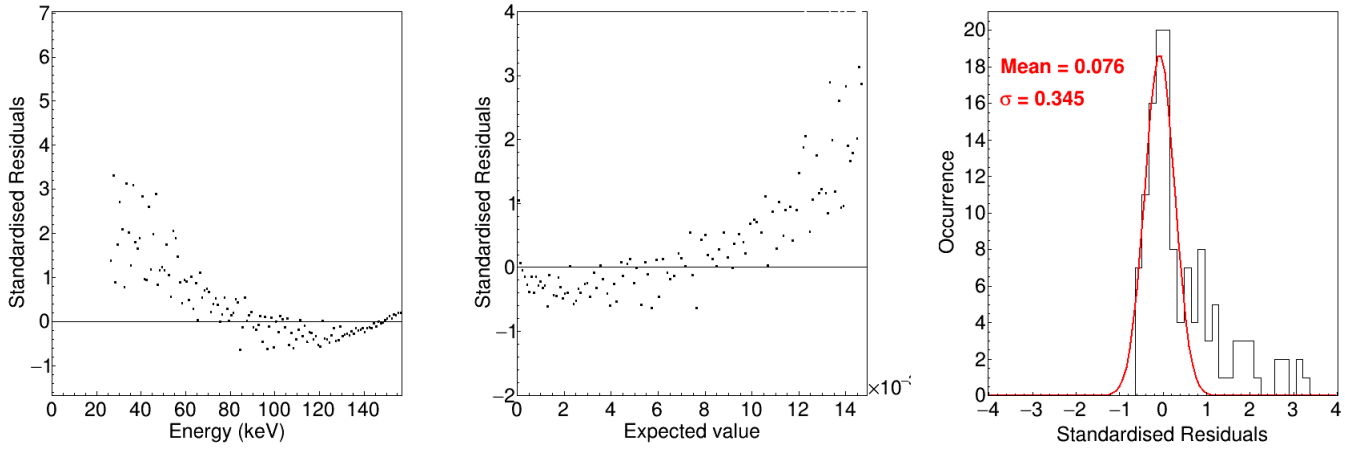

Figure 4.28 – Residuals between the unfolded spectrum and the adjusted spectrum in Figure 4.27.

For the extraction of the shape factors of other measured spectra, it is important to fix the same normalisation in order to compare the fit parameters. The normalisation is thus fixed to 0.955, in addition to $E_{\max}$. In the case of 2π measurement, the adjusted shape led to a β parameter of 0.429 (Figure 4.29) without being able to accurately reproduce the measured spectrum below 60 keV. The corresponding residuals are given in Figure 4.30, and the disagreement (1-R^2) is equal to 0.12% between the measured unfolded spectrum and the adjusted spectrum.

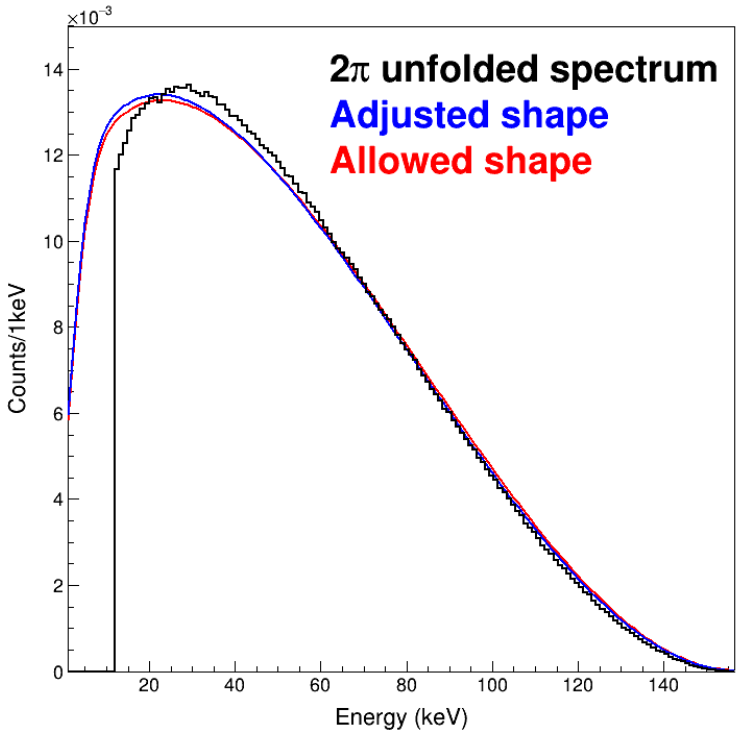

Figure 4.29 – The adjusted shape (blue) of ^{14}C for 2π unfolded spectrum for the extraction of shape factor. The allowed shape (red) is the initial spectrum.

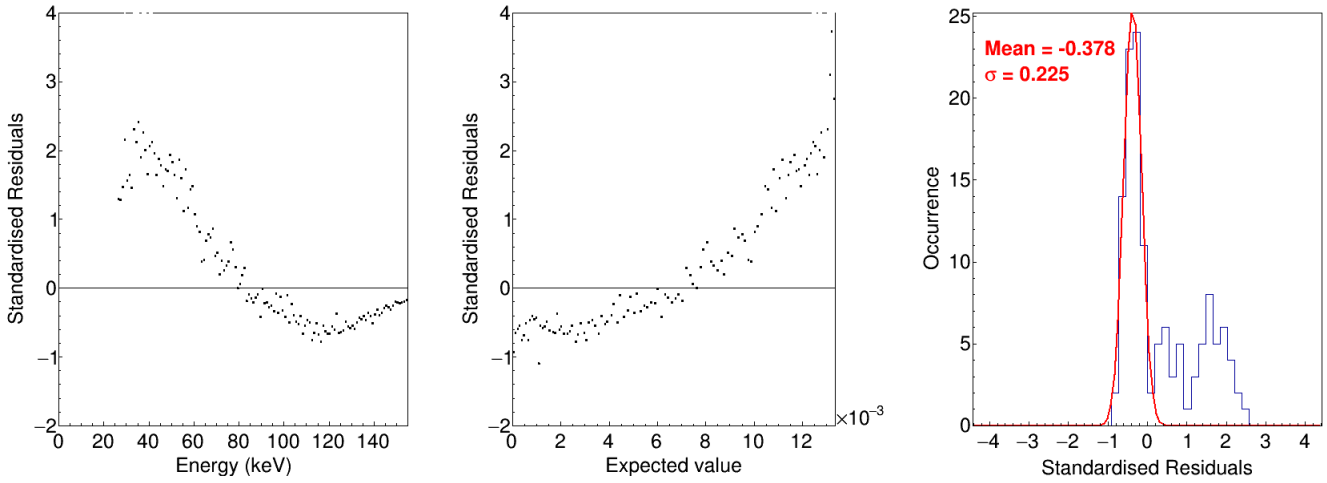

Figure 4.30 – Residuals between the unfolded spectrum and the adjusted spectrum in Figure 4.29.

The shape factor from MMC spectrum has also been extracted with the same procedure, fixing the normalisation to 0.955 (Figure 4.31). The best adjustment is obtained with a β value of 0.51. The residuals show the good quality of the adjustment (Figure 4.32) with a disagreement (1-R^2) of 0.04% between the MMC spectrum and the adjusted spectrum.

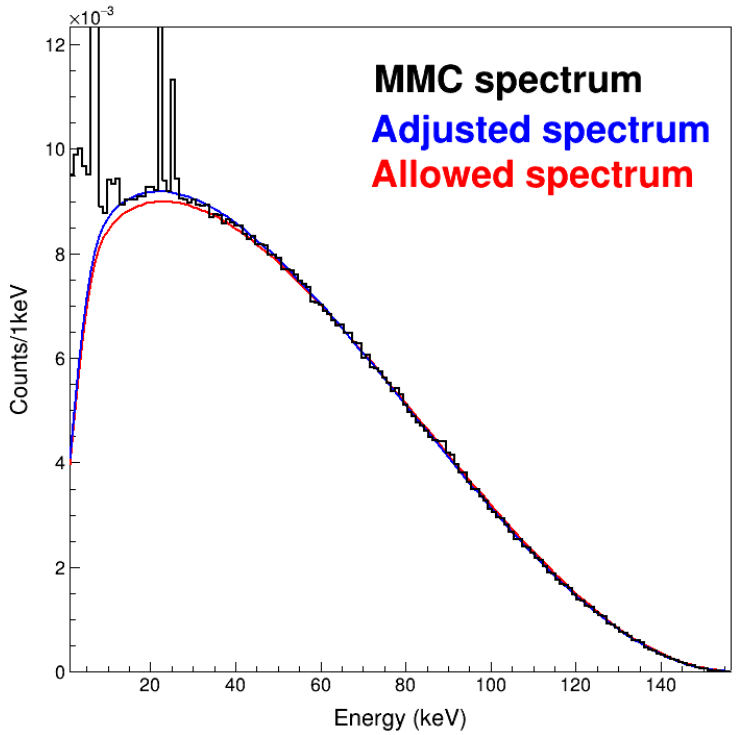

Figure 4.31 – The adjusted shape (blue) of ^{14}C for MMC measured spectrum to the extraction of shape factor. The allowed shape (red) is the initial spectrum.

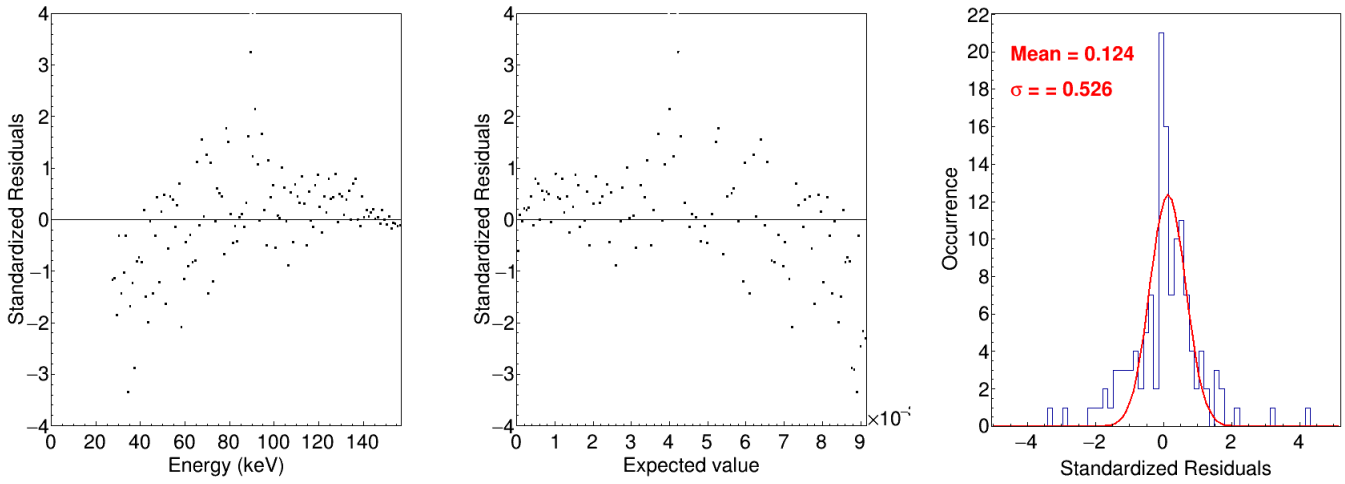

Figure 4.32 – Residuals between the MMC measured spectrum and the adjusted spectrum for ^{14}C decay.

The parameters of the extracted shape factors are listed in Table 4.1 and Figure 4.33 shows these shape factors calculated over the full energy range of the transition. The shape factors from quasi-4π, MMC, and 2π measurements are close to allowed shape with small distortion. The relative difference in the shape factor, between quasi-4π and MMC, is 3.6%, while it is 12% with 2π measurement.

The shape factor provided by Kuzminov is significantly different compared to the one obtained in this work. In Kuzminov's work, the experimental spectrum was measured using a gas proportional counter and the measurement was corrected for the remaining distortions based on a Monte Carlo simulation with the GEANT code in its 1994 version, and using a theoretical input spectrum. We now know that the accuracy of such a simulation for low-energy electron is questionable and this could well explain why Kuzminov's shape factor is so different. It is noteworthy that letting free the normalisation adjustment, C. Bisch found a β parameter very consistent with Kuzminov's result [4]. However, the deconvolution process was only preliminary and definitely not as robust as the one developed in the present work.

Work	Energy range (keV)	$E_{\max}$ (keV)	β (x 10^{-3}. keV^{-1})
This work	26-140	156.476	0.492
Kuzminov [133]	30-140	154.27	1.24 (4)
2π - 2014	26-140	156.476	0.429
MMC - 2018	26-140	156.476	0.51

Table 4.1 – Comparison of the different values for β in the parameterisation of the ^{14}C shape factor from Kuzminov. The values have been extracted from different measurements.

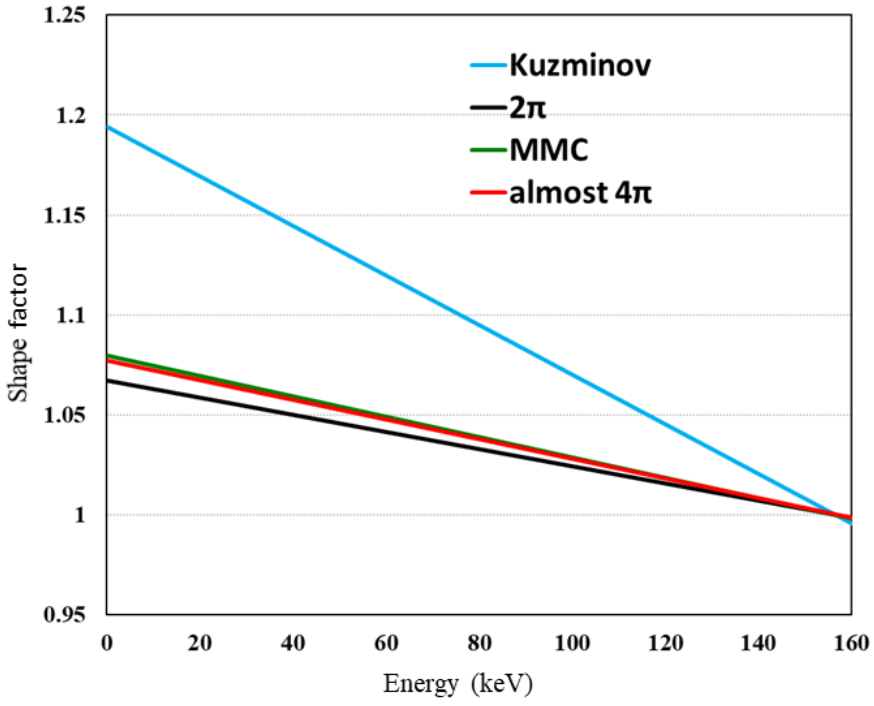

Figure 4.33 – The different shape factors of ^{14}C (Kuzminov, 2π, MMC and quasi-4π) extracted following the procedure described in the text. They are here extrapolated over the full entire energy range.

4.1.3.2 Technetium-99 decay

Second forbidden non-unique β transitions are very sensitive to the structure of the nuclei involved in the decay. For their theoretical calculation, precise nuclear wave functions are required to determine the nuclear matrix elements and nuclear models do not usually have sufficient accuracy. Recently, it has been observed that precise experimental half-lives and shape factors can constrain the theoretical estimates of these matrix elements [153]. Precise measurements of such β spectra are therefore crucial for testing the theoretical predictions. Only a few (almost) pure β decays exist that are second forbidden non-unique, among them ^{99}Tc decay.

As observed in the previous section, our spectrum of ^{99}Tc is in good agreement with Reich's result in the common energy range of the measurements. In order to extract the experimental shape factor, we have used the parameterisation given by Reich:

$$C(W) = q^2 + \lambda p^2 \tag{4.3}$$

for which he found $\lambda = 0.54$ [95].

In the fitting procedure, we have considered the initial shape as allowed and then adjusted the parameter to reach the unfolded spectrum. Of course, the global normalisation has to be adjusted in addition to λ. The energy range has been fixed between 26 keV and 260 keV. The adjusted shape of ^{99}Tc on our unfolded measured spectrum is shown in Figure 4.34. The normalisation parameter has converged to 2.288 and the corresponding λ value is given in Table 4.2. The adjusted shape is in good agreement with the unfolded measured spectrum with (1-R^2) equals 0.023% (Figure 4.35).

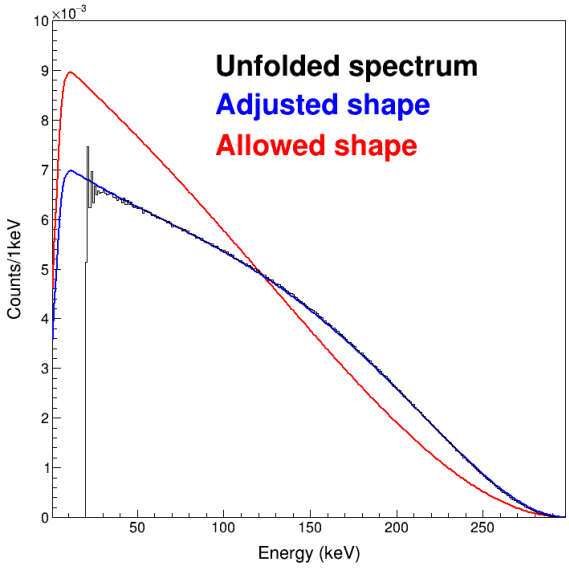

Figure 4.34 – The adjusted spectrum (blue) of ^{99}Tc for the extraction of shape factor. The allowed shape (red) gives the initial spectrum and the black spectrum is the unfolded measured spectrum.

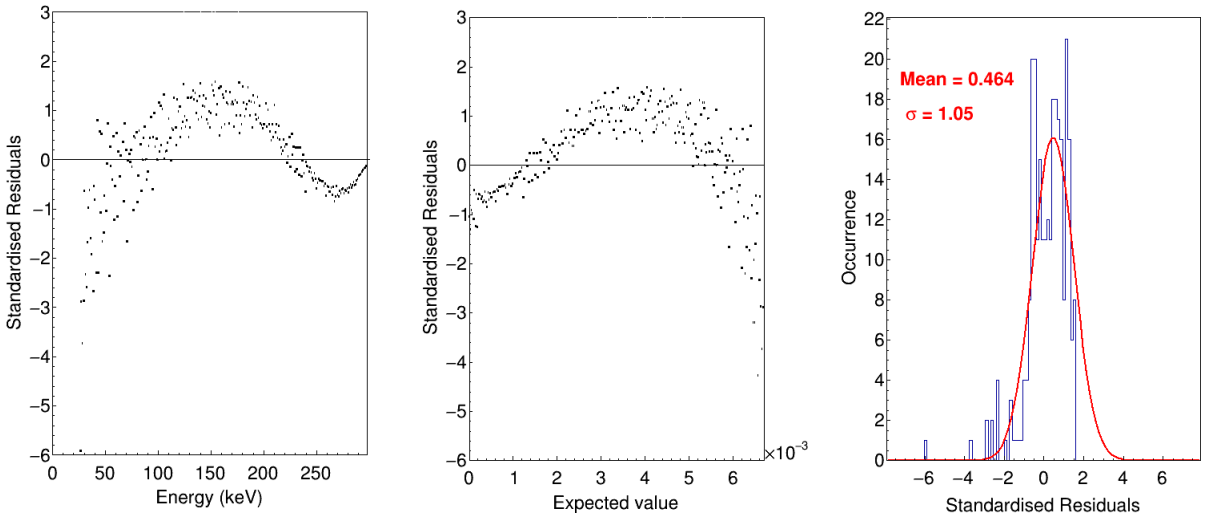

Figure 4.35 – Residuals between the unfolded measured spectrum of ^{99}Tc and the adjusted spectrum given in Figure 4.34.

In the case of 2π measurement, the normalisation has been fixed to 2.288 and the λ parameter obtained is given in Table 4.2 (see Figure 4.36). The residuals demonstrate the good agreement of the fit (see Figure 4.37). The same procedure has been performed for the MMC measured spectrum (see Figure 4.38 and 4.39).

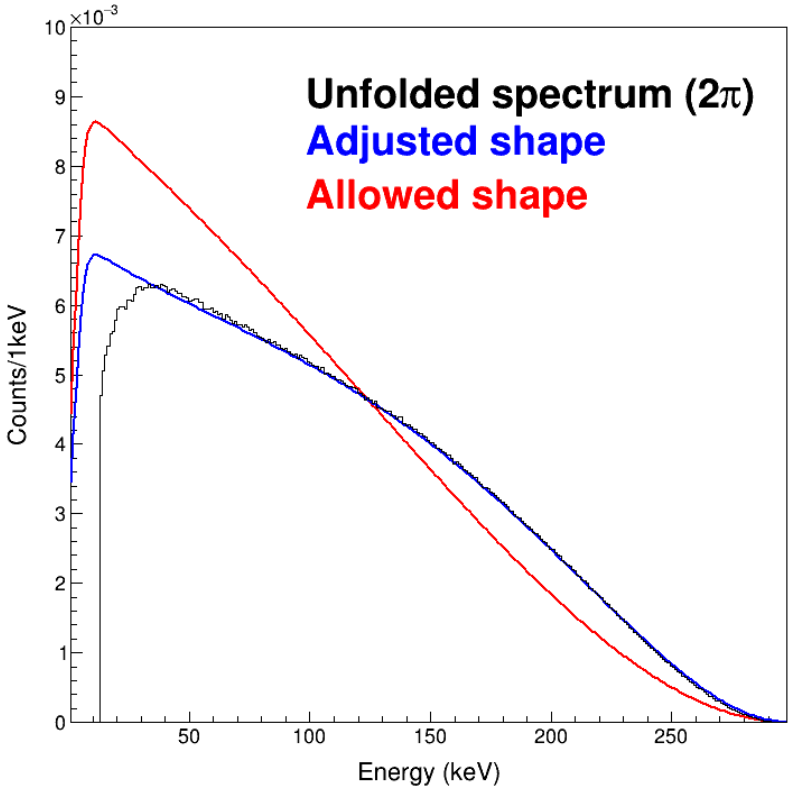

Figure 4.36 – The adjusted spectrum (blue) of ^{99}Tc for 2π measurement. The allowed shape (red) gives the initial spectrum and the black spectrum is the unfolded measured spectrum.

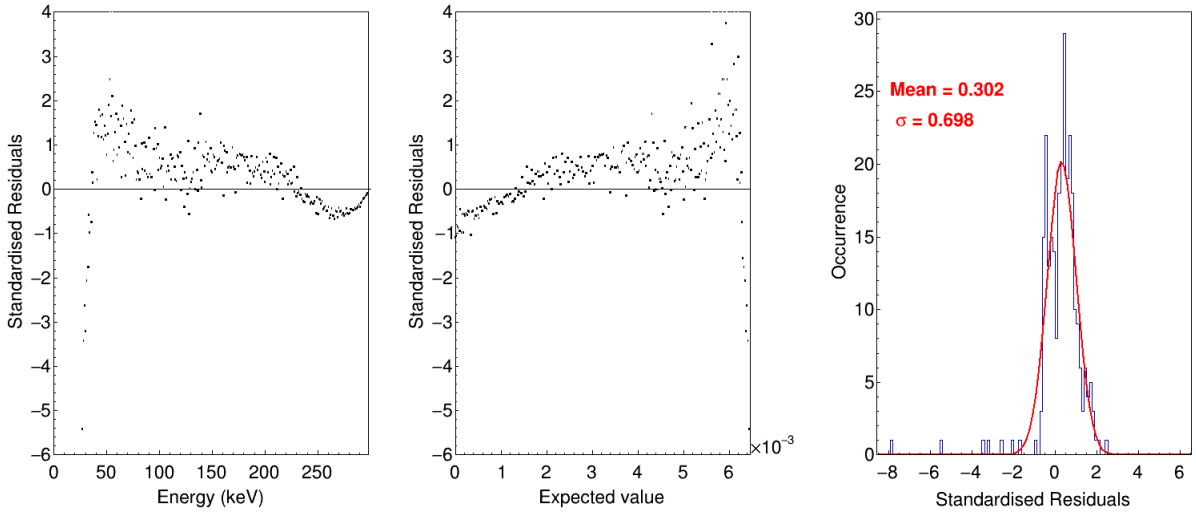

Figure 4.37 – Residuals between the unfolded measured spectrum of ^{99}Tc in 2π geometry and the adjusted spectrum given in Figure 4.36.

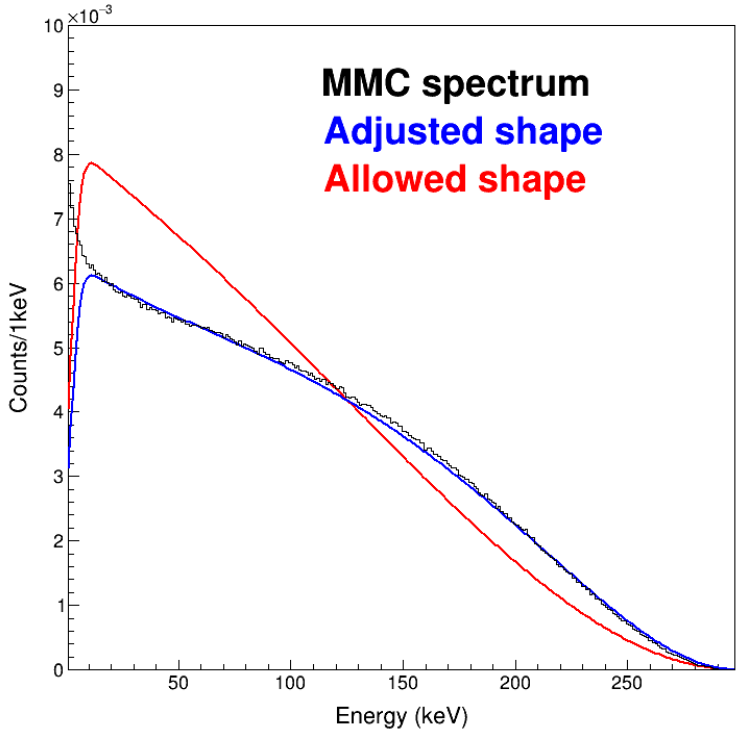

Figure 4.38 – The adjusted spectrum (blue) of ^{99}Tc for MMC measurement. The allowed shape (red) gives the initial spectrum and the black spectrum is the measured MMC spectrum.

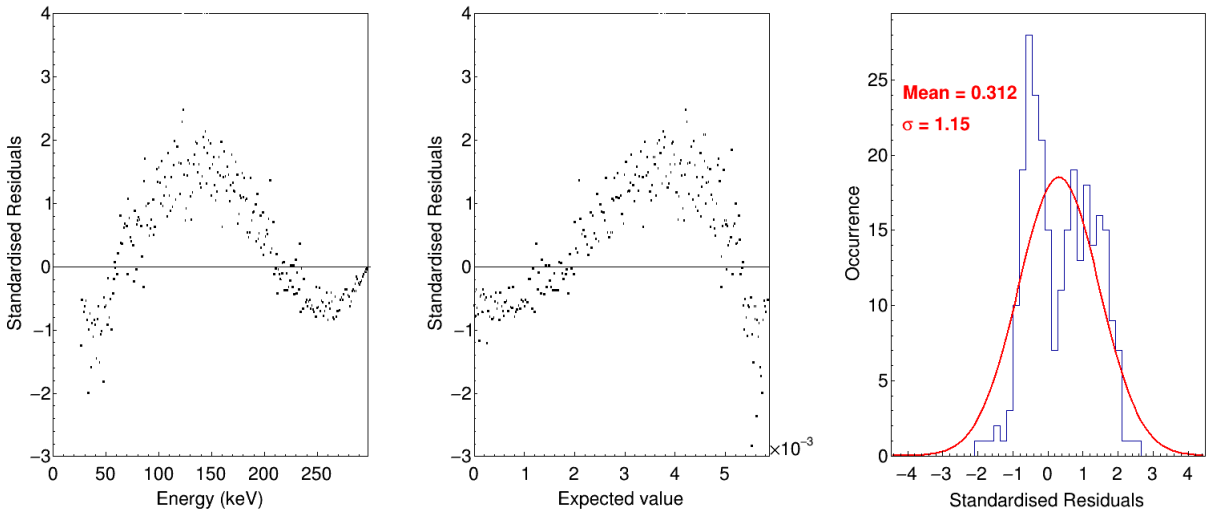

Figure 4.39 – Residuals between the MMC measurement of ^{99}Tc and the adjusted spectrum given in Figure 4.38.

The shape factors calculated using the values of λ in Table 4.2 are plotted in Figure 4.40. Even though they look close to each other, two categories are visible. The shape factor from this work (quasi-4π) is very close to the one from the MMC spectrum, with a relative difference of 1.2%, whereas it is of 5.36% with Reich's shape. Thanks to the high-precision MMC measurement and to the detailed study of the influence of the radioactive source preparation we performed, we can be confident about the accuracy of our result. However, it is clear from the different residuals that a non-linear contribution is still present, which means that Reich's parameterisation of the shape factor is not sufficient to accurately reproduce the measurements.

	Energy range (keV)	λ
This work	26-260	0.583
Reich [95]	55-250	0.54
2π - 2014	26-260	0.55
MMC - 2019	26-260	0.59

Table 4.2 – Comparison of different λ parameters as defined in the parameterisation of ^{99}Tc shape factor by Reich [95]. The values have been extracted from different measurements.

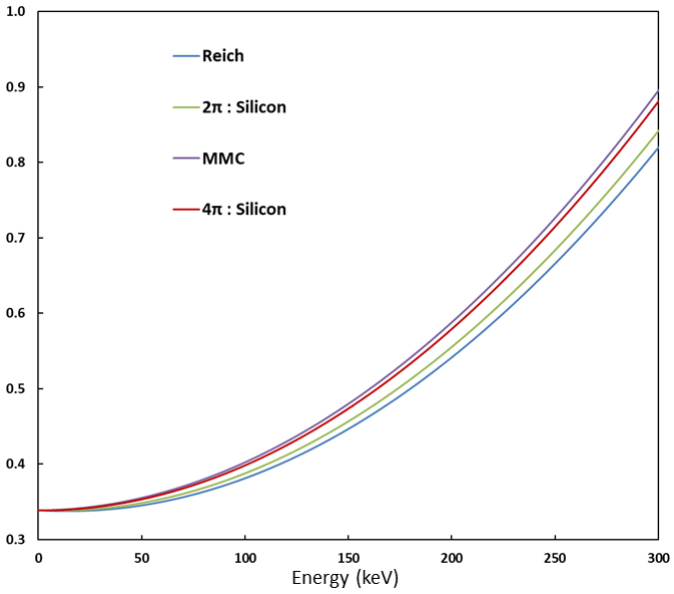

Figure 4.40 – The shape factors of ^{99}Tc extracted following the procedure described in the text and extrapolated over the full entire energy range.

4.1.3.3 Thallium-204 decay

First forbidden-unique transitions are simpler than forbidden non-unique and, in principle, they can be calculated theoretically with good accuracy. However, as for allowed transitions, their experimental validation is still crucial. We saw previously that our spectrum of ^{204}Tl is in good agreement with the experimental shape factor provided by Flothmann in the common energy range of the measurements (190 - 675 keV). To extract the shape factor, the parameterisation given by Flothmann [149] has been used:

$$C(W) = dq^2 + \lambda_2 p^2 \tag{4.4}$$

for which he found $d = 1.097$. The λ_2 parameter is determined from the Coulomb amplitudes of the electron wave functions, as discussed in chapter 1.

In the fitting procedure, the initial shape is considered as allowed and then the parameters are adjusted to reach the unfolded spectrum. The energy range is fixed between 70 keV and 760 keV and the λ_2 parameters, which are energy dependent, have been calculated following the procedure described by Behrens and Janecke in [154]. The adjusted spectrum shown in Figure 4.41 has been obtained by adjusting the global normalisation and the d parameter. The normalisation parameter has converged to 0.47 and the d value equals 1.12. The adjusted shape is in good agreement with (1-R^2), which equals 0.032% (Figure 4.42).

The shape factors from this work and from Flothmann are compared in Figure 4.43 and their excellent agreement in their common measured energy range is clear. The relative difference between the d parameters is of 2%.

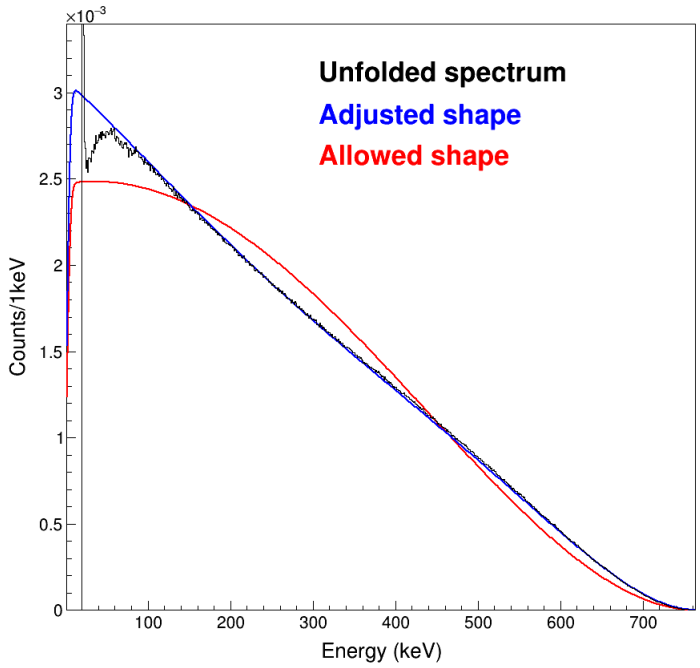

Figure 4.41 – The adjusted spectrum (blue) of ^{204}Tl for the extraction of shape factor between 70 keV and 760 keV. The allowed shape (red) gives the initial spectrum and the black spectrum is the unfolded measured spectrum.

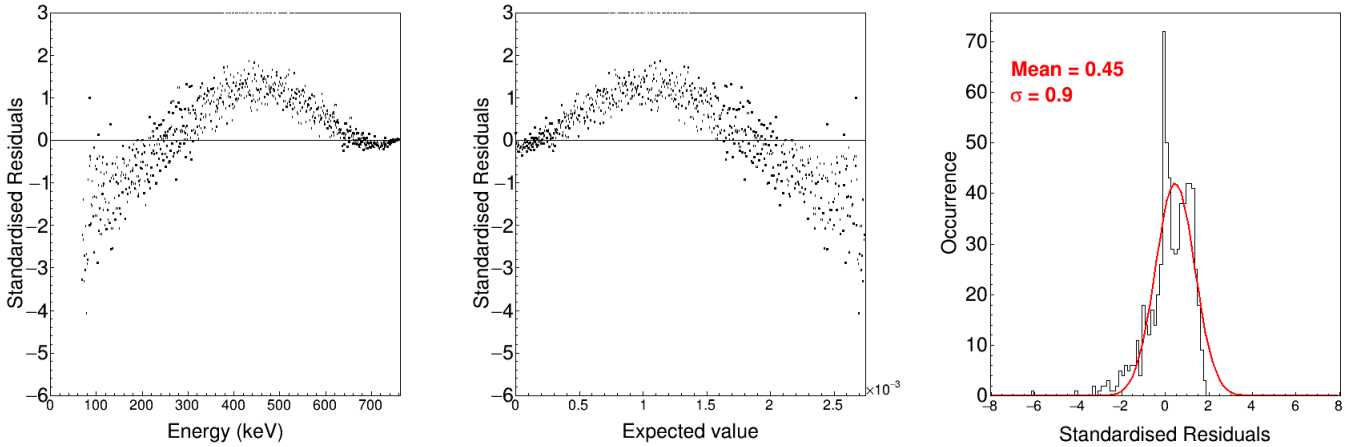

Figure 4.42 – Residuals between the adjusted spectrum and the unfolded measured spectrum given in Figure 4.41.

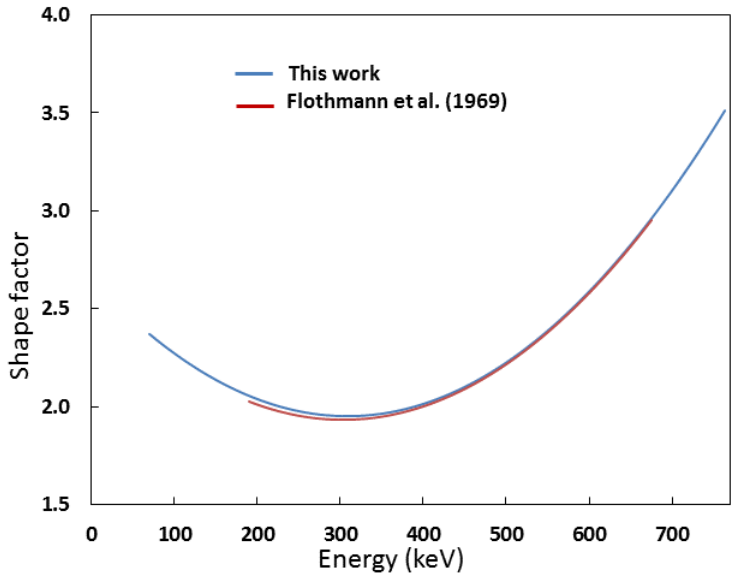

Figure 4.43 – The shape factors of ^{204}Tl extracted by fixing the energy range between 70 keV and 760 keV compared with the Flothmann's shape factor.

We also considered the typical parameterisation of the shape factor of a first forbidden-unique transition:

$$C(W) = q^2 + \lambda p^2 \tag{4.5}$$

The same energy range has been kept. The adjusted spectrum shown in Figure 4.44 has been obtained by adjusting the global normalisation and the λ parameter. The normalisation parameter has converged to 0.54 and the λ value equals 0.57. The adjusted shape is in good agreement with (1-R^2) which equals 0.012% (Figure 4.45).

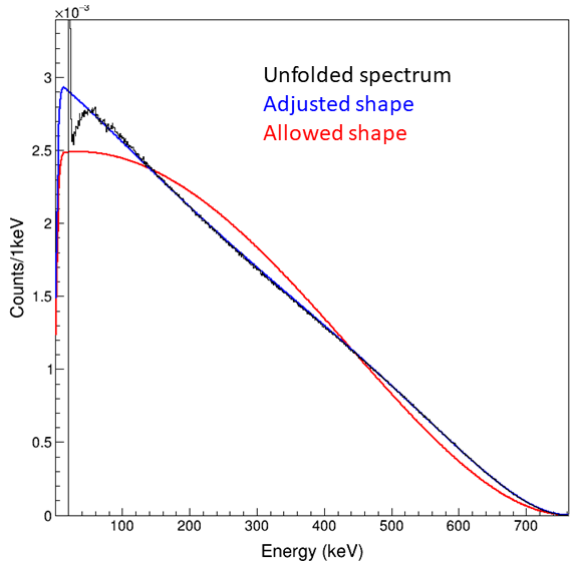

Figure 4.44 – The adjusted spectrum (blue) of ^{204}Tl for the extraction of shape factor between 70 keV and 760 keV. The allowed shape (red) gives the initial spectrum and the black spectrum is the unfolded measured spectrum.

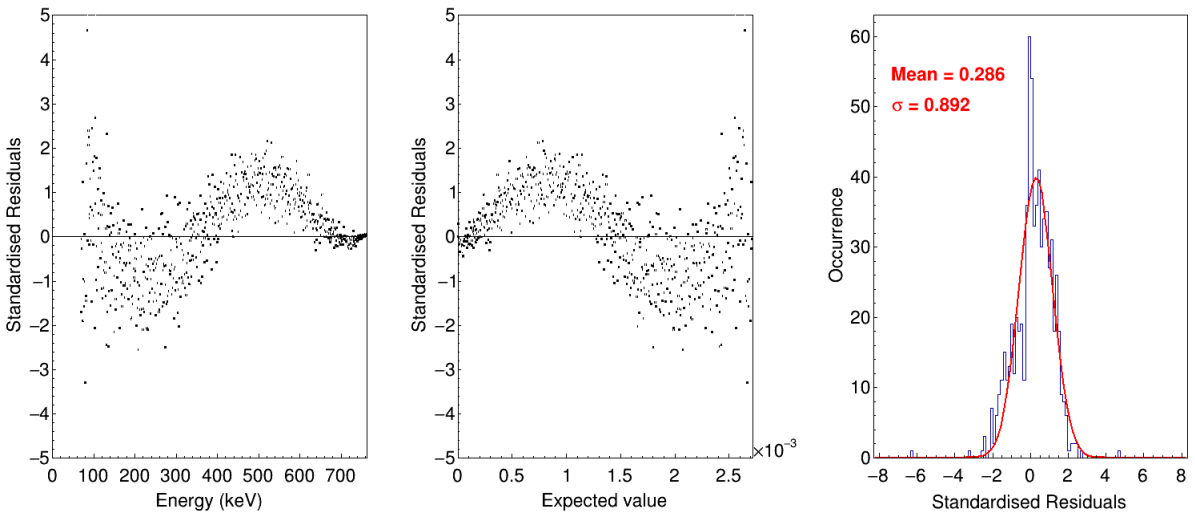

Figure 4.45 – Residuals between the adjusted spectrum and the unfolded measured spectrum given in Figure 4.44.

Another possibility is to start from a calculated first forbidden unique spectrum and to adjust a shape factor that highlights the distortion of the measured spectrum compared to what is expected from theory. For ^{204}Tl, we chose a correction factor as $C(W) = 1 + aW$ that quantifies the residual distortion in first order of the β particle energy. This correction has been applied to the initial spectrum and we obtained from the adjustment a global normalisation of 1.116 and $a = -0.067$ (see Figure 4.46). The residuals show excellent agreement with (1-R^2) which equals 0.024%. The value of the a parameter is consistent with results available in the literature for other first forbidden unique transitions [2]. This distortion could be explained by the influence of the atomic exchange effect. An analysis is ongoing to extract the a parameter starting from a first forbidden unique spectrum which includes such an atomic effect.

The shape factor from this work has been extracted between 70 keV and 760 keV, greatly extending the knowledge of ^{204}Tl β spectrum to the low energies compared with what exists in the literature. Two types of shape factors are provided, by reference to either an allowed shape or a first forbidden-unique shape.

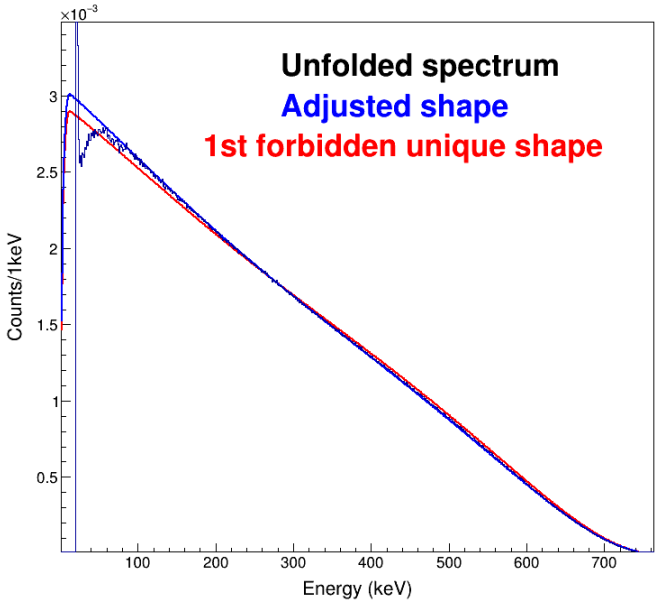

Figure 4.46 – The adjusted spectrum (blue) of ^{204}Tl for the extraction of shape factor between 70 keV and 760 keV. The first forbidden unique shape (red) gives the initial spectrum and the black spectrum is the unfolded measured spectrum.

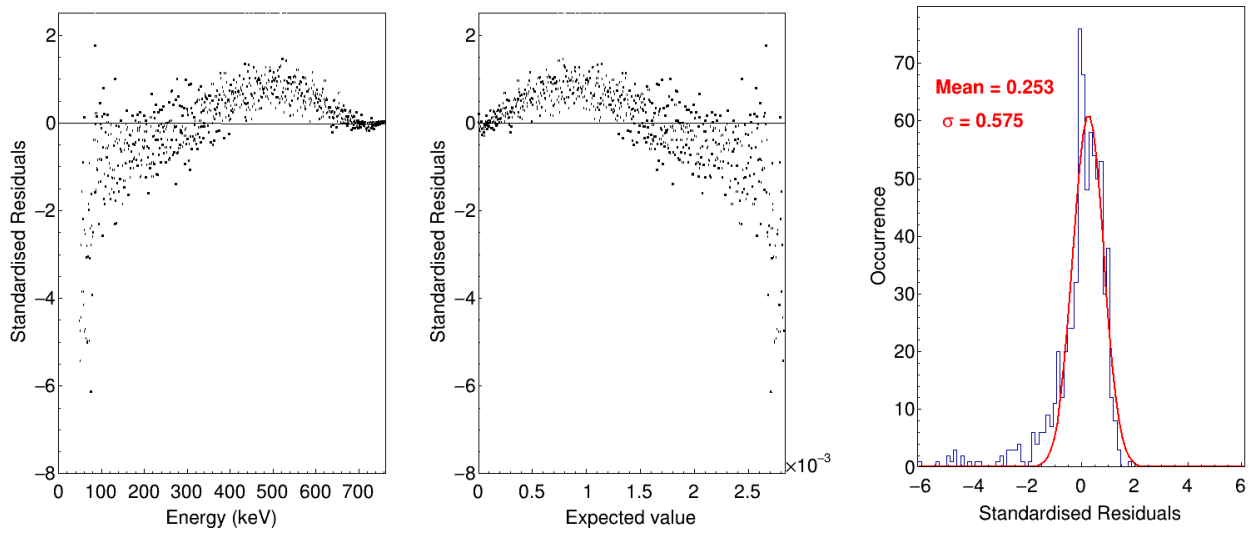

Figure 4.47 – Residuals between the adjusted spectrum and the unfolded measured spectrum given in Figure 4.46.

Conclusion

An unfolding process to remove the remaining distortions in the measured spectrum has been developed. The response function of the detection system has been built by using mono-energetic Monte Carlo simulations. Then, using the matrix inversion method, it has been applied to the measured spectrum.

The measured spectra of ^{14}C, ^{99}Tc and ^{204}Tl decays have been unfolded. The spectra we obtained for ^{14}C and ^{99}Tc decays have been compared with the high-precision MMC measure-

ments and excellent agreement has been found in both cases. This comparison validates the quality of our measurements and the precision of our PENELOPE simulations.

The small, remaining discrepancy between our final ^{99}Tc spectrum and the MMC spectrum can be explained by the use of Monte Carlo simulations for the deconvolution process. Even though the modelling of PENELOPE is exact, it can still cause a bias. In addition, the statistical fluctuations of both measurements may also introduce a very small difference.

The unfolded spectrum of ^{204}Tl has been found to be in excellent agreement with Flothmann's shape in the common energy range of the measurements (190 - 675 keV), and this work provides an extended experimental shape factor between 70 keV and 760 keV. Our result has been compared with a precisely calculated theoretical spectrum taking into account exchange and screening effect and its excellent agreement clearly demonstrates that our measurements are adequately precise to show sensitivity towards atomic effects.

The experimental shape factors of the three radionuclides have been extracted for quasi-4π, 2π and MMC measurements. This allowed us to compare the resulting shape factors from different experiments. The shape factor of ^{14}C from quasi-4π has found be close to MMC measurement but not to the Kuzminov's shape factor. It gives a new reference to the shape of ^{14}C. The shape factors of ^{99}Tc from quasi-4π, MMC, 2π and Reich are consistent among each other within the common energy range of the measurements. With a minimum energy divided by a factor of two compared to Reich's measurement, we have been able to validate the low energy shape found by the MMC measurement that disagrees with the extrapolation of Reich's shape factor below 55 keV. The shape factor of ^{204}Tl has been extracted in three ways, one starting from allowed shape using the parameterisation of Flothmann, second using the typical forbidden-unique shape and the third from first forbidden unique shape. The minimum energy of our result is lower by a factor of three compared to Flothmann's result.

Conclusion and perspectives

The accurate knowledge of the β spectrum shape has served a vast scientific community since the 1940s. For the past ten years, the β spectral studies have known a resurgence of interest. Indeed, it has played an essential role in the understanding of the weak interaction in fundamental physics. Nowadays, it contributes in radionuclide metrology to reduce uncertainties in activity measurements using the liquid scintillation counting method, it brings crucial information to advancements in nuclear medicine, and an increasing demand from the nuclear energy field has been observed in order to enrich the existing databases. A detailed review of the needs of the different users has been carried out in the chapter 1. Improvements of experimental techniques, increasing precision of Monte Carlo simulations and continuous growth of computing power allows revisiting our experimental and theoretical understanding of the β spectra.

At LNHB, a new experimental technique, called metallic magnetic calorimetry, has been developed over the past ten years for very low energy β decays and the first results have made possible to understand some subtle atomic effects, usually neglected. This technique is challenging to implement and is inherently limited to low energy spectra, with end-point energies less than 500 keV, and to very low count rates, about 10 per second. Another complementary technique is therefore required. Thus, the development of a device with a single silicon detector had been implemented in the past. However, the resulting spectra with a less than 2π solid angle suffered from partial energy deposition of the electrons and did not meet the metrological requirements in terms of precision.

This thesis work aimed to develop a new experimental device dedicated to the measurement of β spectra with metrological precision. An experimental set-up based on silicon detectors in an almost 4π solid angle has been developed. This system is adaptable to different types of silicon detectors, PIPS and Si(Li). A detailed study using PENELOPE Monte Carlo simulations was performed in order to minimise the distortions due to geometry and to design the apparatus with the best possible configuration. The experimental device was upgraded by performing several cycles of measurements, improving the set-up after each series of analysis, as discussed in detail in chapter 3. Thanks to the implementation of temperature monitoring, we proved that the cooling system developed in the past was not sufficient for the use of Si(Li) detectors. After upgrading, we observed that, even though the PIPS detectors are operational at room temperature, cooling them at 100 K improves their performances, with an energy resolution

decreased from 12 to 9 keV. Using Monte Carlo simulations, the influence of the radioactive source on the measured spectrum shape has been studied in minute details, something poorly addressed in the literature. The impact of using a 0.7 μm thick Mylar® film as support instead of a more traditional 18 μm thick film have been quantified. Different preparation techniques of the sources and their influence has also been studied. The impact of the crystallisation process has been demonstrated: a solution without carrier salt combined with a freeze-drying process drastically reduces the distortion due to self-absorption, thus helping to improve the measurements.

In this work, four β decaying radionuclides have been studied: ^{14}C, ^{99}Tc, ^{36}Cl and ^{204}Tl. The measured spectra have been compared to the corresponding PENELOPE simulations. The observed inconsistency in the case of measurements at room temperature led to the investigation of the actual geometrical configuration. Varying the distance between the detectors in the simulations, we concluded that the copper pieces had not been machined as precisely as expected at the beginning and that the distance was not 3 mm as designed but 2.5 mm. This fact was also confirmed by direct measurement, and the influence of a precisely known geometry on the spectrum shapes was quantified. The measurement of conversion electron peaks from ^{109}Cd and ^{207}Bi decays allowed us to characterise the detectors from 25 keV to 1060 keV. The final energy threshold was found to be 15 keV and the energy resolution was determined to be 9 keV at 62.5 keV. Standardised residuals have been defined and their analysis, combined with the disagreement parameter $(1 - R^2)$, was used to quantify the excellent agreement between measurements and simulations.

The remaining distortions that were found to be still present on the measured spectra have been corrected in order to retrieve the actual spectra initially emitted from the radionuclides. A deconvolution method based on Monte Carlo simulations has been developed. The response function was built using mono-energetic Monte Carlo simulations. The method has been validated by applying it on simulated spectra: we were able to retrieve the initial input spectra down to at least 10 keV. However, some tests could be performed to go beyond the needs of the present work, such as increasing the statistics of mono-energetic simulations and lowering the binning of the response function. The comparison of some accurate spectra from our quasi-4π detection system with high-precision measurements from metallic magnetic calorimetry (MMC) demonstrated that we could carry out precise studies with our apparatus starting from 30 keV to the end-point energies.

The shape factors have then been extracted from the spectra of ^{14}C, ^{99}Tc and ^{204}Tl decays measured with quasi-4π geometry, and with 2π geometry and MMC when existing. The results have been compared among each other and with results available in the literature. For ^{14}C, the shape was found to be close to regularly allowed transition, perfectly consistent with the high-precision MMC measurement. These results provide a new reference shape of ^{14}C spectrum. For ^{99}Tc, the shape factor from quasi-4π and MMC measurements are in excellent

agreement with each other. An analysis available in the literature was also performed with silicon detectors 45 years ago above 55 keV, and good agreement was found with this result in the common energy range. A detailed study of self-absorption depending on the source preparation technique employed was necessary to ensure an accurate result down to 26 keV. The shape factor extracted for ^{204}Tl from this work shows good agreement with results available in the literature. Comparison with theoretical spectra also highlighted better agreement when considering calculations that include atomic effects, demonstrating the sensitivity of our measurement. All these comparisons of our measured spectra with MMC spectra and results in the literature validate our experimental approach. With silicon detectors arranged in a quasi-4π configuration, many more radionuclides can be measured compared with MMC apparatus, obviously not with similar energy resolution and threshold. The two techniques are definitely complementary for precise β spectrometry studies.

Although our apparatus has been refined by numerous studies and upgrades, there are still some remaining subjects to be considered further. An excellent study of ^{36}Cl decay is still missing. A radioactive source with the smallest possible crystals is still needed to be prepared and measured. As we have already seen that even the freeze-drying technique is not sufficient, a new preparation method must be developed to make a source whose quality fulfils our requirements. It would then be possible to compare with experimental shape factors available in the literature.

We have started to adapt our quasi-4π detection system to two Si(Li) detectors of 5 mm thickness in place of the PIPS detectors. This detection system has already been designed, machined and implemented, and the detectors remain to be tested and characterised. The detectors are larger than the PIPS (500 mm^2 instead of 300 mm^2), and their holders have been adapted. The corresponding electronics inside the chamber has also been improved with stronger connections. Along with the coaxial cables, the whole device requires more space than the PIPS set-up inside the chamber, a cube with external dimensions of 170 mm $\times$ 170 mm $\times$ 170 mm. The whole Si(Li) set-up cannot be securely handled, and a new vacuum chamber should be considered in the future. It would also allow using more detectors in series for higher energy measurements, in a $\Delta E - E$ telescope configuration, or for coincidence measurements with γ-ray detectors.

The results of this study showed excellent agreement with MMC measurements, which are highly precise. To further improve the precision, one can consider for instance a complete 4π measurement with the radionuclide deposited on a silicon wafer and a second wafer glued on the first one, in a sandwich configuration. In this case, silicon wafers with the lowest possible dead layer will be needed, together with excellent radioactive deposition to avoid self-absorption. Such a technique will be expensive as the detectors will not be reusable for another radionuclide. Nevertheless, it would allow testing a complete 4π configuration with silicon detectors and very precise comparison with the spectra from MMC and quasi-4π devices.

"What is now achieved was once only dreamed; everything is impossible until its done."

- Abhilasha

Bibliography

[1] K. Kossert and X. Mougeot, "The importance of the beta spectrum calculation for accurate activity determination of ^{63}Ni by means of liquid scintillation counting," *Applied Radiation and Isotopes*, vol. 101, pp. 40 – 43, 2015.

[2] X. Mougeot, "Reliability of usual assumptions in the calculation of β and ν spectra," *Phys. Rev. C*, vol. 91, p. 055504, 2015.

[3] X. Mougeot and C. Bisch, "Consistent calculation of the screening and exchange effects in allowed β^- transitions," *Phys. Rev. A*, vol. 90, p. 012501, 2014.

[4] C. Bisch, *Étude de la forme des spectres β*. PhD thesis, 2014.

[5] M.-M. Bé, R. Helmer, and V. Chisté, "The "NUCLÉIDE" database for decay data and the "international decay data evaluation project"," *Journal of Nuclear Science and Technology*, vol. 39, pp. 481–484, 2002.

[6] M. A. Kellett and O. Bersillon, "The decay data evaluation project (DDEP) and the JEFF-3.3 radioactive decay data library: Combining international collaborative efforts on evaluated decay data," *EPJ Web of Conferences*, vol. 146, p. 02009, 2017.

[7] M.-M. Bé, V. Chisté, C. Dulieu, E. Browne, V. Chechev, N. Kuzmenko, R. Helmer, A. Nichols, E. Schönfeld, and R. Dersch, *Table of Radionuclides*, vol. 1 of *Monographie BIPM-5*. Pavillon de Breteuil, F-92310 Sèvres, France: Bureau International des Poids et Mesures, 2004.

[8] M.-M. Bé, V. Chisté, C. Dulieu, E. Browne, C. Baglin, V. Chechev, N. Kuzmenko, R. Helmer, F. Kondev, D. MacMahon, and K. Lee, *Table of Radionuclides*, vol. 3 of *Monographie BIPM-5*. Pavillon de Breteuil, F-92310 Sèvres, France: Bureau International des Poids et Mesures, 2006.

[9] M.-M. Bé, V. Chisté, C. Dulieu, E. Browne, V. Chechev, N. Kuzmenko, F. Kondev, A. Luca, M. Galán, A. Pearce, and X. Huang, *Table of Radionuclides*, vol. 4 of *Monographie BIPM-5*. Pavillon de Breteuil, F-92310 Sèvres, France: Bureau International des Poids et Mesures, 2008.

[10] M.-M. Bé, V. Chisté, C. Dulieu, X. Mougeot, E. Browne, V. Chechev, N. Kuzmenko, F. Kondev, A. Luca, M. Galán, A. Nichols, A. Arinc, and X. Huang, *Table of Radionuclides*, vol. 5 of *Monographie BIPM-5*. Pavillon de Breteuil, F-92310 Sèvres, France: Bureau International des Poids et Mesures, 2010.

[11] M.-M. Bé, V. Chisté, C. Dulieu, M. Kellett, X. Mougeot, A. Arinc, V. Chechev, N. Kuzmenko, T. Kibédi, A. Luca, and A. Nichols, *Table of Radionuclides*, vol. 8 of *Monographie BIPM-5*. Pavillon de Breteuil, F-92310 Sèvres, France: Bureau International des Poids et Mesures, 2016.

[12] R. Broda, P. Cassette, and K. Kossert, "Radionuclide metrology using liquid scintillation counting," *Metrologia*, vol. 44, no. 4, pp. S36–S52, 2007.

[13] K. Kossert, J. Marganiec-Gazka, X. Mougeot, and O. J. Nähle, "Activity determination of ^{60}Co and the importance of its beta spectrum," *Applied Radiation and Isotopes*, vol. 134, pp. 212 – 218, 2018. ICRM 2017 Proceedings of the 21st International Conference on Radionuclide Metrology and its Applications.

[14] M. Bardies and J. F. Chatal, "Absorbed doses for internal radiotherapy from 22 beta-emitting radionuclides: beta dosimetry of small spheres," *Physics in Medicine and Biology*, vol. 39, no. 6, pp. 961–981, 1994.

[15] L. Jødal, "Beta emitters and radiation protection," *Acta Oncologica*, vol. 48, no. 2, pp. 308–313, 2009.

[16] A. I. Kassis, "Radiotargeting agents for cancer therapy," *Expert Opinion on Drug Delivery*, vol. 2, no. 6, pp. 981–991, 2005. PMID: 16296803.

[17] A. I. Kassis, "The amazing world of Auger electrons," *International Journal of Radiation Biology*, vol. 80, no. 11-12, pp. 789–803, 2004.

[18] M. Gupta, M. A. Kellett, A. L. Nichols, and O. Bersillon, "Decay heat calculations: Assessment of fission product decay data requirements for Th/U fuel," *IAEA, Nuclear Data Section, INDC(NDS)-0577*, 2010.

[19] J. Hardy, L. Carraz, B. Jonson, and P. Hansen, "The essential decay of pandemonium: A demonstration of errors in complex beta-decay schemes," *Phys. Rev. B*, vol. 71, no. 2, pp. 307 – 310, 1977.

[20] R. Greenwood, R. Helmer, M. Lee, M. Putnam, M. Oates, D. Struttmann, and K. Watts, "Total absorption gamma-ray spectrometer for measurement of beta-decay intensity distributions for fission product radionuclides," *Nuclear Instruments and Methods in Physics Research Section A: Accelerators, Spectrometers, Detectors and Associated Equipment*, vol. 314, no. 3, pp. 514–540, 1992.

[21] R. Greenwood, R. Helmer, M. Putnam, and K. Watts, "Measurement of β–decay intensity distributions of several fission-product isotopes using a total absorption γ-ray spectrometer," *Nuclear Instruments and Methods in Physics Research Section A: Accelerators, Spectrometers, Detectors and Associated Equipment*, vol. 390, no. 1-2, pp. 95–154, 1997.

[22] R. Helmer, "Erratum to - methodology for the measurement of β–decay intensity distributions from the analysis of total absorption γ-ray spectra," *Nuclear Instruments and Methods in Physics Research Section A: Accelerators, Spectrometers, Detectors and Associated Equipment 351 (1993) 406-422*, vol. 361, no. 3, p. 628, 1995.

[23] V. Guadilla, A. Algora, J. L. Tain, J. Agramunt, D. Jordan, A. Montaner-Pizá, S. E. A. Orrigo, B. Rubio, E. Valencia, J. Suhonen, O. Civitarese, J. Äystö, J. A. Briz, A. Cucoanes, T. Eronen, M. Estienne, M. Fallot, L. M. Fraile, E. Ganioğlu, W. Gelletly, D. Gorelov, J. Hakala, A. Jokinen, A. Kankainen, V. Kolhinen, J. Koponen, M. Lebois, T. Martinez, M. Monserrate, I. Moore, E. Nácher, H. Penttilä, I. Pohjalainen, A. Porta, J. Reinikainen, M. Reponen, S. Rinta-Antila, K. Rytkönen, T. Shiba, V. Sonnenschein, A. A. Sonzogni, V. Vedia, A. Voss, J. N. Wilson, and A.-A. Zakari-Issoufou, "Experimental study of ^{100}Tc β decay with total absorption γ-ray spectroscopy," *Phys. Rev. C*, vol. 96, p. 014319, 2017.

[24] V. Guadilla, A. Algora, J. L. Tain, J. Agramunt, J. Äystö, J. A. Briz, A. Cucoanes, T. Eronen, M. Estienne, M. Fallot, L. M. Fraile, E. Ganioğlu, W. Gelletly, D. Gorelov, J. Hakala, A. Jokinen, D. Jordan, A. Kankainen, V. Kolhinen, J. Koponen, M. Lebois, L. Le Meur, T. Martinez, M. Monserrate, A. Montaner-Pizá, I. Moore, E. Nácher, S. E. A. Orrigo, H. Penttilä, I. Pohjalainen, A. Porta, J. Reinikainen, M. Reponen, S. Rinta-Antila, B. Rubio, K. Rytkönen, P. Sarriguren, T. Shiba, V. Sonnenschein, A. A. Sonzogni, E. Valencia, V. Vedia, A. Voss, J. N. Wilson, and A.-A. Zakari-Issoufou, "Total absorption γ-ray spectroscopy of niobium isomers," *Phys. Rev. C*, vol. 100, p. 024311, 2019.

[25] G. Rudstam and K. Aleklett, "Average beta and gamma energies of fission products," tech. rep., NFL-7 (The Studsvik Science Research Laboratory), 1979.

[26] A. Nichols, "Beta-decay and decay heat," *IAEA, Nuclear Data Section, INDC(NDS)-0483*, 2005.

[27] B. Ulmen, P. D. Desai, S. Moghaddam, G. H. Miley, and R. I. Masel, "Development of diode junction nuclear battery using ^{63}Ni," *Journal of Radioanalytical and Nuclear Chemistry*, vol. 282, no. 2, p. 601, 2009.

[28] C. E. Munson, M. Arif, J. Streque, S. Belahsene, A. Martinez, A. Ramdane, Y. E. Gmili, J.-P. Salvestrini, P. L. Voss, and A. Ougazzaden, "Model of Ni-63 battery with realistic PIN structure," *Journal of Applied Physics*, vol. 118, no. 10, p. 105101, 2015.

[29] A. Svintsov, A. Krasnov, M. Polikarpov, A. Polyakov, and E. Yakimov, "Betavoltaic battery performance: Comparison of modeling and experiment," *Applied Radiation and Isotopes*, vol. 137, pp. 184 – 189, 2018.

[30] E. Yakimov, M. Polikarpov, and A. Krasnov, "Prediction of betavoltaic battery output parameters based on SEM measurements," *Journal of Nano- and Electronic Physics*, vol. 8, pp. 04062–1, 2016.

[31] A. Belghachi, K. Bozkurt, H. Moughli, O. Özdemir, B. Amiri, and A. Talhi, "A model for Ni-63 source for betavoltaic application," 2019.

[32] N. A. Kuruoğlu, O. Özdemir, and K. Bozkurt, "Betavoltaic study of a GaN p-i-n structure grown by metal-organic vapour phase epitaxy with a Ni-63 source," *Thin Solid Films*, vol. 636, pp. 746–750, 2017.

[33] Y. R. Uhm, B. G. Choi, J. B. Kim, D.-H. Jeong, and K. J. Son, "Study of a beta-voltaic battery using electroplated Nickel-63 on Nickel foil as a power source," *Nuclear Engineering and Technology*, vol. 48, no. 3, pp. 773 – 777, 2016.

[34] S. M. Namee, "Fabrication of a gap nanowire betavoltaic device using ^{63}Ni," Master's thesis, 2018.

[35] N. Severijns, M. Beck, and O. Naviliat-Cuncic, "Tests of the standard electroweak model in nuclear beta decay," *Rev. Mod. Phys.*, vol. 78, pp. 991–1040, 2006.

[36] J. C. Hardy and I. S. Towner, "Superallowed $0^+ \to 0^+$ nuclear β decays: 2014 critical survey, with precise results for V_{ud} and CKM unitarity," *Phys. Rev. C*, vol. 91, p. 025501, 2015.

[37] T. A. Mueller, D. Lhuillier, M. Fallot, A. Letourneau, S. Cormon, M. Fechner, L. Giot, T. Lasserre, J. Martino, G. Mention, A. Porta, and F. Yermia, "Improved predictions of reactor antineutrino spectra," *Phys. Rev. C*, vol. 83, p. 054615, 2011.

[38] G. Mention, M. Fechner, T. Lasserre, T. A. Mueller, D. Lhuillier, M. Cribier, and A. Letourneau, "Reactor antineutrino anomaly," *Phys. Rev. D*, vol. 83, p. 073006, 2011.

[39] F. P. An, A. B. Balantekin, H. R. Band, M. Bishai, S. Blyth, D. Cao, G. F. Cao, J. Cao, W. R. Cen, Y. L. Chan, J. F. Chang, L. C. Chang, Y. Chang, H. S. Chen, Q. Y. Chen, S. M. Chen, Y. X. Chen, Y. Chen, J.-H. Cheng, J. Cheng, Y. P. Cheng, Z. K. Cheng, J. J. Cherwinka, M. C. Chu, A. Chukanov, J. P. Cummings, J. de Arcos, Z. Y. Deng, X. F. Ding, Y. Y. Ding, M. V. Diwan, M. Dolgareva, J. Dove, D. A. Dwyer, W. R. Edwards, R. Gill, M. Gonchar, G. H. Gong, H. Gong, M. Grassi, W. Q. Gu, M. Y. Guan, L. Guo, R. P. Guo, X. H. Guo, Z. Guo, R. W. Hackenburg, R. Han, S. Hans, M. He, K. M. Heeger,

Y. K. Heng, A. Higuera, Y. K. Hor, Y. B. Hsiung, B. Z. Hu, T. Hu, W. Hu, E. C. Huang, H. X. Huang, X. T. Huang, P. Huber, W. Huo, G. Hussain, D. E. Jaffe, P. Jaffke, K. L. Jen, S. Jetter, X. P. Ji, X. L. Ji, J. B. Jiao, R. A. Johnson, D. Jones, J. Joshi, L. Kang, S. H. Kettell, S. Kohn, M. Kramer, K. K. Kwan, M. W. Kwok, T. Kwok, T. J. Langford, K. Lau, L. Lebanowski, J. Lee, J. H. C. Lee, R. T. Lei, R. Leitner, C. Li, D. J. Li, F. Li, G. S. Li, Q. J. Li, S. Li, S. C. Li, W. D. Li, X. N. Li, Y. F. Li, Z. B. Li, H. Liang, C. J. Lin, G. L. Lin, S. Lin, S. K. Lin, Y.-C. Lin, J. J. Ling, J. M. Link, L. Littenberg, B. R. Littlejohn, D. W. Liu, J. L. Liu, J. C. Liu, C. W. Loh, C. Lu, H. Q. Lu, J. S. Lu, K. B. Luk, Z. Lv, Q. M. Ma, X. Y. Ma, X. B. Ma, Y. Q. Ma, Y. Malyshkin, D. A. M. Caicedo, K. T. McDonald, R. D. McKeown, I. Mitchell, M. Mooney, Y. Nakajima, J. Napolitano, D. Naumov, E. Naumova, H. Y. Ngai, Z. Ning, J. P. Ochoa-Ricoux, A. Olshevskiy, H.-R. Pan, J. Park, S. Patton, V. Pec, J. C. Peng, L. Pinsky, C. S. J. Pun, F. Z. Qi, M. Qi, X. Qian, N. Raper, J. Ren, R. Rosero, B. Roskovec, X. C. Ruan, H. Steiner, G. X. Sun, J. L. Sun, W. Tang, D. Taychenachev, K. Treskov, K. V. Tsang, C. E. Tull, N. Viaux, B. Viren, V. Vorobel, C. H. Wang, M. Wang, N. Y. Wang, R. G. Wang, W. Wang, X. Wang, Y. F. Wang, Z. Wang, Z. Wang, Z. M. Wang, H. Y. Wei, L. J. Wen, K. Whisnant, C. G. White, L. Whitehead, T. Wise, H. L. H. Wong, S. C. F. Wong, E. Worcester, C.-H. Wu, Q. Wu, W. J. Wu, D. M. Xia, J. K. Xia, Z. Z. Xing, J. Y. Xu, J. L. Xu, Y. Xu, T. Xue, C. G. Yang, H. Yang, L. Yang, M. S. Yang, M. T. Yang, M. Ye, Z. Ye, M. Yeh, B. L. Young, Z. Y. Yu, S. Zeng, L. Zhan, C. Zhang, H. H. Zhang, J. W. Zhang, Q. M. Zhang, X. T. Zhang, Y. M. Zhang, Y. X. Zhang, Y. M. Zhang, Z. J. Zhang, Z. Y. Zhang, Z. P. Zhang, J. Zhao, Q. W. Zhao, Y. B. Zhao, W. L. Zhong, L. Zhou, N. Zhou, H. L. Zhuang, and J. H. Zou, "Improved measurement of the reactor antineutrino flux and spectrum at Daya Bay," *Chinese Physics C*, vol. 41, no. 1, p. 013002, 2017.

[40] A. A. Sonzogni, T. D. Johnson, and E. A. McCutchan, "Nuclear structure insights into reactor antineutrino spectra," *Physical Review C*, vol. 91, no. 1, 2015.

[41] M. Cribier, M. Fechner, T. Lasserre, A. Letourneau, D. Lhuillier, G. Mention, D. Franco, V. Kornoukhov, and S. Schönert, "Proposed search for a fourth neutrino with a PBq antineutrino source," *Phys. Rev. Lett.*, vol. 107, p. 201801, 2011.

[42] A. C. Hayes, J. L. Friar, G. T. Garvey, G. Jungman, and G. Jonkmans, "Systematic uncertainties in the analysis of the reactor neutrino anomaly," *Phys. Rev. Lett.*, vol. 112, p. 202501, 2014.

[43] P. Huber, "Determination of antineutrino spectra from nuclear reactors," *Phys. Rev. C*, vol. 84, p. 024617, 2011.

[44] H. Becquerel, "Sur les radiations émises par phosphorescence," *Comptes-rendus de l'Académie des sciences* ***122****, 420, séance du 24 février*, 1896.

[45] H. Becquerel, "Sur les radiations invisibles émises par les corps phosphorescents," *Comptes-rendus de l'Académie des sciences* ***122****, 501, séance du 2 mars*, 1896.

[46] H. Becquerel, "Sur les radiations invisibles émises par les sels d'uranium," *Comptes-rendus de l'Académie des sciences* ***122****, 689, séance du 23 mars*, 1896.

[47] H. Becquerel, "Émission de radiations nouvelles par l'uranium métallique," *Comptes-rendus de l'Académie des sciences* ***122****, 1086, séance du 18 mai*, 1896.

[48] H. Becquerel, "Sur diverses propriétés des rayons uraniques," *Comptes-rendus de l'Académie des sciences* ***123****, 855, séance du 23 novembre*, 1896.

[49] J.-P. Adloff, "Les carnets de laboratoire de Pierre et Marie Curie et la note Présentée par Marie Curie à l'Académie des sciences le 12 avril 1898," *Comptes Rendus de l'Académie des Ssiences - Series IIC - Chemistry*, vol. 1, no. 3, pp. 217–227, 1998.

[50] M.-M. B. X. Mougeot and C. Bisch, "Calculation of beta spectral shapes," *Radioprotection*, vol. 49, no. 4, pp. 269–273, 2014.

[51] W. Gerlach and O. Stern, "Das magnetische Moment des Silberatoms," *Zeitschrift für Physik*, vol. 9, no. 1, pp. 353–355, 1922.

[52] W. Gerlach and O. Stern, "Der experimentelle Nachweis der Richtungsquantelung im Magnetfeld," *Zeitschrift für Physik*, vol. 9, no. 1, pp. 349–352, 1922.

[53] M. Rose, *Relativistic Electron Theory, Wiley, New York.* 1961.

[54] H. Behrens and W. Bühring, *Electron radial wave functions and nuclear beta-decay. Oxford: Clarendon press.* 1982.

[55] B. Stech and L. Schülke, "Nuclear β-decay. I," *Zeitschrift für Physik*, vol. 179, no. 3, pp. 314–330, 1964.

[56] J. Lindskog, "Weak interactions and nuclear beta decay," *Nuclear Instruments and Methods*, vol. 48, no. 2, p. 359, 1967.

[57] G. R. Gilmore, *Practical Gamma-Ray Spectrometry.* John Wiley & Sons, Ltd, 2008.

[58] J. J. Thomson, "Cathode rays," *Philosophical Magazine, 44, 293*, 1897.

[59] G. J. Stoney *Philosophical Magazine, series 5, volume 38, p. 418, 420*, 1894.

[60] E. Rutherford, "LXXIX. The scattering of α and β particles by matter and the structure of the atom," *The London, Edinburgh, and Dublin Philosophical Magazine and Journal of Science*, vol. 21, no. 125, pp. 669–688, 1911.

[61] N. Bohr, "LXXIII. On the constitution of atoms and molecules," *The London, Edinburgh, and Dublin Philosophical Magazine and Journal of Science*, vol. 26, no. 155, pp. 857–875, 1913.

[62] L. de Broglie, "Waves and quanta," *Nature*, vol. 112, no. 2815, pp. 540–540, 1923.

[63] E. Schrödinger, "An undulatory theory of the mechanics of atoms and molecules," *Phys. Rev.*, vol. 28, no. 6, pp. 1049–1070, 1926.

[64] T. N. Prize, "Nobel prize in physics," 2019.

[65] R. Jenkins, R. Manne, R. Robin, and C. Senemaud, "IUPAC—nomenclature system for X-ray spectroscopy," *X-Ray Spectrometry*, vol. 20, no. 3, pp. 149–155, 1991.

[66] IUPAC, "International Union of Pure and Applied Chemistry," 2019.

[67] M. Siegbahn, "Relations between the K and L series of the high-frequency spectra," *Nature*, vol. 96, no. 2416, pp. 676–676, 1916.

[68] R. D. Evan, *The Atomic Nucleus*. Tata McGraw-Hill, 1955.

[69] W. Heitler, *The Quantum Theory of Radiation*. Oxford University Press, 1944.

[70] S. Seltzer, "Stopping-Powers and Range Tables for Electrons, Protons, and Helium Ions, NIST Standard Reference Database 124," 1993.

[71] K. Siegbahn, *Beta and Gamma-ray spectrometry.* North-Holland, 1955.

[72] L. Katz and A. S. Penfold, "Range-Energy Relations for Electrons and the Determination of Beta-Ray End-Point Energies by Absorption," *Rev. Mod. Phys.*, vol. 24, pp. 28–44, 1952.

[73] R. Williams, "Becquerel photovoltaic effect in binary compounds," *The Journal of Chemical Physics*, vol. 32, no. 5, pp. 1505–1514, 1960.

[74] A. Einstein, "Concerning an heuristic point of view toward the emission and transformation of light," *Annalen der Physik 17 : 132-148.*, 1905.

[75] D. Thompson, "John Tyndall (1820–1893) a study in vocational enterprise," *The Vocational Aspect of Education*, vol. 9, no. 18, pp. 38–48, 1957.

[76] P. Lilienfeld, "Gustav Mie: the person," *Applied Optics*, vol. 30, no. 33, p. 4696, 1991.

[77] A. H. Compton, "A quantum theory of the scattering of X-rays by light elements," *Phys. Rev.*, vol. 21, no. 5, pp. 483–502, 1923.

[78] F. Perrin, "Calcul relatif aux conditions éventuelles de transmutation en chaîne de l'uranium," *Comptes Rendus. 208, 1394–6*, 1939.

[79] J. H. Hubbell, W. J. Veigele, E. A. Briggs, R. T. Brown, D. T. Cromer, and R. J. Howerton, "Atomic form factors, incoherent scattering functions, and photon scattering cross sections," *Journal of Physical and Chemical Reference Data*, vol. 4, no. 3, pp. 471–538, 1975.

[80] G. F. Knoll, *Radiation Detection and Measurement*. John Wiley & Sons, fourth edition ed., 2010.

[81] J. Danysz, "Sur les rayons β de la famille du radium," *Le Radium*, vol. 9, no. 1, pp. 1–5, 1912.

[82] C. Weinheimer, "KATRIN, a next generation tritium β decay experiment in search for the absolute neutrino mass scale," *Progress in Particle and Nuclear Physics*, vol. 48, no. 1, pp. 141 – 150, 2002.

[83] E. Otten, J. Bonn, and C. Weinheimer, "The Q-value of tritium β-decay and the neutrino mass," *International Journal of Mass Spectrometry*, vol. 251, no. 2, pp. 173 – 178, 2006.

[84] H. Kallmann, "Scintillation counting with solutions," *Phys. Rev.*, vol. 78, no. 5, pp. 621–622, 1950.

[85] J. S. S. R. Cherry and M. Phelps, *Physics in Nuclear Medicine*. Elsevier, 2012.

[86] J. Willett and E. Spejewski, "A method for resolution correction and shape factor analysis of beta spectra," *Nuclear Instruments and Methods*, vol. 52, pp. 77–85, 1967.

[87] W. Wiesner, D. Flothmann, and H. Gils, "A method for correcting the influence of escaping external bremsstrahlung on β-spectra measured with 4π solid-state spectrometers," *Nuclear Instruments and Methods*, vol. 112, no. 3, pp. 449 – 454, 1973.

[88] D. Flothmann, H. J. Gils, W. Wiesner, and R. Löhken, "Spectral shape of the (7/2- $\rightarrow$ 5/2+) transition in the β-decay of ^{139}Ba," *Zeitschrift für Physik A Atoms and Nuclei*, vol. 272, no. 2, pp. 219–222, 1975.

[89] V. Andersen, "A $4\pi\beta$-spectrometer with Li-Si counters," *Nuclear Instruments and Methods*, vol. 65, no. 2, pp. 225 – 227, 1968.

[90] L. Feldman and C. S. Wu, "Investigation of the beta-spectra of ^{10}Be, ^{40}K,^{99}Tc and ^{36}Cl," *Phys. Rev.*, vol. 87, no. 6, pp. 1091–1099, 1952.

[91] K. Sastry, "Investigation of longitudinal polarization and other properties of some beta-transitions," 1972.

[92] R. G. Johnson, O. E. Johnson, and L. M. Langer, "Beta spectrum of ^{36}Cl," *Phys. Rev.*, vol. 102, no. 4, pp. 1142–1148, 1956.

[93] S. Taimuty, "The beta-spectrum of ^{99}Tc," *Phys. Rev. 81, 461*, 1951.

[94] R. E. Snyder, "Decay of ^{94}Nb and ^{94m}Nb," *Phys. Rev. 147, 867*, 1966.

[95] M. Reich and H. Schüpferling, "Formfaktor des Spektrums von ^{99}Tc," *Z. Physik 271, 107*, 1974.

[96] H. Rotzinger, M. Linck, A. Burck, M. Rodrigues, M. Loidl, E. Leblanc, L. Fleischmann, A. Fleischmann, and C. Enss, "Beta spectrometry with magnetic calorimeters," *Journal of Low Temperature Physics*, vol. 151, no. 3, pp. 1087–1093, 2008.

[97] K. Kossert, A. G. Carles, and O. Nähle, "Cerenkov counting and liquid scintillation counting of ^{36}Cl," *Proceedings of the LSC2010 International Conference, Advances in Liquid Scintillation Spectrometry, P. Cassette Editor*, p. 161, 2010.

[98] A. G. Malonda and A. G. Carles, "The anisotropy coefficient in Cerenkov counting," *Applied Radiation and Isotopes*, vol. 49, no. 9, pp. 1049 – 1053, 1998.

[99] C. Bisch, X. Mougeot, M.-M. Bé, and A.-M. Nourreddine, "Development of a system for measuring the shape of β spectra using a semiconductor si detector," *Nuclear Data Sheets*, vol. 120, pp. 95–98, 2014.

[100] Mirion, 2019.

[101] J. Mayer, "Use of ion implantation techniques to fabricate semiconductor nuclear particle detectors," *Nuclear Instruments and Methods*, vol. 63, no. 2, pp. 141–151, 1968.

[102] J. V. Borany, G. Mende, and B. Schmidt, "Ion implanted nuclear radiation detectors passivated with anodic silicon oxide," *Nuclear Instruments and Methods in Physics Research*, vol. 212, no. 1-3, pp. 489–492, 1983.

[103] S. Sze, *Physics of Semiconductor Devices.* John Wiley & Sons, second edition, 1981.

[104] M. Brunetti, A. Codino, C. Federico, C. Grimani, M. Menichelli, G. Minelli, E. Rongoni, I. Salvatori, P. Picozza, and P. Spillantini, "Leakage current and capacity variation with temperature in silicon detectors of a space calorimeter," *Nuclear Instruments and Methods in Physics Research Section A: Accelerators, Spectrometers, Detectors and Associated Equipment*, vol. 302, no. 2, pp. 362–367, 1991.

[105] M. Nakhostin, "Preamplifiers," in *Signal Processing for Radiation Detectors*, pp. 135–190, John Wiley & Sons, Inc., 2017.

[106] CAEN, "see also `https://www.caen.it/products/dt5724/`," 2018.

[107] labZY, "see also `https://www.labzy.com/products/nanomca/`," 2019.

[108] F. Juget, G. Lorusso, G. Haefeli, Y. Nedjadi, F. Bochud, and C. Bailat, "Development and validation of a double focalizing magnetic spectrometer for beta spectrum measurements," *Nuclear Instruments and Methods in Physics Research Section A: Accelerators, Spectrometers, Detectors and Associated Equipment*, vol. 942, p. 162384, 2019.

[109] J. S. Merritt, J. G. V. Taylor, and P. J. Campion, "Self-absorption in sources prepared for 4π beta counting," *Canadian Journal of Chemistry*, vol. 37, no. 6, pp. 1109–1114, 1959.

[110] B. Denecke, G. Sibbens, T. Szabo, M. Hult, and L. Persson, "Improvements in quantitative source preparation," *Applied Radiation and Isotopes*, vol. 52, no. 3, pp. 351–355, 2000.

[111] D. Carswell and J. Milsted, "A new method for the preparation of thin films of radioactive material," *Journal of Nuclear Energy (1954)*, vol. 4, no. 1, pp. 51–54, 1957.

[112] A. Gomez and K. Tang, "Charge and fission of droplets in electrostatic sprays," *Physics of Fluids*, vol. 6, no. 1, pp. 404–414, 1994.

[113] A. Jaworek, "Micro- and nanoparticle production by electrospraying," *Powder Technology*, vol. 176, no. 1, pp. 18–35, 2007.

[114] L. Rayleigh, "XX. On the equilibrium of liquid conducting masses charged with electricity," *The London, Edinburgh, and Dublin Philosophical Magazine and Journal of Science*, vol. 14, no. 87, pp. 184–186, 1882.

[115] E. Bruninx and G. Rudstam, "Electro-spraying: A method of making samples for β counting allowing accurate correction for self-scattering and self-absorption," *Nuclear Instruments and Methods*, vol. 13, pp. 131–140, 1961.

[116] T. Branger, C. Bobin, M.-G. Iroulart, M.-C. Lépy, I. L. Garrères, S. Morelli, D. Lacour, and J. Plagnard, "Comparative study of two drying techniques used in radioactive source preparation: Freeze-drying and evaporation using hot dry nitrogen jets," *Applied Radiation and Isotopes*, vol. 66, no. 6-7, pp. 685–690, 2008.

[117] J. de Sanoit, B. Leprince, C. Bobin, and J. Bouchard, "Freeze-drying applied to radioactive source preparation," *Applied Radiation and Isotopes*, vol. 61, no. 6, pp. 1391–1395, 2004.

[118] N. M. S. Ulam, "The monte carlo method," *Journal of the American Statistical Association*, Sep.,1949.

[119] F. Salvat, J. Fernandez-Varea, and J. Sempau, *PENELOPE-2014: A Code System for Monte Carlo Simulation of Electron and Photon Transport*. OECD/NEA Data Bank, Issyles-Moulineaux, France, 2015.

[120] S. Agostinelli, J. Allison, K. Amako, J. Apostolakis, H. Araujo, P. Arce, M. Asai, D. Axen, S. Banerjee, G. Barrand, F. Behnerl, L. Bellagamba, J. Boudreau, L. Broglia, A. Brunengo, H. Burkhardt, S. Chauvie, J. Chuma, R. Chytracek, G. Cooperman, G. Cosmo, P. Degtyarenko, A. Dell'Acqua, G. Depaola, D. Dietrich, R. Enami, A. Feliciello, C. Ferguson, H. Fesefeldt, G. Folger, F. Foppiano, A. Forti, S. Garelli, S. Giani, R. Giannitrapani, D. Gibin, J. Cadenas, I. Gonzalez, G. Abril, G. Greeniaus, W. Greiner, V. Grichine, A. Grossheim, S. Guatelli, P. Gumplinger, R. Hamatsu, K. Hashimoto, H. Hasui, A. Heikkinen, A. Howard, V. Ivanchenko, A. Johnson, F. Jones, J. Kallenbach, N. Kanaya, M. Kawabata, Y. Kawabata, M. Kawaguti, S. Kelner, P. Kent, A. Kimura, T. Kodama, R. Kokoulin, M. Kossov, H. Kurashige, E. Lamanna, T. Lampen, V. Lara, V. Lefebure, F. Lei, M. Liendl, W. Lockman, F. Longo, S. Magni, M. Maire, E. Medernach, K. Minamimoto, P. Freitas, Y. Morita, K. Murakami, M. Nagamatu, R. Nartallo, P. Nieminen, T. Nishimura, K. Ohtsubo, M. Okamura, S. O'Neale, Y. Oohata, K. Paech, J. Perl, A. Pfeiffer, M. Pia, F. Ranjard, A. Rybin, S. Sadilova, E. Salvo, G. Santin, T. Sasaki, N. Savvas, Y. Sawada, S. Scherer, S. Sei, V. Sirotenko, D. Smith, N. Starkov, H. Stoecker, J. Sulkimo, M. Takahata, S. Tanaka, E. Tcherniaev, E. Tehrani, M. Tropeano, P. Truscott, H. Uno, L. Urban, P. Urban, M. Verderi, A. Walkden, W. Wander, H. Weber, J. Wellisch, T. Wenaus, D. Williams, D. Wright, T. Yamada, H. Yoshida, and D. Zschiesche, "Geant4 - a simulation toolkit," *Nuclear Instruments and Methods in Physics Research Section A, Accelerators, Spectrometers, Detectors and Associated Equipment*, vol. 506, pp. 250–303, 2003.

[121] J. G. Briesmeister., "A General Monte Carlo N-Particle transport code.," 2000.

[122] I. Kawrakow and D. Rogers., "The EGSnrc code system : Monte carlo simulation of electron and photon transport.," 2003.

[123] M. Wang, G. Audi, F. G. Kondev, W. Huang, S. Naimi, and X. Xu, "The AME2016 atomic mass evaluation (II). Tables, graphs and references," *Chinese Physics C*, vol. 41, no. 3, p. 030003, 2017.

[124] R. Brun and F. Rademakers, "ROOT — an object oriented data analysis framework," *Nuclear Instruments and Methods in Physics Research Section A: Accelerators, Spec-*

trometers, Detectors and Associated Equipment. See also `http://root.cern.ch/`, vol. 389, no. 1-2, pp. 81–86, 1997.

[125] E. García-Toraño, V. Peyres, and F. Salvat, "PenNuc: Monte carlo simulation of the decay of radionuclides," *Computer Physics Communications*, vol. 245, p. 106849, 2019.

[126] M. H. C. J. R. J. S. S T Perkins, D E Cullen and J. H. Hubbell, "Tables and graphs of atomic subshell and relaxation data derived from the LLNL evaluated atomic data library (EADL), z = 1–100," tech. rep., 1991.

[127] H. Ruellan, M. Lépy, M. Etcheverry, J. Plagnard, and J. Morel, "A new spectra processing code applied to the analysis of ^{235}U and ^{238}U in the 60 to 200 keV energy range," *Nuclear Instruments and Methods in Physics Research Section A: Accelerators, Spectrometers, Detectors and Associated Equipment*, vol. 369, no. 2-3, pp. 651–656, 1996.

[128] U. Fano, "On the theory of ionization yield of radiations in different substances," *Phys. Rev.*, vol. 70, no. 1-2, pp. 44–52, 1946.

[129] U. Fano, "Ionization yield of radiations. II. The fluctuations of the number of ions," *Phys. Rev.*, vol. 72, no. 1, pp. 26–29, 1947.

[130] M.-C. Lépy, L. Brondeau, Y. Ménesguen, S. Pierre, and J. Riffaud, "Consistency of photon emission intensities for efficiency calibration of gamma-ray spectrometers in the energy range from 20 keV to 80 keV," *Applied Radiation and Isotopes*, vol. 134, pp. 131–136, 2018.

[131] M.-M. Bé, V. Chisté, C. Dulieu, X. Mougeot, V. Chechev, F. Kondev, A. Nichols, X. Huang, and B. Wang, *Table of Radionuclides*, vol. 7 of *Monographie BIPM-5*. Pavillon de Breteuil, F-92310 Sèvres, France: Bureau International des Poids et Mesures, 2013.

[132] M. Loidl, J. Beyer, L. Bockhorn, C. Enss, S. Kempf, K. Kossert, R. Mariam, O. Nähle, M. Paulsen, P. Ranitzsch, M. Rodrigues, and M. Schmidt, "Beta spectrometry with metallic magnetic calorimeters in the framework of the european EMPIR project MetroBeta," *Applied Radiation and Isotopes*, vol. 153, p. 108830, 2019.

[133] V. V. Kuzminov and N. J. Osetrova, "Precise measurement of 14C beta spectrum by using a wall-less proportional counter," *Physics of Atomic Nuclei*, vol. 63, no. 7, pp. 1292–1296, 2000.

[134] M. Paulsen, K. Kossert, and J. Beyer, "An unfolding algorithm for high resolution microcalorimetric beta spectrometry," *Nuclear Instruments and Methods in Physics Research Section A: Accelerators, Spectrometers, Detectors and Associated Equipment*, vol. 953, p. 163128, 2020.

[135] M. S. Rahman and G. Cho, "Unfolding low-energy gamma-ray spectrum obtained with NaI(tl) in air using matrix inversion method," *Journal of Scientific Research*, vol. 2, no. 2, pp. 221–226, 2010.

[136] D. Love and A. Nelson, "Unfolding the response function of high-quality germanium detectors," *Nuclear Instruments and Methods in Physics Research Section A: Accelerators, Spectrometers, Detectors and Associated Equipment*, vol. 274, no. 3, pp. 541–546, 1989.

[137] N. Starfelt and H. W. Koch, "Differential cross-section measurements of thin-target bremsstrahlung produced by 2.7- to 9.7-Mev electrons," *Phys. Rev.*, vol. 102, no. 6, pp. 1598–1612, 1956.

[138] C. S. Cook, L. M. Langer, and H. C. Price, "Study of the beta-spectra of C14and S35," *Phys. Rev.*, vol. 74, no. 5, pp. 548–552, 1948.

[139] J. Angus, A. Cockroft, and S. Curran, "XLVI. Investigation of soft radiations by proportional counters," *The London, Edinburgh, and Dublin Philosophical Magazine and Journal of Science*, vol. 40, no. 304, pp. 522–530, 1949.

[140] S. D. Warshaw, "The β-spectrum of C14," *Phys. Rev.*, vol. 80, no. 1, pp. 111–112, 1950.

[141] F. P. Calaprice and B. R. Holstein, "Weak magnetism and the beta spectra of 12B and 12N," *Nuclear Physics A*, vol. 273, no. 2, pp. 301–325, 1976.

[142] A. García and B. A. Brown, "Shape of the β spectra in the A=14 system," *Phys. Rev. C*, vol. 52, no. 6, pp. 3416–3427, 1995.

[143] H. J. Rose, O. Häusser, and E. K. Warburton, "Evidence for a nuclear tensor force from mass 14 beta- and gamma-ray data," *Rev. Mod. Phys.*, vol. 40, no. 3, pp. 591–610, 1968.

[144] P. F. Zweifel, "Second-order corrections to beta spectra," *Phys. Rev.*, vol. 95, no. 1, pp. 112–112, 1954.

[145] H. Genz, G. Kuhner, A. Richter, and H. Behrens, "Phenomenological wave functions for the mass A=14 system and a consistent description of beta decay observables," *Zeitschrift fur Physik A Hadrons and Nuclei*, vol. 341, no. 1, pp. 9–24, 1991.

[146] F. E. Wietfeldt, E. B. Norman, Y. D. Chan, M. T. F. da Cruz, A. García, E. E. Haller, W. L. Hansen, M. M. Hindi, R.-M. Larimer, K. T. Lesko, P. N. Luke, R. G. Stokstad, B. Sur, and I. Žlimen, "Further studies on the evidence for a 17-keV neutrino in adoped 14 germanium detector," *Phys. Rev. C*, vol. 52, no. 2, pp. 1028–1040, 1995.

[147] B. Sur, E. B. Norman, K. T. Lesko, M. M. Hindi, R.-M. Larimer, P. N. Luke, W. L. Hansen, and E. E. Haller, "Evidence for the emission of a 17-keV neutrino in the β decay of C14," *Phys. Rev. Lett.*, vol. 66, no. 19, pp. 2444–2447, 1991.

[148] G. Alimonti, G. Angloher, C. Arpesella, M. Balata, G. Bellini, J. Benziger, S. Bonetti, L. Cadonati, F. Calaprice, G. Cecchet, M. Chen, N. Darnton, A. de Bari, M. Deutsch, F. Elisei, F. von Feilitzsch, C. Galbiati, F. Gatti, M. Giammarchi, D. Giugni, T. Goldbrunner, A. Golubchikov, A. Goretti, T. Hagner, F. Hartmann, R. von Hentig, G. Heusser, A. Ianni, J. Jochum, M. Johnson, M. Laubenstein, P. Lombardi, S. Magni, S. Malvezzi, I. Manno, G. Manuzio, F. Masetti, U. Mazzucato, E. Meroni, M. Neff, A. Nostro, L. Oberauer, A. Perotti, A. Preda, R. Raghavan, G. Ranucci, E. Resconi, M. Ruscitti, R. Scardaoni, S. Schönert, O. Smirnov, R. Tartaglia, G. Testera, P. Ullucci, R. Vogelaar, S. Vitale, and O. Zaimidoroga, "Measurement of the 14C abundance in a low-background liquid scintillator," *Phys. Lett. B*, vol. 422, no. 1-4, pp. 349–358, 1998.

[149] D. Flothmann, W. Wiesner, R. Löhken, and H. Rebel, "β-spektroskopie mit Halbleiterdetektoren beim Zerfall von ^{32}P,^{49}Sc, ^{204}Tl und ^{210}Bi," *Zeitschrift für Physik A Hadrons and nuclei*, vol. 225, no. 2, pp. 164–194, 1969.

[150] X. Mougeot, M.-M. Bé, C. Bisch, and M. Loidl, "Evidence for the exchange effect in theβdecay of241pu," *Physical Review A*, vol. 86, oct 2012.

[151] A. Moljk and S. C. Curran, "Beta spectra of C14 and S35," *Phys. Rev.*, vol. 96, no. 2, pp. 395–398, 1954.

[152] W. M. Visscher and R. A. Ferrell, "Beta decay of C14 and nuclear forces," *Phys. Rev.*, vol. 107, no. 3, pp. 781–796, 1957.

[153] A. Kumar, P. C. Srivastava, J. Kostensalo, and J. Suhonen, "Second-forbidden non-unique β- decays of Na24 and Cl36 assessed by the nuclear shell model," *Phys. Rev. C*, vol. 101, no. 6, 2020.

[154] H. Behrens and J. Jänecke, *Numerical Tables for Beta-Decay and Electron Capture*. Springer-Verlag, 1969.

The "nucdat" file created by PenNuc module for ^{207}Bi decay

The file for ^{207}Bi decay is given in Figure 1 and the parameters are described below:

1. The first column contains some specific commands such as PAR: name of the parent nuclide; AZP: A and Z of the parent nucleus; NDA: number of daughter nuclei. In the case of decay paths, it shows the decay mode: BEM for β^-, BEP for β^+, CK, CL1, CL2 for electron capture in the K, L_1, L_2, ... shells. For transitions between excited levels, the γ emission is labelled GA and the internal conversion processes EK, EL1, EL2, ... according to the atomic subshell where internal conversion occurs.

2. *Daughter nuclei:* name of the daughter nucleus (DAU), decay probabilities, number of branches, and uncertainties (DDE), Q-value, and uncertainty (Q). Each daughter nucleus is separated from each other by a line entitled "Daughter Separator".

3. *Disintegration of the daughter nucleus:* decay mode, branching ratio, transition energy, transition inhibition factor (indicates the nature of the transition), and uncertainties. Each decay pathway is separated by a line labelled "Branch Separator".

4. *Excited level of the daughter nuclei.* The following parameters are indicated in the first line of the "Level Separator": level energy; the number of transitions depopulating this level (γ transition, internal conversion or internal pair creation); level lifetime (in seconds); a number that labels the excited levels (starting from 0 for the ground state). The next lines contain information on the subsequent transition that depopulates the level: type of the transition (internal conversion for K, L_1, ... subshells or internal pair creation), intensity and energy, final level and the corresponding uncertainties. The final level gathers transition information for each excited level .

The PenNuc module probes the totality of the decay scheme by random selection and creates a new file named "nucdat " containing all the generated events. The data produced for ^{207}Bi can be found below.

```
PAR BI207
AZP 207 ; 83
NDA 1
COM ***************** Evaluation Date: 06/12/2009 ****************
COM ==================== Daughter Separator ====================
DAU PB207
DDE 1 ;  ; 4 ; 13
Q   2397.5 ; 2.1
COM ---------------------- Branch Separator ----------------------
CL1 0.0422 ; 0.0015 ; 4 ; 57.5520000000001 ; 2.1 ; 0
CL2 0.00359 ; 0.00014 ; 4 ; 57.5520000000001 ; 2.1 ; 0
CM  0.0245 ; 0.0009 ; 4 ; 57.5520000000001 ; 2.1 ; 0
COM ---------------------- Branch Separator ----------------------
CK  0.616 ; 0.007 ; 3 ; 764.132 ; 2.1 ; -1
CL1 0.1489 ; 0.0035 ; 3 ; 764.132 ; 2.1 ; -1
CL2 0.0118 ; 0.0025 ; 3 ; 764.132 ; 2.1 ; -1
CL3 0.00648 ; 0.00017 ; 3 ; 764.132 ; 2.1 ; -1
CM  0.058 ; 0.0009 ; 3 ; 764.132 ; 2.1 ; -1
COM ---------------------- Branch Separator ----------------------
COM ---------------------- Branch Separator ----------------------
BEP 0.00012 ; 0.00002 ; 1 ; 805.797 ; 2.1 ; 1
CK  0.0701 ; 0.0048 ; 1 ; 1827.797 ; 2.1 ; 1
CL1 0.0122 ; 0.0009 ; 1 ; 1827.797 ; 2.1 ; 1
CL2 0.00097 ; 0.00011 ; 1 ; 1827.797 ; 2.1 ; 1
CM  0.00431 ; 0.00031 ; 1 ; 1827.797 ; 2.1 ; 1
COM ---------------------- Branch Separator ----------------------
COM -------------- Level Separator - T1/2 in seconds -------------
LED 2339.948 ; 0.011 ; 14 ;  ;  ; 4
GA  0.001315 ; 0.000022 ; 1442.2 ; 0.2 ; 2
EK  0.00000356 ; 0.00000008 ; 1354.2 ; 0.2 ; 2
EL1 0.000000512 ; 0.000000012 ; 1426.34 ; 0.2 ; 2
EL2 0.0000000831 ; 0.0000000018 ; 1427 ; 0.2 ; 2
EL3 0.00000002101 ; 0.00000000046 ; 1429.16 ; 0.2 ; 2
EM  0.0000001444 ; 0.0000000032 ; 1439.09 ; 0.2 ; 2
EN  0.0000000438 ; 0.000000001 ; 1441.71 ; 0.2 ; 2
GA  0.06871 ; 0.00026 ; 1770.228 ; 0.009 ; 1
EK  0.000235 ; 0.0000035 ; 1682.232 ; 0.009 ; 1
EL1 0.0000352 ; 0.0000006 ; 1754.375 ; 0.009 ; 1
EL2 0.000002707 ; 0.000000042 ; 1755.036 ; 0.009 ; 1
EL3 0.0000002714 ; 0.0000000042 ; 1757.201 ; 0.009 ; 1
EM  0.00000888 ; 0.00000013 ; 1767.128 ; 0.009 ; 1
EN  0.000002704 ; 0.000000042 ; 1769.746 ; 0.009 ; 1
COM -------------- Level Separator - T1/2 in seconds -------------
LED 1633.368 ; 0.005 ; 7 ; 8.06E-1 ; 6.E-3 ; 3
GA  0.7458 ; 0.0022 ; 1063.656 ; 0.003 ; 1
```

Figure 1 – The file for ^{207}Bi decay used by the PenNuc module in PENELOPE.

Parent nuclide: BI207   (Z = 83, A =207)
 Number of daughters = 1

 EC = electron capture, IC = internal conversion.
 BR= branching ratio,   PR = probability.

 Daughter nuclide number   1: PB207   (Z = 82, A =207)
   Q = 2.397500E+06 eV, BR = 1.000000E+00

 Excited levels:
   4, E = 2.339948E+06 eV, half-life = 0.000000E+00 sec
   3, E = 1.633368E+06 eV, half-life = 8.060000E-01 sec
   2, E = 8.978000E+05 eV, half-life = 0.000000E+00 sec
   1, E = 5.697030E+05 eV, half-life = 1.305000E-10 sec

 Decay branches:
   ECL1 to level   4, BR = 4.220000E-02
   ECL2 to level   4, BR = 3.590000E-03
   ECM   to level   4, BR = 2.450000E-02
   ECK   to level   3, BR = 6.160000E-01
   ECL1 to level   3, BR = 1.489000E-01
   ECL2 to level   3, BR = 1.180000E-02
   ECL3 to level   3, BR = 6.480000E-03
   ECM   to level   3, BR = 5.800000E-02
   BETA+ to level   1, BR = 1.200000E-04, E = 8.057970E+05 eV
   ECK   to level   1, BR = 7.010000E-02
   ECL1 to level   1, BR = 1.220000E-02
   ECL2 to level   1, BR = 9.700000E-04
   ECM   to level   1, BR = 4.310000E-03

 Transitions from level   4
   4 -->   1 ICMN , E = 1.769746E+06 eV, PR = 2.704000E-06
   4 -->   1 ICMN , E = 1.767128E+06 eV, PR = 8.880000E-06
   4 -->   1 ICL3 , E = 1.757201E+06 eV, PR = 2.714000E-07

```
   4 -->   1 ICL2  ,  E = 1.755036E+06 eV,  PR = 2.707000E-06
   4 -->   1 ICL1  ,  E = 1.754375E+06 eV,  PR = 3.520000E-05
   4 -->   1 ICK   ,  E = 1.682232E+06 eV,  PR = 2.350000E-04
   4 -->   1 GAMMA ,  E = 1.770228E+06 eV,  PR = 6.871000E-02
   4 -->   2 ICMN  ,  E = 1.441710E+06 eV,  PR = 4.380000E-08
   4 -->   2 ICMN  ,  E = 1.439090E+06 eV,  PR = 1.444000E-07
   4 -->   2 ICL3  ,  E = 1.429160E+06 eV,  PR = 2.101000E-08
   4 -->   2 ICL2  ,  E = 1.427000E+06 eV,  PR = 8.310000E-08
   4 -->   2 ICL1  ,  E = 1.426340E+06 eV,  PR = 5.120000E-07
   4 -->   2 ICK   ,  E = 1.354200E+06 eV,  PR = 3.560000E-06
   4 -->   2 GAMMA ,  E = 1.442200E+06 eV,  PR = 1.315000E-03

 Transitions from level   3
   3 -->   1 ICMN  ,  E = 1.063169E+06 eV,  PR = 1.424000E-03
   3 -->   1 ICMN  ,  E = 1.060551E+06 eV,  PR = 4.410000E-03
   3 -->   1 ICL3  ,  E = 1.050624E+06 eV,  PR = 1.290000E-03
   3 -->   1 ICL2  ,  E = 1.048459E+06 eV,  PR = 2.910000E-03
   3 -->   1 ICL1  ,  E = 1.047798E+06 eV,  PR = 1.365000E-02
   3 -->   1 ICK   ,  E = 9.756545E+05 eV,  PR = 7.110000E-02
   3 -->   1 GAMMA ,  E = 1.063656E+06 eV,  PR = 7.458000E-01

 Transitions from level   2
   2 -->   0 ICMN  ,  E = 8.973100E+05 eV,  PR = 2.770000E-07
   2 -->   0 ICMN  ,  E = 8.946900E+05 eV,  PR = 9.100000E-05
   2 -->   0 ICL3  ,  E = 8.847600E+05 eV,  PR = 3.200000E-08
   2 -->   0 ICL2  ,  E = 8.826000E+05 eV,  PR = 3.400000E-07
   2 -->   0 ICL1  ,  E = 8.819400E+05 eV,  PR = 3.530000E-06
   2 -->   0 ICK   ,  E = 8.098000E+05 eV,  PR = 2.340000E-05
   2 -->   0 GAMMA ,  E = 8.978000E+05 eV,  PR = 1.284000E-03
   2 -->   1 GAMMA ,  E = 3.281100E+05 eV,  PR = 4.400000E-05

Transitions from level   1
   1 -->   0 ICMN  ,  E = 5.692093E+05 eV,  PR = 3.188000E-04
   1 -->   0 ICMN  ,  E = 5.665908E+05 eV,  PR = 1.057000E-03
```

```
  1 -->   0 ICL3  ,  E = 5.566638E+05 eV,  PR = 5.240000E-04
  1 -->   0 ICL2  ,  E = 5.544990E+05 eV,  PR = 1.501000E-03
  1 -->   0 ICL1  ,  E = 5.538382E+05 eV,  PR = 2.268000E-03
  1 -->   0 ICK   ,  E = 4.816945E+05 eV,  PR = 1.548000E-02
  1 -->   0 GAMMA ,  E = 5.696980E+05 eV,  PR = 9.776000E-01
-----------------------------------------------------------------
Branching ratios to daughters (normalized):
1.000000E+00

***  END  ***
```

Résumé en français

Introduction

Cette étude a été menée au Laboratoire National Henri Becquerel (LNE-LNHB) qui a été désigné comme laboratoire national de métrologie dans le domaine des rayonnements ionisants. Il fait partie de l'un des laboratoires de l'institut LIST (Laboratoire d'Intégration des Systèmes et des Technologies), situé sur le site de Paris-Saclay du Commissariat à l'Énergie Atomique (CEA). La métrologie française en général est fédérée et coordonnée par le Laboratoire National de métrologie et d'Essais (LNE).

La mission du LNE-LNHB depuis 1970 est de mettre en œuvre, maintenir et transférer les unités dérivées du Système International d'unités (SI) pour la radioactivité et la dosimétrie : le becquerel (Bq), le sievert (Sv) et le gray (Gy). Cela consiste essentiellement à réaliser des étalons et à assurer leur cohérence, tant au niveau international que national. Ces activités s'appuient sur une chaîne de traçabilité solide et continue, depuis les étalons primaires de la plus haute précision jusqu'aux utilisateurs finaux.

En métrologie de la radioactivité, une certaine connaissance préalable des données sur la décroissance radioactive est nécessaire afin de choisir l'instrumentation et la méthode les plus appropriées pour l'étalonnage d'un radionucléide donné. Le LNHB est très impliqué dans la mesure et l'évaluation des données de désintégration et coordonne le projet international DDEP (Decay Data Evaluation Project), qui sont officiellement recommandés par le BIPM (Bureau International des Poids et Mesures) pour la communauté de la métrologie des rayonnements ionisants.

L'une des principales techniques de mesure primaire de la radioactivité, à savoir la technique de comptage par scintillation liquide, nécessite la connaissance précise du spectre en énergie des particules émises dans la désintégration bêta afin de modéliser l'émission de lumière. La partie de basse énergie du spectre est particulièrement importante car le rendement de détection diminue considérablement dans cette région. Le bilan des incertitudes sur l'activité de l'étalon doit inclure une composante qui reflète le degré de connaissance sur ce paramètre [1].

Il y a quelques années, un code théorique appelé "BetaShape" a été développé au LNHB pour le calcul des désintégrations bêta. Ce code calcule notamment les spectres en énergie des particules β émises dans les transitions permises et interdites uniques, et inclut une base

de données de 130 facteurs de forme expérimentaux disponibles dans la littérature. Ces types de transition peuvent être calculés avec une bonne précision sans tenir compte de la structure nucléaire. Les calculs sont plus complexes dans le cas des transitions interdites non-uniques en raison de leur grande sensibilité à la structure nucléaire. Comme chaque transition interdite non-unique nécessiterait une étude détaillée et un modèle nucléaire précis, BetaShape traite une telle transition comme une permise ou une interdite unique de variation du moment angulaire total identique, selon l'approximation ξ [2]. Ces prédictions théoriques doivent être validées, ou contraintes, par des résultats expérimentaux, en particulier dans le cas des transitions interdites non-uniques.

Cependant, les mesures de spectres bêta sont assez rares dans la littérature actuelle. De nombreuses expériences ont été réalisées jusque dans les années 1970 et le sujet a souffert d'un intérêt limité depuis lors. Les expériences étaient principalement réalisées avec des spectromètres magnétiques et se concentraient sur les transitions permises et premières interdites. La mesure précise de la désintégration β présente de nombreuses difficultés car les spectres peuvent être facilement déformés en raison de l'auto-absorption au sein de la source radioactive ou de la rétrodiffusion sur le détecteur, par exemple. Afin d'éliminer ces déformations, les spectres doivent être corrigés à l'aide d'un processus de déconvolution utilisant la connaissance précise de la fonction de réponse du dispositif expérimental. Ce type d'étude a rarement été observé dans la littérature.

Au LNHB, une technique de haute précision appelée "Calorimétrie métallique magnétique" (MMC) a été développée et adaptée ces dix dernières années à la mesure des décroissances β jusqu'à 500 keV d'énergie maximale. Les mesures effectuées avec cette technique ont déjà contribué à la validation de certains calculs théoriques, mettant en évidence l'influence des effets atomiques sur la forme des spectres β [3]. Malgré leurs performances, les calorimètres métalliques magnétiques sont limités aux spectres de faible énergie et sont trop difficiles à mettre en œuvre pour produire des mesures de qualité en quantité. Par conséquent, une autre technique de mesure complémentaire à la MMC mais plus flexible, est essentielle. C'est pourquoi, une approche expérimentale avec des détecteurs silicium a été lancée au LNHB. Les premières mesures ont été effectuées avec un seul détecteur silicium (angle solide inférieur à 2π). Les résultats ont mis en évidence la forte déformation des spectres due à la rétrodiffusion, qui induit un dépôt partiel d'énergie des électrons dans le détecteur [4]. Bien que ces déformations aient pu être corrigées, leur contribution à l'incertitude finale est trop importante. L'amélioration de cette technique est nécessaire pour atteindre de meilleures performances, pour minimiser les corrections et donc pour obtenir une meilleure précision.

L'objectif principal de ce travail de thèse est de construire un spectromètre β précis basé sur des détecteurs silicium. Le dispositif expérimental doit prendre en compte toutes les origines des déformations et les limiter au maximum. La réponse du système de détection doit être connue avec précision afin de corriger les déformations résiduelles et obtenir ainsi le spectre

initialement émis. Les facteurs de forme expérimentaux doivent être extraits et comparés aux résultats existants dans la littérature et aux calculs théoriques.

Système de mesure

Afin de maximiser l'absorption des particules bêta, il est nécessaire d'avoir une géométrie avec un angle solide de détection de 4π. Un système à deux détecteurs placés à l'intérieur de la chambre à vide a été conçu avec beaucoup de soin en optimisant sa géométrie à l'aide de simulations de Monte Carlo PENELOPE. Quatre détecteurs silicium sont dédiés à la spectrométrie β : deux détecteurs en silicium planaires passivement implanté (PIP) et deux détecteurs en silicium-lithium [Si(Li)].

Pour une mesure très précise, surtout dans le cas des particules β, il est préférable d'avoir un détecteur avec une fenêtre d'entrée la plus fine possible afin de minimiser la perte d'énergie dans la zone morte du détecteur. La technique d'implantation ionique a le grand avantage de fournir une épaisseur maximale de 50 nm équivalen silicium pour la fenêtre d'entrée du PIPS, ce qui correspond à des électrons ayant une énergie cinétique de 1,3 keV. Le premier appareil de mesure est conçu pour la détection d'électrons d'une énergie maximale de 850 keV. Cette configuration se compose de deux détecteurs PIPS identiques, chacun d'une épaisseur de 1 mm et d'une surface de 300 mm^2.

La configuration idéale pour une géométrie 4π est un sandwich de deux détecteurs avec une source radioactive au milieu. Cependant, un sandwich direct d'une source radioactive contaminerait les détecteurs et les supports de détecteurs, ce qui doit bien sûr être évité. De plus, les deux PIPS, fabriqués par Mirion Technologies, sont encapsulés dans un boîtier métallique avec une distance de 0,9 mm entre la surface métallique et la surface de cristal de silicium. L'objectif était donc de trouver le meilleur compromis en fonction des exigences et des contraintes.

Le système de détection a été réalisé à l'aide du logiciel de CAO 3D (conception assistée par ordinateur) SOLIDWORKS. Ces pièces ont d'abord été imprimées à l'aide d'une imprimante 3D en plastique disponible au LNHB (voir igure 2). L'ensemble de la configuration du support permet une géométrie compacte et se compose de quatre pièces : deux pièces pour placer les détecteurs et deux plaques de fermeture. Dans la partie centrale des deux supports de détecteurs, une encoche spécifique permet de placer une source radioactive (Figure 2b), garantissant un positionnement reproductible. De plus, la structure semi-cylindrique de chaque support de détecteur (Figure 2a,b) est conçue pour fixer le système de détection assemblé sur un doigt de cuivre dans la chambre de détection. Un petit trou servant de cheminée pour faciliter le vide autour de la source radioactive également a été ajouté. La Figure 2 montre le prototype des pièces imprimées en 3D et testées en plaçant les détecteurs à l'intérieur.

La configuration finale emploie deux détecteurs Si (Figure2.5), placés l'un en face de l'autre,

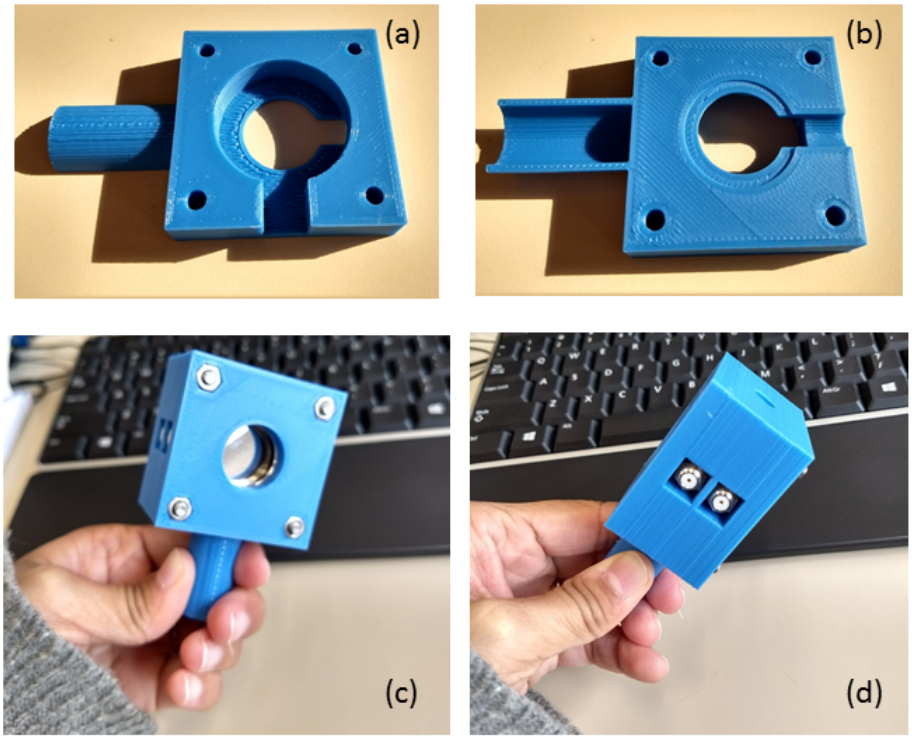

Figure 2 – Les supports des détecteurs sont imprimés en plastique à l'aide d'une imprimante 3D pour l'optimisation et le test. En haut (a,b) se trouvent les supports de chaque détecteur. En bas (c,d), le système de détection en plastique après avoir inséré les détecteurs.

ce qui donne une géométrie proche de 4π sr. Les détecteurs sont refroidis par un système d'azote liquide, et la chambre de détection fonctionne sous ultra-vide (UHV). Le fonctionnement des détecteurs sous UHV limite la diffusion des électrons et empêche due la condensation de l'humidité sur la surface froide du silicium. Cependant, le fonctionnement continu de la pompe à vide génère des vibrations pendant la mesure, ce qui dégrade le rapport signal sur bruit du détecteur. Ces vibrations ont été atténuées très efficacement comme détaillé ci-dessous.

Le deuxième dispositif de mesure, d'une géométrie proche de 4π sr, a été mis au point pour deux détecteurs Si(Li) dans la même configuration que le système de détection PIPS® (Figure 4). De plus, nous avons réussi à minimiser la distance entre les surfaces des détecteurs à 2,4 mm. Une étude Monte Carlo a été réalisée pour un spectre β du ^{90}Y d'énergie maximale 2278,5 (16) keV en utilisant cette géométrie de dispositif Si(Li).

La chambre de détection (Figure 5) existait déjà [4]. Cette partie du système de mesure est le seul composant majeur utilisé des développements précédents. Il s'agit d'un cube de 170 mm, fabriqué à partir d'un alliage d'aluminium (duraluminium). Les six côtés de la chambre sont fermés par des brides *DN 100 ISO*. Chacun d'entre eux a une bride spécifique, comme expliqué ci-dessous :

(i) Sur la partie du haut de la chambre de détection, la bride contient un passage sous vide avec une bride CF40[1], qui est spécialisé pour une traversée électronique.

[1]CF signifie ConFlat flange utilisant un joint torique en cuivre pour obtenir un vide ultra-élevé. Le CF40 a

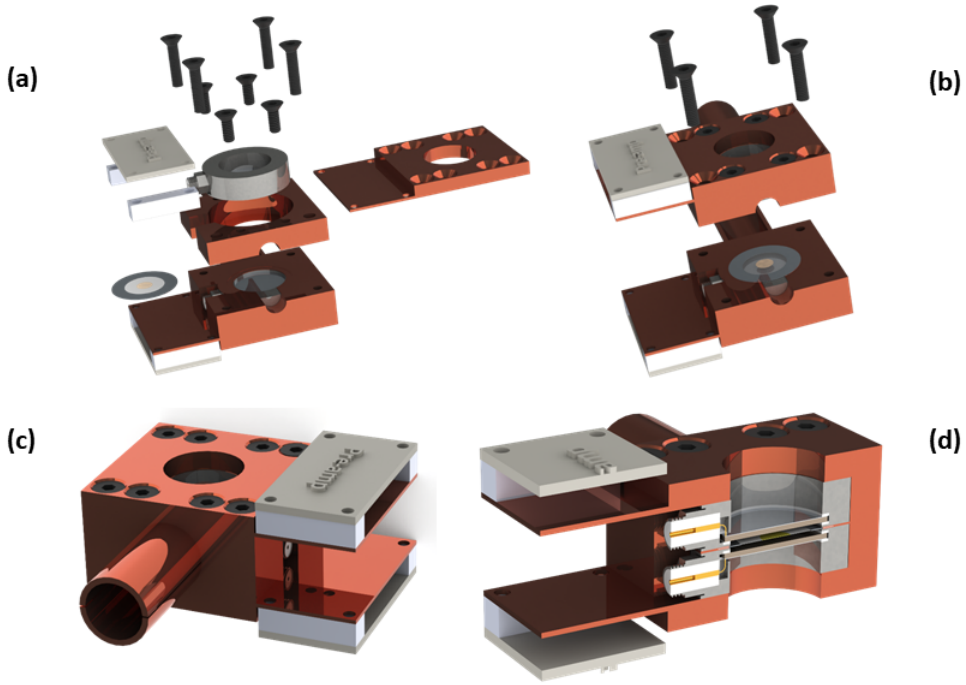

Figure 3 – Images en 3D du système de détection. (a) Une vue éclatée des pièces du système de détection. (b) Deux détecteurs dans leur porte-détecteur respectif. (c) L'ensemble du système de détection en configuration de mesure. (d) Une vue en coupe au milieu du système de détection.

(ii) Sur la face arrière de la chambre, qui n'apparaît pas sur la Figure 5, une jauge à vide a été connectée afin de mesurer la pression à l'intérieur de la chambre de détection.

(iii) La bride placée sur le côté gauche de la chambre est reliée à un Dewar à azote liquide *via* une tige de cuivre entourée d'un tube en acier inoxydable, comme le montre la Figure 6. Cette connexion a été améliorée dans le présente étude.

(iv) Sur le côté droit de la chambre, une pompe à vide est connectée *via* un long tube à vide. Un bac à sable est placé entre la pompe à vide et la chambre de détection : le tube à vide traverse le sable afin d'atténuer les vibrations (voir Figure 6).

(v) La bride placée en bas de la chambre est reliée à une valve avec une minuscule ouverture filtrée, qui permet une entrée d'air fine afin de casser le vide "en douceur".

(vi) La bride placée à l'avant de la chambre a été conservée comme une solide bride vierge. Elle permet un accès facile à l'intérieur de la chambre, ce qui est particulièrement utile pour les manipulations diverses.

un diamètre de 40 mm. La traversée CF40 utilisée pour le passage sous vide est le modèle "Mil-C-26482 CF40" de FULLVAC.

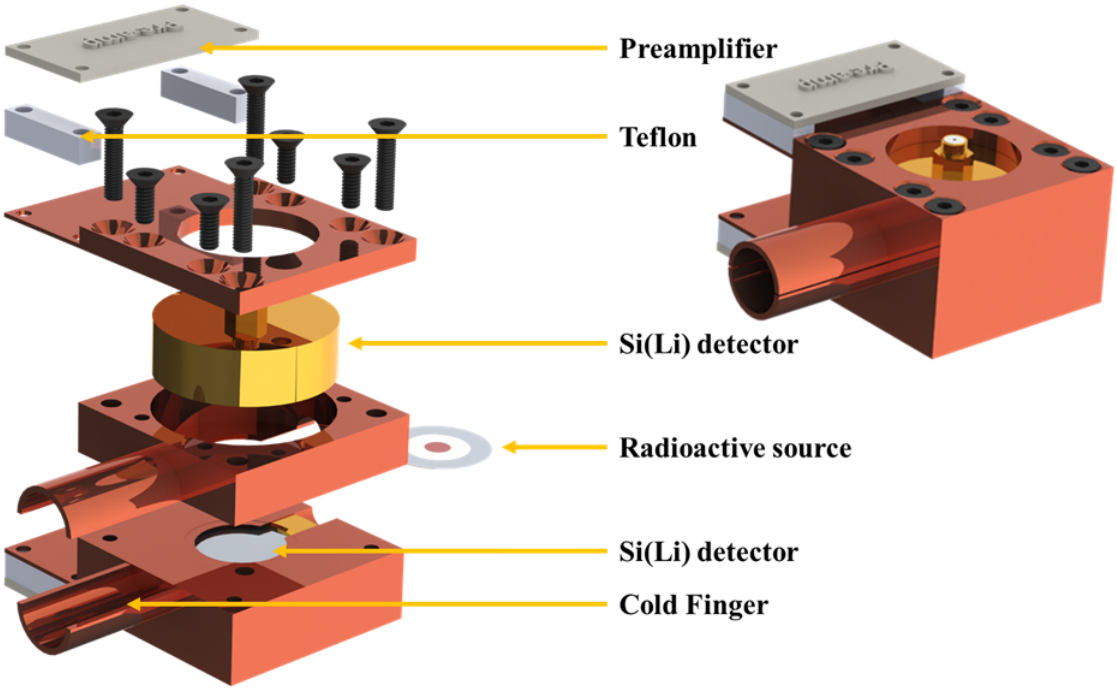

Figure 4 – Images en 3D du système de détection avec les détecteurs Si(Li). La distance entre les détecteurs est de 2,4 mm dans la configuration de mesure (à droite).

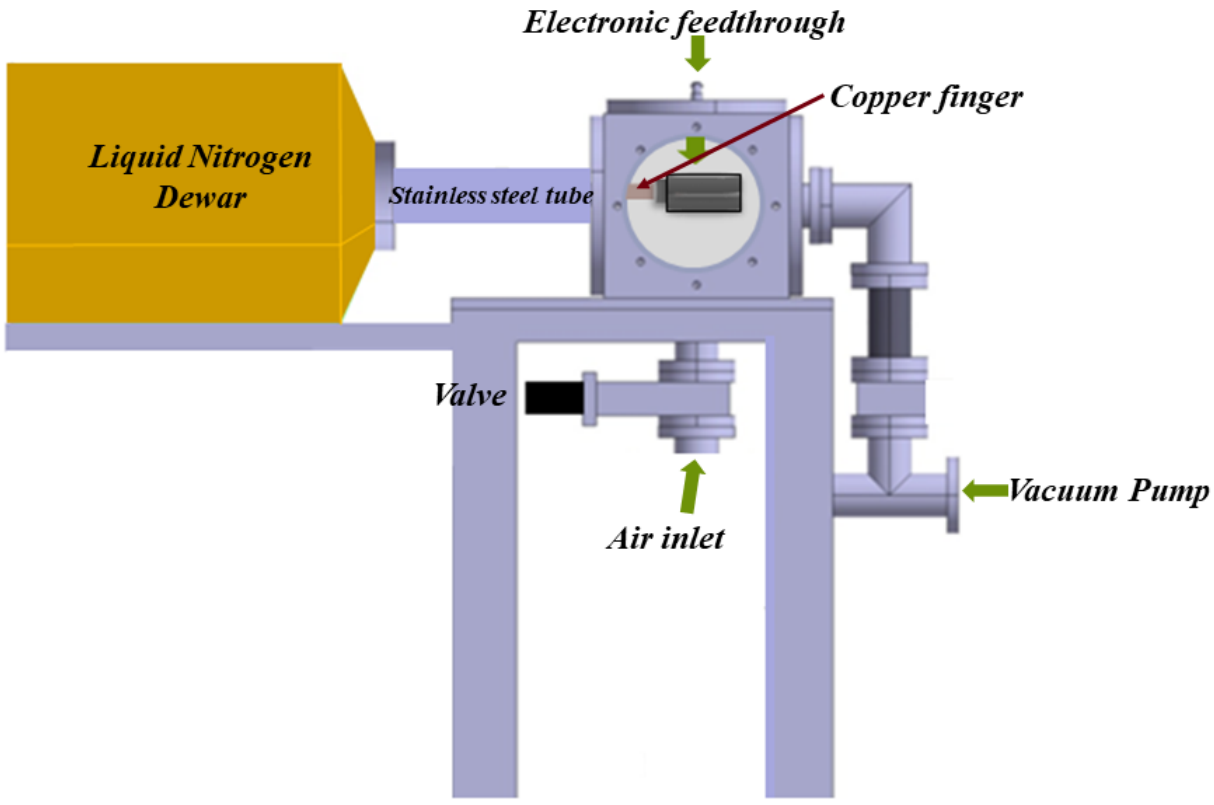

Figure 5 – Diagramme du spectromètre β développé au LNHB dans ce travail. Le cadre noir représente la chambre de détection et les autres composants sont étiquetés en noir.

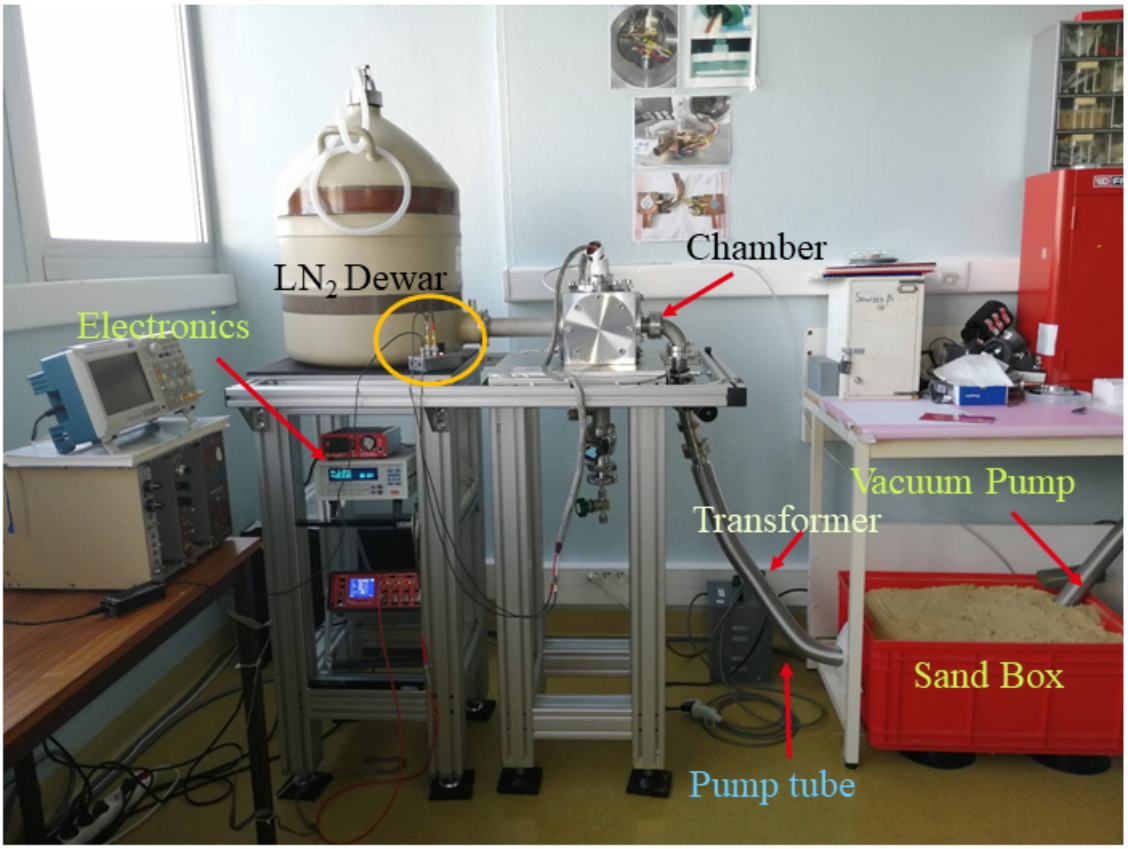

Figure 6 – Photo du nouveau dispositif expérimental de spectrométrie β.

Sources radioactives

La préparation d'une source radioactive joue un rôle majeur dans la mesure précise du spectre en énergie des électrons. Sa qualité peut déformer de manière significative la forme des spectres β [108]. Une source radioactive solide est préparée en effectuant un dépôt radioactif, qui correspond à la répartition d'un certain nombre d'atomes radioactifs sur une zone de définie du support. Afin de garantir que le spectre émergeant de la source soit aussi proche que possible du spectre d'émission réel, il est nécessaire de limiter les phénomènes physiques induits par le support ainsi que par le dépôt radioactif lui-même : rétrodiffusion et auto-absorption.

Les sources radioactives sont préparées sur un support en Mylar. La procédure est la suivante 7 :

(i) Préparation du support de film sur un anneau en acier inoxydable ;

(ii) Électro-pulvérisation de microsphéres de latex qui servent d'agent d'ensemencement ;

(iii) Dépôt de gouttes radioactives ;

(iv) Séchage (au four ou par lyophilisation).

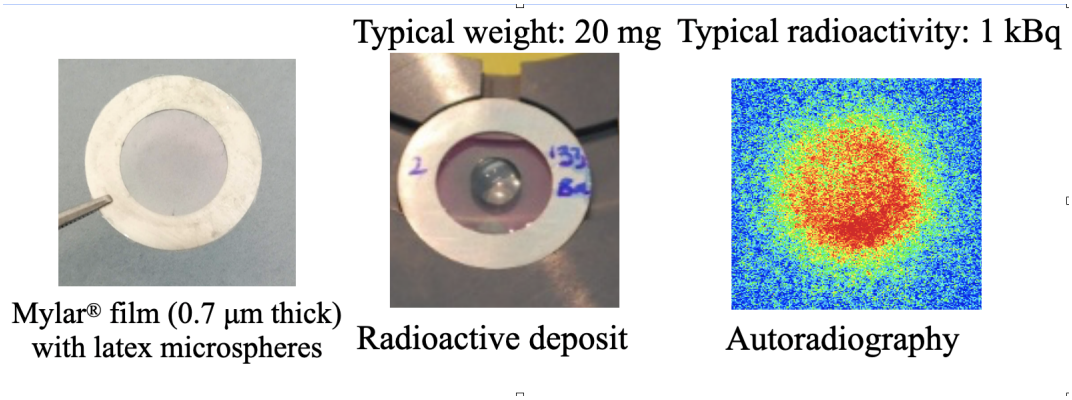

Figure 7 – (1): Un support de source préparé avec un film de Mylar® es des microsphères de latex électro-pulvérisées (2): Dépôt de gouttes radioactives de ^{133}Ba. (3): Autoradiographie d'une source séchée au four.

Résultats

Dans ce travail, les spectres β des désintégrations des ^{14}C, ^{36}Cl, ^{99}Tc et ^{204}Tl ont été mesurés. L'étalonnage en énergie du système de détection a été réalisé en mesurant les particules émises dans les désintégrations ^{109}Cd et ^{207}Bi, qui fournissent une large gamme d'énergies bien définies.

Le spectre bêta mesuré avec notre système de détection ne correspond pas entièrement au spectre émis initialement. En effet, il est déformé par plusieurs facteurs tels que la couche morte des détecteurs, la distance entre les détecteurs, la source radioactive, etc. Cependant, le travail vise à déterminer avec précision le spectre initialement émis. Pour y parvenir, les déformations résiduelles doivent être supprimées, ce qui nécessite une procédure de déconvolution.

Dans cette section, les résultats obtenus pour la décroissance du ^{14}C et ^{99}Tc seront discutés, d'abord, l'influence de l'auto-absorption sur la forme du spectres β, en comparant la mesure avec sa simulation Monte Carlo, puis, les spectres finaux obtenus après la déconvolution qui seront comparé aux spectres mesurés des calorimètres magnétiques métalliques, qui sont très précis et permettent une bonne comparaison et validation.

Influence de la préparation de la source

La mesure du ^{99}Tc a montré un écart entre les spectres mesurés et simulés. En étudiant en détail toutes les causes de deformation, la seule possibilité cohérente et réaliste identifiée était le phénomène d'auto-absorption dans la source radioactive. Pour tester cette dernière hypothèse, de nouvelles sources radioactives ont été préparées avec la méthode de lyophilisation pour contrôler la cristallisation du dépôt.

Pour cette étude, des solutions radioactives avec et sans entraîneur (NH_4TcO_4) ont été utilisées. La présence d'entraîneur (un sel porteur) dans la solution favorise la cristallisation lors du processus de séchage. L'étuvage (processus de séchage au four) est le processus habituel de séchage au LNHB et a été utilisé pour dans une premiére approche. Le processus de lyophil-

isation réduisant la taille des cristaux et donc l'auto-absorption [116], une comparaison a été décidée entre les deux processus de séchage.

De nouvelles sources radioactives ont donc été préparées avec deux types de solution radioactive : une solution contenant un sel porteur et une autre exempte de sel porteur. Ces sources ont été séchées selon deux méthodes : la lyophilisation et l'étuvage. Chaque mesure a été comparée avec le spectre simulé, tout en conservant le spectre mesuré par le MMC comme entrée. Les spectres ont été normalisés par intégration entre 200 keV et 250 keV. L'analyse a permis de tirer les conclusions suivantes :

– Source radioactive avec sel porteur, séchée au four (Figure 8) On observe un désaccord entre la mesure et la simulation en dessous de 60kev à cause du spectre mesuré qui présente une forte déformation. Le paramètre de désaccord est de 1,48 % entre les 22 keV et $E_{\max}$.

– Source radioactive avec sel porteur, lyophilisée (Figure 9) Le spectre mesuré est nettement plus proche du spectre simulé par rapport au cas précédent, ce qui met en évidence le fort impact du processus de séchage. La Figure 10 présente la distribution des résidus et met en évidence une faible déformation à basse énergie (30 - 60 keV), même si le paramètre de désaccord $(1 - R^2)$ n'est que de 0,041 % entre 22 keV et $E_{\max}$. Ce résultat peut s'expliquer par la présence du sel porteur, qui crée des cristaux plus gros dans la source radioactive. En effet, plus la concentration de sel porteur dans la solution est élevée, plus le nombre de cristaux inactifs est important et plus la taille des cristaux dans la source radioactive est grande. Cela augmente l'effet d'auto-absorption, qui est critique pour des électrons de faible énergie.

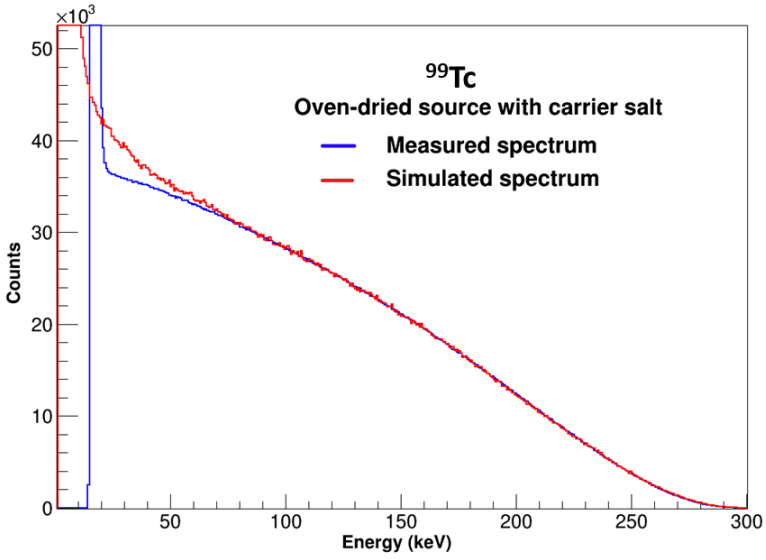

Figure 8 – Comparaison du spectre mesuré du ^{99}Tc avec une solution radioactive avec une solution de sel porteur séchée au four, et du spectre simulé à partir du spectre MMC en entrée.

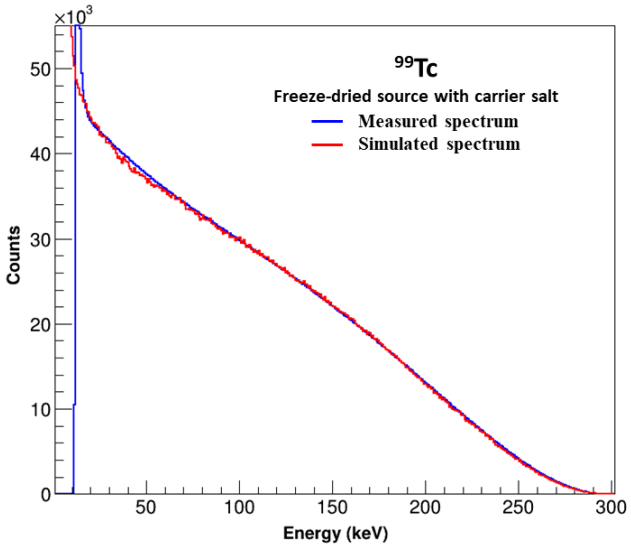

Figure 9 – Comparaison du spectre mesuré du ^{99}Tc avec une solution radioactive avec un sel porteur, séchée par lyophilisation, et du spectre simulé à partir du spectre MMC en entrée.

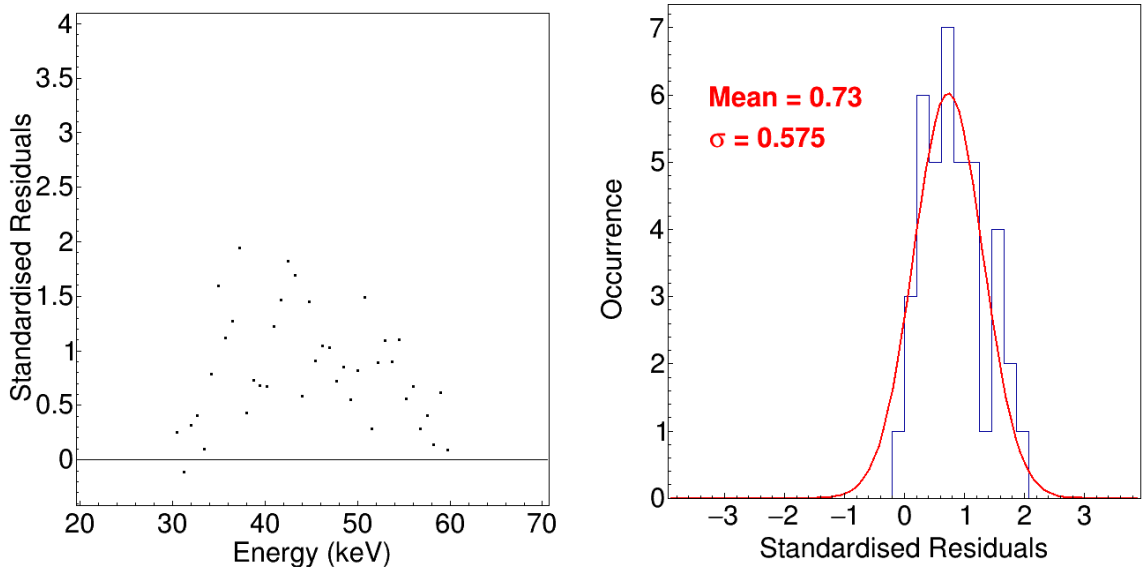

Figure 10 – Résidus des spectres obtenus par en comparant le spectre mesuré de la source préparée avec une solution radioactive avec sel porteur et séchée par lyophilisation (Figure 9) et le spectre simulé en utilisant le spectre MMC comme entrée pour la désintégration du ^{99}Tc.

- Source radioactive sans sel porteur, séchée au four (Figure 11) Le spectre mesuré présente une déformation à basse énergie identique à celle de la source préparée avec une solution contenant du sel porteur et séchée au four. Cela révèle que pour le ^{99}Tc, la technique de préparation de la source, en particulier le processus de séchage, est plus importante que la solution radioactive en elle-même.

- Source radioactive sans sel porteur, lyophilisée (Figure 12) Le spectre mesuré s'avère être en excellent accord avec la simulation jusqu'à 20 keV. Les résidus entre 30 et 60 keV sont

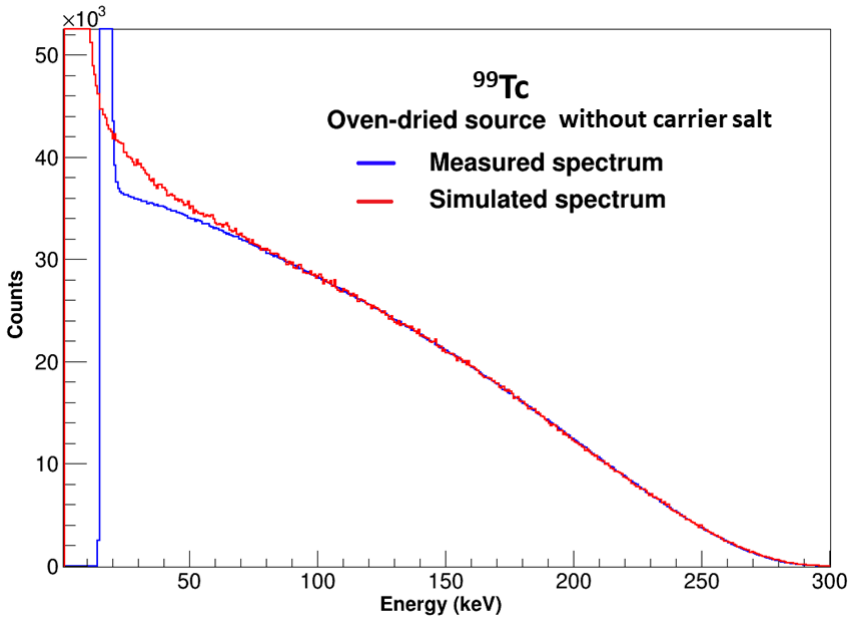

Figure 11 – Comparaison du spectre mesuré de ^{99}Tc pour une solution radioactive sans sel porteur séchée au four, et du spectre simulé à partir du spectre MMC en entrée.

indiqués sur la Figure 13, montrant une déformation moindre par rapport à la Figure 10. Elle montre une influence faible mais existante du choix de la solution radioactive sur la croissance des cristaux. Le paramètre de désaccord (1-R^2) est de 0,035 % entre 22 keV et $E_{\max}$, à comparer avec 1,47 % dans la mesure précédente (séchage au four avec une solution de sel porteur). Le désaccord restant entre la mesure et la simulation semble provenir de l'entrée de la simulation, qui est le spectre mesuré par la MMC. Le spectre mesuré par le MMC (au LNHB) a été comparé à une autre mesure du ^{99}Tc effectuée avec l'installation MMC récemment développée au PTB (Allemagne) [132]. Une légère différence est observée dans la même gamme d'énergie. Cependant, cette différence n'est pas significative en raison de la faible statistique de mesure[2].

Cependant, la procédure de lyophilisation, ainsi que la solution sans entraîneur, ont montré une forte influence sur la forme du spectre β.

Cette étude permet d'obtenir une image globale et cohérente de la situation. Nous avons démontré que le phénomène d'auto-absorption était la principale cause de l'écart observé en-dessous de 60 keV entre les différents spectres de ^{99}Tc mesurés. La méthode de séchage au four semble produire de gros cristaux, dans lesquels les particules β émises perdent une quantité importante de leur énergie cinétique. Le procédé de lyophilisation semble produire des cristaux de taille plus réduite, ce qui minimise le phénomène d'auto-absorption. En outre, il a été observé que la solution radioactive sans sel porteur entraîne une déformation minimale du spectre mesuré, et devrait donc être préférable pour une étude exacte.

[2]Une nouvelle mesure avec plus de statistique est en cours au PTB et une comparaison des mesures du spectre de ^{99}Tc par MMC au LNHB et au PTB, et par détecteurs Si (ce travail) sera effectuée.

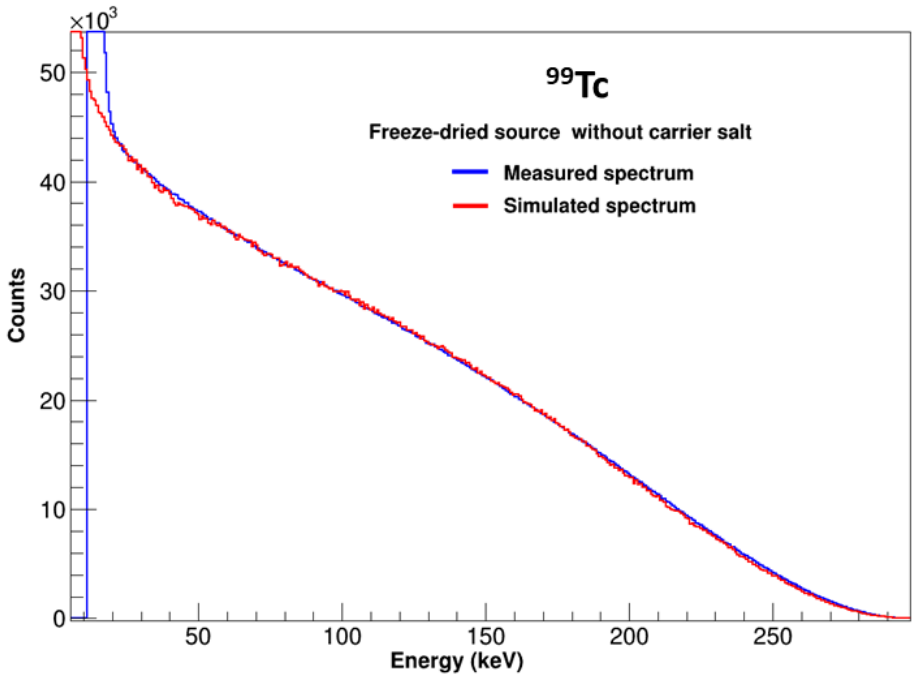

Figure 12 – Comparaison du spectre mesuré de la source ^{99}Tc pour une solution radioactive sans sel porteur séchée par lyophilisation, et du spectre simulé à partir du spectre MMC en entrée.

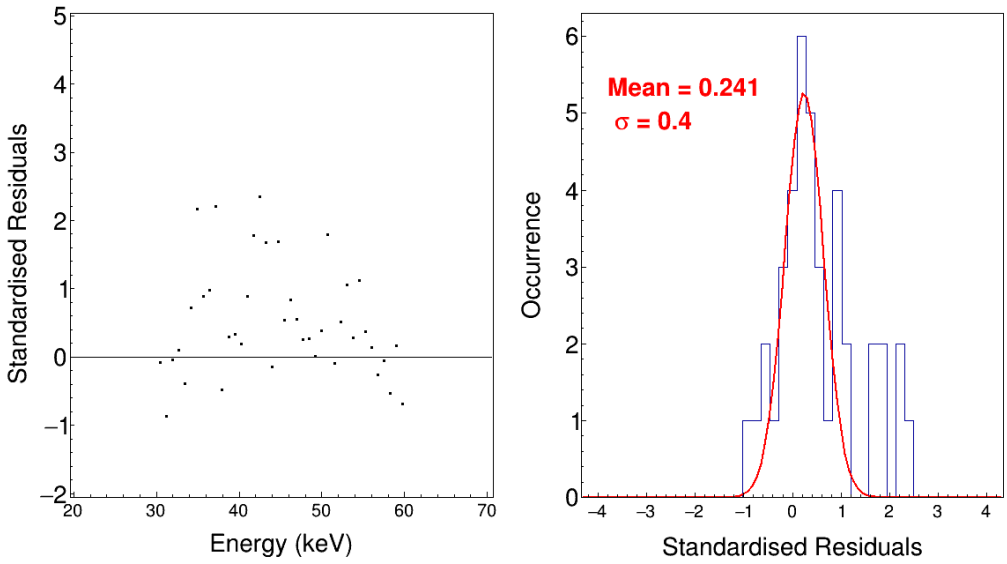

Figure 13 – Résidus des spectres obtenus par la comparaison entre le spectre mesuré d'une source radioactive préparée sans sel et la méthode de lyophilisation (Figure 12) et le spectre simulé en utilisant le spectre MMC comme entrée pour la désintégration ^{99}Tc.

Déconvolution et spectres finaux

Le spectre mesuré résulte de la convolution du spectre initialement émis avec la réponse du système de détection. Afin d'extraire le spectre sans déformation, il est nécessaire de déterminer la fonction de réponse et de déconvoluer le spectre mesuré. La méthode développée dans ce travail est basé sur la méthode d'inversion de matrice, qui a déjà été appliquée dans plusieurs

travaux [134–137]. L'idée a été principalement inspirée de [134] et le détail des justifications mathématiques se trouve dans cet article.

La procédure proposée est une solution exacte à condition que le problème ne soit pas mathématiquement mal posé. L'objectif principal est de déterminer comment le contenu d'un bin en énergie $[E_i, E_{i+1}]$ est réparti sur les autres bins. Pour ce faire, on utilise des simulations mono-énergétiques, une pour chaque bin. Il est alors possible de construire une matrice de réponse du système de détection qui est indépendante de la connaissance du spectre bêta. En appliquant l'inverse de cette matrice au spectre mesuré, on obtient le spectre déconvolué. La fonction de réponse est une matrice carrée et triangulaire. Le spectre mesuré $\mathrm{M}(E_i)$ résulte alors de la multiplication de la matrice de réponse $\mathrm{R}(E_i + \Delta E, E_i)$ du système de détection par le spectre initial $\mathrm{S}(E_i)$:

$$\begin{pmatrix} M(E_0) \\ \vdots \\ \vdots \\ \vdots \\ M(E_N) \end{pmatrix} = \begin{pmatrix} R(E_0+\Delta E, E_0) & \cdots & R(E_N+\Delta E, E_0) \\ \vdots & & \vdots \\ \vdots & \ddots & \vdots \\ \vdots & & \vdots \\ R(E_0+\Delta E, E_N) & \cdots & R(E_N+\Delta E, E_N) \end{pmatrix} \times \begin{pmatrix} S(E_0) \\ \vdots \\ \vdots \\ \vdots \\ S(E_N) \end{pmatrix} \tag{6}$$

Tous les spectres mesurés sont déconvolués en utilisant la même procédure.

Décroissance du carbon-14

Le spectre de ^{14}C mesuré avec le système de détection quasi-4π a été déconvolué. Le spectre résultant est proche d'une forme permise (Figure 14) et pas de la forme de Kuzminov [133]. Les spectres ont été normalisés par une intégration entre 40 et 150 keV. Le paramètre de désaccord $(1 - R^2)$ entre le spectre déplié et la forme de Kuzminov est de 0,28 % entre 22 keV et $E_{\max}$, alors que, avec la forme autorisée, il est de 0,04 % entre 22 keV et $E_{\max}$.

Certaines fluctuations en dessous de 30 keV peuvent être dues au processus de déploiement lui-même, en raison de statistiques insuffisantes pour les simulations de pulse ou d'un binning trop important si proche du seuil d'énergie. Une telle étude nécessiterait beaucoup plus de simulations et n'a pas encore été testée. Fait remarquable, le paramètre de désaccord descend à 0,008 % pour le spectre autorisé entre 26 keV et $E_{\max}$.

La comparaison entre le spectre final (déconvolué) et le spectre mesuré par la MMC, donnée sur la Figure 15, montre un excellent accord jusqu'à 26 keV avec un paramètre de désaccord $(1 - R^2)$ égal à 0,05 %, ce qui valide la qualité de notre mesure. Les résidus correspondants sont uniformément distribués à l'intérieur de 2σ (Figure 16). Les pics à basse énergie dans le spectre des MMC sont dus à des sources d'étalonnage de l'énergie.

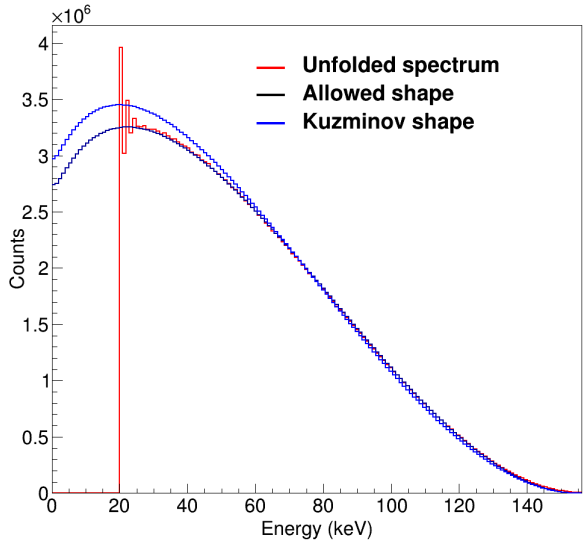

Figure 14 – Le spectre déconvolué de ^{14}C (rouge), le spectre permise (noir) et le spectre de Kuzminov (bleu).

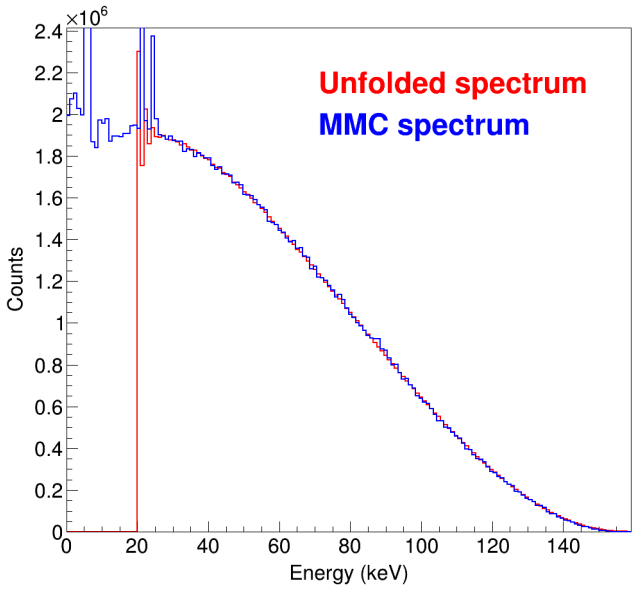

Figure 15 – Spectre déconvolué de ^{14}C (rouge) et spectre mesuré par la MMC (bleue).

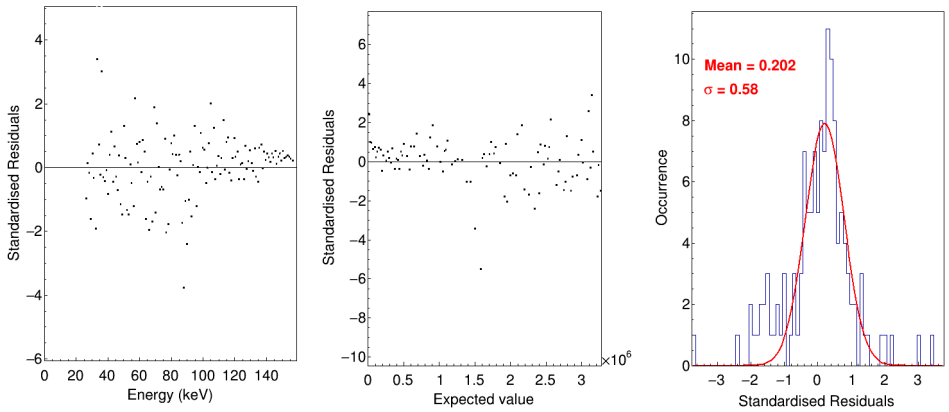

Figure 16 – Résidus entre le spectre déconvolué du ^{14}C et le spectre MMC, tous deux montrés en Figure 15

Décroissance du technétium-99

Le spectre du ^{99}Tc mesuré avec le système de détection quasi-4π a été déconvolué. Le spectre final, déconvolué, s'avère être en excellent accord avec la mesure MMC au LNHB (Figure 17). Les spectres ont été normalisés par intégration entre 40 et 290 keV. Le paramètre de désaccord $(1 - R^2)$ est égal à 0,06 % entre 26 keV et $E_{\max}$. Les résidus sont distribués dans un intervalle de 2σ (Figure 18), ce qui montre un excellent accord entre les deux mesures. Cependant, une petite tendance peut encore être observée dans la distribution de l'énergie des résidus, qui pourrait provenir de l'une ou l'autre des deux mesures.

Le spectre a également été comparé à la forme déterminée par Reich [95] et au spectre déconvolué de la mesure 2π effectuée au LNHB en 2014 (voir Figure 19). Notre spectre est en bon accord avec tous les spectres au-delà de 120 keV. Le facteur de forme de Reich a été extrait à partir de la mesure du spectre entre 55 keV et 250 keV. Le spectre correspondant sur la Figure 19 est construit en appliquant ce facteur de forme sur toute la gamme en énergie, ce qui explique son incohérence manifeste avec notre mesure et la mesure MMC à basse énergie. Les mêmes raisons que pour le spectre ^{14}C, à savoir un fort effet de rétrodiffusion à corriger et une préparation différente de la source, peuvent expliquer la différence entre le spectre 2π et les deux autres spectres.

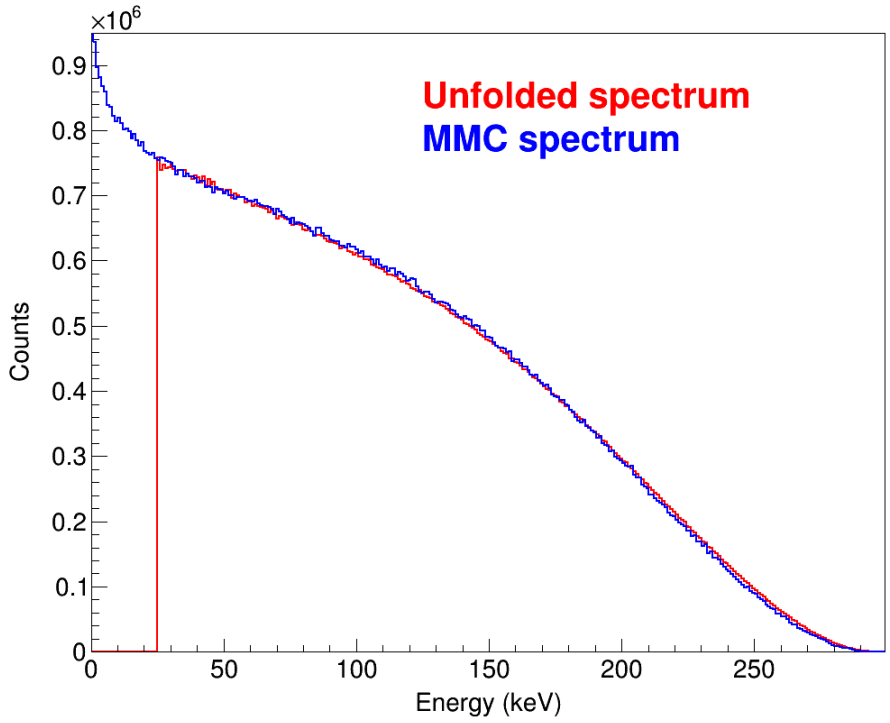

Figure 17 – Le spectre déconvolué de ^{99}Tc (rouge), comparé au spectre mesuré par MMC (bleu).

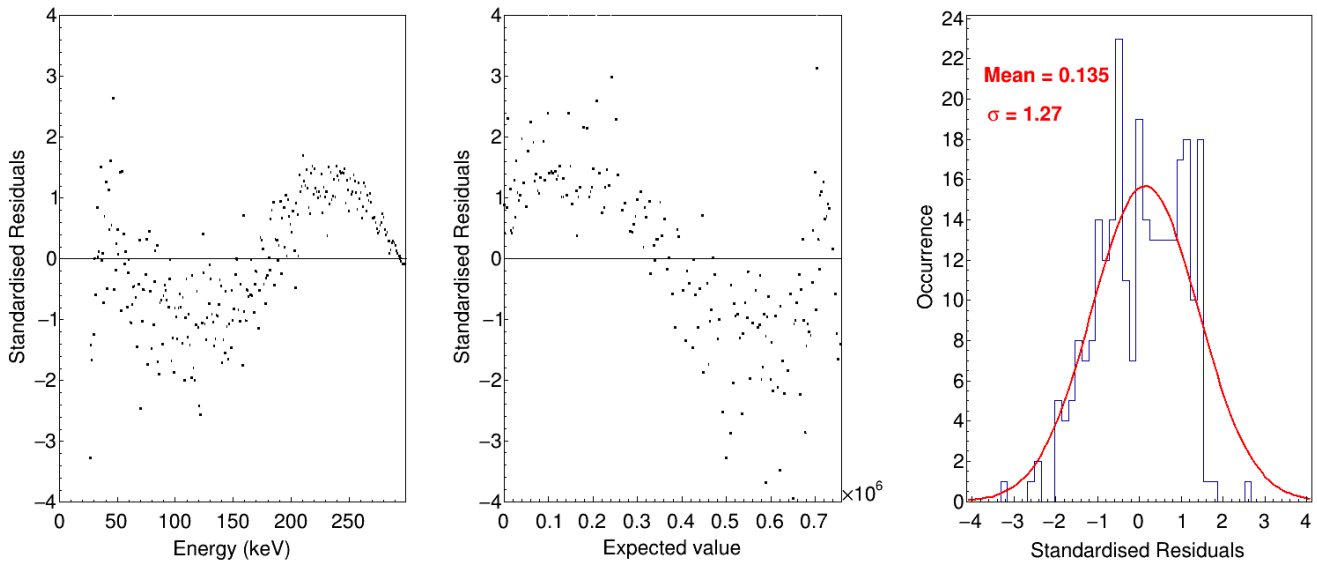

Figure 18 – Résidus entre le spectre déconvolué du ^{99}Tc et le spectre MMC, tous deux montrés en figure 17.

Conclusion et perspectives

La connaissance précise de la forme du spectre β a servi une vaste communauté scientifique depuis les années 1940. Au cours des dix dernières années, l'étude de la désintégration β a connu un regain d'intérêt. En effet, elle a joué un rôle essentiel dans la compréhension de l'interaction faible en physique fondamentale. Aujourd'hui, elle contribue en métrologie de la radioactivité à réduire les incertitudes des mesures d'activité par la méthode de comptage par scintillation liquide. Elle apporte également des informations cruciales aux développements récents en médecine nucléaire, et les acteurs du domaine de l'énergie nucléaire demandent un enrichissement des bases de données existantes. L'amélioration des techniques expérimentales, la précision croissante des simulations Monte Carlo et la croissance continue de la puissance de calcul permettent de revoir notre compréhension expérimentale et théorique des spectres β.

Au LNHB, une nouvelle technique expérimentale, appelée calorimétrie métallique magnétique, a été mise au point au cours des dix dernières années pour les désintégrations β de très basse énergie. Les premiers résultats ont permis de comprendre certains effets atomiques subtils, généralement négligés. Cette technique est difficile à mettre en œuvre et est intrinsèquement limitée aux spectres de faible énergie, avec des énergies maximales inférieures à 500 keV, et à des taux de comptage très faibles, environ 10 coups par seconde. Une autre technique complémentaire est donc nécessaire. Ainsi, le développement d'un dispositif avec un seul détecteur silicium avait été mis en œuvre dans le passé. Cependant, les spectres mesurés avec un angle solide inférieur à 2π sr souffraient d'un dépôt partiel d'énergie des électrons et ne répondaient pas aux exigences métrologiques en termes de précision.

Ce travail de thèse visait à développer un nouveau dispositif expérimental dédié à la mesure

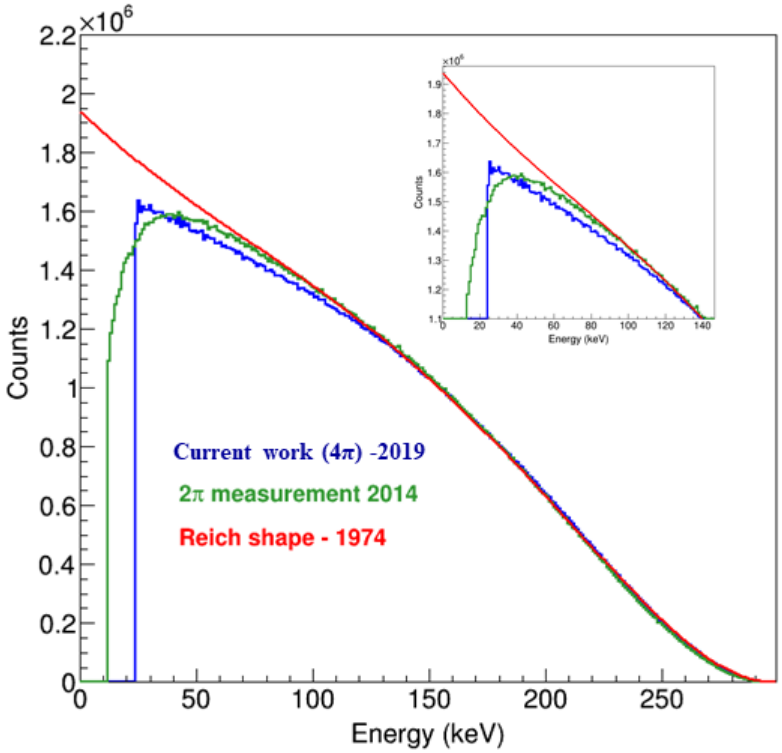

Figure 19 – Comparaison des spectres ^{99}Tc deconvolué de mesures dans des géométries 2π et quasi-4π avec un spectre basé sur le facteur de forme expérimental de Reich [95].

des spectres β avec une précision métrologique. Un dispositif expérimental basé sur des détecteurs silicium dans un angle solide de près de 4π sr a été développé. Ce système est adaptable à différents types de détecteurs silicium, PIPS et Si(Li). Une étude détaillée utilisant des simulations Monte Carlo PENELOPE a été réalisée afin de minimiser les déformations dues à la géométrie et d'optimiser la configuration du dispositif. L'appareil expérimental a été mis à niveau en effectuant plusieurs cycles de mesures, améliorant la configuration après chaque série d'analyses. Grâce à la mise en place d'un contrôle de la température, nous avons prouvé que le système de refroidissement développé dans le passé n'était pas suffisant pour l'utilisation de détecteurs Si(Li). Avec le nouveau système que nous avons développé, nous avons observé que, même si les détecteurs PIPS sont opérationnels à température ambiante, les refroidir à 100 K améliore leurs performances, avec une résolution en énergie réduite de 12 à 9 keV. En utilisant des simulations Monte Carlo, l'influence de la source radioactive sur la forme du spectre mesuré a été étudiée très précisément, un sujet rarement traité dans la littérature. L'influence de l'utilisation d'un film Mylar de 0,7 μm d'épaisseur comme support au lieu d'un film plus traditionnel de 18 μm d'épaisseur a été quantifiée. Les différentes techniques de préparation de source et leur influence ont également été étudiées. L'impact du processus de cristallisation a été démontré : une solution sans sel porteur combinée à un processus de lyophilisation réduit drastiquement la déformation due à l'auto-absorption, ce qui permet d'améliorer les mesures.

Dans ce travail, quatre radionucléides se désintégrant par transition β ont été étudiés : ^{14}C,

^{99}Tc, ^{36}Cl et ^{204}Tl. Les spectres mesurés ont été comparés aux simulations PENELOPE correspondantes. L'incohérence observée dans le cas des mesures à température ambiante a conduit à l'étude de la configuration géométrique réelle. En variant la distance entre les détecteurs dans les simulations, nous avons conclu que les pièces de cuivre n'avaient pas été usinées aussi précisément que prévu au départ et que la distance n'était pas de 3 mm comme prévu mais de 2,5 mm. Ce fait a également été confirmé par des mesures directes, et l'influence d'une géométrie connue avec précision sur la forme du spectre a été quantifiée. La mesure des pics d'électrons de conversion du ^{109}Cd et du ^{207}Bi nous a permis de caractériser les détecteurs de 25 keV à 1060 keV. Le seuil de détection en énergie est de 15 keV et la résolution en énergie est de 9 keV à 62,5 keV. Des résidus standardisés ont été définis et leur analyse, combinée au paramètre de désaccord (1-R^2), a permis de quantifier l'excellent accord entre les mesures et les simulations. Les déformations résiduelles qui se sont avérées être encore présentes dans les spectres mesurés ont été corrigées pour obtenir les spectres réels émis initialement par les radionucléides. Une méthode de déconvolution basée sur des simulations Monte Carlo a été développée. La fonction de réponse a été construite à l'aide de simulations Monte Carlo mono-énergétiques. La méthode a été validée en l'appliquant sur des spectres simulés : nous avons pu retrouver les spectres d'entrée initiaux au-delà de 10 keV. La comparaison de certains spectres précis de notre système de détection quasi-4π avec des mesures de grande précision par calorimétrie métallique magnétique (MMC) a démontré que nous pouvions effectuer des études précises avec notre appareil de 30 keV jusqu'à l'énergie maximale.

Les facteurs de forme ont ensuite été extraits des spectres mesurés pour les ^{14}C, ^{99}Tc et ^{204}Tl, avec des géométries quasi-4π et 2π, et par MMC lorsqu'ils existent. Les résultats ont été comparés entre eux et avec les résultats disponibles dans la littérature. Pour le ^{14}C, il a été constaté que la forme du spectre était plus proche qu'attendu d'une transition permise standard, avec un excellent accord entre les mesures quasi-4π et par MMC. Ces résultats fournissent un nouveau facteur de forme de référence du spectre du ^{14}C. Pour le ^{99}Tc, le facteur de forme provenant des mesures quasi-4π et par MMC sont en excellent accord l'un avec l'autre. Une analyse disponible dans la littérature a également été réalisée avec des détecteurs silicium il y a 45 ans au-dessus de 55 keV, et un bon accord a été trouvé avec ce résultat dans la gamme d'énergie commune. Une étude détaillée de l'auto-absorption en fonction de la technique de préparation de source utilisée a été nécessaire pour garantir un résultat précis jusqu'à 26 keV. Le facteur de forme extrait pour le ^{204}Tl de notre mesure quasi-4π montre un bon accord avec les résultats disponibles dans la littérature. La comparaison avec les spectres théoriques a également mis en évidence un meilleur accord lorsque l'on considère une modélisation incluant les effets atomiques, ce qui démontre la sensibilité de notre mesure. Toutes ces comparaisons valident notre approche expérimentale. Avec un dispositif expérimental basé sur des détecteurs silicium en configuration quasi-4π, il est possible de mesurer beaucoup plus de radionucléides par rapport aux appareils MMC. Bien évidemment, les résolutions et les seuils en énergie

similaires ne sont pas comparables. Les deux techniques sont définitivement complémentaires pour des études précises de spectrométrie β.

Bien que notre dispositif ait été perfectionné tout au long de ce travail, il reste encore quelques sujets à approfondir. Il manque encore une excellente étude de la désintégration de ^{36}Cl. Une source radioactive avec des cristaux les plus petits possibles doit encore être préparée et mesurée. Comme nous avons déjà vu que même la technique de lyophilisation n'est pas suffisante, une nouvelle méthode de préparation doit être mise au point pour fabriquer une source dont la qualité répond à nos exigences. Il serait alors possible de comparer avec les facteurs de forme expérimentaux disponibles dans la littérature.

Nous avons commencé à adapter notre système de détection quasi-4π à deux détecteurs Si(Li) de 5 mm d'épaisseur en remplacement des détecteurs PIPS. Ce système de détection a déjà été conçu, usiné et mis en œuvre, et les détecteurs doivent encore être testés et caractérisés. Les détecteurs sont plus grands que les PIPS (500 mm^2 au lieu de 300 mm^2), et leurs supports ont été adaptés. Ils sont également plus épais (5 mm au lieu de 1 mm), ce qui permettra de mesurer des spectres β jusque vers 3 MeV. L'électronique correspondante à l'intérieur de la chambre a également été améliorée avec des connexions plus robustes. L'ensemble du dispositif nécessite plus d'espace à l'intérieur de la chambre que pour les PIPS. L'ensemble du dispositif Si(Li) ne peut pas être manipulé en toute sécurité, et une nouvelle chambre à vide devrait être envisagée à l'avenir. Cela permettrait également d'utiliser davantage de détecteurs en série pour des mesures à plus haute énergie, dans une configuration de télescope $\Delta E - E$, ou pour des mesures en coïncidence avec des détecteurs de rayons γ.

Les résultats de cette étude ont montré un excellent accord avec les mesures par MMC, les plus précises actuellement. Pour améliorer encore notre précision, on peut par exemple envisager une mesure complète 4π avec le radionucléide déposé directement sur un wafer de silicium et un second wafer collée sur le premier, dans une configuration en sandwich. Dans ce cas, des wafers de silicium avec une couche morte la plus faible possible seront nécessaires, ainsi qu'un excellent dépôt radioactif pour éviter l'auto-absorption. Une telle technique sera coûteuse car les détecteurs ne seront pas réutilisables pour un autre radionucléide. Néanmoins, elle permettrait de tester une configuration complète 4π avec des détecteurs silicium et une comparaison très précise avec les spectres des dispositifs MMC et quasi-4π.

List of Tables

List of Figures

Abstract

Since the 1970s, the study of the β shape has been limitedly investigated. A growing interest has been noticed from several users from ionising radiation metrology, nuclear medicine, nuclear energy for the residual power of reactors, and from fundamental physics. The existing databases are incomplete and lack of accuracy to meet their requirements. This thesis aims to develop an experimental set-up dedicated to precise β spectrometry. A β spectrometer has been developed based on two silicon detectors and a radioactive source in the middle, and has been optimised in order to reach a quasi-4π geometry. Different source preparation techniques have been studied and their influence on the shape of the β spectrum has been quantified. The device has been characterised using the conversion electron peaks of ^{109}Cd and ^{207}Bi decays, and the β spectra from ^{14}C, ^{36}Cl, ^{99}Tc and ^{204}Tl decays have been studied. Even though being minimised, some distortions remain in the measured spectra that are not compatible with the precision sought. An unfolding method has been developed to correct for these distortions based on PENELOPE Monte Carlo simulations. The response function of the detection system has been built from mono-energetic simulations and the measured spectra have been unfolded by applying the matrix inversion method. Finally, the resulting spectra have been compared with some high-precision measurements performed with Metallic Magnetic Calorimeters, showing excellent agreement in the common energy range. The experimental shape factors have been extracted for ^{14}C, ^{99}Tc and ^{204}Tl spectra and compared with results available in the literature.

Key-words

Beta spectra, Silicon detectors, Ultra-thin radioactive sources, Spectral deconvolution, Experimental shape factor, Carbon-14, Technetium-99, Thallium-204.

Résumé

Depuis les années 1970, la forme des spectres β n'a été étudiée que de manière très limitée. Différents utilisateurs manifestent un intérêt de plus en plus grand en métrologie des rayonnements ionisants et en médecine nucléaire, ainsi que pour le calcul de la puissance résiduelle des réacteurs nucléaires et pour certains sujets de physique fondamentale. Les bases de données actuelles sont incomplètes et manquent de précision pour satisfaire leurs besoins. Cette thèse vise à développer un dispositif expérimental dédié à l'étude précise des spectres β. Un spectromètre β a été développé à partir de deux détecteurs silicium et d'une source radioactive placée en leur centre, et a été optimisé pour obtenir un angle solide de détection aussi proche que possible de 4π sr. Différentes techniques de préparation de source ont été étudiées et leur influence sur la forme du spectre β a été quantifiée. Le dispositif a été caractérisé par les pics des électrons de conversion émis lors des désintégrations du ^{109}Cd et du ^{207}Bi, et les spectres β issus des désintégrations du ^{14}C, du ^{36}Cl, du ^{99}Tc et du ^{204}Tl ont été étudiés. Les spectres mesurés présentent encore des déformations incompatibles avec la précision recherchée, malgré nos efforts pour les minimiser. Une méthode de déconvolution spectrale a été développée pour corriger ces déformations en s'appuyant sur le code de simulation Monte Carlo PENELOPE. La fonction réponse du système de détection a été construite à l'aide de simulations mono-énergétiques et les spectres mesurés ont été déconvolués grâce à la méthode d'inversion matricielle. Les spectres ainsi déterminés ont été comparés à des spectres très précis mesurés par calorimétrie métallique magnétique et un excellent accord a été mis en évidence dans la gamme de mesure commune. Les facteurs de forme expérimentaux ont été extraits pour les spectres du ^{14}C, du ^{99}Tc et du ^{204}Tl et ont été comparés avec les résultats disponibles dans la littérature.

Mots-clés

Spectres bêta, Détecteurs silicium, Sources radioactives ultra-minces, Déconvolution spectrale, Facteurs de forme expérimentaux, Carbone-14, Technétium-99, Thallium-204.